



**NTNU – Trondheim**  
Norwegian University of  
Science and Technology

# Impact Against Offshore Pipelines

Experiments and Numerical Simulations

**Morten Sagbakken Hovdelien**  
**Vegard Aune**

Civil and Environmental Engineering

Submission date: June 2012

Supervisor: Tore Børvik, KT

Co-supervisor: Odd Sture Hopperstad, KT

Norwegian University of Science and Technology  
Department of Structural Engineering





## MASTER THESIS 2012

SUBJECT AREA: Structural mechanics	DATE: 11th June 2012	NO. OF PAGES: 14 + 158 + 27
---------------------------------------	-------------------------	--------------------------------

TITLE: <b>Impact against offshore pipelines</b>  Støt på offshore rørledninger	
BY:  Vegard Aune and Morten S. Hovdelien	 

### SUMMARY:

In the present thesis impact against offshore pipelines was studied. Incipient fracture in the pipes after impact was of special interest. The present work was a continuation of previous theses on the subject, and part of an ongoing research program between SIMLab (NTNU) and Statoil ASA.

Component tests and numerical simulations using ABAQUS/Explicit and LS-DYNA were carried out to investigate the problem. Two pipes were impacted at different velocities in the pendulum accelerator at the Department of Structural Engineering, NTNU. The most exposed regions were investigated metallurgically to examine the material behavior at large deformations due to the impact.

Pre-compressed notched tension tests at large compressive plastic strains (up to 40 %) were conducted. A material model with combined kinematic and isotropic work-hardening was calibrated based on the material tests. Inverse modeling was carried out with the optimization tool LS-OPT. In addition, the material model consisted of an uncoupled fracture criterion. The combined material model was used in the numerical simulations.

The material tests revealed a distinct Bauschinger effect, transient and permanent softening, as well as a work-hardening stagnation during reversed loading. Simulations of the material tests in ABAQUS/Explicit corresponded well with the experiments. However, simulations of the pipe in ABAQUS/Explicit revealed little improvement regarding the global response compared to previous theses. Further, the volume element model in LS-DYNA revealed hydrostatic tension in the critical element during rebound, where incipient fracture was assumed to appear. This was supported by metallurgical investigations revealing a crack through 75 % of the thickness after impact at the highest velocity. It is clear that this decreases the strength of the pipes. Hence, cracks will propagate through the thickness earlier than expected during stretching in the simulations. This indicates that the single-parameter assumption regarding the fracture criterion used in this thesis ceases to be valid for the component test. To recreate the fracture in the impacted pipes an additional formulation must be included.

RESPONSIBLE TEACHER: Tore Børvik

SUPERVISOR(S): Tore Børvik and Odd Sture Hopperstad

CARRIED OUT AT: Norwegian University of Science and Technology (NTNU)





## MASTEROPPGAVE 2012

FAGOMRÅDE: Beregningsmekanikk	DATO: 11.06.2012	ANTALL SIDER: 14 + 158 + 27
----------------------------------	---------------------	--------------------------------

TITTEL:

**Støt på offshore rørledninger**

Impact against offshore pipelines

UTFØRT AV:

Vegard Aune og  
Morten S. Hovdelien



SAMMENDRAG:

Hensikten med oppgaven var å studere støt på offshore rørledninger. Hovedfokuset var et eventuelt brudd under støtfasen. Oppgaven er en videreføring av to tidligere masteroppgaver, og inngår som en del av et forskningsprosjekt mellom SIMLab (NTNU) og Statoil ASA.

For å undersøke problemet ble det gjennomført komponenttester, og numeriske simuleringer i ABAQUS/Explicit og LS-DYNA. To rør ble utsatt for støt med ulik hastighet i pendel akseleratoren ved Institutt for konstruksjonsteknikk, NTNU. Metallurgiske undersøkelser ble gjennomført i samarbeid med SINTEF for å undersøke oppførselen til materialet ved store deformasjoner.

Det ble utført trykk-strekk tester med 40 % plastisk tøyning i trykk før disse ble strekkpåkjent. En kombinert materialmodell bestående av kinematisk og isotrop fastning ble kalibrert med bakgrunn på disse testene. Dette ble gjort ved invers modellering i optimeringsprogrammet LS-OPT. Materialmodellen bestod også av et ukoblet bruddkriterium, og ble benyttet i de numeriske simuleringene.

Resultatene fra trykk-strekk testene viste en tydelig Bauschinger effekt og stagnering av fastningen ved reversert last. De numeriske simuleringene av trykk-strekk testene ble utført i ABAQUS/Explicit og samsvarte med forsøkene. Materialmodellen ga derimot ingen stor forbedring i simuleringene av komponenttesten sammenlignet med tidligere år.

Modellen i LS-DYNA bestående av volumelementer viste hydrostatisk strekk under spenningsomlagringen etter støtet. Det forventes at brudd oppstår i denne fasen. Dette ble underbygget av de metallurgiske undersøkelsene av det mest påkjente røret, da det ble oppdaget en sprekk gjennom 75 % av veggtykkelsen. Denne sprekken er antatt å redusere styrken i røret etter støtet. Utsettes røret for påfølgende strekk vil bruddet utvikle seg raskere enn først antatt, da en sprekk allerede er initiert. Det er derfor vanskelig å beskrive bruddet ved hjelp av bare en parameter. For å gjenskape bruddet på en tilfredsstillende måte bør derfor flere parametere inkluderes i bruddkriteriet.

FAGLÆRER: Tore Børvik

VEILEDER(E): Tore Børvik og Odd Sture Hopperstad

UTFØRT VED: Norges Teknisk Naturvitenskapelige Universitet (NTNU)



## **MASTER THESIS 2012**

for

*Vegard Aune og Morten Hovdelien*

### **Impact against offshore pipelines**

*Støt på offshore rørledninger*

Guidelines have been worked out on how to design subsea pipelines in fishing areas subjected to interference by trawl gear. Three load scenarios are covered; 1) impact, 2) pull-over and 3) hooking. Impact is associated with the transfer of the impacting trawl-board energy to the pipeline for a short duration of time, and causes local deformation/indentation of the pipeline. During pull-over, the trawl board is pulled over the pipeline by the trawl cable. The pull-over scenario has a longer duration and may cause large transverse deformations of the pipeline. In the third load scenario, the trawl-gear crossing of the pipeline may cause the trawl gear to get stuck (hooked) underneath the pipeline. The guidelines are limited to trawl-board masses up to 3500 kg, which is much less than the new trawl-board masses that are expected to be used in the northern part of the North Sea in the future. Currently these guidelines are being replaced with a new recommended practice with updated trawl gear data (largest trawl board up to 5000 kg and clamp weights up to 9000 kg). However, the present guidelines do not say anything about the residual strength of a damaged pipeline and what kind of acceptance criteria that shall be used with respect to incipient fracture. The effects of the pipes being filled with a liquid or gas, and the effects of internal pressure, are also subject to further investigation.

In this master thesis the topics described above shall be studied by means of some material and component tests combined with finite element simulations. The candidates shall first carry out a literature study on pipes subjected to impact loading relevant for the problem at hand. Impact tests on both empty and filled scaled pipes have previously been carried out in SIMLab's laboratory for dynamic testing, before they were stretched straight at Statoil's laboratory at Rotvoll in an attempt to compel fracture. Some of these tests may be repeated in the present thesis. The numerical analyses shall be supported by material tests to calibrate relevant material models. In addition to existing material test data, tensile tests on specimens first compressed to various levels of plastic strain should be conducted to study the effect of damage under compression of ductile materials. When the finite element model is validated against the component tests, the stress history in the critical area should be investigated. Incipient fracture in the pipes after impact is of special interest. The present work is a part of an ongoing research programme between SIMLab, Centre for Research-based Innovation, NTNU and Statoil ASA.

*Supervisors:* Tore Børvik and Odd Sture Hopperstad (NTNU)

The thesis must be written according to current requirements and submitted to Department of Structural Engineering, NTNU, no later than June 11<sup>th</sup>, 2012.

NTNU, January 16<sup>th</sup>, 2012

Tore Børvik

Professor



## Acknowledgements

Our supervisors during this master's thesis have been Professor Tore Børvik and Professor Odd Sture Hopperstad at the Structural Impact Laboratory (SIMLab), Department of Structural Engineering, Norwegian University of Science and Technology (NTNU). Their continuous support, guidance and encouragement throughout this work are highly appreciated. In addition, we wish to thank PhD Candidate Martin Kristoffersen and Professor Magnus Langseth for valuable input and discussions.

Dr. Håvar Iltad and Dr. Erik Levold at Statoil ASA research center (Rotvoll) are acknowledged for motivating this project and their contribution.

The experimental work in this thesis has been carried out at the laboratories at the Department of Structural Engineering, NTNU. The assistance of the laboratory staff is acknowledged, in particular Trond Auestad and Tore Kristensen (SINTEF), who carried out the experimental tests. We also appreciate the contribution received from Hans Lange at SINTEF during the material tests.

We wish to thank research scientist Dr. Ida Westermann at SINTEF for conducting the metallurgical study, and for her guidance on the topic. Also, we wish to thank research scientist Dr. Torodd Berstad at the Department of Structural Engineering for his assistance in terms of the Finite Element Method (FEM), and in particular for his modeling contribution and general use of the FEM software LS-DYNA. We must also mention research scientist Dr. Stéphane Dumoulin at SINTEF, who introduced and guided us in the use of the optimization tool LS-OPT.

Thanks to the inspiring and friendly working environment at SIMLab.

Trondheim, June 11 2012

---

Vegard Aune

---

Morten S. Hovdelien



## Abstract

In the present thesis impact against offshore pipelines was studied. Incipient fracture in the pipes after impact was of special interest. The present work was a continuation of previous theses on the subject, and part of an ongoing research program between SIMLab (NTNU) and Statoil ASA.

Component tests and numerical simulations using ABAQUS/Explicit and LS-DYNA were carried out to investigate the problem. Two pipes were impacted at different velocities in the pendulum accelerator at the Department of Structural Engineering, NTNU. The most exposed regions were investigated metallurgically to examine the material behavior at large deformations due to the impact.

Pre-compressed notched tension tests at large compressive plastic strains (up to 40 %) were conducted. A material model with combined kinematic and isotropic work-hardening was calibrated based on the material tests. Inverse modeling was carried out with the optimization tool LS-OPT. In addition, the material model consisted of an uncoupled fracture criterion. The combined material model was used in the numerical simulations.

The material tests revealed a distinct Bauschinger effect, transient and permanent softening, as well as a work-hardening stagnation during reversed loading. Simulations of the material tests in ABAQUS/Explicit corresponded well with the experiments. However, simulations of the pipe in ABAQUS/Explicit revealed little improvement regarding the global response compared to previous theses. Further, the volume element model in LS-DYNA revealed hydrostatic tension in the critical element during rebound, where incipient fracture was assumed to appear. This was supported by metallurgical investigations revealing a crack through 75 % of the thickness after impact at the highest velocity. It is clear that this decreases the strength of the pipes. Hence, cracks will propagate through the thickness earlier than expected during stretching in the simulations. This indicates that the single-parameter assumption regarding the fracture criterion used in this thesis ceases to be valid for the component test. To recreate the fracture in the impacted pipes an additional formulation must be included.



# Contents

<b>Acknowledgements</b>	<b>vii</b>
<b>Abstract</b>	<b>ix</b>
<b>1 Background and motivation</b>	<b>1</b>
<b>2 Theory</b>	<b>5</b>
2.1 Review of previous research . . . . .	5
2.1.1 Load reversal at large strains . . . . .	5
2.1.2 Numerical damage models . . . . .	10
2.2 Impact load and energy absorption . . . . .	14
2.3 Deformation of simply supported pipes loaded at the midspan . . . . .	15
2.4 Analytical models for calculating impact capacity of pipes . . . . .	17
2.5 Mechanics of materials . . . . .	21
2.5.1 Yield criterion and plastic flow rule . . . . .	21
2.5.2 Work-hardening . . . . .	25
2.5.3 Large strains . . . . .	29
2.5.4 Necking . . . . .	32
2.5.5 Bridgman’s analysis . . . . .	34
2.6 Physical mechanisms of fracture . . . . .	36
2.6.1 Ductile fracture . . . . .	37
2.6.2 Cleavage fracture . . . . .	40
2.7 Fracture criteria . . . . .	42
<b>3 Introductory studies</b>	<b>45</b>
3.1 Identification of material parameters by the method of least squares . . . . .	46
3.2 Identification of material parameters with LS-OPT . . . . .	48
3.2.1 Numerical modeling . . . . .	48
3.2.2 Optimization in LS-OPT . . . . .	49

## CONTENTS

---

3.2.3	Results . . . . .	51
3.3	Geometry for pre-compressed tension tests . . . . .	53
3.3.1	Numerical simulations in ABAQUS/Explicit . . . . .	54
3.3.2	Results . . . . .	55
3.3.3	Energy balance check . . . . .	58
<b>4</b>	<b>Material testing</b>	<b>59</b>
4.1	The X65 steel . . . . .	59
4.2	Uniaxial tests . . . . .	60
4.2.1	Quasi-static tensile tests . . . . .	60
4.2.2	Dynamic tensile tests . . . . .	62
4.2.3	Reversed loading . . . . .	63
4.3	Notched tests with reversed loading . . . . .	64
4.3.1	Set-up and geometry . . . . .	65
4.3.2	Results . . . . .	66
4.3.3	Metallurgical investigation . . . . .	73
<b>5</b>	<b>Material model</b>	<b>77</b>
5.1	Numerical simulations of the pre-compressed tension tests . . . . .	77
5.2	Identification of material parameters by the method of least squares . . . . .	80
5.3	Identification of material parameters by inverse modeling . . . . .	86
5.4	Numerical simulations with new material models . . . . .	91
5.5	Fracture criterion . . . . .	93
5.6	Evaluation of material model . . . . .	95
<b>6</b>	<b>Component tests</b>	<b>99</b>
6.1	Impact and stretching of empty pipes . . . . .	99
6.2	Impact against filled pipes . . . . .	101
6.3	Impact against empty pipes . . . . .	102
6.3.1	Measurement of the pipes . . . . .	102
6.3.2	Set-up . . . . .	103
6.3.3	Results . . . . .	104
6.3.4	Correction of the displacement . . . . .	108
6.3.5	Metallurgical investigation . . . . .	109
<b>7</b>	<b>Finite Element Analyses (FEA)</b>	<b>117</b>
7.1	FEM theory . . . . .	117

7.1.1	Dynamic equilibrium . . . . .	118
7.1.2	Explicit integration . . . . .	118
7.1.3	Implicit integration . . . . .	122
7.1.4	Contact . . . . .	123
7.2	Numerical simulations in ABAQUS/Explicit . . . . .	125
7.2.1	Comparing material models . . . . .	128
7.2.2	Critical element in ABAQUS/Explicit . . . . .	130
7.3	Numerical simulation in LS-DYNA . . . . .	132
7.3.1	Global response during impact . . . . .	136
7.3.2	Critical element in LS-DYNA . . . . .	138
<b>8</b>	<b>Discussion</b>	<b>141</b>
<b>9</b>	<b>Conclusion</b>	<b>149</b>
<b>10</b>	<b>Further work</b>	<b>151</b>
	<b>References</b>	<b>153</b>
	<b>Appendices</b>	<b>159</b>
<b>A</b>		<b>161</b>
A.1	Material certificate . . . . .	162
<b>B</b>		<b>163</b>
B.1	Measurement pipes . . . . .	164
B.2	Summary impact against empty pipes . . . . .	168
<b>C</b>		<b>169</b>
C.1	Input file ABAQUS/Explicit . . . . .	170
C.2	Input files LS-DYNA . . . . .	174
C.2.1	Material card . . . . .	174
C.2.2	Impact analysis . . . . .	175
C.2.3	Springback analysis . . . . .	180
<b>D</b>		<b>183</b>
D.1	Machine drawings . . . . .	184
D.1.1	Material testing series 1 . . . . .	184
D.1.2	Material testing series 2 . . . . .	185

## CONTENTS

---

# 1 Background and motivation

The present thesis is part of an ongoing research program at the Structural Impact Laboratory (SIMLab, NTNU) in collaboration with Statoil ASA. The project is motivated by an accident experienced by Statoil at the Kvitebjørn oil field on 1<sup>st</sup> November 2007 [1]. An anchor dragged a gas pipeline out of its position and Statoil had to temporarily shut down the production until January 2008. Statoil found the residual strength in the pipeline sufficient until the next scheduled maintenance in 2009. However, in August 2008 a leak in the damaged pipe was discovered. The Kvitebjørn field was therefore immediately closed for repairs, and reopened in January 2009 [2]. The damaged pipe and anchor are shown in Figure 1.1.

A scenario of special interest is a pipeline first subjected to an impact by an object. After the impact, hooking causes the pipeline to be dragged along the seabed. When the hooked object is released the pipeline is straightened due to the presence of large axial forces. The material in the impacted area will undergo severe deformations and complex stress and strain history, which can lead to fracture.

Slåttedalen and Ørmen were the first to deliver a master's thesis within this subject in 2010 [3]. They established an experimental set-up for impact and stretching of scaled pipelines. In addition, they performed uniaxial tension tests and dynamic tests of the material, i.e. the X65 steel. The material testing showed that the X65 steel was an isotropic material. Thus, the plastic yielding was found independent of the direction of the initial loading. Based on the uniaxial tension tests, a material model with isotropic work-hardening and a Cockcroft-Latham based fracture criterion was introduced. Slåttedalen and Ørmen found a good compliance between the numerical simulations and the impact experiments. However, simulations of the stretch tests overestimated the load level of the experiments, and emphasized the need for further investigations of this observation.

Fornes and Gabrielsen continued the work in 2011 [4], by conducting uniaxial material tests with reversed loading and experiments on open and closed pipes filled with water. The tests performed on open pipes indicated that mass effects from the content may be neglected.

## 1. BACKGROUND AND MOTIVATION

---

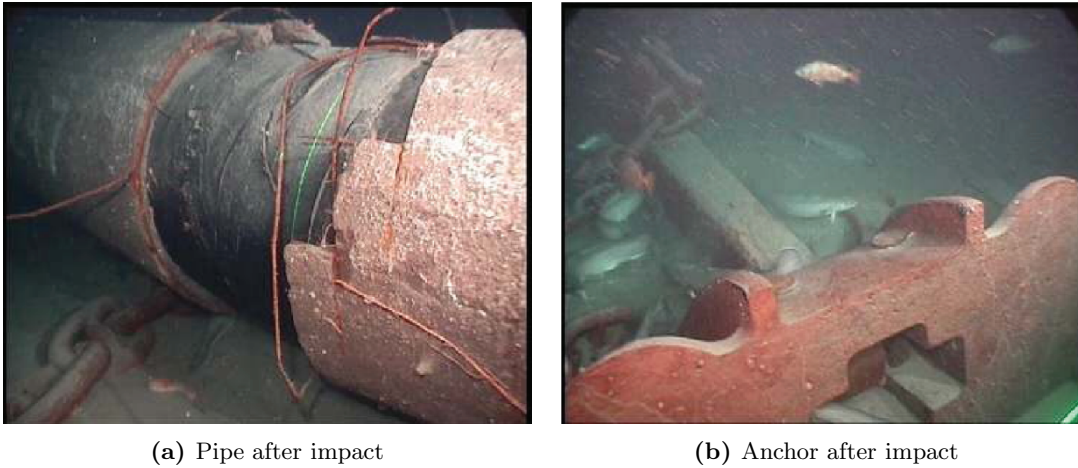


**Figure 1.1:** Impact against offshore pipeline at Kvitebjørn [1].

Thus, the global behavior of the open pipes was similar to that of the empty pipes. The closed pipes showed a somewhat stiffer behavior. The uniaxial tests revealed a kinematic behavior in the X65 steel. It was therefore introduced a constitutive relation with combined kinematic and isotropic work-hardening in the numerical simulations. However, only small differences were seen when comparing the results with the material model suggested by Slåttedalen and Ørmen. Furthermore, it was observed no significant difference between the two material models' ability to describe the damage growth in the numerical simulations.

Therefore, it still remains to calibrate a material model with a fracture criterion able to predict the damage initiation observed in the laboratory tests. Incipient fracture in the pipes after impact is therefore of special interest in this thesis. The objective of the experiments is to investigate the damage behavior of the X65 steel at large strains. During impact and stretching the pipe experience large compressive and tensile states of stress. Hence, the influence of compression on damage evolution is of great interest, both with respect to ductility and void nucleation. Therefore, it was decided to perform material tests at large compressive deformations before stretching to fracture. In addition, impact experiments on scaled pipelines were conducted. Based on these experiments it was calibrated a new material model and a metallurgical investigation of the material was conducted. The metallurgical study is an ongoing activity in collaboration between SIMLab and Statoil carried out by Dr. Ida Westermann (SINTEF). The thesis is organized as follows

**Chapter 2** presents a review of previous research and a brief introduction to the theory used in this thesis. In addition, a study of relevant theory for impact problems on pipelines is presented. The latter is mainly a recapitulation of previous theses.

---

**Chapter 3** contains introductory studies regarding the use of the optimization tool LS-OPT in inverse modeling, and finding a suited geometry for pre-compressed tension tests at large strains in compression.

**Chapter 4** presents a review of previous material testing and results from the pre-compressed tension tests. In addition, compression tests at large strains are presented. Metallurgical investigations are performed on the notched specimens with a scanning electron microscope (SEM).

**Chapter 5** describes the modeling, calibration and evaluation of the material model. Two constitutive relations with combined kinematic and isotropic work-hardening were calibrated based on two different approaches, i.e. the method of least squares and inverse modeling. The former was calibrated with respect to the material tests from previous theses, while the latter was based on the pre-compressed tension tests. The inverse modeling was performed by using the optimization tool LS-OPT.

**Chapter 6** presents the laboratory experiments on scaled pipes. Impact testing in the pendulum accelerator at NTNU mainly focusing on incipient fracture. Metallurgical investigation of the impacted pipes was performed with SEM.

**Chapter 7** contains a brief introduction to the theory of the Finite Element Method (FEM) and numerical analyses of the described loading scenario. Numerical simulations were performed with both shell and volume elements in ABAQUS/Explicit and LS-DYNA, respectively. The material model suggested in this thesis was compared with the previous theses in terms of the global response during the impact and stretching. Furthermore, the analysis of the volume model in LS-DYNA was used to study the stress state during impact and springback.

It should be noted that the calibration of a material model based on the previous material tests was demanding, i.e. the numerical verification of the tests gave odd results. This motivated new tension tests close upon delivery of this thesis. The objective was to investigate if the X65 steel used in this thesis had similar material properties as in previous theses. The results are discussed in Chapter 8.

## 1. BACKGROUND AND MOTIVATION

---

## 2 Theory

The objective of this chapter is to give a theoretical understanding of the material behavior during impact loading, and a basic foundation of the work presented in the following chapters. Both macroscopic and microscopic properties of the material will be briefly looked into. As an introduction to this chapter, a review of previous research and an approach to estimate the impact deformation analytically are presented. The last part of this chapter focus on the basic theory on macroscopic and microscopic properties of materials. Through this chapter the reader will be introduced to definitions and concepts that are essential to model and understand the behavior of a metal subjected to impact.

### 2.1 Review of previous research

The literature reveals numerous experimental data, and corresponding constitutive relations, of cyclic plasticity for various metals. However, to the authors best knowledge there are quite limited numbers of published papers regarding cyclic deformation of metals at large strain ranges. One of the reasons is that the conventional tension-compression (and vice versa) are impractical at large strains due to buckling and barreling. In the following, the research related to this topic is presented. In addition, previous research regarding the terminology and numerical modeling of fracture initiation are presented.

#### 2.1.1 Load reversal at large strains

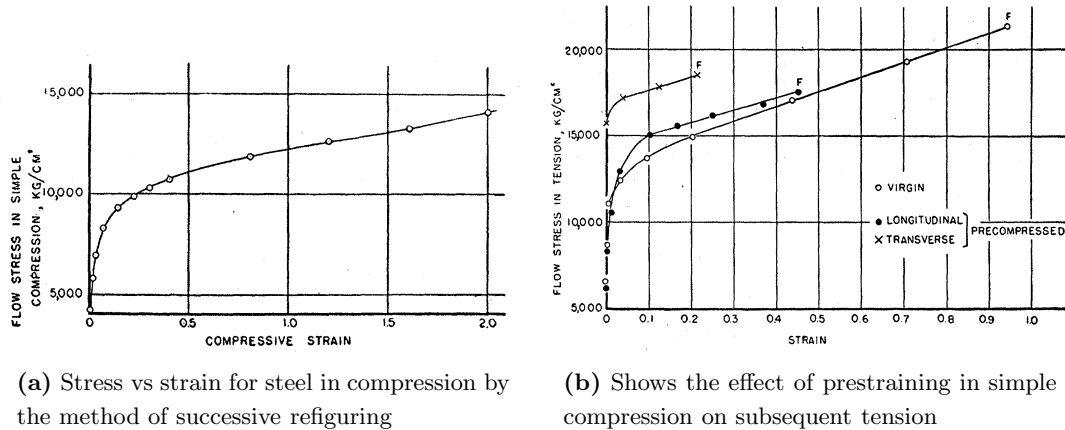
Already in 1945, Bridgman investigated the effect of large compression strains before tension, by conducting plain compression and pre-compressed tension tests [5]. He pointed out the difficulties regarding large strains in compression, and based on previous research, suggested a procedure which made it possible to conduct such tests. Bridgman suggested to perform the experiments in successive comparatively small stages, and machining the specimen back

## 2. THEORY

to the original proportions between the stages. In this way the effects of barreling and the undesired stress components arising from terminal friction were avoided.

The result from one test in compression is illustrated in Figure 2.1a. Bridgman emphasized that this figure was typical for all his results on loading in compression. In the initial stage, the stress-strain curve in compression was concave toward the strain axis. At high strains it became approximately straight and continued to rise. In addition, he noticed that there was a light inflection at higher strain, and the curve eventually became slightly concave upwards.

Bridgman also conducted pre-compressed tension tests. The tests revealed that tension specimens cut in different directions from the pre-compressed material failed to show isotropy at fracture. Bridgman pointed out that pre-compressed tests fractured at strains and stresses markedly lower than for the virgin material (Figure 2.1b).



(a) Stress vs strain for steel in compression by the method of successive refiguring

(b) Shows the effect of prestraining in simple compression on subsequent tension

**Figure 2.1:** Stress vs strain at large strains in compression and pre-compressed tension tests [5].

Bouchard et al. conducted pre-compressed tension tests to examine the effect of ductility for two different anisotropic steel grades [6]. Diabolo-shaped geometry was used to prevent buckling in compression (Figure 2.2a). Three levels of pre-compression, followed by stretching until fracture, were conducted. The tests revealed that pre-compression increased the ductility in the material (Figure 2.2b). This was in contrast to previous research, which stated that the ductility decreases with increasing pre-compression [5]. Bouchard assumed that the particular inclusions population played a critical role in this phenomenon. This was also pointed out by Peeters et al. which stated that dislocation structures are often regarded as an explanation for softening/hardening effects during changing strain paths [7].

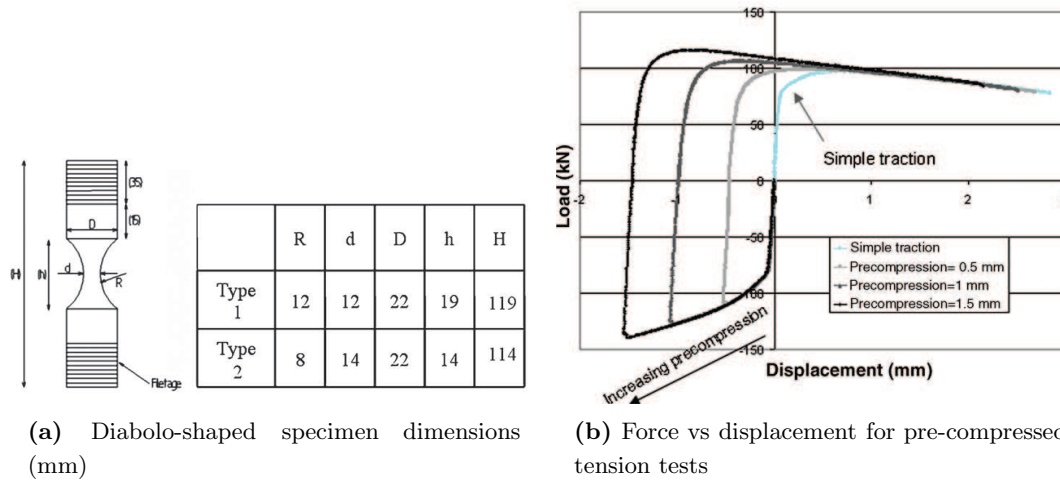


**Figure 2.2:** Diabolo-shaped specimen geometry and load-displacement curve for pre-compressed tension tests [6].

Yoshida et al. revealed interesting observations regarding the springback phenomenon, and deformation characteristics at load reversal for large strains. They discussed the performance of typical existing constitutive relations in describing large strains in cyclic plasticity [8]. Tests were performed under in-plane cyclic tension-compression for two types of steel, a mild steel and a high strength steel, loaded up to a strain range of 25 % and 13 %, respectively.

The results from this study supported previous research [9, 10], suggesting that the numerical results of springback are strongly influenced by modeling of the Bauschinger effect. The Bauschinger effect could be characterized by two distinct phenomena of stress-strain responses. One is the transient softening, also denoted transient Bauschinger effect, which is the smooth transient stress-strain response at the early stage of load reversal. The subsequent is the permanent softening appearing after the transient period. This is schematically illustrated in Figure 2.3.

Yoshida et al. concluded that the constitutive relation used in their study, i.e. the model proposed by Chaboche and Rousselier [11], failed to recreate the transient softening and work-hardening stagnation in the experiments. Furthermore, they reported interesting experimental observations regarding the evolution of Young's modulus as a function of prestrain, and its influence on springback. A noticeable decrease in the Young's modulus with increasing prestrain was observed, and it approached an asymptotic value when the prestrain became large. These observations were supported by previous studies, e.g. Yamaguchi et al. [12].



where  $\mathbf{s}$  and  $\boldsymbol{\alpha}$  denotes the Cauchy stress deviator and the backstress deviator, respectively.  $Y$  is the radius of the yield surface in the deviatoric stress space. The bounding surface  $F$  is expressed by

$$F = \frac{3}{2}(\mathbf{s} - \boldsymbol{\beta}) : (\mathbf{s} - \boldsymbol{\beta}) - (B + R)^2 = 0 \quad (2.3)$$

where  $\boldsymbol{\beta}$  denotes the center of the bounding surface,  $B$  is the initial size and  $R$  is the isotropic hardening component.

The kinematic hardening of the yield surface describes the transient Bauschinger deformation characterized by early re-yielding and the subsequent rapid change of work-hardening rate. Yoshida and Uemori assumed that this was mainly due to the motion of less stable dislocations, such as piled-up dislocations. The isotropic hardening of the bounding surface represents the global work-hardening, which is associated with the formation of stable dislocation structures, such as cell walls. Christodoulou et al. showed that the permanent softening and work-hardening stagnation is caused by the dissolution of dislocation cell walls performed during forward deformation and the formation of new dislocation microstructure during reverse deformation [14].

It should be noted that Yoshida and Uemori define their non-isotropic-hardening surface in the stress space, and not in the plastic strain space like Chaboche et al. [15].

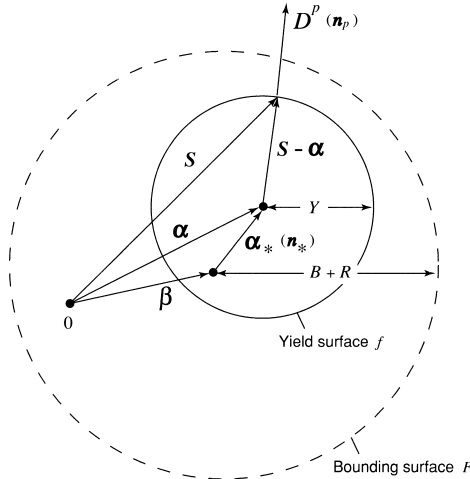


Figure 2.4: Schematic illustration of the two-surface model [13].

## 2. THEORY

---

### 2.1.2 Numerical damage models

The classical  $J_2$  (von Mises) theory of metal plasticity assumes that the hydrostatic (or mean) stress  $\sigma_H$  has no or negligible effect on the material strain-hardening, and that the flow stress is independent of the third deviatoric stress invariant  $J_3$  [16]. Fracture initiation is often preceded by large plastic deformations and considerable stress and strain gradients around the point of fracture. In these situations, the infinitesimal  $J_2$  theory of plasticity is not accurate enough, and more refined plasticity models have to be introduced. This has been confirmed by recent experiments on metals, suggesting that both the effect of hydrostatic stress and the third deviatoric stress invariant should be included in the constitutive description of the material, e.g. [17, 18, 19].

The effect of hydrostatic stress  $\sigma_H$  has been widely used in the literature regarding ductile fracture, e.g. [20, 21], and may be included through the triaxiality ratio as

$$\eta = \sigma^* = \frac{\sigma_H}{\sigma_{eq}} \quad (2.4)$$

where  $\eta$  and  $\sigma^*$  are common symbols for the triaxiality ratio, and  $\sigma_{eq}$  is the equivalent von Mises stress.

To account for the effect of the third deviatoric stress invariant, the Lode parameter has recently been given more attention. W. Lode introduced the Lode stress parameter  $\mu_\sigma$  already in 1926 [22]. However, the connection between the shape of the yield surface and Lode parameter has only been noticed recently. The Lode parameter is commonly expressed in the Haigh-Westergaard space (Figure 2.5) with respect to principal stresses as

$$\mu_\sigma = \frac{2\sigma_2 - \sigma_3 - \sigma_1}{\sigma_3 - \sigma_1} = -\sqrt{3} \tan \theta \quad (2.5)$$

where  $-\frac{\pi}{6} \leq \theta \leq \frac{\pi}{6}$  and  $-1 \leq \mu_\sigma \leq 1$ , assuming  $\sigma_1 > \sigma_2 > \sigma_3$ .

Hopperstad showed some special cases regarding the Lode parameter  $\mu_\sigma$  [23], i.e. axisymmetric tension ( $\sigma_1 = \sigma_{eq}$  and  $\sigma_2 = \sigma_3 = 0$ ), pure shear ( $\sigma_1 = \frac{1}{\sqrt{3}}\sigma_{eq}$ ,  $\sigma_2 = 0$  and  $\sigma_3 = -\frac{1}{\sqrt{3}}\sigma_{eq}$ ) and balanced biaxial tension ( $\sigma_1 = \sigma_2 = \sigma_{eq}$  and  $\sigma_3 = 0$ ). By using Equation (2.5), this results in  $\mu_\sigma = 1$ ,  $\mu_\sigma = 0$  and  $\mu_\sigma = -1$ , respectively.

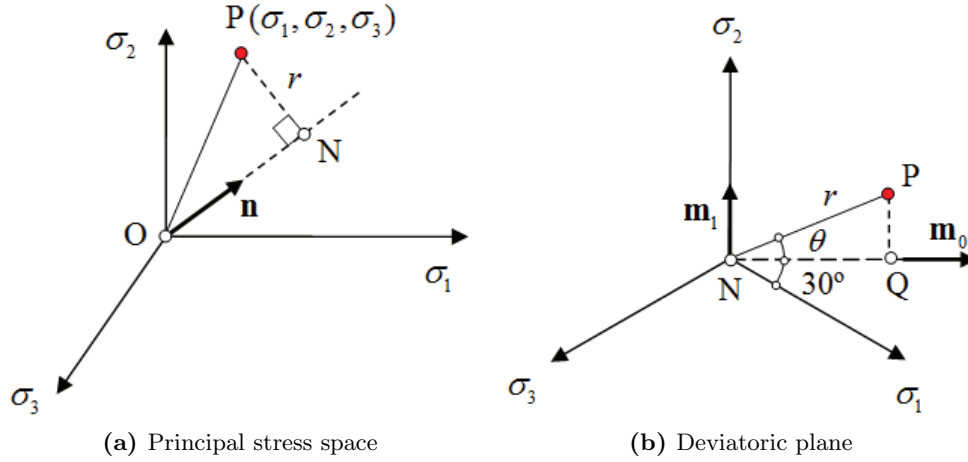


**Figure 2.5:** Stress representation in Haigh-Westergaard space [23].

Wierzbicki and Xue showed a unique relation for the Lode parameter and stress triaxiality in the special case of plane stress ( $\sigma_3 = 0$ ) as [24]

$$\xi = \cos \left[ \frac{\pi}{2} (1 - \bar{\theta}) \right] = -\frac{27}{2} \eta \left( \eta^2 - \frac{1}{3} \right) \quad (2.6)$$

It should be noted that they used a somewhat different notation than Hopperstad, i.e. the Lode angle  $\theta$  was related to the normalized third deviatoric stress invariant  $\xi$  through

$$\xi = \frac{3\sqrt{3}}{2} \frac{J_3}{J_2^{3/2}} = \cos 3\theta \quad (2.7)$$

and the normalized Lode angle  $\bar{\theta}$  was given as

$$\bar{\theta} = 1 - \frac{6\theta}{\pi} = 1 - \frac{2}{\pi} \arccos \xi \quad (2.8)$$

The range of the Lode angle is  $0 \leq \theta \leq \frac{\pi}{3}$ , thus  $\xi$  is  $-1 \leq \xi \leq 1$ .

Bai and Wierzbicki used Equation (2.6) and showed a conceptual representation of the initial stress states in the space of triaxiality ratio and Lode angle parameter [17]. This is summarized in Figure 2.6 where 10 types of traditional specimens and tests are presented.

## 2. THEORY

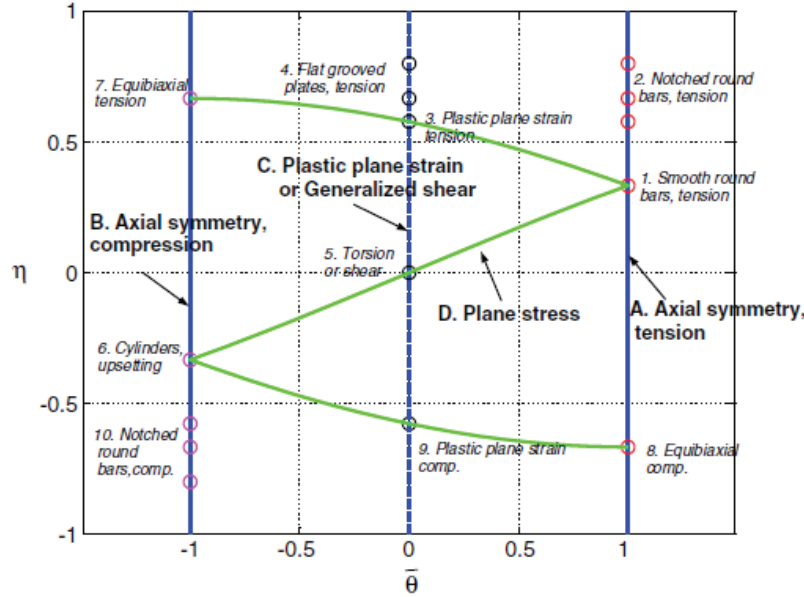


**Figure 2.6:** Conceptual representation of the initial stress states on the plane of  $\bar{\theta}$  and  $\eta$  [17].

Furthermore, the above relations have recently been applied to the calibration of a fracture criterion in the space of triaxiality ratio, Lode parameter and fracture strain. This was suggested by, among others, Li et al. [25]. They showed that the Modified Mohr-Coulomb (MMC) fracture criterion is applicable to problems involving ductile fracture of materials and sheets. In addition to the traditional ductile failure mode in terms of necking, they discussed the importance of including the possibility of shear fracture in the numerical simulations of deep-drawing punch tests. In the limiting case of plane stress, the fracture locus consists of four branches when represented on the plane of equivalent strain to fracture and stress triaxiality. Li et al. performed a transformation of this fracture locus to the space of principal strains and revealed the existence of two new branches, i.e. the branches between uniaxial tension and compression (branch 3 and 4 in Figure 2.8). Furthermore, they concluded that these branches explain the formation of shear induced fracture. Thus, they found the MMC fracture criterion to be applicable to the whole range of strain ratios ( $-2 \leq \alpha < 1$ ), and that it could successfully capture the experimentally observed shear-induced fracture in punch forming. It should be noted that the strain increment ratio was defined as  $d\varepsilon_2 = \alpha d\varepsilon_1$ .

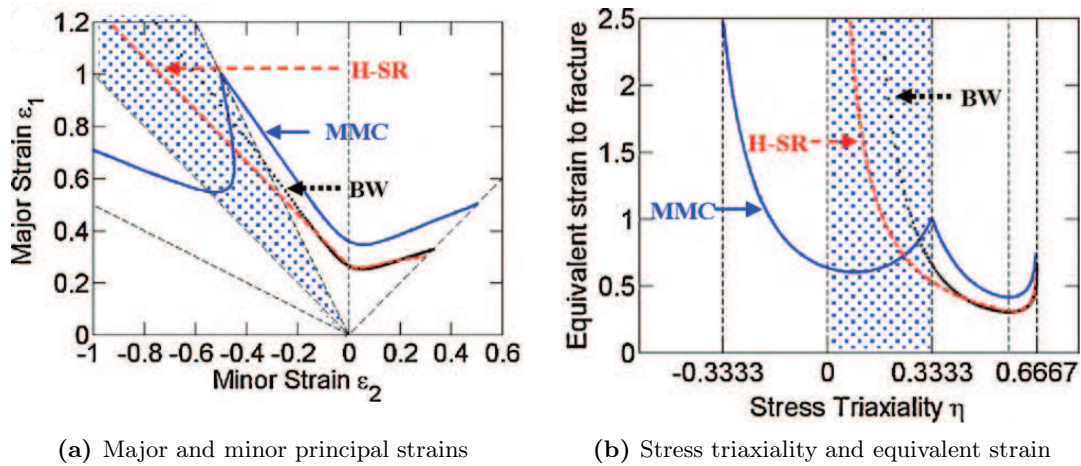


**Figure 2.7:** Comparison of MMC Fracture Forming Limit Diagram (FFLD) and Forming Limit Diagrams (FLD) in two spaces [25].

The range of the traditionally necking failure criteria is in the region of the equi-biaxial tension to uniaxial tension (Figure 2.8a). Li et al. stressed the importance of the shaded area in Figure 2.7 which represent the range where shear fracture could occur in sheet metal forming operations. Furthermore, a fracture locus for a high strength steel was calibrated. This fracture envelope is presented in Figure 2.8a and its corresponding curve in the space of principal strains are shown in Figure 2.8b.

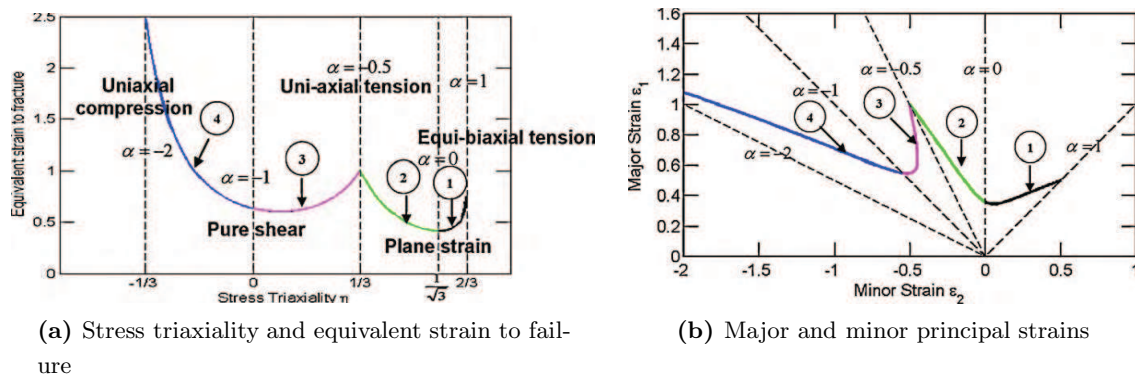


**Figure 2.8:** 2D MMC plane stress fracture locus [25].

## 2. THEORY

---

### 2.2 Impact load and energy absorption

The following three Sections (2.2, 2.3 and 2.4) are based on the master's thesis by Slåttedalen and Ørmen [3]. Impact problems such as collisions, explosions and blasts are in general transient dynamic loads, since the deformation occurs over a short period of time. However, if the time duration of the impact is at least four times as long as the natural period of the impacted structure, it can be considered quasi-static [26]. The energy from damping and inertia forces are then negligible, and the entire impact has to be absorbed by the stiffness of the loaded structure. Mass, velocity and geometry of the striking object, together with the direction of motion of the striker relative to the structure, are quantities describing the load. If the structure is supported, i.e. no rigid body translations or rotations are allowed, the kinetic energy  $E_k$  in the striker must be absorbed as elastic energy  $E_e$  and plastic dissipated energy  $E_p$  in the structure as

$$E_k = E_e + E_p \quad (2.9)$$

where the kinetic energy is calculated as

$$E_k = \frac{1}{2} M v^2 \quad (2.10)$$

and  $M$  is the mass and  $v$  is the velocity of the striker before impact. The external work  $W_{ext}$  is the work performed by the striker on the structure, which again is equal to the area under the force-displacement curve

$$W_{ext} = \int_{u_0}^{u_f} F(u) du \quad (2.11)$$

where  $F$  is the contact force between the striker and the structure,  $u$  is the displacement in the direction of the force, and  $u_0$  and  $u_f$  is the initial and final displacement, respectively. The work energy theorem states that if a force  $F$  acting upon a rigid object is causing the kinetic energy to change, then the external work  $W_{ext}$  is equal to the change in kinetic energy. Since the initial velocity of the pipe is zero, the energy balance equation can be written as

$$W_{ext} = \Delta E_k = W_{int} = E_e + E_p \quad (2.12)$$

---

## 2.3 Deformation of simply supported pipes loaded at the midspan

---

By combining Equation (2.9), (2.10), (2.11) and (2.12), Equation (2.13) can be established.

$$\frac{1}{2}Mv^2 = \int_0^{u_f} F(u)du \quad (2.13)$$

The properties of the striker are known in this thesis, and thus the size of the integral for the given system can be found. Hence, the governing problem is to correctly describe the force-displacement curve.

### 2.3 Deformation of simply supported pipes loaded at the midspan

Several studies have been carried out on this subject. The common conclusion is that the deformation process is complex, involving the transfer of kinetic energy from the striker to the pipe.

Langseth et al. pointed out that the energy absorption takes place in two phases, namely the transient and the global mode phase (Figure 2.9) [27]. In the transient phase, elastic and plastic waves propagate away from the impact point. The energy absorption is then a function of the mass ratio between the striker and the pipe. The response of the pipe is a function of the material properties, slenderness of the cross-section, support conditions and the contact area between the striker and pipe. The global mode phase starts when the elastic and plastic waves reach the end supports. If the mass of the striker is heavy compared to the pipe, the transient phase may be neglected. Thus, the problem can be considered quasi-static.

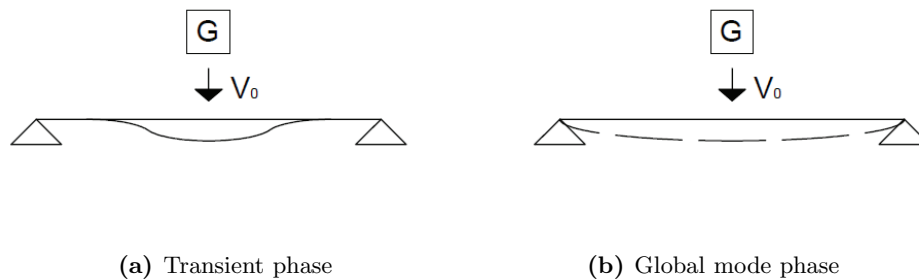


**Figure 2.9:** Transient and global mode phase for impact loading [3].

## 2. THEORY

Thomas et al. conducted a series of experiments on simply supported aluminum and steel pipes under transverse loading [28, 29, 30]. Deformation modes, for a given wall thickness  $t$  and diameter  $d$ , depends on the pipe length  $l$  [28]. For a short span ( $l < 1.5d$ ), the pipe behaves like a ring. For longer spans three deformation modes were identified (Figure 2.10):

- The initial phase is pure crumpling, and is recognized by localized crumpling at the top surface of the pipe. During this deformation mode the force rises steeply. The bending capacity of the cross-section is reduced as the top surface crumbles, and after a given crumpling deformation, the bottom surface starts to deflect. This occurs as the force reaches a level where pure crumpling phase changes to crumpling and bending phase.
- In the secondary phase (bending and crumpling phase) the deformation involves further crumpling of the pipe in combination with bending. During this phase, the slope of the force-displacement curve decreases, and the force continues to rise until it reaches its maximum force  $P_{max}$ .
- The last phase (structural collapse) occurs after maximum force  $P_{max}$  is reached. Structural collapse is recognized by pure bending of the pipe and large rotations at the supports.

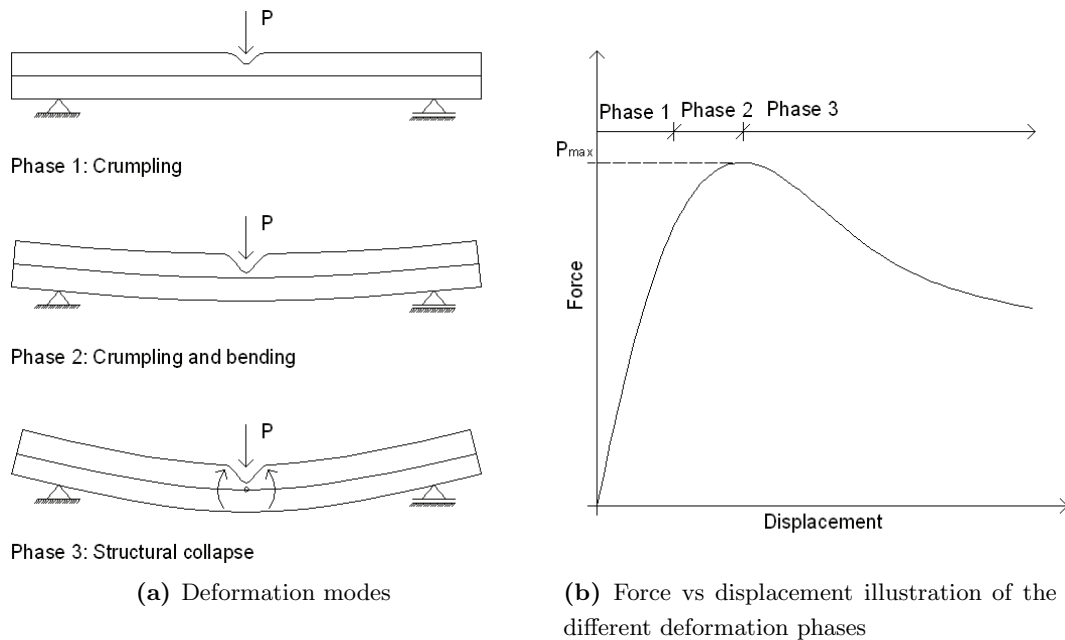


**Figure 2.10:** Identified deformation modes [3].

## 2.4 Analytical models for calculating impact capacity of pipes

As Section 2.3 elaborates, the deformation process for an impacted pipe is complex. It is therefore demanding to derive a simple analytical model for the calculation of the entire force-displacement curve. Because of the difficulties finding an analytical universal solution, a numerical approach will be used in this thesis. However, the following section will give an understanding of how to estimate a solution analytically. Søreide investigated the impact capacities of circular tube steel jackets [31]. The calculations in the following section are based on Søreide, since the geometry in the jacket and pipes is similar. To derive a simplified analytical solution, three approximations are assumed:

- The material is assumed rigid-perfectly plastic. Hence, the material does not work-harden and this approximation underestimates the load level.
- Local denting and global bending response must be separated.
- Quasi-static behavior of the problem must be assumed.

If the span of the pipe is short relative to the diameter, the ovalization of the pipe can be studied as a simple ring model. The model consists of a ring compressed between two rigid plates. Figure 2.11 shows the ring before and after deformation, respectively. The mechanism for ovalization contains plastic hinges at the initial contact points  $A$  and  $B$ , and at the other two quarter points  $C$  and  $D$  (Figure 2.11b).

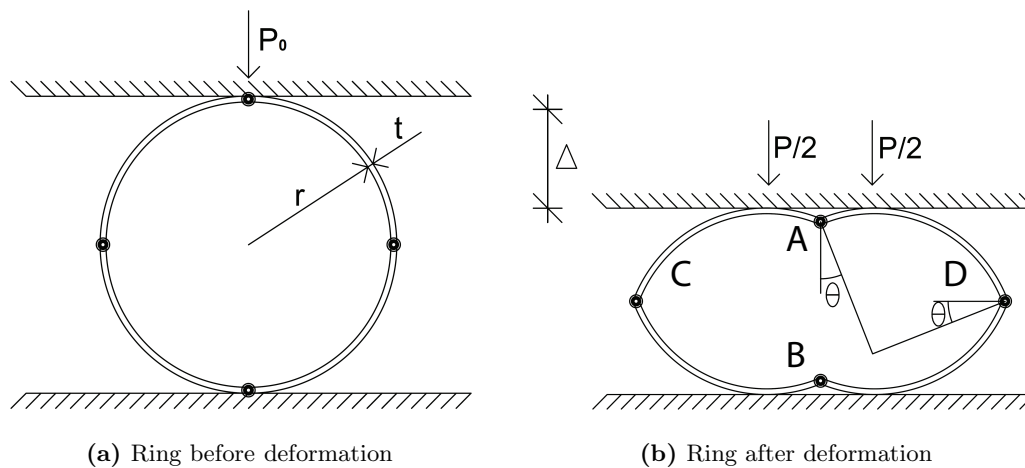


**Figure 2.11:** Rigid-perfectly plastic deformation of the ring [3].

## 2. THEORY

---

The displacement  $\Delta$  at the end of the impact is given as

$$\Delta = 2r \cdot \sin \theta \quad (2.14)$$

where  $r$  is the initial radius and  $\theta$  is the rotation of a quarter. The incremental form of Equation (2.14) can be given as

$$\delta\Delta = 2r \cdot \delta\theta \cdot \cos \theta \quad (2.15)$$

The external and internal work expressions refer to the deformed configuration (Figure 2.11b) and are given, respectively, as

$$\delta W_{ext} = P\delta\Delta \quad (2.16)$$

$$\delta W_{int} = 8m_p\delta\theta \quad (2.17)$$

where the plastic bending moment capacity per unit length  $m_p$  can be given as  $m_p = \frac{1}{4}t^2\sigma_0$  [32]. The thickness is denoted  $t$  and  $\sigma_0$  is the initial yield strength of the material. Applying the principle of virtual work yields

$$\delta W_{ext} = \delta W_{int} \implies P = \frac{8m_p\delta\theta}{\delta\Delta} \implies P = \frac{4m_p}{r} \frac{1}{\cos \theta} \quad (2.18)$$

By expressing  $\cos \theta$  with  $\sin \theta$  and using Equation (2.14), the plastification load  $P$  can be given as

$$P = \frac{4m_p}{r} \frac{1}{\sqrt{1 - \left(\frac{\Delta}{2r}\right)^2}} \quad (2.19)$$

The initial plastification load  $P_0$  can be obtained by inserting  $\Delta = 0$ . It must be emphasized that this equation is only valid when the pipe deforms as a ring and  $\Delta \leq \frac{r}{\sqrt{2}}$ .

$$P_0 = \frac{4m_p}{r} \quad (2.20)$$

As pointed out in Section 2.3, the deformation process becomes more complex when the length of the pipe increases. Based on a collapse mechanism used for tubular jacket legs

## 2.4 Analytical models for calculating impact capacity of pipes

by Sørdeide [31], the more complex deformation process of the pipe can be estimated. The local collapse mechanism of the impacted pipe is illustrated in Figure 2.12. The mechanism consists of a flat rectangular zone at the area of impact, and two triangular surfaces in the adjacent region. As Sørdeide points out, the plastic dissipation of energy during deformation includes three major effects:

- Dissipation of energy due to rotation of the four outer hinge lines of the triangle (length  $l_s/4$ ) and the two outer hinge lines of the rectangle (length  $B$ ).
- Dissipation of energy due to plastic change of curvature in the circumferential direction.
- Plastic work associated with membrane forces.

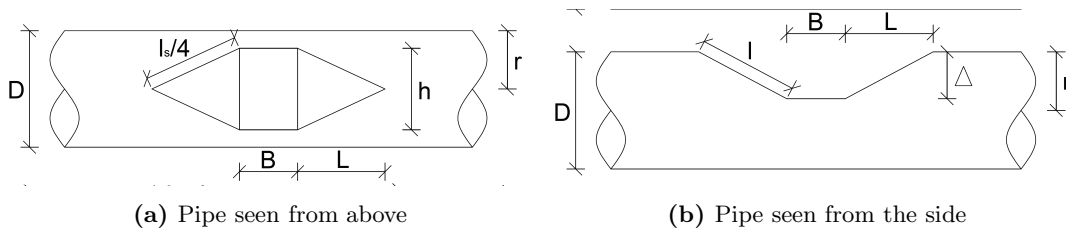


**Figure 2.12:** Mechanism for estimating the load and displacement for impacted pipes [3].

Derivation of the initial moment capacity is a recapitulation of Slåttedalen and Ørmen, and the formulas are given in the exact same manner. For a more detailed derivation it is referred to Appendix A in Slåttedalen and Ørmen [3]. The rotation  $\Gamma_r$  of the two hinge lines of the rectangle can be expressed as

$$\Gamma_r = \frac{\pi}{2} - \arcsin\left(1 - \frac{\Delta}{r}\right) \quad (2.21)$$

The rotation  $\Gamma_t$  of the four hinge lines around the triangle is not constant along the lines. As an approximation, the average value of the rotation can be used

$$\Gamma_t = \frac{1}{2} \arctan \left( \frac{\sqrt{(1 + 2\frac{\Delta r}{L^2})(\frac{\Delta}{r}(2 - \frac{\Delta}{r}))}}{(1 + 2\frac{\Delta r}{L^2} - (\frac{\Delta}{L})^2)(1 - \frac{\Delta}{r})} \right) + \arctan \left( \left(\frac{\Delta}{L}\right)^2 \frac{\sqrt{2\frac{r}{\Delta} - 1}}{\sqrt{1 + 2\frac{\Delta r}{L^2}}} \right) \quad (2.22)$$

Since the rotation of the lines along the rectangle is constant and the average value of the rotation is used, the work can be simplified as

## 2. THEORY

---

$$W = W_r + W_t \quad (2.23)$$

where the internal work in the plastic hinge lines along the rectangle  $W_r$  is given as

$$W_r = \frac{\sigma_0 B t^2}{2} \left( \frac{\pi}{2} - \arcsin\left(1 - \frac{\Delta}{r}\right) \right) \quad (2.24)$$

and the internal work in the plastic hinge lines of the triangle  $W_t$  is given as

$$W_t = \sigma_0 t^2 \Delta \sqrt{2 \frac{r}{\Delta} + \left(\frac{L}{\Delta}\right)^2} \cdot \Gamma_t \quad (2.25)$$

The incremental force-displacement curve can be estimated as

$$\delta P = \frac{W(\Delta_2) + W(\Delta_1)}{\Delta_2 + \Delta_1} \quad (2.26)$$

A good approximation of the force-displacement curve is not straight forward to obtain from the above equations, i.e. the dent depends on both the geometrical and material properties of the pipe. However, by inserting  $\Delta = 0$ , the initial plastic moment capacity for the undeformed pipe can be calculated (Equation (2.27)). The last transition applies for thin walled pipes [31]. As the dent size increases, the cross-section deforms as indicated in Figure 2.13b, and the value of  $M_p$  drops because of the decreased moment arm.

$$M_{p0} = \frac{1}{6} ((2r)^3 - (2r - 2t)^3) \sigma_0 \approx 4r^2 t \sigma_0 \quad (2.27)$$

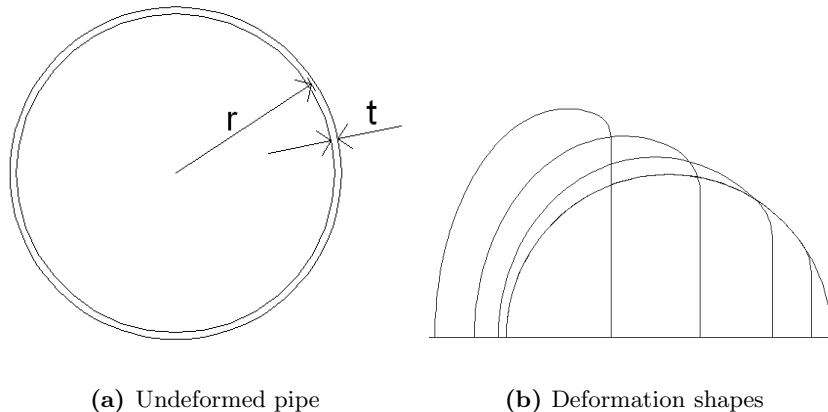


**Figure 2.13:** Deformation of circular cross sections [3].

## 2.5 Mechanics of materials

This thesis includes a wide range of theory in terms of mechanics of materials. Therefore, it is essential to establish a basis on the topic. An important part of mechanics of materials, is the theory of plasticity, which consists of three main parts:

- Yield criterion
- Flow rule
- Work-hardening

The following section is mainly based on Hopperstad and Børvik [33, 34].

### 2.5.1 Yield criterion and plastic flow rule

When a body made of metal is subjected to forces, the force-displacement path<sup>1</sup> will typically follow the curve illustrated in Figure 2.14a. Starting from the initial condition and traveling along the path to  $F_0$  ( $= \sigma_0 A_0$ ), the relation between force and displacement is typically linear elastic, i.e. there is a linear relationship between stresses and strains (Hooke's law). When the force level reaches  $F_0$ , the material has reached its initial yield limit  $\sigma_0$  and plastic deformation occurs. The transition between the elastic and plastic domain may be abrupt or more general depending on the type of metal [33].

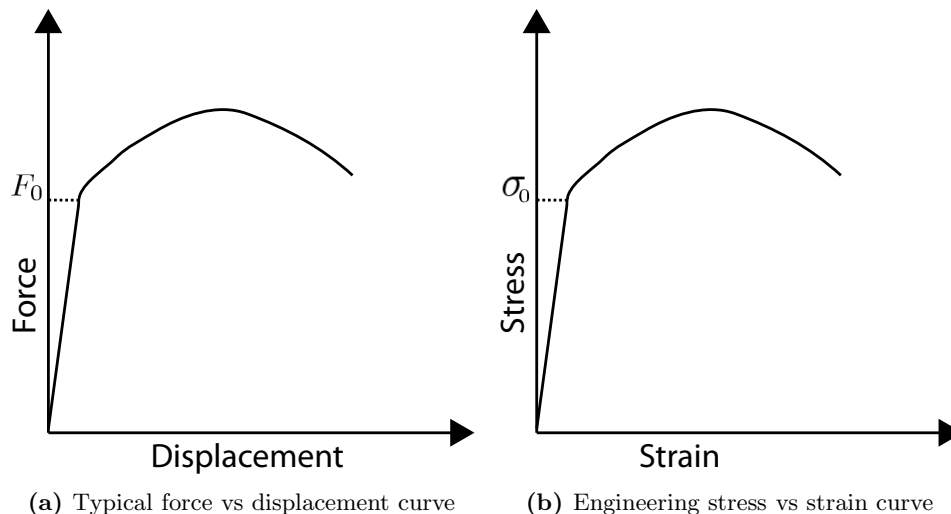


**Figure 2.14:** Typical force-displacement and engineering stress-strain curves for mild steels.

<sup>1</sup>Engineering stress-strain curve follow the same path as force-displacement curve

## 2. THEORY

---

Mathematically the yield limit  $\sigma_0$  is described by the yield criterion, given as

$$f(\boldsymbol{\sigma}) = 0 \quad (2.28)$$

where the yield function is denoted  $f(\boldsymbol{\sigma})$ . Geometrically  $f(\boldsymbol{\sigma}) = 0$  can be considered to define a surface in stress space, and is denoted the yield surface. When  $f(\boldsymbol{\sigma}) < 0$  the material is in the elastic region, and will only undergo elastic deformations. A situation where  $f(\boldsymbol{\sigma}) > 0$  is not allowed for typical metals, and will not be discussed any further. Figure 2.15 illustrates graphically the three stress states in a two dimensional stress space, where  $\boldsymbol{\sigma}_1$ ,  $\boldsymbol{\sigma}_2$  and  $\boldsymbol{\sigma}_3$  represents the elastic domain, yield surface and inadmissible region, respectively [33].

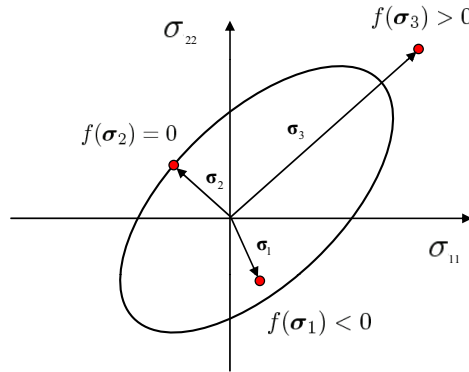


**Figure 2.15:** Elastic domain, yield surface and inadmissible region [33].

The yield function is often depicted as

$$f(\boldsymbol{\sigma}) = \varphi(\boldsymbol{\sigma}) - \sigma_0 \quad (2.29)$$

where the equivalent stress  $\sigma_{eq} = \varphi(\boldsymbol{\sigma})$ , which measures the magnitude of the stress state to which the metal is subjected, and  $\sigma_0$  is the yield limit of the metal. The equivalent stress is assumed to be a positive homogeneous function of order one of the stress [33].

Metals are regarded pressure insensitive, meaning that the yield criterion depend only on the deviatoric stress state. The deviatoric stress can be obtained by subtracting the hydrostatic stress from the total stress. The reason for the pressure insensitivity in metals is that the plastic deformation to a large extent takes place by plastic slip, which is a shear-driven deformation mode [33].

Plastic yielding of metals is in most cases assumed to be isotropic, meaning that the yield function is independent of the direction of the initial loading. The yield function is most

conveniently written in terms of the principle invariants of the stress deviator  $f(J_2, J_3) = 0$ . For a ductile metal undergoing plastic deformation, there are two widely used yield criteria, namely Tresca and von Mises.

Tresca yield criterion is an isotropic and pressure independent criterion. It is assumed that yielding occur when the maximum shear stress  $\tau_{max}$  is reached. A common representation of the Tresca criterion is given as

$$f(\sigma_1, \sigma_2, \sigma_3) = \frac{1}{2}(|\sigma_1 - \sigma_2| + |\sigma_2 - \sigma_3| + |\sigma_3 - \sigma_1|) - \sigma_0 = 0 \quad (2.30)$$

where  $\sigma_1, \sigma_2$  and  $\sigma_3$  are the principal stresses and  $\sigma_0$  is the yield limit.

The von Mises yield criterion assumes isotropy and pressure insensitivity of the material. It is assumed that yielding occurs when the second principal invariant of the stress deviator  $J_2$  reaches a critical value  $k^2$ . A common representation of von Mises, expressed in terms of deviatoric stress components  $\sigma'_{ij}$ , is given as

$$f(\boldsymbol{\sigma}) = \sqrt{\frac{3}{2}\sigma'_{ij}\sigma'_{ij}} - \sigma_0 = 0 \quad (2.31)$$

A graphical illustration that highlights the differences between Tresca and von Mises is given in a two-dimensional stress space in Figure 2.16. As the figure depicts, Tresca yield surface is circumscribed by von Mises, and it predicts yielding for stress states that are still elastic according to von Mises.

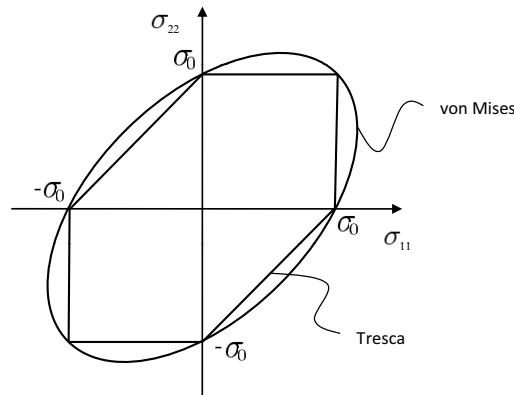


**Figure 2.16:** Geometric representation of the Tresca and von Mises yield criteria for plane stress conditions ( $\sigma_{12} = 0$ ) [33].

## 2. THEORY

Another important aspect in the theory of plasticity is the plastic flow rule. Plastic deformations are dissipative deformation processes. The plastic flow rule defines the plastic strain rate tensor  $\dot{\varepsilon}_{ij}^p$  in a way that ensures non-negative dissipation [33]. In the plastic state the dominant direction of flow is determined by the direction of dominant stress [5]. On general form, the plastic flow rule is given as

$$\dot{\varepsilon}_{ij}^p = \dot{\lambda} h_{ij} \quad (2.32)$$

where  $h_{ij}$  is the flow function depending on the stress state of the material, and  $\dot{\lambda}$  is a non-negative scalar denoted the plastic parameter. The present thesis is limited to the associated flow rule, given as

$$\dot{\varepsilon}_{ij}^p = \dot{\lambda} \frac{\partial f}{\partial \sigma_{ij}} \quad (2.33)$$

It is called the associated flow rule, since the plastic potential function is associated with the yield function. The associated flow rule, also known as the normality rule, implies that the incremental plastic strain vector is normal to the yield locus. This is visualized for Tresca and von Mises in Figure 2.17.

It should be noted that the associated flow rule implies that the shape of the yield function determines both the stress state and the direction of the loading in the metal.

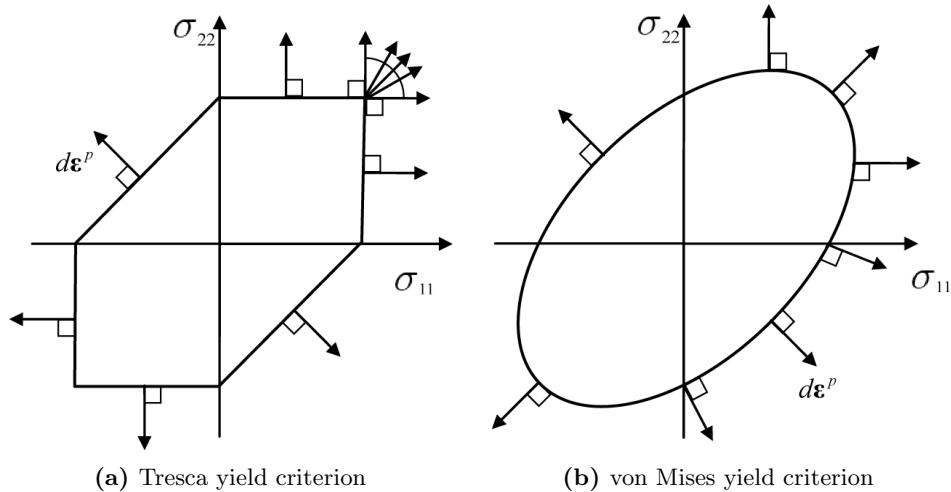


**Figure 2.17:** Graphical illustration of the associated flow rule in the Tresca and von Mises yield criteria [33].

The von Mises yield criterion is uniquely described at every point along the yield surface (Figure 2.17b). In addition, the criterion is applicable to isotropic materials and widely used in FEM software [35, 36]. Therefore, this yield criterion will be used in the present thesis.

An important relation regarding the loading history in the material is the equivalent plastic strain  $p$ , also referred to as the accumulated plastic strain. This is a monotonically increasing function of time, given as

$$p = \int_0^t \dot{p} dt \equiv \int_0^t \dot{\lambda} dt \quad (2.34)$$

assuming  $\dot{p} = \dot{\lambda}$ , the equivalent plastic strain rate can be given as

$$\dot{p} = \sqrt{\frac{2}{3} \dot{\epsilon}_{ij}^p \dot{\epsilon}_{ij}^p} \quad (2.35)$$

### 2.5.2 Work-hardening

To account for the work-hardening of the material it is necessary to include an additional parameter in the yield function. Materials work-harden during plastic deformation and the strength increases. Thus, the evolution of the yield surface should also include the equivalent plastic strain. There are various approaches of describing the work-hardening of the material, however, this thesis will be limited to the following cases:

- Isotropic
- Kinematic
- A combination of isotropic and kinematic

**Isotropic work-hardening** leads to an increase of the elastic domain as the material is plastically deformed. This is due to an increase of the dislocation density of the material [33]. To account for the increase of the flow stress, it is introduced an isotropic hardening variable  $R$  depending on the accumulated plastic strain  $p$ . Thus, the yield criterion of an elastic-plastic material with isotropic hardening can be expressed as

$$f(\boldsymbol{\sigma}, R) = \varphi(\boldsymbol{\sigma}) - \sigma_y(R) = \sigma_{eq}(\boldsymbol{\sigma}) - [\sigma_0 + R(p)] \quad (2.36)$$

## 2. THEORY

---

During plastic deformations the hardening variable  $R$  and thus the flow stress  $\sigma_y$  are increasing, resulting in an enlarged elastic region of the material (Figure 2.18).

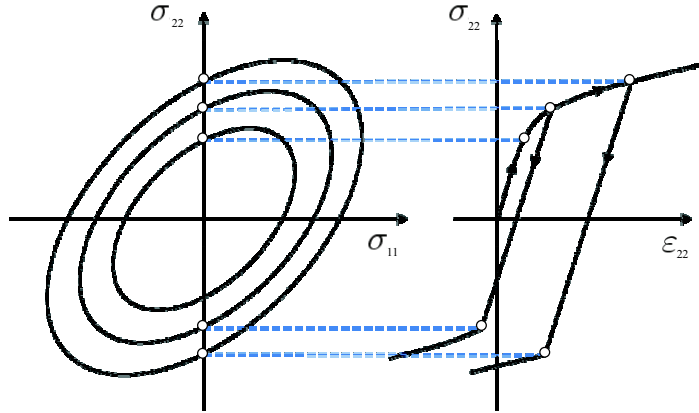


**Figure 2.18:** Expansion of the yield surface in stress space due to isotropic work-hardening [33].

The isotropic hardening rule is defined, quite generally, as

$$\dot{R} = H_R \dot{\lambda} \quad (2.37)$$

where the associated flow rule is assumed, i.e. the equivalent plastic strain rate  $\dot{p}$  equals the plastic parameter  $\dot{\lambda}$ . Furthermore, the hardening modulus  $H_R$  depends on the state of the material.

Two frequently used isotropic work-hardening rules are the Power law and the Voce rule, given in Equation (2.38) and (2.39), respectively.

$$R(p) = K p^n \quad (2.38)$$

$$R(p) = Q_i (1 - e^{-b_i p}) \quad (2.39)$$

Where  $K$ ,  $n$ ,  $Q_i$  and  $b_i$  are hardening parameters determined from material tests.

**Kinematic work-hardening** is strongly related to the Bauschinger effect. Figure 2.19 illustrates this effect for a one dimensional problem. A brief introduction on this topic is given by following the loading path in the figure and explaining the key points. As before, the initial yield stress is denoted  $\sigma_0$ , and it is assumed that plastic yielding occurs at this stress magnitude independent of the direction of initial loading. First step in Figure 2.19 is loading the material from its initial condition into the plastic domain in tension to a stress  $\sigma_A$ . During this step the material work-hardens, thus  $\sigma_A > \sigma_0$ . The material is then unloaded elastically from  $\sigma_A$  to zero stress, and then reloaded in the reverse direction. When loading in the reverse direction, yielding occurs at  $\sigma_B$ . For most materials  $\sigma_B < \sigma_A$ , and often  $\sigma_B < \sigma_0$  [33]. This reduction in yield stress is denoted the Bauschinger effect.

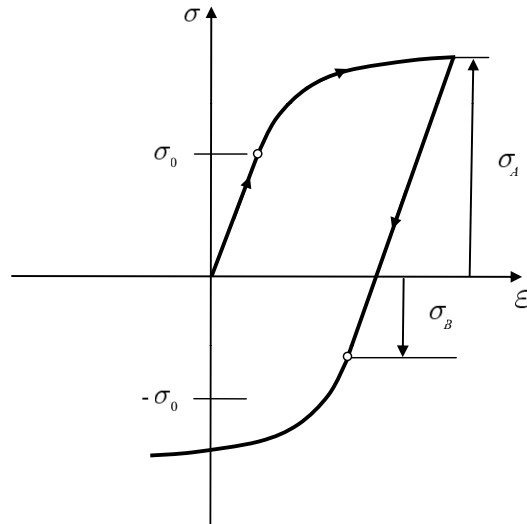


**Figure 2.19:** The Bauschinger effect [33].

Kinematic work-hardening describing the Bauschinger effect can be described by introducing a backstress tensor<sup>2</sup>  $\chi$ . The backstress tensor defines the center of the elastic region in stress space. It acts like a residual stress, and lowers the yield strength under reversed loading. To account for kinematic hardening, the yield function is re-defined as

$$f(\boldsymbol{\sigma} - \boldsymbol{\chi}, R) = \varphi(\boldsymbol{\sigma} - \boldsymbol{\chi}) - \sigma_y(R) \tag{2.40}$$

where the equivalent stress  $\sigma_{eq} = \varphi(\boldsymbol{\sigma} - \boldsymbol{\chi})$ . The kinematic hardening variable  $\boldsymbol{\chi}$  describes the translation of the elastic domain in the direction of plastic loading (Figure 2.20). Thus,  $\boldsymbol{\sigma} - \boldsymbol{\chi}$  acts as an effective stress. It is the magnitude of this effective stress that determines

<sup>2</sup>No discussion on tensors will be given, and it is up to the readers to examine this themselves.

## 2. THEORY

---

whether or not the material yields plastically for given values of yield stress  $\sigma_0$  and isotropic hardening  $R$ . To describe the Bauschinger effect,  $\chi$  should develop positive values in tension and negative values in compression.

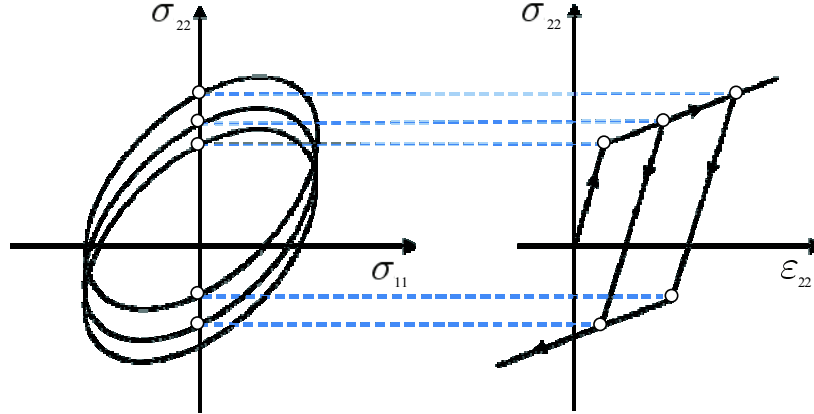


**Figure 2.20:** Translation of the yield surface in stress space due to kinematic work-hardening [33].

The evolution equation for the backstress tensor is generally defined as

$$\dot{\chi}_{ij} = H_{ij}^{\chi} \dot{\lambda} \quad (2.41)$$

where the second-order tensor  $H_{ij}^{\chi}$  depends on the state of the material through  $\sigma$ ,  $\chi$  and  $R$ . Two frequently used kinematic hardening rules are the linear (Equation (2.42)) and the nonlinear hardening rule (Equation (2.43)), suggested by Ziegler, and by Armstrong and Fredrick, respectively [35].

$$\dot{\chi}_{ij} = C \frac{\sigma_{ij} - \chi_{ij}}{\sigma_{eq}} \dot{p} \quad (2.42)$$

$$\dot{\chi}_{ij} = \left( C_k \frac{\sigma_{ij} - \chi_{ij}}{\sigma_{eq}} - \gamma_k \chi_{ij} \right) \dot{p} \quad (2.43)$$

Where  $C_k$  is the initial kinematic hardening moduli, and  $\gamma_k$  determine the rate at which the kinematic hardening moduli decreases with increasing plastic deformation. These material parameters are usually determined from cyclic tests.

**Combined work-hardening** is actually already presented in Equation (2.40), and is nothing else than the combination of the isotropic and kinematic work-hardening. Thus, the yield surface is allowed to both expand and translate in the stress space. A frequently used combined hardening rule is the Chaboche model [35, 37]. This model express the equivalent stress  $\sigma_{eq}$  as the sum of the initial yield stress  $\sigma_0$ ,  $R$  (Equation (2.44)) and  $\chi$  (Equation (2.45)).

$$R = \sum_{i=1}^N R_i \quad (2.44)$$

$$\chi = \sum_{k=1}^N \chi_k \quad (2.45)$$

The isotropic and kinematic components are assumed to evolve independently as the Voce (Equation (2.39)) and Armstrong-Fredricks (Equation (2.43)) hardening rule, respectively [37].

### 2.5.3 Large strains

Impact against offshore pipelines involves large deformations and large strains. To be able to understand how the material behaves when subjected to an outer force, it is necessary to perform material tests. A widely used method to obtain information regarding the mechanical properties of a ductile material is the uniaxial tension test. The test is conducted with a suitable specimen geometry, subjected to an increasing axial tensile elongation until fracture. The applied force  $F$  and the change in length  $\Delta L$  or diameter  $\Delta d$  are measured, and the output is a force-displacement curve.

**Engineering strain and stress** can be calculated from the force-displacement curve using Equation (2.46) and (2.47), respectively [34].

$$\varepsilon_e = \frac{\Delta L}{L_0} = \frac{L - L_0}{L_0} \quad (2.46)$$

$$\sigma_e = \frac{F}{A_0} \quad (2.47)$$

## 2. THEORY

---

At initial configuration, the undeformed length is given as  $L_0$  and the undeformed cross-sectional area as  $A_0$ . Since  $L_0$  and  $A_0$  are constants, the engineering stress-strain and force-displacement curve have similar shape (Figure 2.14). The current gauge length is  $L$ , and  $F$  is the applied axial force. The engineering stress is calculated as the average longitudinal stress in the specimen, while the engineering strain is calculated as the average strain. Figure 2.21 shows a typical engineering stress-strain curve for a mild steel, e.g. the X65 steel.

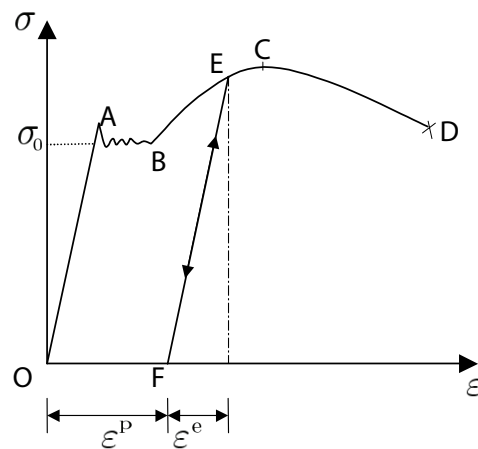


**Figure 2.21:** Typical engineering stress-strain curve during uniaxial tension [38].

To understand the terminology, the engineering stress-strain curve in Figure 2.21 is followed from initial condition until fracture. Important parameters used to describe the material are the yield limit, tensile strength, percent elongation and reduction in area [39]. From point O to point A the stress increases linearly with increasing strain, this is the basis of the theory of elasticity. The slope of the elastic region gives the modulus of elasticity, also referred to as the Young's modulus. Point A is called the upper yield point. When the stress exceeds this point, the material will experience permanent deformations after removal of the applied force. Applying more force after reaching the upper yield point leads to a drop in stress to the lower yield point. It is often seen that the stress oscillates around this value until reaching point B. The lower yield point is usually taken as the initial yield limit  $\sigma_0$  [38]. Between point B and C the material work-hardens until reaching ultimate tensile strength at point C. Unloading of the material in this region will follow the path indicated between point E and F, i.e. only the elastic part of the strain is recovered. The path will have the same slope as the initial elastic region.

The total strain (Equation (2.49)) consists of two terms. The permanent part is the plastic

strain  $\varepsilon^p$  and the recovered part is the elastic strain  $\varepsilon^e$  (Equation (2.48)).

$$\varepsilon^e = \frac{\sigma}{E} \quad (2.48)$$

$$\varepsilon = \varepsilon^e + \varepsilon^p \quad (2.49)$$

When reaching the ultimate tensile strength (point  $C$ ), the stress will decrease with increasing strain due to instability (diffuse necking) of the specimen. This trend will continue until fracture at point  $D$  [40]. Detailed theory regarding necking is given in Section 2.5.4.

**True stress and strain** are used to examine the actual stress-strain state at large deformations. Engineering strain and stress are calculated based on the initial dimensions of the gauge length and cross-section. However, these values change during deformation and the stresses and strains based on engineering values do not describe the true behavior of the material. Therefore, a more correct description of stresses and strains is achieved by the true strain  $\varepsilon_t$  and true stress  $\sigma_t$ , given in Equation (2.50) and (2.51), respectively.

$$\varepsilon_t = \int_{L_0}^L \frac{dL}{L} = \ln \frac{L}{L_0} \quad (2.50)$$

$$\sigma_t = \frac{F}{A} \quad (2.51)$$

Where  $A$  is the deformed cross-sectional area, and  $L$  is the current gauge length of the specimen. For metals the elastic strains remain small and the plastic deformation is assumed volume preserving (Equation (2.52)). The reason is, as mentioned in Section 2.5.1, that plastic strains occur by plastic slip.

$$A_0 L_0 = AL \quad (2.52)$$

Thus, the true strain and stress can be calculated, respectively, as

$$\varepsilon_t = \ln \frac{L}{L_0} = \ln \frac{A_0}{A} = 2 \ln \frac{d_0}{d} \quad (2.53)$$

$$\sigma_t = \frac{F}{A} = \frac{F}{\left(\frac{\pi}{4}\right)d^2} \quad (2.54)$$

## 2. THEORY

---

where  $d_0$  is the initial diameter and  $d$  is the current diameter. The latter equality in the above equations is only valid for circular specimens.

The true strain  $\varepsilon_l$  is often referred to as the logarithmic strain. The relation between the engineering strain  $\varepsilon_e$  and logarithmic strain  $\varepsilon_l$  is given as

$$\varepsilon_l = \ln \frac{L}{L_0} = \ln \left( \frac{L_0 + \Delta L}{L_0} \right) = \ln(1 + \varepsilon_e) \quad (2.55)$$

In the tensile test, the force  $F$  and change in length or diameter are continuously measured. If the initial gauge length  $L_0$  and area  $A_0$  are known, the engineering stress and strain can be calculated. Combining Equation (2.51), (2.53) and (2.55) gives the true stress as a function of the engineering stress and strain

$$\sigma_t = \sigma_e \exp(\varepsilon_l) = \sigma_e(1 + \varepsilon_e) \quad (2.56)$$

### 2.5.4 Necking

As pointed out in Section 2.5.3, when the ultimate tensile strength is reached (point  $C$  in Figure 2.21) the deformation becomes highly localized, and necking occurs. The formation of the necked region introduces a triaxial stress state. Hence, the average true stress at the neck, which is the axial force divided by the cross-sectional area at the neck, will be higher than the stress that is required to cause flow in simple tension [38]. From a physical point of view, necking can be seen as when the increase in stress due to the decrease in cross-section area, becomes greater than the increase in the load-carrying ability of the material due to strain-hardening. Mathematically, necking is defined by  $dP = 0$  and  $d\sigma_e = 0$  [34].

Based on Equation (2.56), the necking criterion  $d\sigma_e = 0$  can be rewritten as

$$d\sigma_e = 0 \implies \sigma_t = \frac{d\sigma_t}{d\varepsilon_l} \quad (2.57)$$

where  $d\sigma_t$  and  $d\varepsilon_l$  are the incremental change in true stress and logarithmic strain, respectively. Figure 2.22 illustrates the necking criterion graphically.

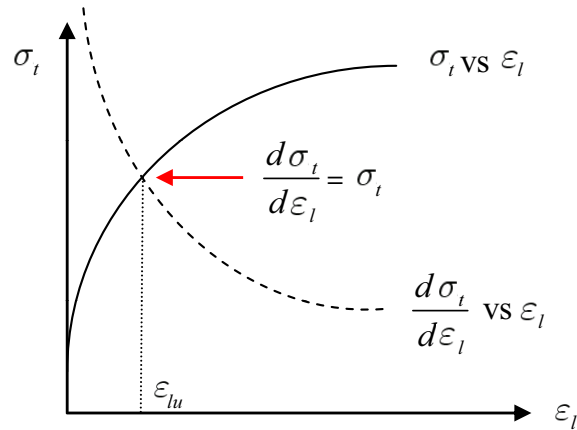


**Figure 2.22:** Illustration of necking criterion, where  $\varepsilon_{lu}$  is the logarithmic strain at necking [34].

The stress state of a necked specimen is practically the same as in a notched specimen. A notched specimen causes non-uniform stress and strain distributions close to the discontinuity, and a local stress peak occurs at the notch root (Figure 2.23). The plastic flow begins at the root when the local stress reaches the yield strength of the material [40]. In addition to the concentration of stress near the discontinuity, a notch will also create a localized condition of triaxial stress. A triaxial stress state will increase the value of the longitudinal stress.

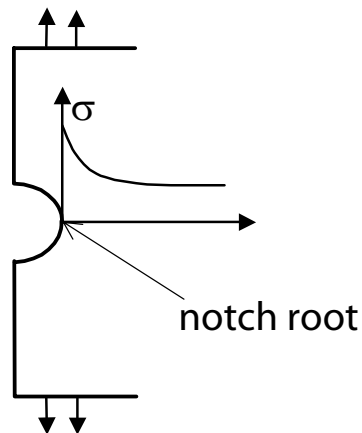


**Figure 2.23:** Stress concentration due to a notch [38].

## 2. THEORY

---

### 2.5.5 Bridgman's analysis

A simplified mathematical model to calculate the stress beyond the point of maximum load was proposed by Bridgman [39]. The idea behind the Bridgman method is that a formation of a neck in a tensile specimen introduces a complex triaxial stress state. It is therefore necessary to correct the stress for triaxiality. The Bridgman analysis is based on 4 assumptions:

- The contour of the neck is approximated by the arc of a circle.
- The cross-section of the necked region remains circular throughout the test.
- The von Mises yield criterion applies.
- The strains are constant over the cross-section of the neck.

The equivalent stress after necking is then given as

$$\sigma_{eq} = \frac{\sigma_t}{\left(1 + \frac{2R}{a}\right) \ln\left(1 + \frac{a}{2R}\right)} \quad (2.58)$$

and Le Roy's empirical model yields

$$\frac{a}{R} = 1.1(p - \varepsilon_{lu}^p) \quad (2.59)$$

where  $\varepsilon_{lu}^p$  is the plastic strain at necking [34]. The parameters  $a$  and  $R$  are the radius of the current cross-section and the radius of the curvature at the neck (Figure 2.24), respectively.

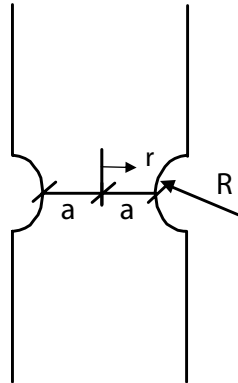


**Figure 2.24:** Sketch of necked specimen [38].

The triaxial stress state  $\sigma^*$  is given as

$$\sigma^* = \frac{\sigma_H}{\sigma_{eq}} \tag{2.60}$$

where  $\sigma_H$  is the hydrostatic stress and  $\sigma_{eq}$  is the equivalent stress. The hydrostatic stress is defined as the mean principal stress. Dey has shown that the initial triaxiality ratio at the center of the notched specimen, i.e. the maximum value when  $r = 0$ , is given as [38]

$$\sigma_{eq}^* = \frac{1}{3} + \ln \left( 1 + \frac{a}{2R} \right) \tag{2.61}$$

A typical result from a Bridgman correction is depicted in Figure 2.25. Bridgman’s analysis was originally performed for a necked tensile specimen, but it may also be applied as an approximation to pre-notched specimens [20].

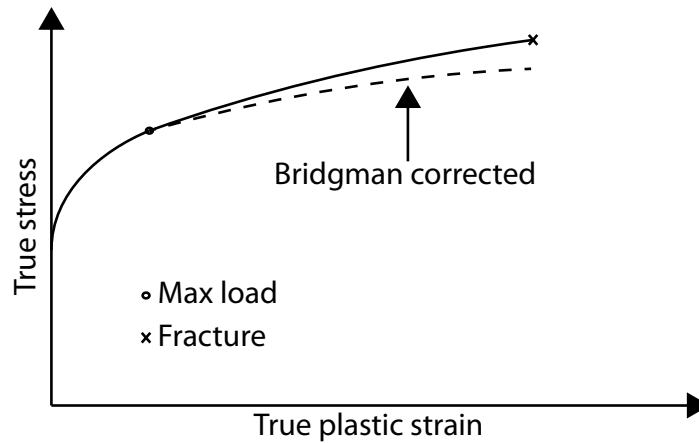


**Figure 2.25:** Comparing true stress vs strain with Bridgman corrected curve.

### 2.6 Physical mechanisms of fracture

So far in this thesis, the material has been studied from a solid mechanics point of view, i.e. only continuum models have been used. In certain cases this is a good approximation, but in other cases it may be necessary to consider the microscopic details of fracture. The following section is mainly based on the theory by Anderson [41].

Three types of fracture mechanisms are common for metals:

- Ductile fracture
- Cleavage fracture
- Intergranular fracture

Ductile materials usually fail as the result of nucleation, growth, and the coalescence of microscopic voids that initiate at inclusions and second-phase particles (Figure 2.26a). Cleavage fracture involves separation along specific crystallographic planes (Figure 2.26b). Note that the fracture path in Figure 2.26b is transgranular. Although cleavage is often called brittle fracture, it can be preceded by large-scale plasticity and ductile crack growth. Intergranular fracture occurs when the grain boundaries are the preferred fracture path in the material (Figure 2.26c). In most cases metals do not fail along grain boundaries. Ductile metals usually fail by the coalescence of voids formed at inclusions and second-phase particles, while brittle metals typically fail by transgranular cleavage [41]. Therefore, only ductile and cleavage fracture will be discussed.

For information regarding intergranular fracture it is referred to Anderson [41].

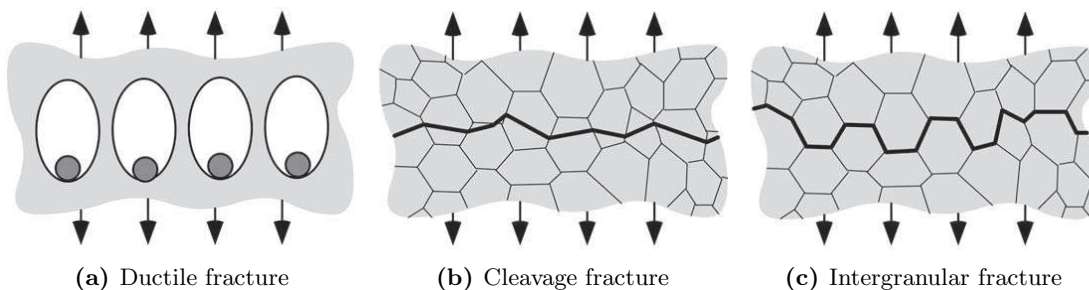


**Figure 2.26:** Illustration of ductile, cleavage and intergranular fracture in metals [41].

2.6.1 Ductile fracture

The vast majority of ordinary metals contain impurities, which makes them weaker. In a ductile fracture situation the microvoids grow together to form a macroscopic flaw, which leads to fracture. There are three commonly observed stages in ductile fracture [41]:

- Formation of a free surface at an inclusion or second-phase particle by either interface decohesion or particle cracking.
- Growth of void around the particle, by means of plastic strain and hydrostatic stress.
- Coalescence of the growing void with adjacent voids.

In materials where the second-phase particles and inclusions are well-bonded to the matrix, void nucleation is often the critical step, and fracture occurs soon after the voids form. A void forms around a second-phase particle or inclusion when sufficient stress is applied to break the interfacial bonds between the particle and matrix. Once the voids form, further plastic strain and hydrostatic stress cause the voids to grow and eventually coalesce. If void nucleation occurs with little difficulty, the fracture properties are controlled by the growth and coalescence of the voids. The growing voids reach a critical size, relative to their spacing, and a local plastic instability develops between the voids resulting in failure. Figure 2.27 illustrates the stages graphically [41].

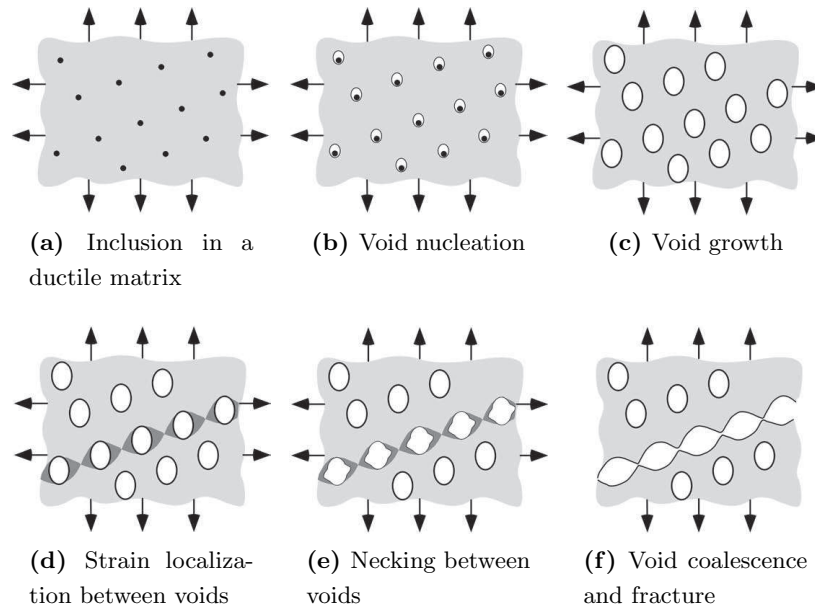


Figure 2.27: Void nucleation, growth and coalescence in ductile metals [41].

## 2. THEORY

---

Figure 2.27 is representable if the initial void fraction is low ( $< 10\%$ ). Then each void can be assumed to grow independently before interacting with neighboring voids. Plastic strain is concentrated along a sheet of voids, and local necking instabilities develop.

A commonly observed fracture surface for circular uniaxial tensile tests is the "cup and cone" fracture surface (Figure 2.28). As mentioned in Section 2.5.4, necking will occur when applying sufficient tensile force to the test specimen. The neck produces a triaxial stress state in the center of the specimen, which gives rise to void nucleation and growth in the larger particles. Applying more force causes the voids to coalesce, resulting in a penny-shaped flaw. The hydrostatic stress is smallest at the outer ring of the test specimen. Therefore, there will be relatively few voids in the outer ring compared to the center. The penny-shaped flaw produces deformation bands at  $45^\circ$  from the longitudinal axis (Figure 2.28b). This concentration of strains provides sufficient plasticity to nucleate voids in the smaller more numerous particles. Since the small particles are closely spaced, an instability occurs soon after these smaller voids form, resulting in total fracture of the specimen and the appearance of the cup and cone fracture surface (Figure 2.28c). Typically, the central region of the fracture surface has a fibrous appearance, while the outer region is relatively smooth [41].

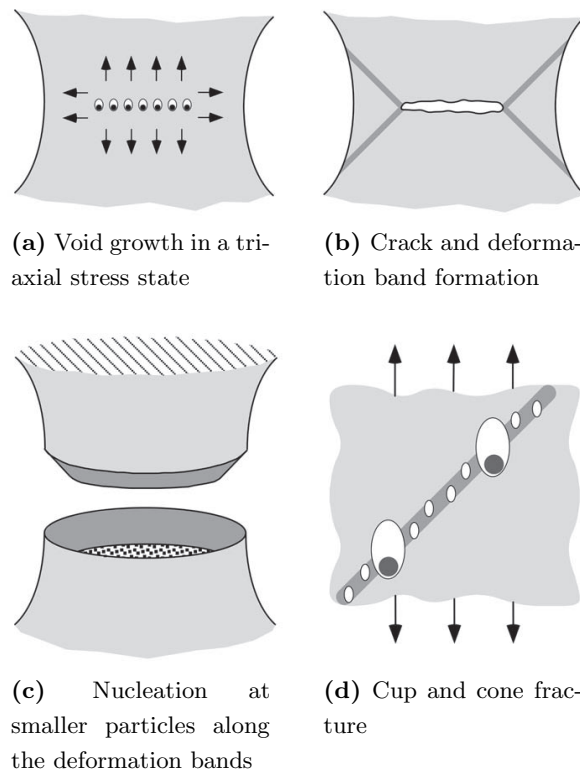


**Figure 2.28:** Formation of cup and cone fracture surface [41].

## 2.6 Physical mechanisms of fracture

The mechanism for a ductile pre-existing crack growth is illustrated in Figure 2.29a, 2.29b and 2.29c. As the cracked structure is loaded, strains and a triaxial stress state localizes at the crack tip (Figure 2.29e). In most materials, this stress state is sufficient to initiate void nucleation. These voids grow and eventually link with the main crack, resulting in a growing crack. Thus, the growth and coalescence of microvoids are usually the critical steps in ductile crack growth. Ductile crack growth is usually stable because it produces a rising resistance curve, and a typical zigzag fracture pattern is observed (Figure 2.29d) [41].

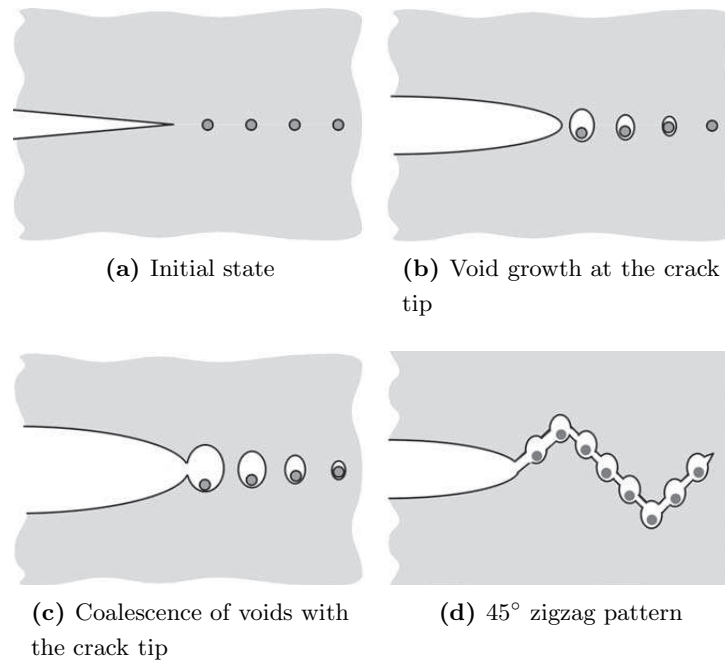


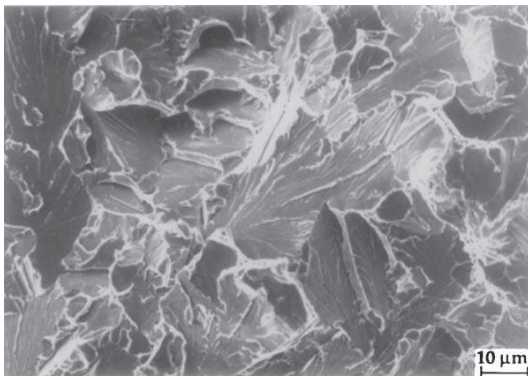
**Figure 2.29:** Mechanism for ductile crack growth and zigzag pattern [41].

## 2. THEORY

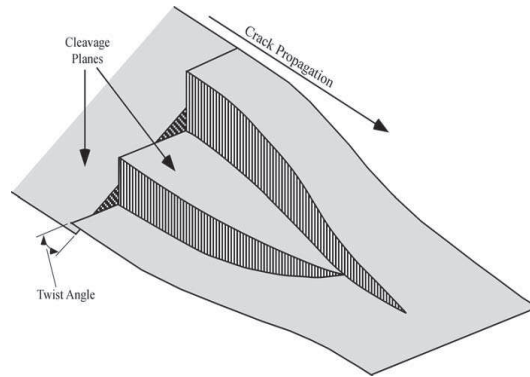
---

### 2.6.2 Cleavage fracture

Another important fracture mechanism for metals is cleavage. Since X65 is a ferritic steel, this thesis is limited to this type. Cleavage fracture can be defined as the rapid propagation of a crack along a particular crystallographic plane. Cleavage may be brittle, however, as mentioned earlier it can be preceded by large-scale plastic flow and ductile crack growth. The preferred cleavage planes are those with the lowest packing density, since fewer bonds must be broken and the spacing between planes is greater. Figure 2.30a shows a multifaceted surface where a "river pattern" can be seen. This is typical for cleavage. Figure 2.30b illustrates how river patterns are formed. A propagating cleavage crack encounters a grain boundary where the nearest cleavage plane in the adjacent grain is oriented at a finite twist angle from the current cleavage plane. Initially, the crack positions the twist mismatch by forming on several parallel planes (Figure 2.30b). As multiple cracks propagate, they are joined by tearing between planes. There is a tendency for the multiple crack to converge into a single crack [41].



(a) SEM fractographs of cleavage plane



(b) Formation of river patterns

**Figure 2.30:** SEM fractographs and formation of river patterns [41].

## 2.6 Physical mechanisms of fracture

Since cleavage involves breaking bonds, there must be a local discontinuity ahead of the macroscopic crack that is sufficient to exceed the bond strength. For steels, a common mechanism for microcrack formation involves inclusions and second-phase particles. Figure 2.31a illustrates this mechanism. The macroscopic crack provides a local stress and strain concentration. A second-phase particle, such as a carbide or inclusion, cracks because of the plastic strain in the surrounding matrix. If the stress ahead of the macroscopic crack is sufficient and the fracture stress is exceeded over a characteristic distance (Figure 2.31b), the microcrack propagates into the matrix causing failure by cleavage. Hence, the microcrack can be treated as a Griffith crack [41].

It is referred to Anderson [41] for a more detailed description regarding the above theory, e.g. the Griffith Crack.

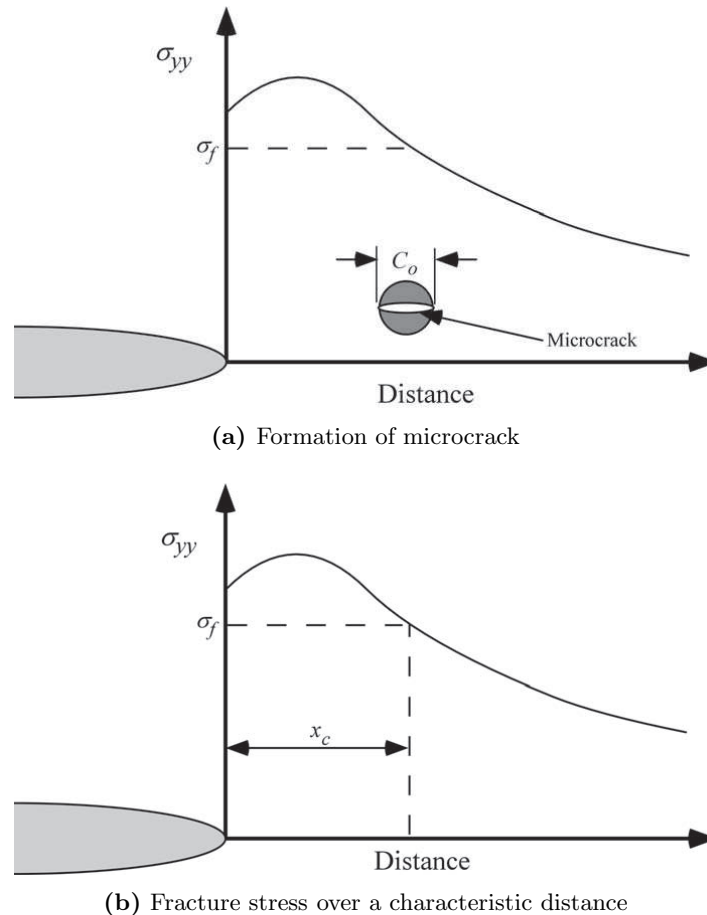


**Figure 2.31:** Initiation of cleavage at a microcrack that forms in a second-phase particle ahead of a macroscopic crack [41].

## 2. THEORY

---

### 2.7 Fracture criteria

It should be emphasized that a material model is not complete without some form of material degradation or failure. The degradation or damage in a material is usually given in terms of a damage parameter, and failure occurs through damage evolution [38]. As described in Section 2.6.1, ductile fracture arises from the nucleation, growth and coalescence of microscopic voids that initiate at inclusions and second phase particles. The voids around particles grow when subjected to plastic strain and hydrostatic tension. Furthermore, experimental investigations showed that the ductility depends on the triaxiality  $\sigma^*$  of the stress state [41]. Thus, it follows that a complete model for ductile failure should be dependent on the triaxiality. This thesis is limited to considering two ductile fracture criteria, i.e. the Cockcroft-Latham and Johnson-Cook criteria.

Cockcroft and Latham suggested a very simple fracture criterion which was based on plastic work per unit volume [42]. They reasoned that the fracture criterion needed to be based on some combination of stress and strain, and damage accumulates during straining until a critical value  $W_c$  was reached at  $\varepsilon^p = \varepsilon_f$ . To account for hydrostatic tension they based the criterion on the magnitude of the major principal stress  $\sigma_1$  as

$$W_c = \int_0^{\varepsilon_f} \langle \sigma_1 \rangle d\varepsilon^p \quad (2.62)$$

where  $W_c$  is the Cockcroft-Latham parameter determined based on the uncorrected data from a smooth uniaxial tension test,  $\varepsilon^p$  and  $\varepsilon_f$  are the equivalent plastic strain<sup>3</sup> and fracture strain, respectively. The expression  $\langle \sigma_1 \rangle$  is equivalent to the function  $\max(0, \sigma_1)$ . Hence, only positive values of the maximum principal stress  $\sigma_1$  contribute to the Cockcroft-Latham parameter.

Johnson and Cook introduced a constitutive relation and fracture criterion dependent on temperature, strain rate and strain path [21, 43]. They defined the equivalent von Mises stress  $\sigma_{eq}$  and failure strain  $\varepsilon_f$ , respectively, as

$$\sigma_{eq} = (A + B\varepsilon^{p^n})(1 + C \ln \dot{\varepsilon}^{p^*})(1 + T^{*m}) \quad (2.63)$$

$$\varepsilon_f = (D_1 + D_2 e^{D_3 \sigma^*})(1 + D_4 \ln \dot{\varepsilon}^{p^*})(1 + D_5 T^*) \quad (2.64)$$

---

<sup>3</sup>In a uniaxial tension test with no previous strain history, the plastic strain  $\varepsilon^p$  equals the equivalent plastic strain  $p$ .

where  $A$ ,  $B$ ,  $C$ ,  $n$ ,  $m$  and  $D_i$  are material constants determined from material tests. The dimensionless strain rate  $\dot{\varepsilon}^p$  and the homologous temperature  $T^*$  are given as

$$\dot{\varepsilon}^{p*} = \frac{\dot{\varepsilon}^p}{\dot{\varepsilon}_0} \quad \text{and} \quad T^* = \frac{T - T_f}{T_m - T_r} \quad (2.65)$$

In the former expression  $\dot{\varepsilon}^p$  is the equivalent plastic strain rate and  $\dot{\varepsilon}_0$  is the reference strain rate. In the latter expression,  $T$  is the absolute temperature, and the subindices  $r$  and  $m$  indicate room and melting temperature, respectively.

Johnson and Cook based their fracture criterion on damage evolution, where the damage  $D$  of a material element is defined as

$$D = \sum \left( \frac{\Delta \varepsilon^p}{\varepsilon_f} \right) \quad (2.66)$$

where  $\Delta \varepsilon^p$  is the incremental equivalent plastic strain, and failure is assumed to occur when  $D$  equals unity.

Dey has shown that the fracture criterion suggested by Johnson and Cook could be related to the Cockcroft-Latham criterion [38]. However, it should be emphasized that an axisymmetric stress state is assumed. By using Equation (2.60), the major principal stress  $\sigma_1$  can be expressed as

$$\sigma_1 = \sigma_H + \frac{2}{3} \sigma_{eq} = \left( \frac{2}{3} + \sigma^* \right) \sigma_{eq} \quad (2.67)$$

Inserting Equation (2.63) for  $\sigma_{eq}$  in Equation (2.67) gives the major principal stress as

$$\sigma_1 = \left( \frac{2}{3} + \sigma^* \right) (A + B \varepsilon^{p^n}) (1 + C \ln \dot{\varepsilon}^{p*}) (1 + T^{*m}) \quad (2.68)$$

Using the latter expression in Equation (2.62), the Cockcroft-Latham criterion may be expressed as

$$W_c = \int_0^{\varepsilon_f} \left\langle \left( \frac{2}{3} + \sigma^* \right) (A + B \varepsilon^{p^n}) (1 + C \ln \dot{\varepsilon}^{p*}) (1 + T^{*m}) \right\rangle d\varepsilon^p \quad (2.69)$$

It should be noted that the stress triaxiality, strain rate and temperature are assumed constant during the tensile tests.

## 2. THEORY

---

Finally, by integrating the latter equation, a nonlinear expression for the fracture strain  $\varepsilon_f$  is given as

$$A\varepsilon_f + \frac{B}{n+1}\varepsilon_f^{n+1} - \frac{W_c}{\left(\frac{2}{3} + \sigma^*\right)(1 + C \ln \dot{\varepsilon}^{p^*})(1 + T^{*m})} = 0 \quad (2.70)$$

It is important to emphasize that this is an approximation, considering that the stress triaxiality and strain rate increase in a developing neck (Figure 2.23).

### 3 Introductory studies

As mentioned in Chapter 1, the objective of the experiments is to investigate the damage behavior of the X65 steel at large strains. During impact and stretching the pipe experience large compressive and tensile states of stress. Hence, the influence of compression on damage evolution was of great interest, both with respect to ductility and void nucleation. The literature shows that there is a discussion about both these topics regarding compressive states of stress [6, 44]. Therefore, it was decided to perform pre-compressed tension tests at different load levels.

To perform these experiments, a geometry that could withstand large compressive loading without any geometrical instabilities was needed. It was therefore carried out an introductory study to find a suitable geometry for the material testing. In addition, an introductory study regarding inverse modeling was performed. The objective was to evaluate the advantage and use of the optimization tool LS-OPT. The tension test performed by Slåttedalen and Ørmen was used as a basis for this study [3]. Initially, a calibration based on the method of least squares was conducted. This was used as a comparison with the inverse modeling.

### 3. INTRODUCTORY STUDIES

---

#### 3.1 Identification of material parameters by the method of least squares

An isotropic material model was calibrated based on the uniaxial tension test performed by Slåttedalen and Ørmen using the method of least squares. The objective of this study was to establish a basis for comparison with material models in this thesis. This was performed by locating the point where necking occurred (Figure 3.1a), and correcting the true stress-strain curve based on the method suggested by Bridgman (Section 2.5.5). Hence, the constitutive relation was calibrated based on the equivalent stress from the experiments (Figure 3.1b and Table 3.1). In addition, a minor study was performed regarding the difference of calibrating the constitutive relations based on small and large strains (Figure 3.1c), i.e. in this study before and after necking, respectively.

The constitutive relations considered were the Voce rule ( $i=2$ ) and Power law. When neglecting the effect of strain rate and temperature dependence, the Johnson-Cook relation suggested by Slåttedalen and Ørmen (Table 3.1) is mathematically the same as the Power law.

**Table 3.1:** Material parameters based on small and large strains.

Material model	Isotropic hardening				
	$\sigma_0$ [MPa]	$Q_1$ [MPa]	$b_1$	$Q_2$ [MPa]	$b_2$
Voce rule (Small)	478.10	275.90	7.20	1.00	1.00
Voce rule (Large)	475.70	142.20	14.36	760.40	0.41
	A		B		n
	[MPa]				
Power law (Small)	482.10		930.00		0.83
Power law (Large)	452.50		424.60		0.44
Johnson-Cook	465.5		410.83		0.48

### 3.1 Identification of material parameters by the method of least squares

The constitutive relation that gave the best fit with the experimental data was the Voce rule (Equation (2.39) and Figure 3.1c-3.1d). Hence, this was used as the basis for the introductory studies. It is also worth noting the advantage of calibrating against large strains (Figure 3.1c). The second term in the Voce rule calibrated based on small strains could be neglected due to its insignificant contribution to the hardening. This was confirmed by the behavior of this relation, which showed that it converged to its asymptote very rapidly (Figure 3.1c).

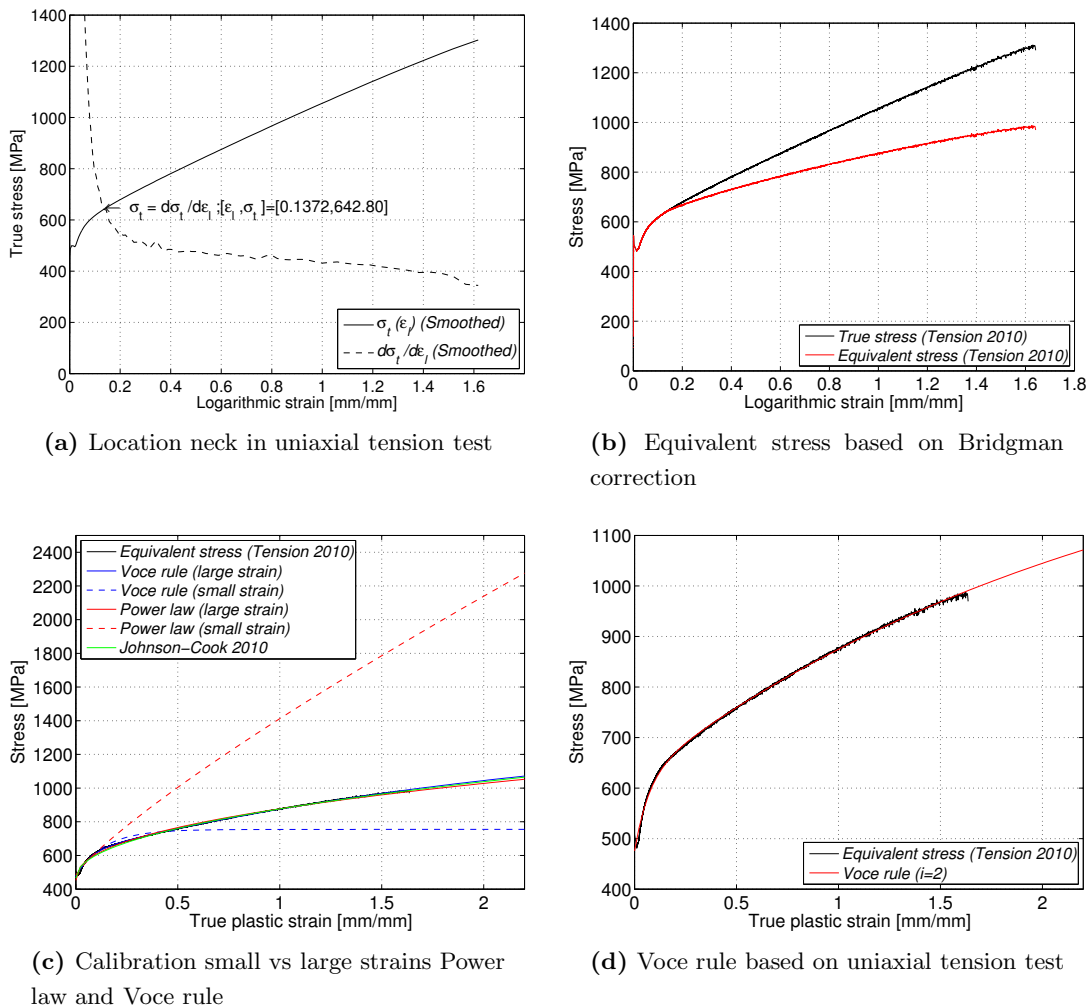


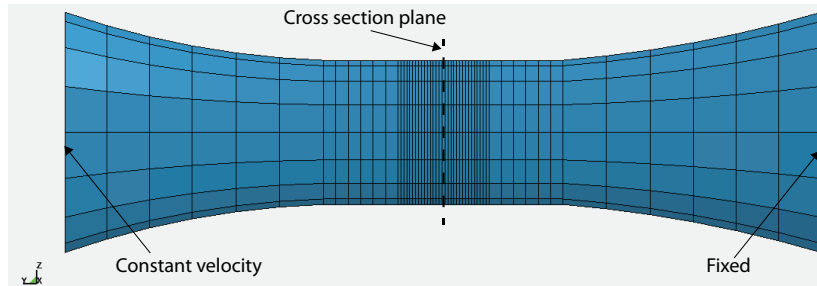
**Figure 3.1:** Identification of material parameters by the method of least squares.

## 3.2 Identification of material parameters with LS-OPT

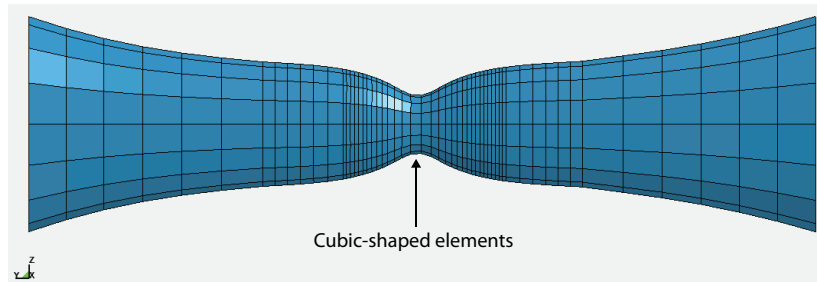
An introductory study was carried out to investigate two different approaches to determine the material parameters in a constitutive relation. The uniaxial tension test performed by Slåttedalen and Ørmen was used as a basis for this study. The constitutive relation used in the present thesis consists of nine material parameters (Section 2.5.2). However, the nature of a tension test involves no cyclic loading. Therefore, this study was limited to isotropic hardening and the material model described in Section 3.1. The study included inverse modeling using the Finite Element Method (FEM) and the method of least squares. The latter is usually the preferred method, and often called a direct calibration. The objective was to investigate if the inverse modeling using LS-OPT, gave a better fit to the experimental data compared to the direct approach.

### 3.2.1 Numerical modeling

LS-OPT uses parameterized simulations with the FEM software LS-DYNA to perform an automated calibration to the experimental data. The objective is to minimize the error between the experiments and numerical simulations with respect to user-defined variables [45]. Thus, a solid element model was established in LS-DYNA. The model consisted of 1815 eight-node linear brick elements with element height and width between 1 to 0.06 mm and 1 to 0.6 mm, respectively. At the bottom end all degrees of freedom were fixed, while the upper end was given a constant velocity. Since the experiment lasted several minutes and LS-DYNA is an explicit FEM code, time scaling was used to speed up the simulation, i.e. the velocity was increased and the time period was reduced. The analysis was performed using 52200 time-steps for a period of 0.00056 s with a maximum displacement of 2.8 mm. Thus, the deformation velocity was 5000 mm/s. The loading was applied by a smooth loading curve, to avoid numerical instabilities in the incipient loading. The test was considered quasi-static, i.e. there was assumed no rate dependency. A plane was defined through the cross-section normal to the longitudinal axis at the center of the specimen (Figure 3.2a), where the force and cross-sectional area were used as output. To obtain good results the cutting-plane should cleanly pass through the middle of the elements, distributing them equally on either side [36]. It was desirable to have cubic-shaped elements at large strains in tension (Figure 3.2b). Therefore, at initial configuration the center of the specimen contained highly rectangular elements (Figure 3.2a).



(a) Model in LS-DYNA



(b) Quadratic element shape at large strains in tension

**Figure 3.2:** Numerical model in LS-DYNA.

#### 3.2.2 Optimization in LS-OPT

LS-OPT calibrates the material parameters based on a target curve and a computed curve. The computed curve was the result from the numerical simulations in LS-DYNA, which in this case was chosen as the true stress and plastic strain. Stresses and strains were calculated based on the force and area in the cutting-plane (Figure 3.2a). The target curve was based on the experimental data. The experimental data contained some noise and did not have equally spaced increments along the abscissa. Therefore, the data was smoothed and the total number of sampling points were reduced to get an equally weighted curve in terms of the plastic strain increments (Figure 3.3). The plastic strain increments were determined by the number of sampling points, which in this case was chosen as one hundred<sup>4</sup>. The main objective of the optimization in LS-OPT was to minimize the mean square error between these curves in terms of the user-defined variables, i.e. the material parameters. The user need to specify the initial, minimum and maximum values of these parameters. The initial values were found using the method of least squares (Table 3.1). The optimization problem was run with 10 iterations. All other settings were kept as default. It should be noted that

---

<sup>4</sup>Note that the target curve in Figure 3.3 consists of only 50 points to give a better illustration of the equal increments along the abscissa. However, the curve used in the optimization consisted of 100 points.

### 3. INTRODUCTORY STUDIES

---

the Cockcroft-Latham parameter  $W_c$  was set to a large value to avoid fracture and zero area in the numerical analysis.

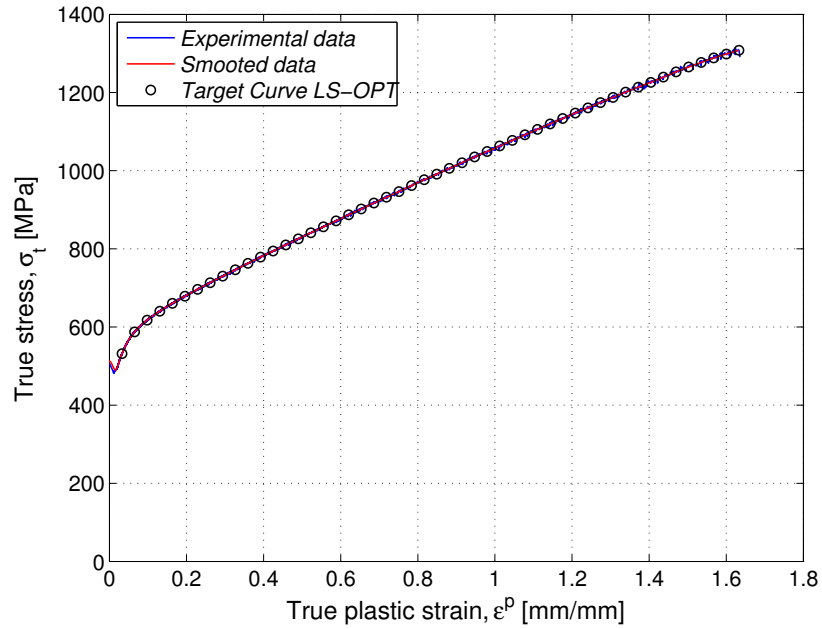


**Figure 3.3:** Target curve used in LS-OPT.

3.2.3 Results

The results from the direct calibration and inverse modeling were analyzed in terms of true stress-plastic strain from LS-DYNA, and compared to the experimental data. The material parameters from the direct calibration and inverse modeling are presented in Table 3.2. The plastic strain versus equivalent stress and true stress are plotted in Figure 3.4, respectively.

Table 3.2: Material parameters for the Voce hardening rule.

Method	$\sigma_0$ [MPa]	$Q_1$ [MPa]	$b_1$	$Q_2$ [MPa]	$b_2$
Direct calibration	475.70	142.20	14.36	760.40	0.41
Inverse modeling	459.70	150.00	18.70	705.70	0.48

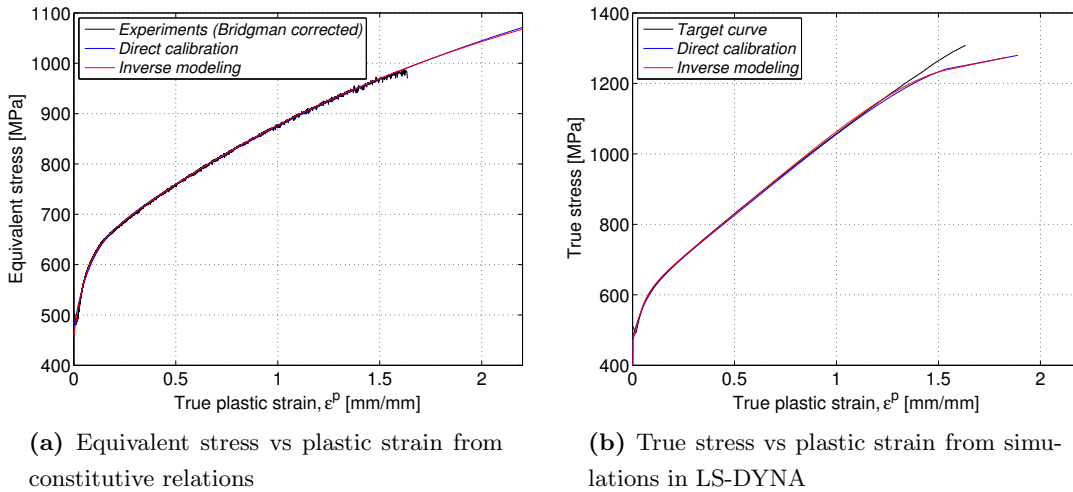


Figure 3.4: Direct calibration vs inverse modeling.

Since the method of least squares gave a good fit, the optimization with LS-OPT yields little improvement for the uniaxial tension test (Figure 3.4). The marginal benefit of using LS-OPT was in this case offset by the fact that a direct calibration was less time consuming. However, for the purpose of a calibration based on a more complex stress state or multiple cases, LS-OPT should be considered and may be preferable compared with a direct calibration.

It is worth noting that both approaches failed to recreate the behavior at the end of the tension test ( $\epsilon^p > 1.25$  in Figure 3.4b). The trend was observed for both cases. The explanation may therefore stem from the modeling in LS-DYNA. This observation may be explained from the

### 3. INTRODUCTORY STUDIES

---

lost cross-sectional area due to the linear element representation (Figure 3.5a). The model in LS-DYNA consisted of 16 elements around the circumference, which introduced an error of 2.5 % in the representation of the cross-sectional area (Figure 3.5b). It is assumed that this will affect the stiffness of the specimen.

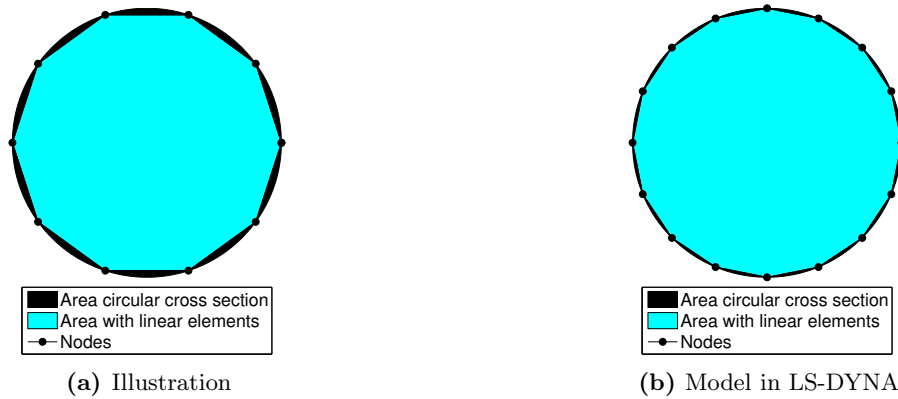


**Figure 3.5:** Reduced area due to linear elements.

The reduction in cross-sectional area due to linear volume elements could be avoided by using an axisymmetric model or smaller elements around the circumference. A quadratic element formulation could also be used, however, LS-DYNA only supports elements with eight nodes or less [36].

Another explanation of the deviation at large strains in Figure 3.4b may stem from the fact that necking was localized in the nodes (Figure 3.2b). The area used to calculate the stress and strain was extracted from the cross-sectional plane (Figure 3.2a). Thus, at the end of the simulation, the stress and strain were calculated based on an area that was outside the smallest cross-section. Therefore, the area used to calculate the response was too large and the stress was underestimated.

However, none of these possible explanations change the conclusion regarding the use of LS-OPT for the uniaxial tension test. Good results could be achieved with direct calibration, and the gain by using LS-OPT in this case disappears in the shadow of the CPU cost associated with this optimization.

It must be emphasized that there was not used equally spaced strain increments in the direct calibration. Thus, the direct approach may be somewhat improved by using equally spaced sampling points.

### 3.3 Geometry for pre-compressed tension tests

An introductory study was carried out to find a suitable geometry for the material testing. Experiments involving compression, especially at large deformations, are exposed to buckling and barreling. Buckling occurs when axial strain energy is converted into bending strain energy without any change in applied load, and may result in large lateral deflection [26]. Barreling occurs when the unconstrained material near the middle of the specimen deforms laterally to a greater extent than the constrained material near the edges [39].

The literature revealed that there has been conducted similar testing on diabolo-shaped<sup>5</sup> specimens with two different geometries [6]. It was therefore decided to use these geometries by scaling them according to the thickness of the pipe (Figure 3.6 and Table 3.3). Numerical simulations were run in ABAQUS/Explicit to verify if the diabolo-shape could be used in the experiments.

**Table 3.3:** Geometries introductory study.

Type	R [mm]	d [mm]	D [mm]	h [mm]	H [mm]
1	5.5	5.5	10	8.6	54.1
2	3.6	6.4	10	6.4	51.8

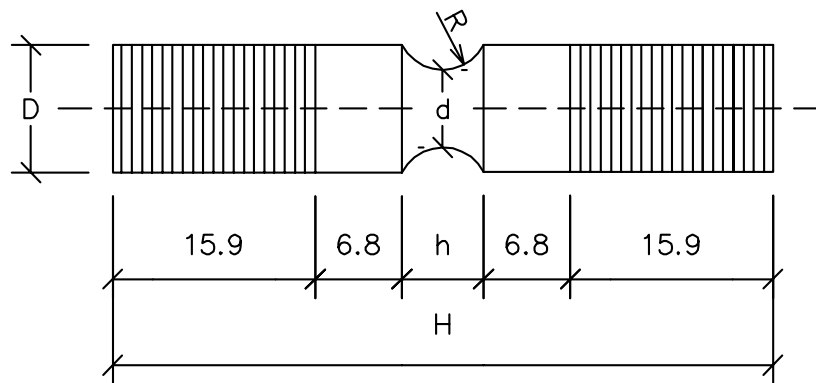


**Figure 3.6:** Geometry introductory study.

The main difference between the two geometries was the radius, which modifies the stress triaxiality ratio at the center and stiffness.

<sup>5</sup>A diabolo-shaped specimen is often referred to as a notched specimen in the literature.

### 3. INTRODUCTORY STUDIES

---

#### 3.3.1 Numerical simulations in ABAQUS/Explicit

A volume element model was established to study the two geometries presented in Table 3.3. The model was small and not very CPU costly. It was therefore decided to model the whole diabolo. The model consisted of 2616 linear hexahedral elements of type C3D8R with element size between 0.5 and 1 mm (Figure 3.7a). The simulations were performed with reduced integration and hourglass control. By using linear elements it was preferred to use a fine mesh to represent a circular cross-section and correct stiffness (Figure 3.5a). Geometrical instabilities were assumed to occur in the smallest cross-sectional area. Therefore, the element size in this region was chosen to minimize the error in cross-sectional area and at the same time maintain a reasonable CPU cost. By using 32 elements around the circumference of the cross-section an error of approximately 2 % was introduced and the CPU cost was reasonable (Figure 3.7b and Table 3.4).

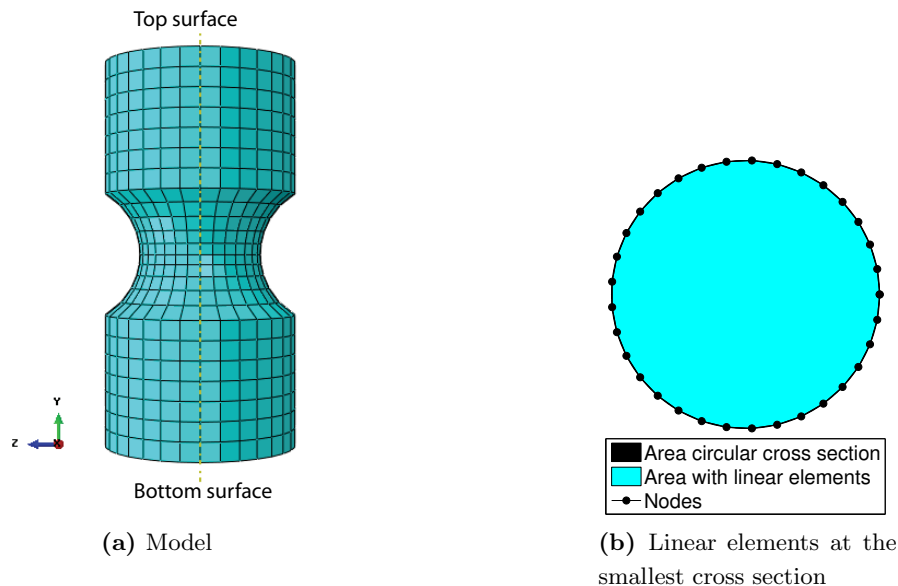


**Figure 3.7:** Model in ABAQUS/Explicit.

To simulate the experiments, the region between the threaded areas was modeled (Figure 3.7a). All degrees of freedom were fixed at the bottom surface, while the top surface was given a constant velocity. The model consisted of a smooth loading curve to avoid numerical instabilities in the incipient loading. Both simulations were run with a velocity of 1000 mm/s and a period of 0.005 s, which resulted in a displacement of 5 mm for the top surface. The experiments were planned to be quasi-static, i.e. there was assumed no rate dependency. The

analyses were run with one step in compression, and the isotropic material model found with inverse modeling in Section 3.2.3 was used (Table 3.2).

#### 3.3.2 Results

The equivalent plastic strain, reaction force and change in diameter were the output from the simulations. The equivalent plastic strain was calculated as both the average value at the smallest cross-section and extracted from selected nodes. The reaction force was calculated as the sum of nodal forces at the bottom surface. The results were evaluated based on two observations:

- (1) Visual inspection (Figure 3.8 and 3.9).
- (2) Plot of the equivalent plastic strain of selected nodes in the notched region (Figure 3.10a and 3.10b).

Both observations were performed to detect geometrical instability due to the large deformations in compression. The latter observation was based on the equivalent plastic strain extracted from three nodes in the notched region. The nodes were neighboring nodes in the longitudinal direction starting from a node at the smallest cross-section (Figure 3.8a and 3.8b). The node at the smallest cross-section is hereinafter named the center-node (Node 73 and 143 in Figures 3.8a and 3.8b, respectively). This observation was to ensure that the center-node contained the maximum equivalent plastic strain. If the neighboring nodes exceeded the level of equivalent plastic strain in the center-node, the specimen was assumed to have geometrical instabilities and could not be used in the experiments.

The numerical simulations revealed that type 1 was unsuitable for plastic strains larger than 44.6 %. Deformations exceeding this level resulted in barreling. This was confirmed by both the visual inspection and plot of the equivalent plastic strain in the neighboring nodes (Figure 3.8a and 3.10a). Type 2 showed no signs of geometrical instabilities (Figure 3.8b and 3.10b). The latter geometry also showed a stiffer behavior (Figure 3.10c), which was expected since it has a larger diameter  $d$  at the center (Table 3.3). Hence, type 2 was used in the experiments to study the influence of compression on damage evolution.

The triaxial stress state was also computed based on the numerical simulations. The results showed that type 1 had a lower triaxial stress state than type 2 (Figure 3.10d). This is confirmed by previous observations, indicating that a higher radius yields a lower triaxial stress state at the center [6].

### 3. INTRODUCTORY STUDIES

---

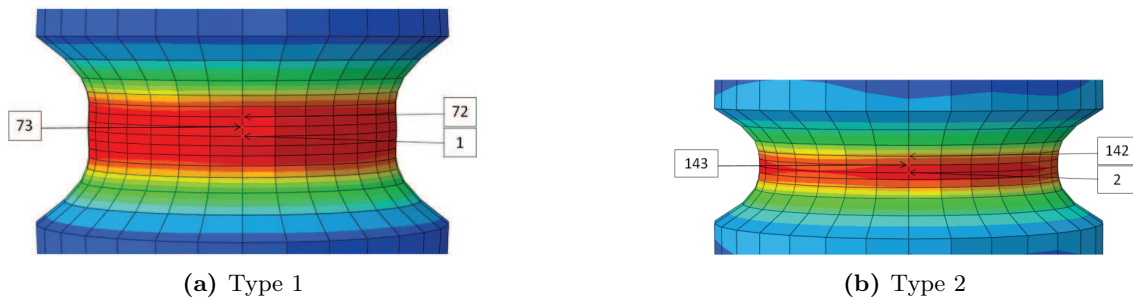


**Figure 3.8:** PEEQ selected nodes at end of simulation (displacement top surface 5 mm).

To highlight and better illustrate the visual observations, the simulations were extended in terms of deformation for the top surface (Figure 3.9).

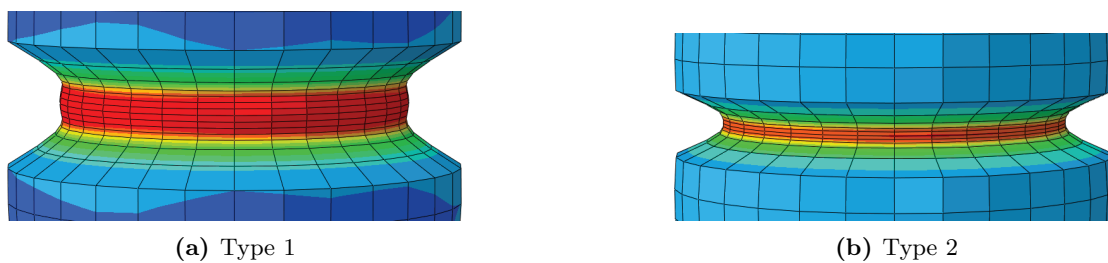


**Figure 3.9:** Displacement top surface 8 mm (visual inspection).

### 3.3 Geometry for pre-compressed tension tests

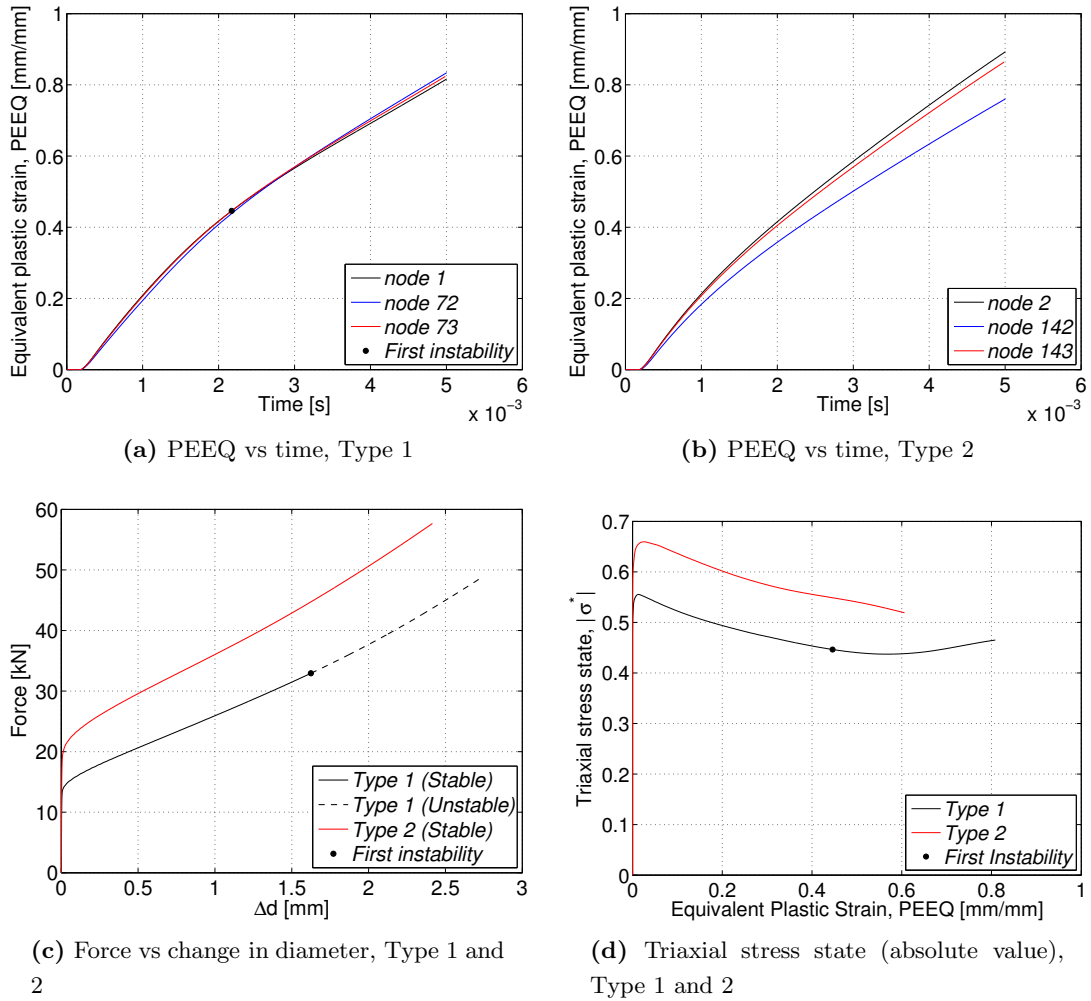


Figure 3.10: Results from numerical simulations in ABAQUS/Explicit.

### 3. INTRODUCTORY STUDIES

#### 3.3.3 Energy balance check

When nonlinear dynamic problems are solved by an explicit method, it is important to perform an energy balance check to warn against possible numerical instability. In nonlinear simulations, numerical instability may be dissipated by energy-dissipating nonlinear material behavior, e.g. the elastic-plastic material behavior described in Section 3.2.3 [26]. Therefore, artificially introduced energy due to numerical instability may be difficult to detect because the solution may appear reasonable.

The simulations should be quasi-static and the level of artificial energy should be small. Hence, the contribution from the kinetic energy and artificial energy should be small compared to the internal energy. The numerical simulations fulfill these requirements (Figure 3.11 and Table 3.4), and the results presented in Section 3.3.2 are therefore assumed to be representative for the experiments.

**Table 3.4:** Energy balance at the end of the analyses.

Type	$E_k$ [kJ]	$E_i$ [kJ]	$E_a$ [kJ]	$\frac{E_k}{E_i}$ [%]	$\frac{E_a}{E_i}$ [%]	CPU* [s]
1	0.002	164.6	0.472	0.001	0.287	140.6
2	0.002	204.3	0.817	0.001	0.400	118.6

\*The simulations were run with 6 parallel processors.

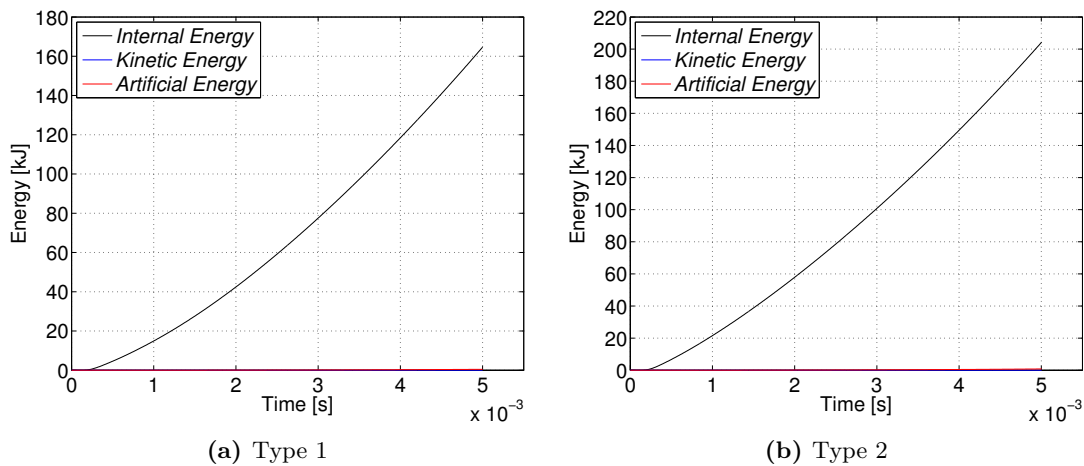


**Figure 3.11:** Energy balance numerical simulations in ABAQUS/Explicit.

## 4 Material testing

The following study was a continuation of the two previous master's theses [3, 4]. Slåttedalen and Ørmen studied strain-hardening, strain-rate effect, possible anisotropy and homogeneity of the material, by conducting uniaxial tensile tests. Fornes and Gabrielsen continued the work by investigating the effect of reversed loading by performing uniaxial compression-tension tests (and vice versa). Since uniaxial test specimens are not very useful for large strains in compression, the notched specimen from Section 3.3 was used to withstand a larger force in compression. However, by changing the specimen geometry a complex triaxial stress state was introduced. In addition, a metallurgical investigation of the notched tests was conducted.

### 4.1 The X65 steel

The X65 steel is mainly used in the oil and gas industry as one of the primary steels in pipelines. The X65 steel has high strength, and is relatively inexpensive to manufacture compared to other higher-performing steels. Pipelines are exposed to high pressure and consumed in large quantities each year, making the X65 a suitable choice for pipelines. In terms of chemistry, the steel is quite simple when compared to other higher-performing steels. After iron *Fe*, the most abundant elements are carbon *C* (0.09%), silicon *Si* (0.25%), manganese *Mn* (1.13%), chromium *Cr* (0.04%) and molybdenum *Mo* (0.09%). In addition, other elements like calcium *Ca*, sulfur *S*, aluminum *Al*, magnesium *Mg*, oxygen *O*, titanium *Ti*, vanadium *V* and nitrogen *N* are found, but in smaller concentrations. Titanium and vanadium are added to get the desired toughness [46]. It should be noted that the X65 is a ferritic steel with relatively small grain size.

For a more detailed information regarding the composition of the material, it is referred to the material certificate in Appendix A.1.

### 4.2 Uniaxial tests

To study strain-hardening, strain-rate effect, possible anisotropy and homogeneity, uniaxial tensile tests were taken at different locations and orientations in the pipe. For a detailed description regarding the location and orientation turn to Slåttedalen and Ørmen [3]. Quasi-static tests were conducted to determine the strain-hardening effect. To determine the strain-rate effect the Split-Hopkinson Tension Bar was used. Uniaxial tests with reversed loading were conducted by Fornes and Gabrielsen to examine the kinematic behavior of the material.

#### 4.2.1 Quasi-static tensile tests

Quasi-static tensile tests were conducted at room temperature with a deformation controlled stretching machine. The diameter reduction was measured by a purpose-built laser device, and calculated as the average of two orthogonal diameters. Beyond necking, the true stress  $\sigma_t$  was corrected for the triaxial stress state that arise in the neck according to Bridgman (Section 2.5.5). Figure 4.1 shows the Bridgman correction for one of the tests.

Two parallel tests were performed at each location to highlight any differences between the specimens. As can be seen in Figure 4.2a, the curves at different locations over the cross-section are almost identical, except for a small deviation in the south direction. The curves in Figure 4.2b are seen to deviate more, however, this deviation is insignificant compared to some of the differences between parallel tests. The material was therefore assumed to be homogeneous and isotropic. The circular fracture surfaces in Figure 4.3 also supported this conclusion. Young's modulus  $E$  was calculated as 208000 MPa, the initial yield limit  $\sigma_0$  as 472 MPa and ultimate tensile strength  $\sigma_u$  as 565 MPa.

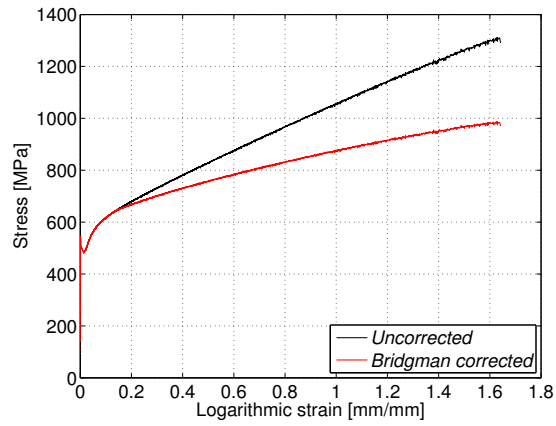
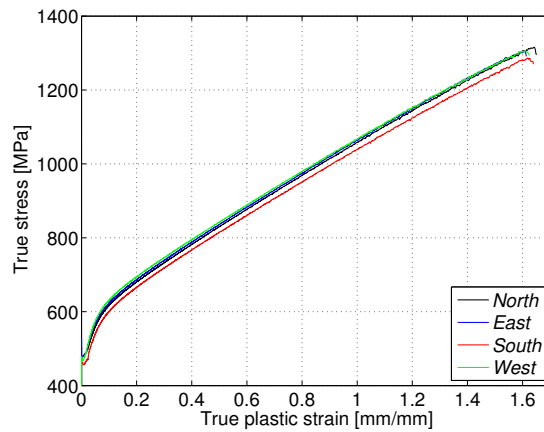
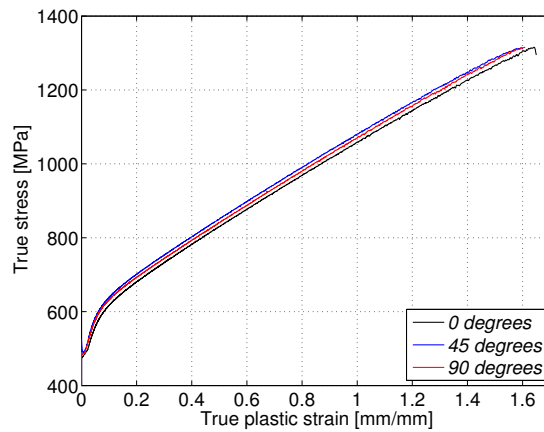


Figure 4.1: Uniaxial tension test corrected with Bridgman [3].



(a) Different location over the cross-section



(b) Different rotation about the longitudinal direction

Figure 4.2: True stress vs strain from uniaxial tension tests [3].

## 4. MATERIAL TESTING

---

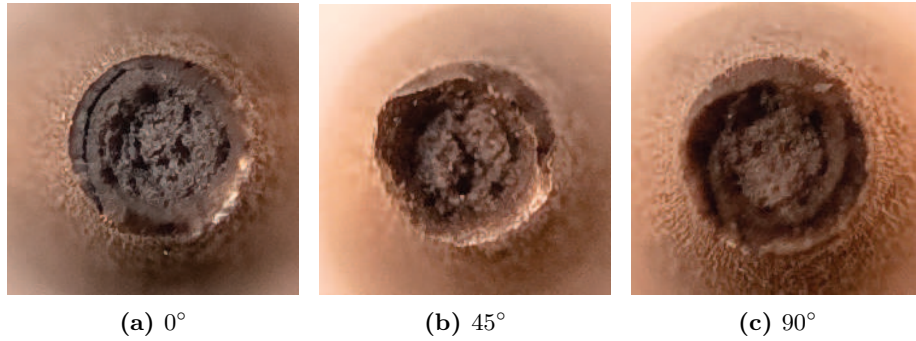


**Figure 4.3:** Fracture surface at different orientations [3].

### 4.2.2 Dynamic tensile tests

The dynamic tensile tests were conducted using a Split-Hopkinson Tension Bar and the output was stress-strain curves. Two parallel tests at three different strain-rates ( $\dot{\epsilon} = 240 \text{ s}^{-1}$ ,  $\dot{\epsilon} = 535 \text{ s}^{-1}$  and  $\dot{\epsilon} = 830 \text{ s}^{-1}$ ) were conducted. The results are plotted, together with the quasi-static tensile test ( $\dot{\epsilon} = 0.001 \text{ s}^{-1}$ ), in Figure 4.4. The dynamic tests revealed that the flow stress, and to some extent, the fracture strain were affected by the strain rate. The flow stress increased when the strain-rate increased, and the fracture strain was negligible reduced with increased strain-rates (Figure 4.5).

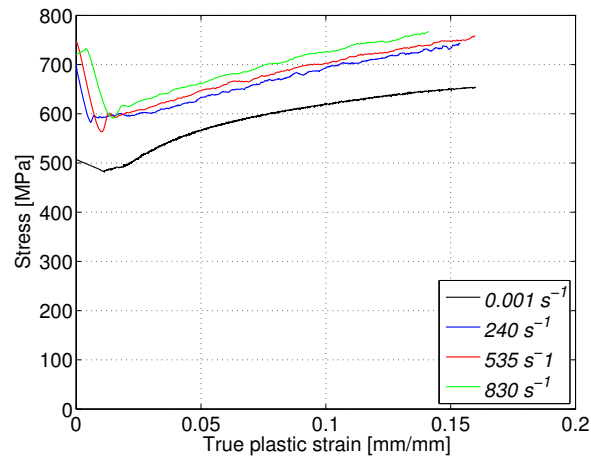


**Figure 4.4:** Characteristic stress-strain curves at different strain rates [3].

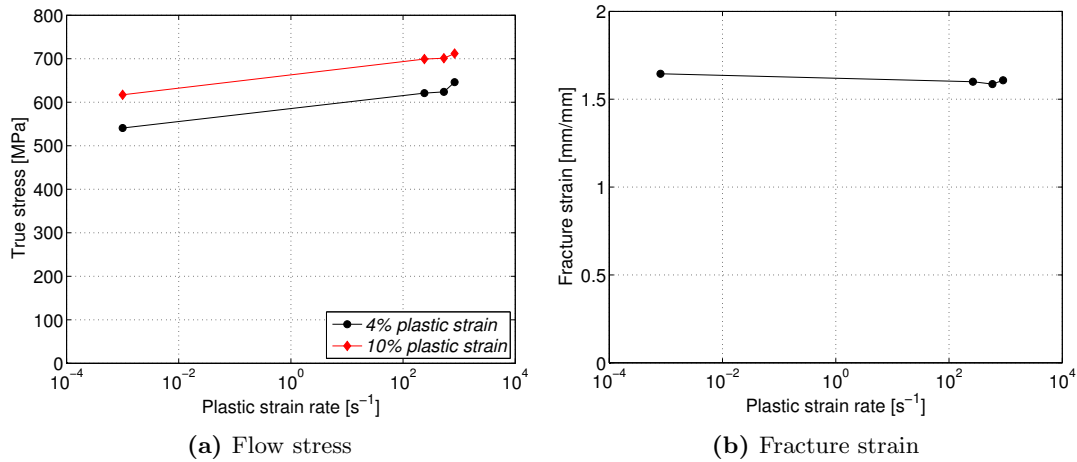


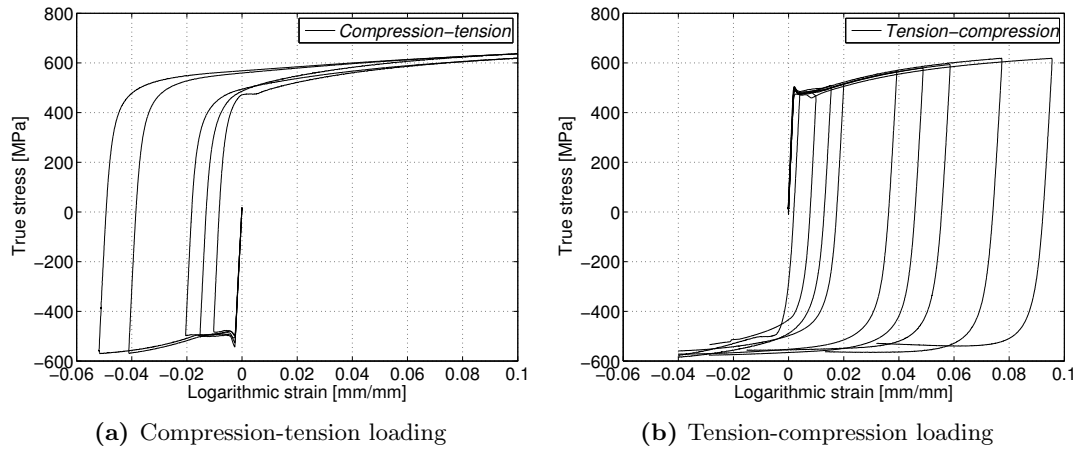
**Figure 4.5:** The effect of increasing strain-rates (averaged values) [3].

### 4.2.3 Reversed loading

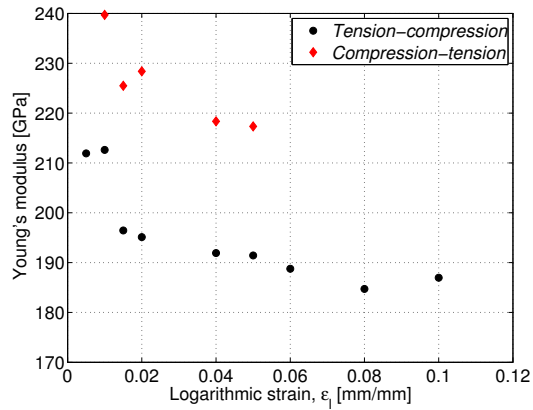
It was considered appropriate to expose the smooth specimens first to tension before compression, due to problems connected with buckling. However, the pipes studied, are first exposed to compression then tension. It was therefore conducted tests for both compression-tension and tension-compression to investigate possible differences between initial load direction. Double-sided extensometers were applied, and tendency to buckling was controlled by observing that the strain measured by the two extensometers did not differ significantly. For a more detailed review on the test set-up and specimen geometry it is referred to Fornes and Gabrielsen [4].

Figure 4.6a shows the results for compression-tension tests. The tension-compression tests revealed no significant difference to the specimens initial loaded in compression (Figure 4.6b). It is important to emphasize that these tests only describe the behavior of the material at small strains. The initial yield limit  $\sigma_0$  of the material was calculated as 480 MPa. The tests revealed a decrease in Young's modulus  $E$  for increasing strain, and it was larger for tests initial loaded in compression (Figure 4.7).

## 4. MATERIAL TESTING



**Figure 4.6:** Test results for uniaxial specimens loaded in compression-tension (and vice versa) [4].



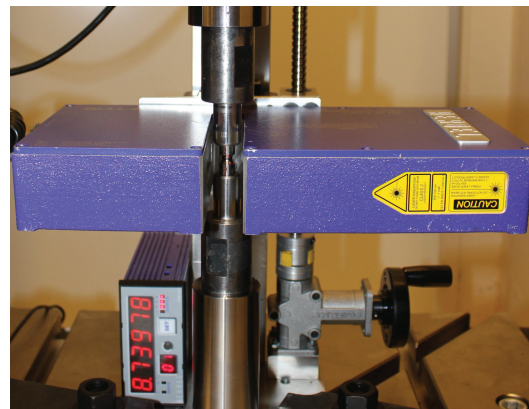
**Figure 4.7:** Young's modulus  $E$  decreasing for increasing strain.

### 4.3 Notched tests with reversed loading

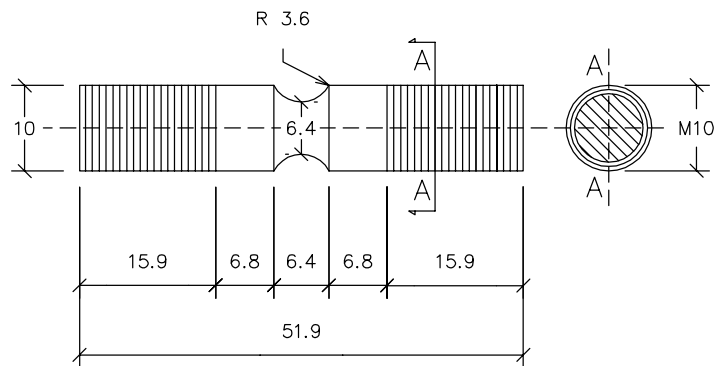
Notched pre-compressed tension tests were conducted with the objective of examining the behavior of the material exposed to large strains in compression, and how this influenced the fracture strain, ductility and kinematic behavior. In addition, a selection of test specimens were exposed to compression only. A metallurgical investigation of the tests was carried out to study the microstructural behavior.

4.3.1 Set-up and geometry

The tests were conducted with a deformation controlled Instron 100 kN testing machine. The deformation rate was kept constant at 0.2 mm/min, corresponding to a strain-rate of  $1.4 \cdot 10^{-3} \text{ s}^{-1}$ . A purpose built laser device was used to measure the change in diameter in two perpendicular directions. The operator ensured that the laser was measuring the critical diameter during the tests, i.e. the largest diameter in compression and smallest in tension. Figure 4.8 shows the experimental set-up and initial specimen geometry, respectively. The test specimen geometry was based on the studies in Section 3.3. To control for buckling and barreling, visual inspection during the tests together with a thorough examination of the  $F-\Delta d$  curve, was performed.



(a) Experimental set-up



(b) Initial specimen geometry

Figure 4.8: Experimental set-up and geometry.

## 4. MATERIAL TESTING

### 4.3.2 Results

In total 20 notched test specimens were available, it was therefore decided to split the testing into two series. The first series consisted of two parallel tests at different strain level in compression before tension. One regular tension test and four pre-compressed tension tests were conducted. The test program is given in Table 4.1. The results and test set-up were then examined, and the specimen geometry was modified before conducting test series 2.

**Table 4.1:** Test program for pre-compressed tension tests series 1.

Test ID	CT0-1	CT10-1	CT20-1	CT30-1	CT40-1
Strain [%]	0	10	20	30	40
Test ID	CT0-2	CT10-2	CT20-2	CT30-2	CT40-2
Strain [%]	0	10	20	30	40

The results from the first parallel of test series 1 are shown in Figure 4.9. Higher magnitude of  $\Delta d$  in compression is equivalent to higher magnitude of plastic strain. The true stress-plastic strain curves are shown in Figure 4.9b, and were calculated using Equation (2.51) and (2.50), respectively. Figure 4.11 shows the  $F$ - $\Delta d$  curves at increasing load levels in compression for both parallels in test series 1. Thus, the scatter between the two parallel tests was low.

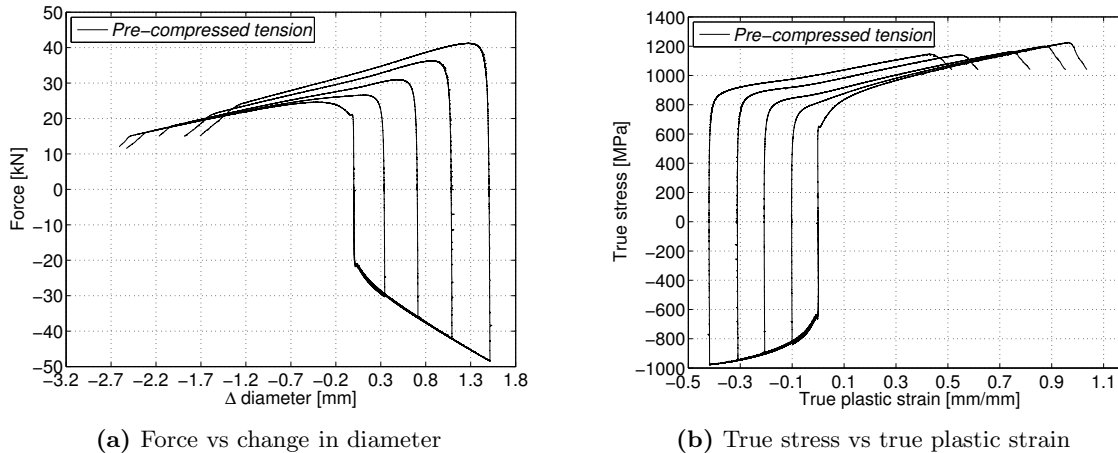


**Figure 4.9:** Experimental results for pre-compressed tension tests for parallel 1 in series 1.

When comparing the work-hardening of the material in pre-compressed tension and tension, a rather large difference is seen. In tension, the work-hardening is gradually increasing, this behavior was expected with reference to Section 2.5.2. However, when the pre-compressed material was loaded in tension, the work-hardening deviates from what was experienced in tension (Figure 4.10). The true stress-plastic strain curves under reversed deformation are

depicted in Figure 4.10. As can be seen in the figure, the reversed deformation has two distinct stages:

- (1) The transient Bauschinger effect characterized by early re-yielding and the rapid change of work-hardening rate  $d\sigma_t/d\varepsilon^p$ .
- (2) The permanent softening characterized by the flow stress offset observed in a region after the transient period, where the reversed work-hardening rate is lower than (or almost equal) that during the forward deformation.

Work-hardening stagnation is clearly seen in the reversed curves, where the work-hardening rate stays below the forward one. Consequently, in the transient stage, the stress-strain curves under reversed deformations are not parallel to the forward curve for this range of deformations. However, for larger reversed deformations, the work-hardening gradient is similar to what is experienced in tension.

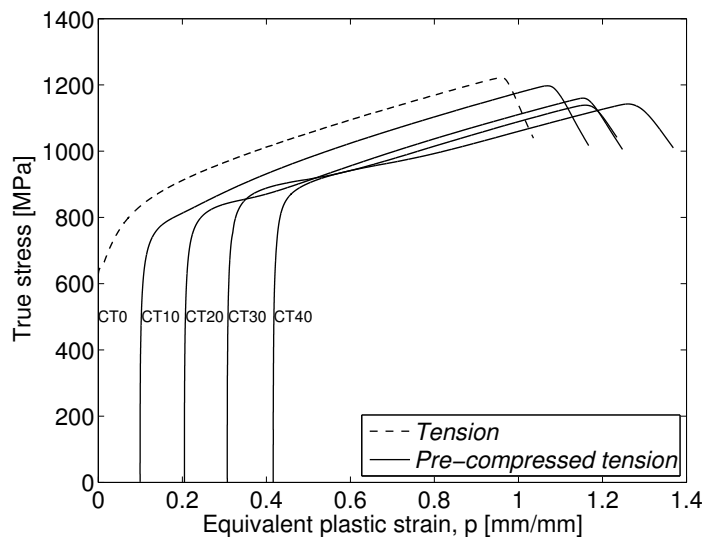


**Figure 4.10:** True stress vs plastic strain under reversed deformation during parallel 1 in test series 1.

From a physical point of view, the transient Bauschinger effect is attributed to the motion of less stable dislocations, i.e. piled-up dislocations. On the other hand, the permanent softening associated with the work-hardening stagnation, is mainly caused by the dissolution of dislocation cell walls performed during forward deformation and the formation of new dislocation microstructures during reversed deformation (Section 2.1.1).

## 4. MATERIAL TESTING

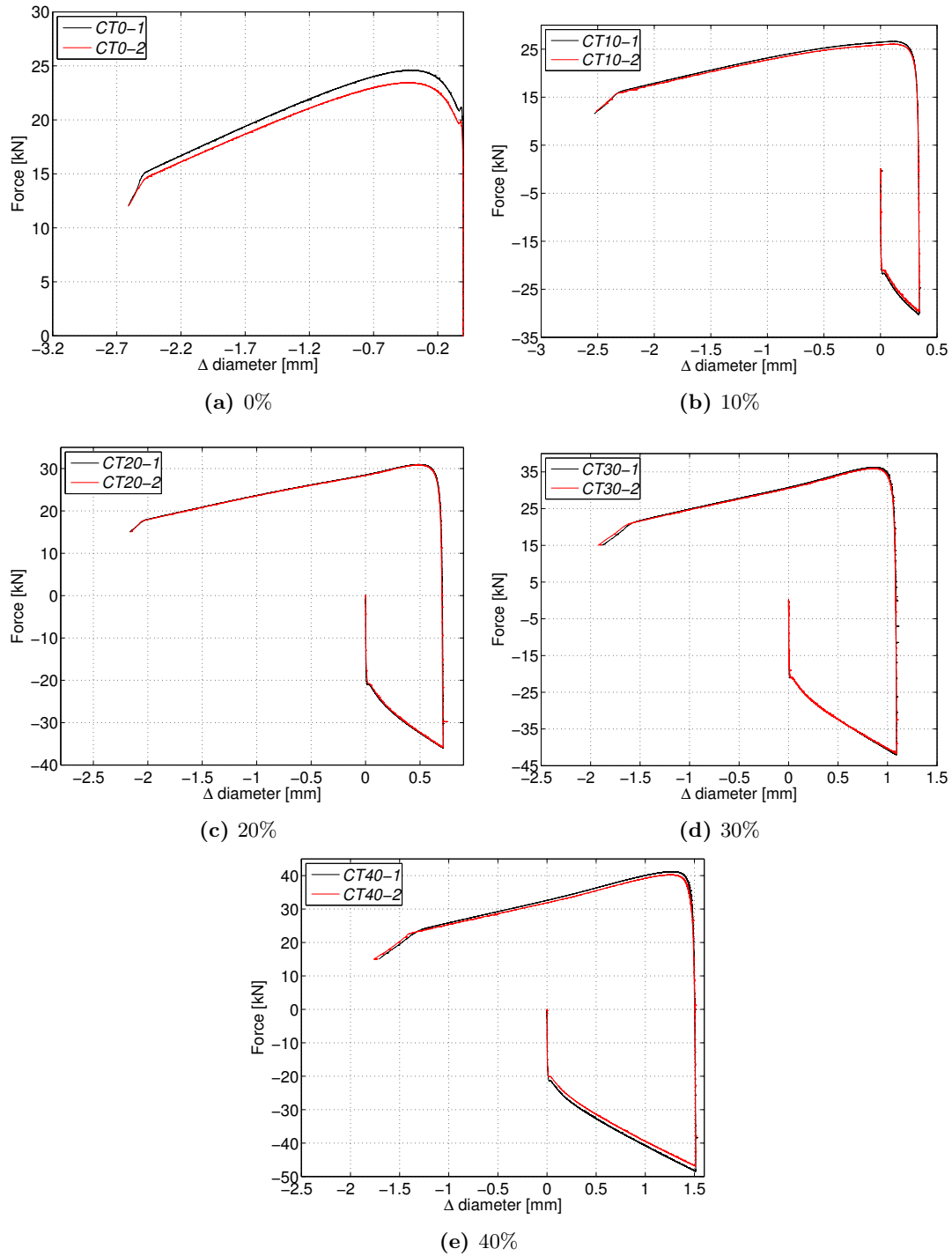


**Figure 4.11:** Pre-compressed tension tests at various plastic strain levels in compression (test series 1).

### 4.3 Notched tests with reversed loading

Figure 4.12a and 4.12b shows the work and fracture strain for the pre-compressed tension tests, respectively. As the figures shows, both the work during hydrostatic tension and fracture strain decrease all the way up to a plastic strain in compression of 30 %. However, from 30 % to 40 % plastic strain, the trend deviates. It is also noted that the total work, due to the maximum principal stress, increases successively for increasing pre-compression (Figure 4.12a). Further investigation of these trends formed the basis of test series 2. A minor eccentricity in the experimental set-up made it necessary to modify the test geometry to withstand higher strains than 40 %. This minor eccentricity became more visible at increased loading (Figure 4.12c and 4.12d). However, this was expected to have little impact on the results up to 40 % plastic strain. Figure 4.9 shows no significant irregularities in the material behavior. Based on the experience from test series 1, the test geometry was modified to withstand an increased compressive load (Figure 4.13).

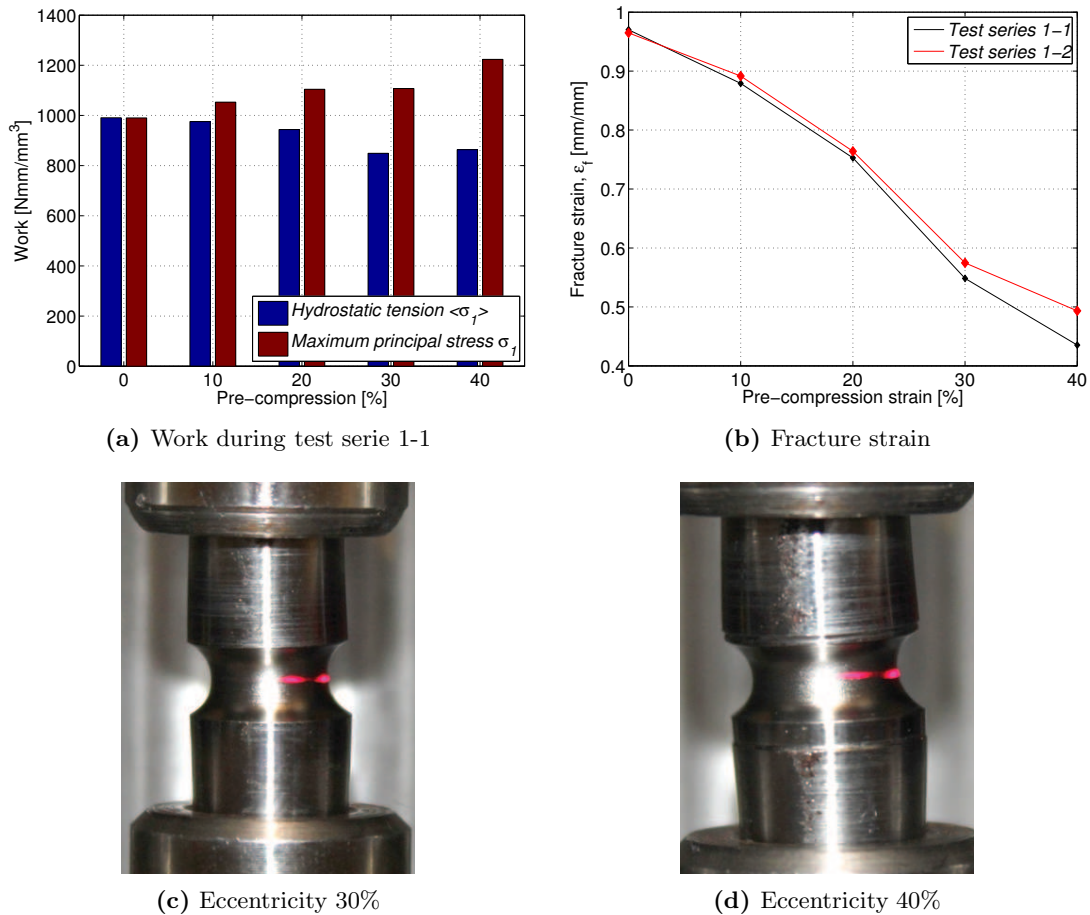


Figure 4.12: Results test series 1.

## 4. MATERIAL TESTING

The program for test series 2 is given in Table 4.2. The first test (CT60-1) was compressed to 60 % plastic strain before tension. However, unexpected necking occurred in the threaded area (Figure 4.14), and therefore the results were not valid. To be able to conduct such tests, the specimen must be taken out of the test machine and adjusted before stretching, similar to that suggested by Bridgman (Section 2.1.1). However, this is time consuming and will be left to further work. It was therefore decided to do compression tests ranging from 20 % to 80 % plastic strain to study the microstructural behavior of the material. Figure 4.15 shows  $F-\Delta d$  curves for successively increasing plastic strain levels. Initially ( $\Delta d < 0.75$ ) the  $F-\Delta d$  curves are concave towards the abscissa. At increasing displacement ( $\Delta d \sim 0.75-1.5$ ) the curves become approximately linear and continue to rise. At higher displacement ( $\Delta d > 1.5$ ) an inflection is seen and the curves become concave towards the ordinate. Hence, the change in diameter  $\Delta d$  is increasing with a larger rate than the applied force, thus, the change in gradient. Figure 4.16 shows a photo taken at the end of each plastic strain level. The test with 80 % plastic strain had to be cut out of the test machine because the specimen got stuck.

**Table 4.2:** Test program for pre-compressed tension tests series 2.

Test ID	CT60-1	C20-1	C40-1	C60-1	C80-1
Strain [%]	60	20	40	60	80

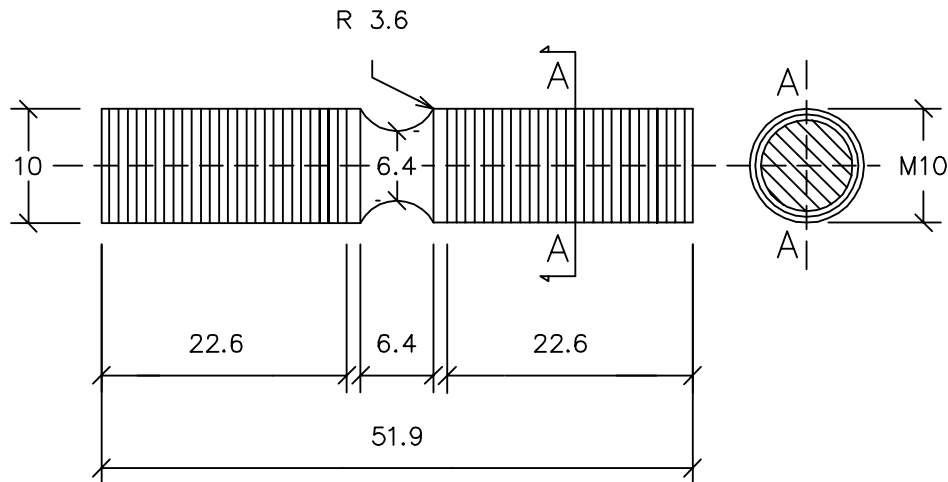


**Figure 4.13:** Specimen geometry for test series 2.

### 4.3 Notched tests with reversed loading

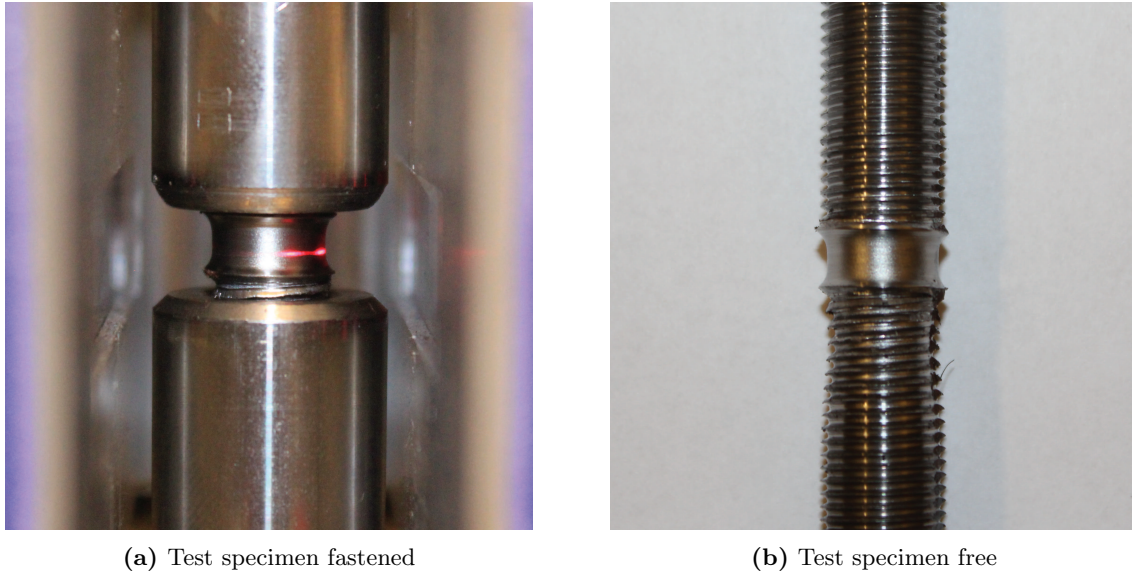


Figure 4.14: Test specimen mounted and free for 60 % plastic strain in compression.

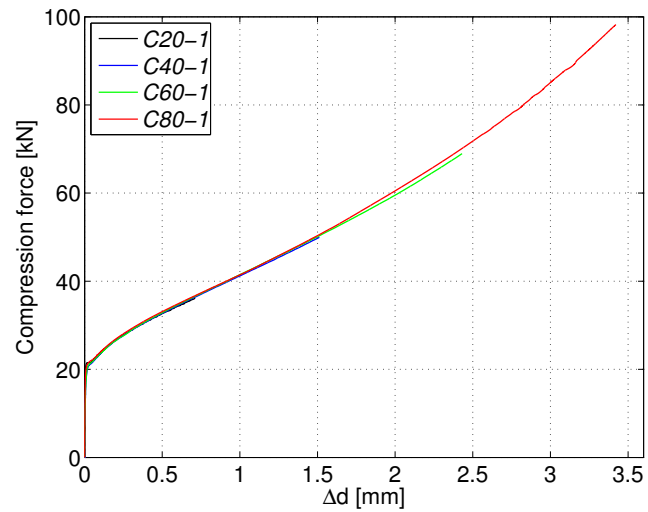
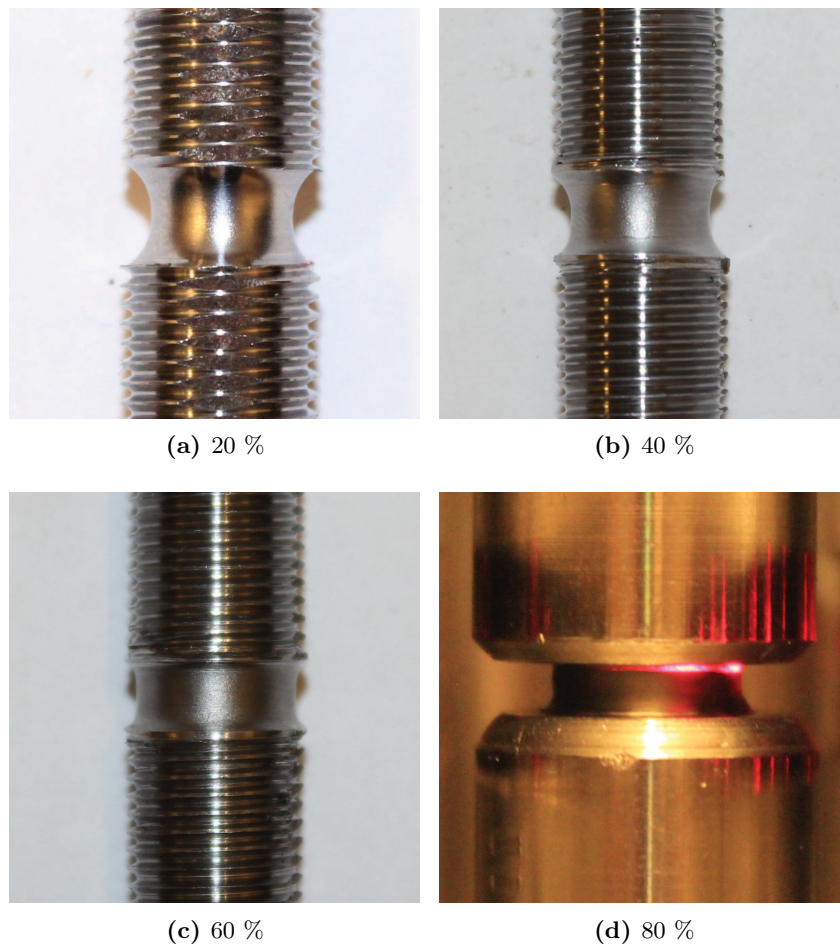


Figure 4.15:  $F$  vs  $\Delta d$  at different plastic strains in compression.

## 4. MATERIAL TESTING

---



**Figure 4.16:** Compressed tests ranging from 20 % to 80 % plastic strain. The test with 80 % plastic strain had to be cut out of the test machine because the specimen got stuck.

### 4.3.3 Metallurgical investigation

In the following section the fracture surface of the pre-compressed tension tests was studied. In addition, the matrix and particle composition in the material have been examined. This work has been carried out in collaboration with research scientist Dr. Ida Westermann at SINTEF.

Macroscopic photos in Figure 4.17 shows the fracture surface of the pre-compressed tension tests. As can be seen in the figure, the fracture surface is typical "cup and cone" (Section 2.6.1). There is a high concentration of microvoids in the center of the necked specimen compared to the edges. The central portion of the specimen exhibits a dimpled appearance, while the outer regions appear to be relatively smooth, this is typical for "cup and cone" [41].

Figure 4.18 shows the fracture surface for *CT10-1* at different magnification levels. This figure clearly depicts the distinct dimpled appearance. This dimpled surface is characteristic of microvoid coalescence. It should also be pointed out that the fracture surfaces seem relatively isotropic (circular in Figure 4.17), supporting the results from Slåttedalen and Ørmen.

Further investigation of selected particles revealed some interesting findings (Figure 4.19). At high magnification the particles appear to be crushed, with rather large voids surrounding them. With reference to Section 2.6, this finding is very important because it lowers the fracture strength of the material.

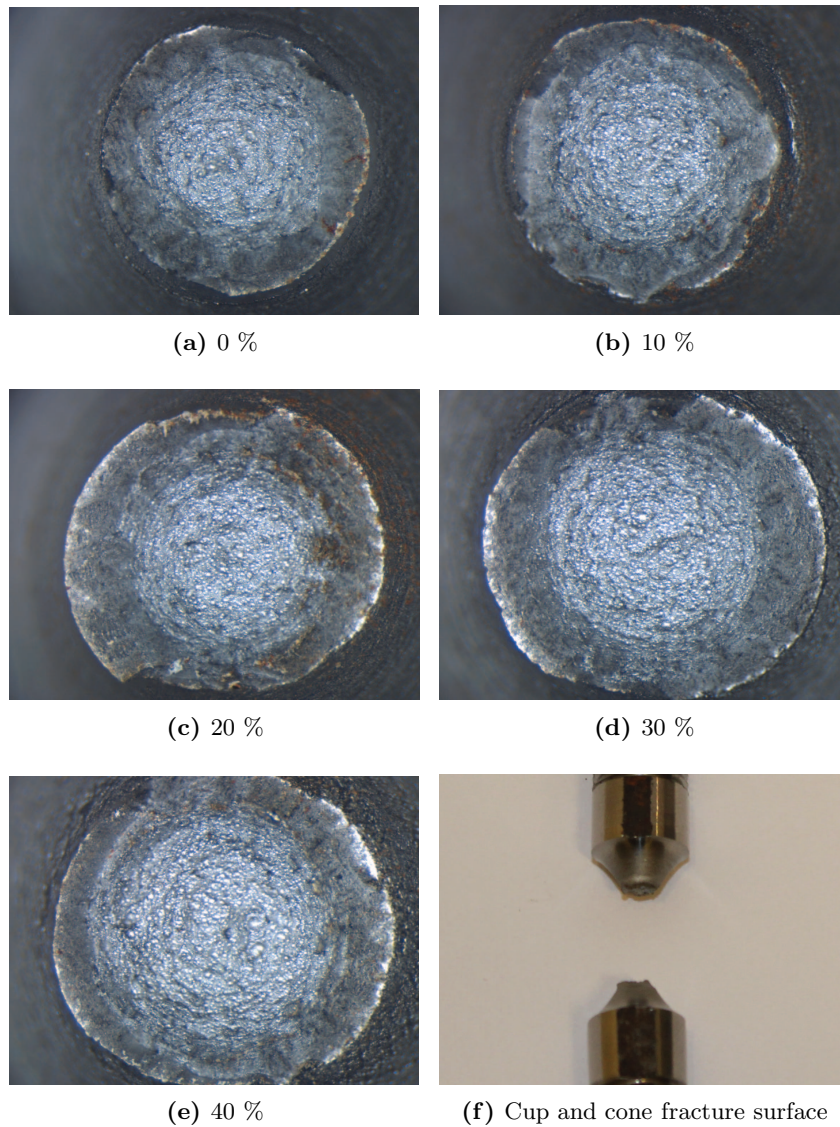
Figure 4.20 shows microstructural photos at successively increasing plastic strain levels in compression only. The tests are cross-sectional cuts along the longitudinal axis. Voids highlighted with a red circle were found in all the tests. However, they are typically found outside the notched area, hence, they may be assumed as initial defects in the material. These tests were unable to highlight the particle behavior satisfyingly. To get a clearer picture, the compression tests should be stretched almost up to fracture, before studying the microstructural behavior.

Figure 4.21 shows SEM micrographs of the matrix and two typical types of particles found in the material. The analysis concluded that the matrix consisted of iron *Fe*, manganese *Mn* and carbon *C*. Particle type 1 (Figure 4.21b) consisted of calcium *Ca*, sulfur *S*, aluminium *Al*, magnesium *Mg* and oxygen *O*. This particle is most likely a calcium-aluminate particle, and a high content of it was discovered in the material. The particle is spherical and the size varies from approximately 2 to 25  $\mu\text{m}$ . Particle type 2 (Figure 4.21c) consisted of titanium

#### 4. MATERIAL TESTING

---

$Ti$ , nitrogen  $N$  and a small amount of carbon  $C$ . This particle is most likely a titanium-carbonitride particle. In the light optical microscope these particles appear yellow/orange with a typical angular morphology. In comparison with type 1 particle, type 2 is smaller ( $\sim 5 \mu\text{m}$ ) and found in much smaller quantities.



**Figure 4.17:** Macrostructure of pre-compressed tension tests at various plastic strains.

### 4.3 Notched tests with reversed loading

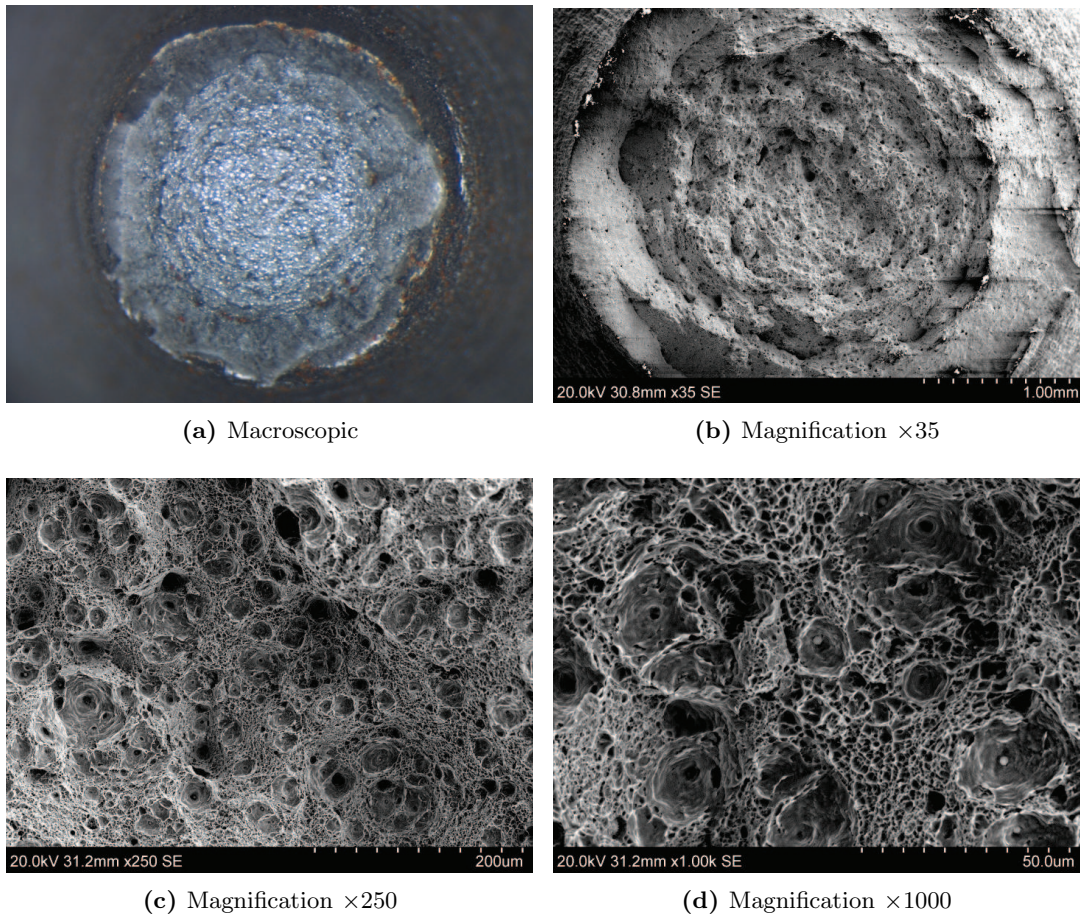


**Figure 4.18:** Fracture surface for pre-compressed tension test (10 %) at increasing magnification.

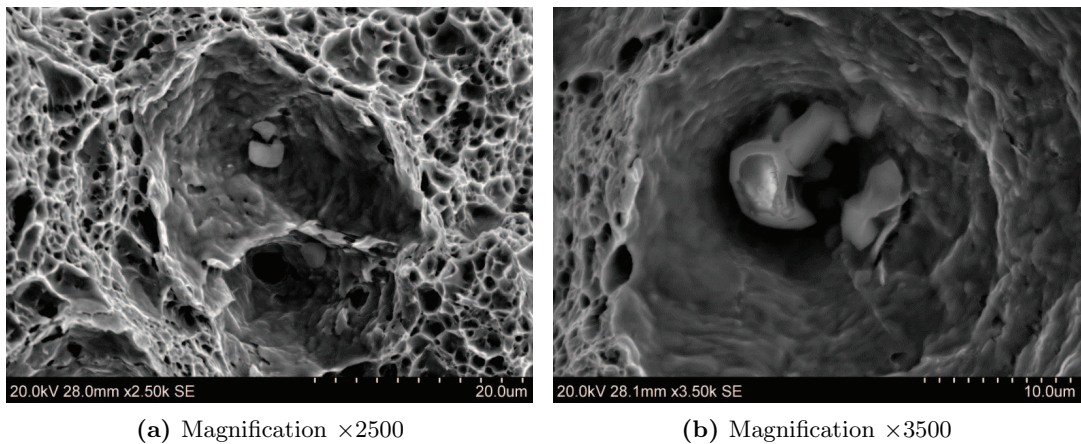


**Figure 4.19:** Cracked particles for pre-compressed tension test (40 %) at different magnification.

## 4. MATERIAL TESTING

---

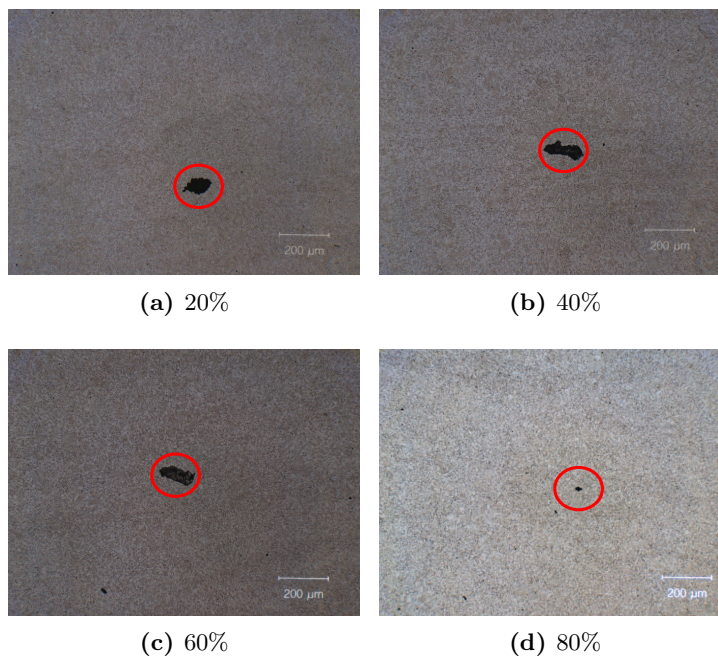


**Figure 4.20:** Microscopic investigation at successively increasing plastic strain levels in compression (cross-sectional cut along the longitudinal axis).

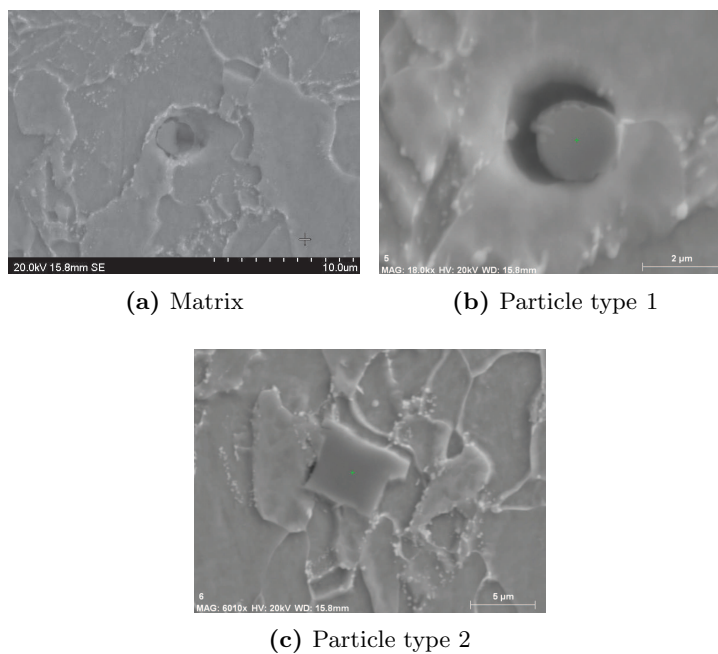


**Figure 4.21:** Matrix and particle composition.

## 5 Material model

Fornes and Gabrielsen suggested a combined isotropic and kinematic work-hardening model based on the uniaxial tension-compression tests conducted at small strains (Table 5.1) [4]. This material model was used in the numerical simulations of the experiments with the notched specimen (Section 4.3). In addition, two combined isotropic and kinematic hardening models were suggested and used in the simulations. The hardening models were calibrated by the method of least squares for the uniaxial tension-compression tests at small strains, and inverse modeling of the notched tests at large strains.

**Table 5.1:** Material parameters combined work-hardening 2011 [4].

Isotropic hardening					Kinematic hardening			
$\sigma_0$	$Q_1$	$b_1$	$Q_2$	$b_2$	$C_1$	$\gamma_1$	$C_2$	$\gamma_2$
[MPa]	[MPa]		[MPa]		[MPa]		[MPa]	
330.30	703.60	0.47	50.50	34.70	115640.00	916.00	2225.00	22.00

### 5.1 Numerical simulations of the pre-compressed tension tests

The material model suggested by Fornes and Gabrielsen (Table 5.1) gave satisfactory results for a uniaxial stress state at small strains. The objective of the experiments presented in Section 4.3 was to investigate the material behavior at large deformations in compression. Therefore, it was of interest to examine the combined isotropic and kinematic hardening model suggested by Fornes and Gabrielsen based on these experiments. Hence, the first parallel of test series 1 was simulated numerically using ABAQUS/Explicit. The FE model presented in Section 3.3.1 was used as the basis. To get cubic-shaped elements and better representation of the stiffness at fracture (Figure 5.1b), the mesh was refined at the center of the specimen (Figure 5.1a). This resulted in an increase from 2616 to 3052 elements. As in

## 5. MATERIAL MODEL

---

Section 3.3.1, it was used linear hexahedral elements of type C3D8R with 11 elements over the diameter at the notch (Figure 5.1c).

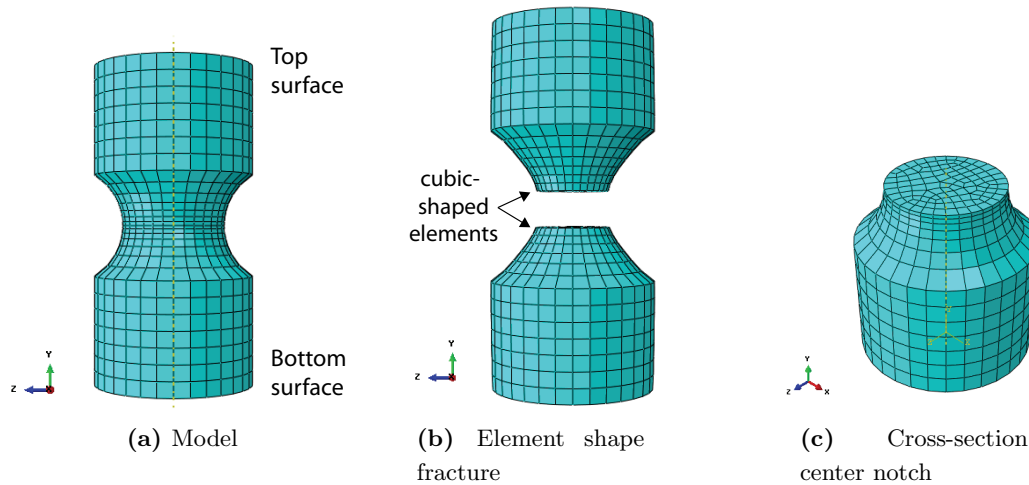


**Figure 5.1:** Numerical model in ABAQUS/Explicit.

All degrees of freedom were fixed at the bottom surface, while the top surface was given a constant velocity. The model consisted of two loading steps, i.e. compression and tension. The loading was applied by a smooth loading curve, to avoid numerical instabilities in the incipient loading. To retain the quasi-static nature of the experiments, the numerical simulations were performed with the same velocity and time period. As an explicit FEM software was used, mass scaling was used to speed up the simulations, i.e. the density of the specimen was increased. As for the experiments, the analyses had different levels of pre-compression before stretched to fracture. The numerical simulations were performed using approximately 35000 to 80000 time increments (Table 5.2). As in Section 3.3.3, an energy balance check was performed to ensure that the kinetic and artificial energies were insignificant compared to the absorbed strain energy. Since the isotropic hardening component (Voce rule) can not be implemented directly into ABAQUS if  $N > 1$ , the data was applied in tabular form. It should also be noted that the fracture criterion suggested by Slåttedalen and Ørmen was used.

As mentioned earlier, the numerical simulations conducted by Fornes and Gabrielsen showed a satisfactory fit for the uniaxial tests at small strains. However, the numerical simulations of the pre-compressed tension tests revealed interesting results. The simulations failed to recreate the load level both in the compression and tension step (Figure 5.2). Fornes and Gabrielsen expanded the constitutive relation for large strains, by extrapolating the isotropic hardening component to fit the tension test performed by Slåttedalen and Ørmen. Thus, the

## 5.1 Numerical simulations of the pre-compressed tension tests

**Table 5.2:** Numerical simulations of the notched experiments.

Pre-compression [%]	Time period* [s]	Velocity [mm/s]	Displacement top surface* [mm]	Time increments*
0	0(726)	0.0033	0(2.26)	0(35091)
10	170(803)	0.0033	-0.39(1.90)	55065(4892)
20	300(889)	0.0033	-0.87(1.50)	54053(8992)
30	475(964)	0.0033	-1.44(1.08)	53657(14785)
40	760(988)	0.0033	-2.42(0.58)	54656(25502)

\*The brackets refers to the stretching step, i.e. {pre-compression}({stretching}).

material model should give a better fit for the initial loading in compression. The soft behavior in compression was therefore not expected. The overly stiff behavior at large deformations in the reversed loading could be explained with the constitutive relation suggested by Fornes and Gabrielsen (Table 5.1). This behavior was of special interest. Previous studies, regarding the impacted pipes, experienced that the numerical simulations of the stretch test overestimated the load level observed in the experiments [3, 4].

Further examining of the numerical simulations showed that the simulations succeeded to recreate some of the kinematic behavior observed in the experiments. A minor decrease in the yielding at reversed loading was observed, thus, the Bauschinger effect was present (Figure 5.2).

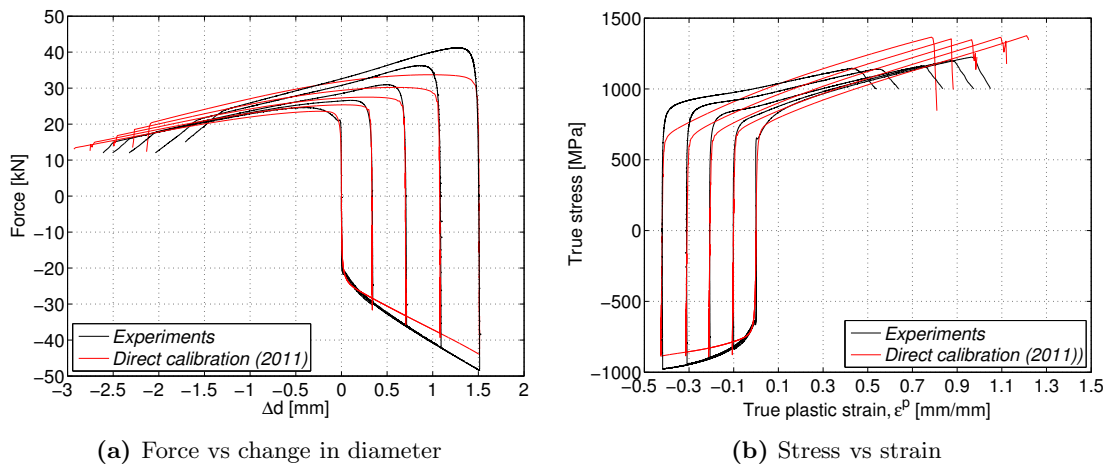


**Figure 5.2:** Numerical simulations with material model suggested by Fornes and Gabrielsen.

## 5. MATERIAL MODEL

---

### 5.2 Identification of material parameters by the method of least squares

Based on the observations in Section 5.1, it was decided to calibrate a new material model. A closer study of the previous material model revealed a deviation between the experiments and constitutive relation in terms of the gradient at reversed loading (Figure 5.3). This deviation could result in an overly stiff behavior at large strains. Therefore, a calibration was conducted to get a better compliance between the experiments and the constitutive relation in terms of the reversed loading. Fornes and Gabrielsen showed that there was no significant difference between the specimens first loaded in tension or compression. Thus, the plastic yielding is independent of the initial loading direction and could be calibrated based on the uniaxial tension-compression tests, and vice versa (Section 2.5.1). Therefore, the test first loaded in tension until approximately 5 % was used as basis for the calibration (Figure 5.3).

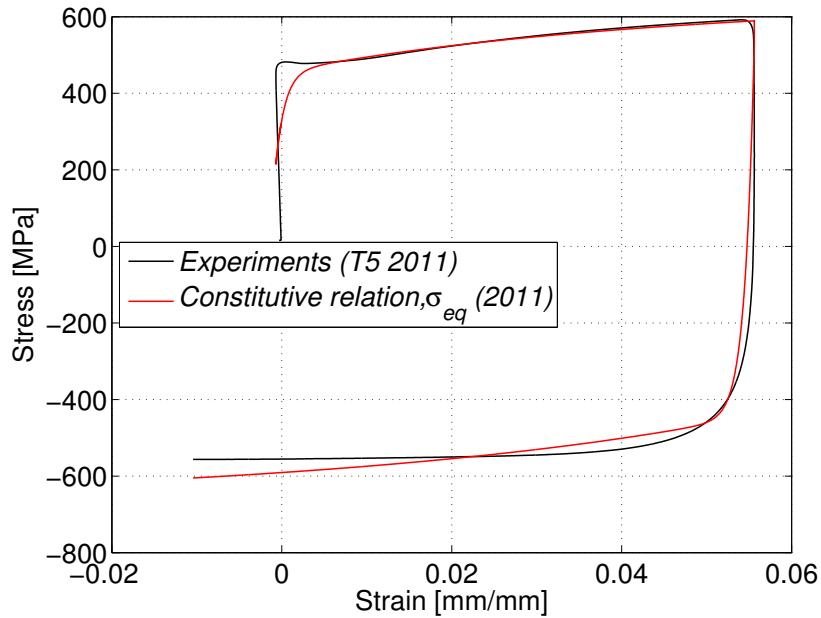


Figure 5.3: Constitutive relation suggested by Fornes and Gabrielsen.

## 5.2 Identification of material parameters by the method of least squares

---

Since these experiments are valid only for small strains, some assumptions needed to be made regarding the material behavior at large strains. Based on observations from the experiments presented in Section 4.2.3 and 4.3, the kinematic hardening component was assumed to saturate to its maximum value at small strains ( $\varepsilon^p < 0.1$ ). Hence, the combined hardening at large strains is driven by the isotropic component and can be assumed to have the same shape as the tension tests performed by Slåttedalen and Ørmen (Figure 4.1). The constitutive relation was therefore calibrated based on the tension-compression test for small strains (5 % in tension) and the uniaxial tension test at large strains. It should be noted that the raw data from the experiments was used in the direct calibration, thus, equally spaced strain increments was not used.

As mentioned earlier, the constitutive relation consisted of two components in terms of a nonlinear isotropic and kinematic hardening component. The isotropic hardening component  $\sigma_{IH}$  describes the change of the equivalent stress  $\sigma_{eq}$ , defining the size of the yield surface as a function of plastic deformation. The isotropic component was calibrated using the Voce hardening rule (Equation (2.39)), given as

$$\sigma_{IH} = \sigma_0 + R(p) = \sigma_0 + \sum_{i=1}^N Q_i (1 - e^{-b_i p}) \quad (5.1)$$

where  $\sigma_0$  is the initial yield stress,  $p$  is the equivalent plastic strain and  $Q_i$  and  $b_i$  are material parameters. The maximum change in size of the yield surface is defined by  $\sigma_0 + \sum_{i=1}^N Q_i$ , and  $b$  defines the rate at which the size of the yield surface changes as plastic straining develops.

The kinematic hardening component  $\sigma_{KH}$  describes the translation of the yield surface in stress space through the backstress tensor  $\chi$ . The kinematic component was calibrated using the Armstrong-Fredricks nonlinear kinematic hardening rule (Equation (2.43)), given as

$$\sigma_{KH} = \chi(\varepsilon^p) = \sum_{k=1}^N \frac{C_k}{\gamma_k} (1 - e^{-\gamma_k \varepsilon^p}) \quad (5.2)$$

where  $N$  is the number of backstresses,  $C_k$  is the initial kinematic hardening moduli and  $\gamma_k$  determine the rate at which the kinematic hardening moduli decreases with increasing plastic deformation (Section 2.5.2). It is seen that the kinematic hardening component has similarities to the Voce hardening rule through the following expressions

## 5. MATERIAL MODEL

---

$$\frac{C_k}{\gamma_k} = Q_i \quad \text{and} \quad \gamma_k = b_i \quad (5.3)$$

Thus, the ratio between  $C_k$  and  $\gamma_k$  could be seen as the maximum translation of the elastic region, and  $\gamma_k$  the rate at which the translation of the elastic region evolves as plastic straining develops.

To identify the material parameters it was necessary to establish an expression for the uniaxial stress state as a function of the plastic strain within a half-cycle. This was obtained by expressing the yield criterion as

$$f(\sigma - \chi, R) = |\sigma - \chi| - (\sigma_0 + R) = 0 \quad (5.4)$$

where it was assumed that the plastic strain is  $\varepsilon_0^p$  at the beginning of the half-cycle, the equivalent plastic strain is  $p_0$  and the backstress equals  $\chi_0$ . The yield criterion gives the stress as a function of the plastic strain within the half-cycle as [33]

$$\sigma = \vartheta(\sigma_0 + R(p)) + \sum_{k=1}^N \chi_k(\varepsilon^p) \quad (5.5)$$

The relation between the equivalent plastic strain  $p$  and the plastic strain  $\varepsilon^p$  within each half-cycle is given as  $p = p_0 + \vartheta(\varepsilon^p - \varepsilon_0^p)$ . Thus, the stress is seen to be a unique function of the plastic strain within the half-cycle. It should also be noted that the notation  $\vartheta = \text{sgn}(\sigma - \chi)$  was introduced and the relations  $\dot{p} = \vartheta \dot{\varepsilon}^p$  and  $|\sigma - \chi| = \vartheta(\sigma - \chi)$  were used.

The backstress was expressed as

$$\chi(\varepsilon^p) = \sum_{k=1}^N \chi_k(\varepsilon^p) = \sum_{k=1}^N \left[ \vartheta \frac{C_k}{\gamma_k} + \left( \chi_0 - \vartheta \frac{C_k}{\gamma_k} \right) e^{(-\vartheta \gamma_k (\varepsilon^p - \varepsilon_0^p))} \right] \quad (5.6)$$

## 5.2 Identification of material parameters by the method of least squares

Based on the uniaxial tension-compression test at 5 % strain, Equation (5.5) and the method of least squares, the constitutive relation in Table 5.3 was calibrated.

**Table 5.3:** Material parameters fit for small strains and reversed loading.

Isotropic hardening					Kinematic hardening			
$\sigma_0$	$Q_1$	$b_1$	$Q_2$	$b_2$	$C_1$	$\gamma_1$	$C_2$	$\gamma_2$
[MPa]	[MPa]		[MPa]		[MPa]		[MPa]	
310.30	35.30	223.20	846.80	0.42	67440.30	425.10	716.30	9.30

It is worth noting the similarities regarding the second term ( $Q_2$  and  $b_2$ ) in the isotropic hardening component in Table 5.3 and 3.1. This stems from the fact that both are driven by the isotropic hardening in the tension test performed by Slättendalen and Ørmen (Figure 4.1).

The new constitutive relation showed an improvement in terms of the gradient at reversed loading (Figure 5.4).

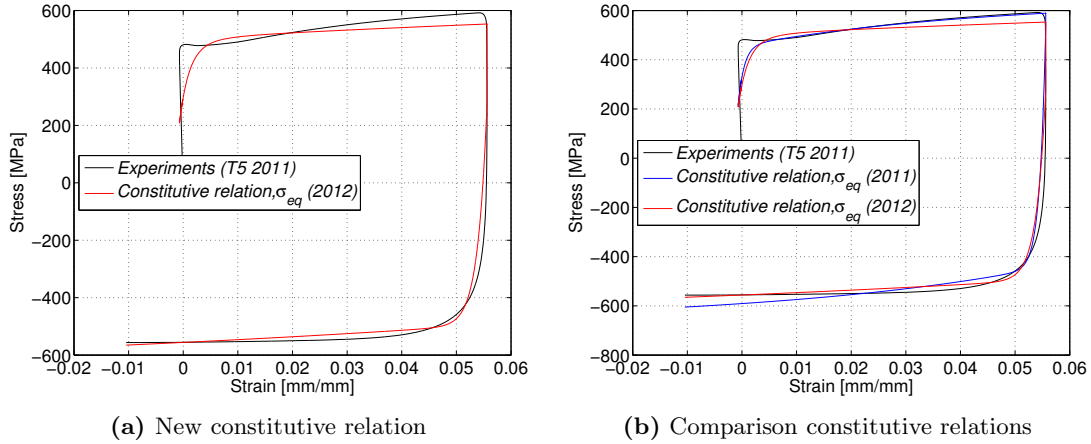


**Figure 5.4:** Comparison of calibrations based on the method of least squares.

As the material parameters were calculated based on only one of the uniaxial tension-compression tests, it was of interest to compare this constitutive relation with the rest of the tests. This was obtained by calculating the isotropic and kinematic part of the hardening from the experiments, respectively, as [47]

$$\sigma_{IH} = \frac{U - R}{2} \qquad \sigma_{KH} = \frac{U + R}{2} \qquad (5.7)$$

## 5. MATERIAL MODEL

---

where  $U$  is the point of unloading and  $R$  is the point of reversed loading. Point  $R$  was calculated as  $\varepsilon^p(R) = \varepsilon^p(U) - 0.0005$  [48]. This was conducted by Fornes and Gabrielsen and is shown for the tension-compression tests in Table 5.4. It should be noted that there was used a unique  $E$  for each test when calculating point  $R$  (Figure 5.5).

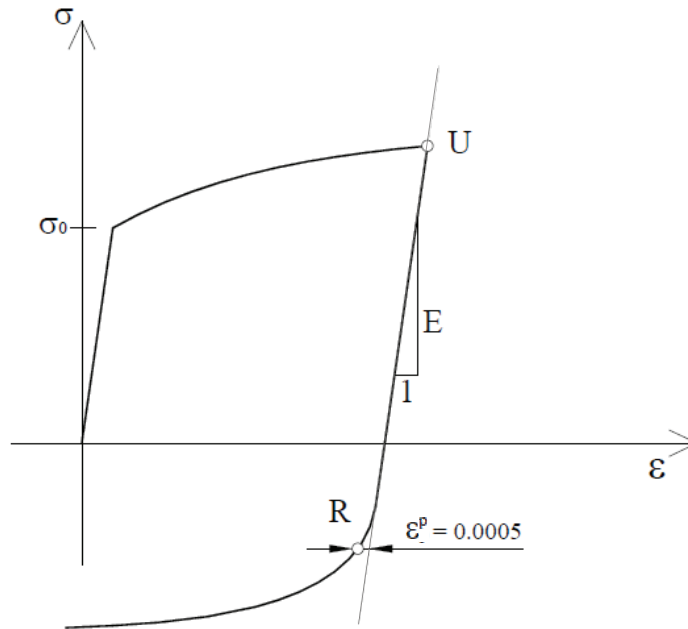


**Figure 5.5:** Elastic region for calculation of isotropic and kinematic hardening [48].

The points of unloading  $U$  and reloading  $R$  are plotted together with the calculated isotropic and kinematic part of the hardening for the tests first loaded in tension (Figure 5.6). As shown in Figure 5.4b, a better fit in the reversed loading results in a poorer match in the initial loading direction. The assumption regarding quick saturation of the kinematic behavior is well depicted in Figure 5.6b.

It is important to emphasize that these figures do not show how the constitutive relations evolve at large strains in reversed loading. Therefore, in the next section it will be presented an inverse modeling based on the notched pre-compressed tension tests. Hence, the inverse modeling was based on experiments at larger strains, both in compression and tension.

## 5.2 Identification of material parameters by the method of least squares

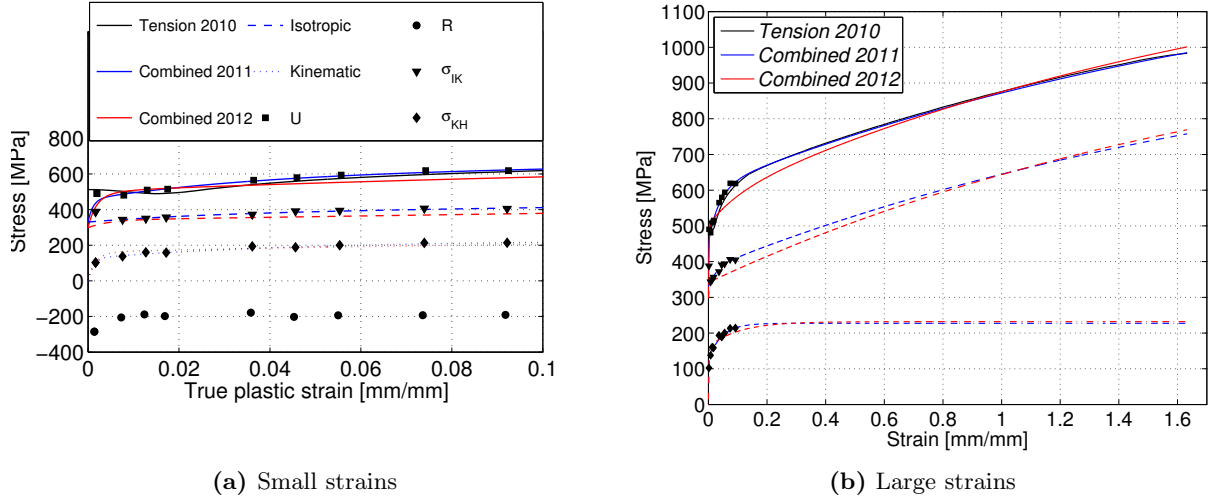


**Figure 5.6:** Constitutive relations compared to uniaxial tension-compression tests.

**Table 5.4:** Data from the uniaxial tension-compression tests [4].

Test id	Max strain $\epsilon_{max}$	Yield stress initial loading $\sigma_{0.2}$ [MPa]	Stress at unloading U [MPa]	Yield stress reversed loading R [MPa]	Isotropic hardening $\sigma_{IH}$ [MPa]	Kinematic hardening $\sigma_{KH}$ [MPa]
T-2	0.0100	472.7	481.1	-205.5	343.3	137.8
T-3	0.0202	477.7	515.0	-197.9	356.4	158.6
T-4	0.0400	475.9	565.2	-178.5	371.8	193.4
T-5	0.0604	477.0	594.0	-193.6	393.8	200.2
T-6	0.0804	486.3	619.2	-192.8	406.0	213.2
T-7	0.1003	470.5	618.8	-190.8	404.8	214.0
T-12	0.0500	475.2	579.8	-202.2	391.0	188.8
T-13	0.0041	471.9	490.3	-285.5	387.9	102.4
T-14	0.0156	481.8	509.7	-188.8	349.3	160.5

### 5.3 Identification of material parameters by inverse modeling

As noted in the previous section, the material parameters in Table 5.3 were calibrated in terms of small strains during reversed loading. The introductory study performed in Section 3.1 illustrated the importance of calibrating the material parameters in terms of the expected strain range (Figure 3.1c). Therefore, it was chosen to calibrate a material model based on the first parallel in test series 1. Due to the triaxial stress state in the notched specimens it was preferred to do an inverse modeling approach. Thus, the material parameters were calibrated in terms of the pre-compressed tension test exposed to the largest strain in compression, i.e. CT40-1 (Table 4.1). As in Section 3.2, the inverse modeling was performed by an optimization of the material parameters in LS-OPT.

The numerical model from Section 5.1 was converted to LS-DYNA (Figure 5.7a), and the setup of the optimization was based on the experience from Section 3.2. Hence, the calibration was run based on the  $F - \Delta d$  curve to optimize the material parameters in terms of the raw data from the experiments. The target curve consisted of an equal amount of points in each direction of loading, i.e. in total 200 points (Figure 5.7b). However, the reversed loading spans over a larger strain range, resulting in coarser strain increments for this part of the target curve. The computed curve was calculated from the nodal displacement of a node at the center of the specimen (node 1 in Figure 5.7a), and the force was extracted from a predefined cross-section plane. The cross-sectional plane was defined normal to the longitudinal axis and equally spaced between the center and neighboring nodes (Figure 5.7a). It should also be noted that no fracture criterion was implemented to avoid fracture and zero area in the numerical analyses.

The combined work-hardening described in Section 5.2 is not part of the standard usage package in LS-DYNA. Therefore, this relation was implemented with the SIMLab Metal Model (SMM). The hardening components described in Equation (5.1) and (5.2) could easily be implemented in the SMM. However, it should be noted that SMM uses a different notation. The isotropic and kinematic components are described, respectively, as [49]

$$R = \sum_{i=1}^N R_i, \quad dR_i = \theta_{Ri} \left( 1 - \frac{R_i}{Q_{Ri}} \right) dp \quad (5.8)$$

### 5.3 Identification of material parameters by inverse modeling

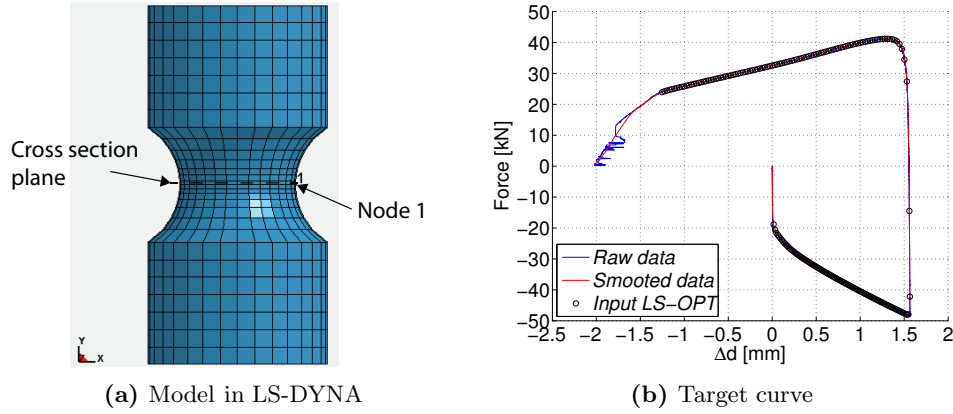


**Figure 5.7:** Input for the inverse modeling in LS-OPT.

$$\hat{\chi} = \sum_{i=1}^N \hat{\chi}_i, \quad d\hat{\chi}_i = \theta_{\chi_i} \left( \frac{\hat{\eta}}{\sigma_{eq}} - \frac{\hat{\chi}_i}{Q_{\chi_i}} \right) dp \quad (5.9)$$

where  $\hat{\chi}$  and  $\hat{\eta} = \hat{\sigma} - \hat{\chi}$  are the backstress and effective stress tensor<sup>6</sup>, respectively.

In terms of the Voce (Equation (5.1)) and Armstrong-Fredricks (Equation (5.2)) hardening rules this results in the following relations

$$Q_{Ri} = Q_i, \quad \theta_{Ri} = b_i Q_i, \quad Q_{\chi_i} = \frac{C_k}{\gamma_k}, \quad \theta_{\chi_i} = C_k \quad (5.10)$$

The initial values of the inverse modeling were the parameters found using the method of least squares (Table 5.3). The results from the previous optimization were used as starting values in the next optimization, e.g. the results from attempt 1 were used as the initial values for attempt 2. The results in terms of material parameters from the inverse modeling are shown in Table 5.5.

**Table 5.5:** Material parameters from the inverse modeling.

Attempt	$\sigma_0$ [MPa]	$\theta_{R1}$	$Q_{R1}$ [MPa]	$\theta_{R2}$	$Q_{R2}$ [MPa]	$\theta_{\chi_1}$	$Q_{\chi_1}$ [MPa]	$\theta_{\chi_2}$	$Q_{\chi_2}$ [MPa]
Initial	310.3	7879.0	35.3	100	355.7	67400.3	158.7	716.3	77.0
1	299	4000	160	100	400	50401	129	1279	100
2	310	3946	120	0	7	79970	139	1120	221
3	280	3373	123	-8	-72	96675	178	1000	217

<sup>6</sup> $\hat{D}$  indicates tensor notation, i.e.  $D$  is a tensor.

## 5. MATERIAL MODEL

Attempt 2 was considered unsuccessful since the optimization resulted in  $\theta_{R2}$  equal zero (Table 5.5). This was due to the boundaries chosen for this parameter. Therefore, the range of the lower boundary was expanded to include negative values (Figure 5.10d). The convergence of the material parameters in attempt 3 was considered sufficient (Figure 5.10), and the inverse modeling was stopped after this optimization.

The results from Table 5.5 were analyzed in terms of  $F-\Delta d$  and true stress-plastic strain in LS-DYNA (Figure 5.8). The strain and stress were calculated based on the  $F-\Delta d$ , using Equation (2.50) and (2.51), respectively.

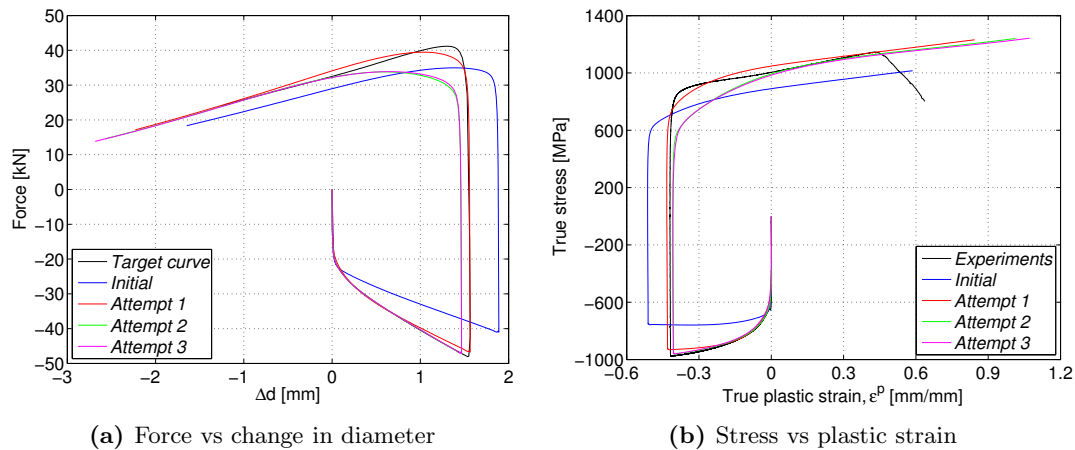


**Figure 5.8:** Numerical simulations in LS-DYNA with constitutive relations from inverse modeling.

Attempt 2 and 3 appears to emphasize the loading direction with the finest strain increments, i.e. the loading in compression. A better fit in terms of the material parameters may therefore be obtained. Modifying the target curve in terms of equal strain increments in both directions may result in a better fit to the experimental data. However, the result in attempt 1 was considered sufficient in terms of the compliance between the numerical simulations and the experimental data (Figure 5.8).

The optimization history in terms of the material parameters is illustrated in Figure 5.9 and 5.10 for attempt 1 and 3, respectively. Although attempt 1 gave the best fit, the optimization history of attempt 3 had a better convergence with respect to the boundary conditions (Figure 5.10).

### 5.3 Identification of material parameters by inverse modeling

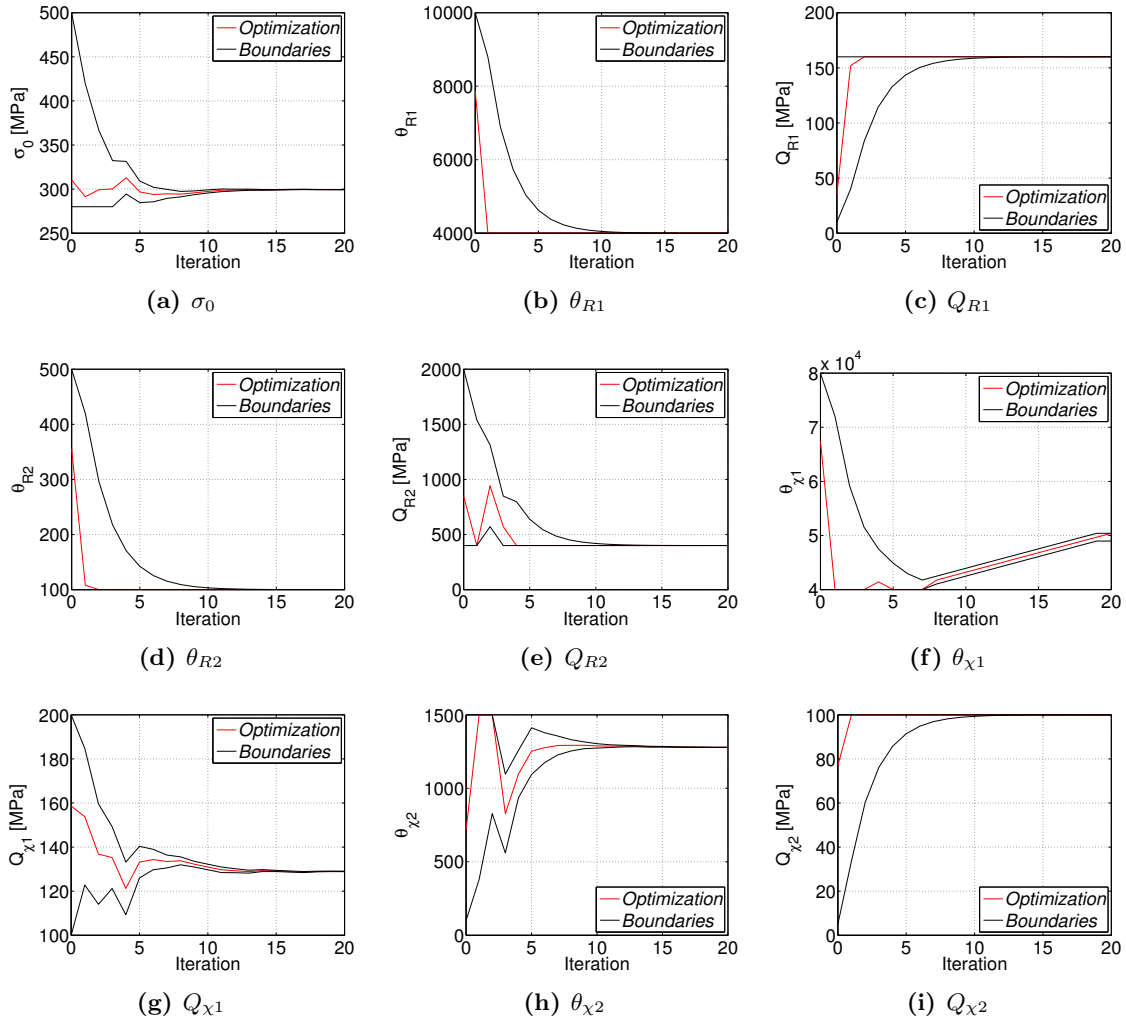


Figure 5.9: Optimization of material parameters in LS-OPT (Attempt 1).

## 5. MATERIAL MODEL

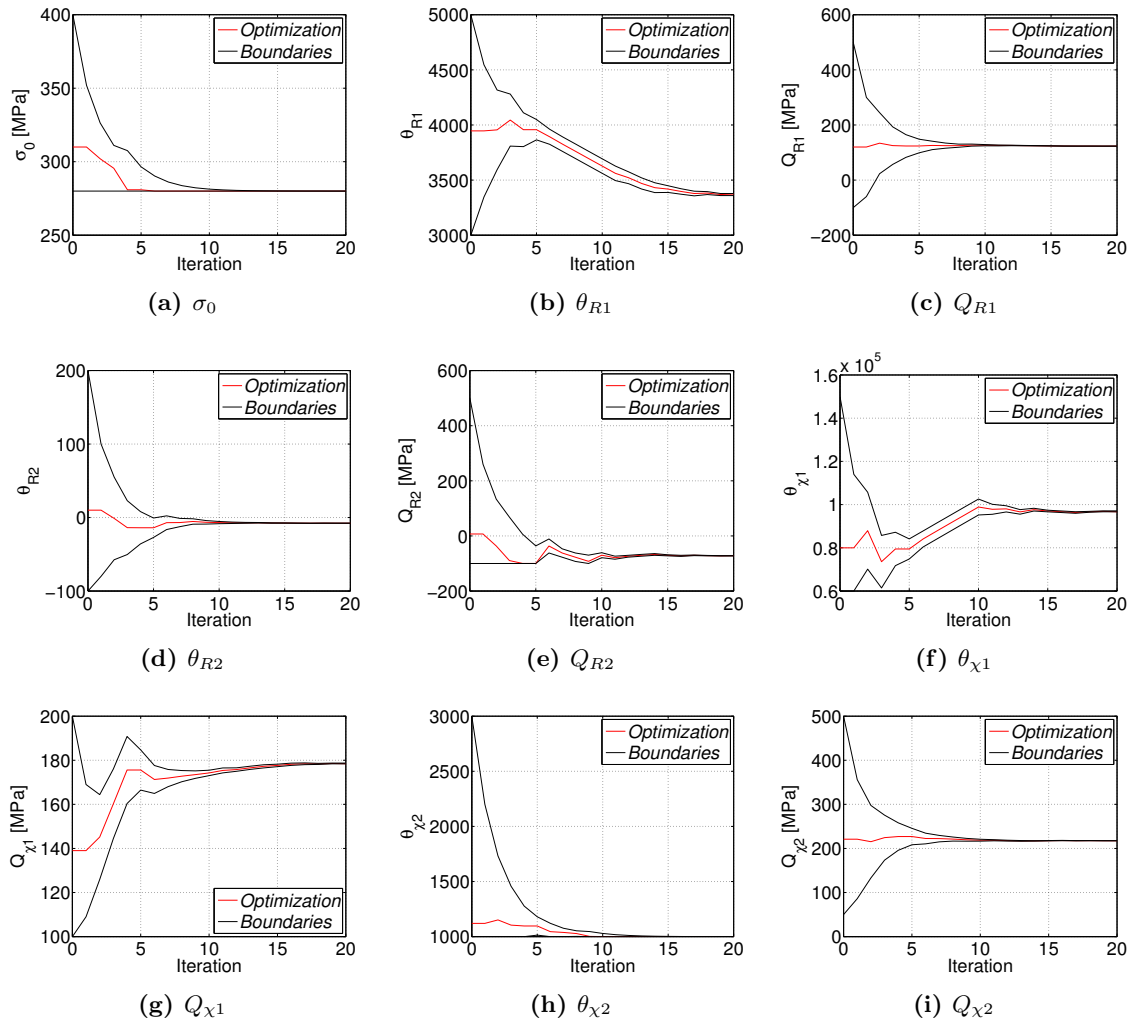


Figure 5.10: Optimization of material parameters in LS-OPT (Attempt 3).

## 5.4 Numerical simulations with new material models

As in Section 5.1, numerical simulations were performed in ABAQUS/Explicit based on the constitutive relations suggested in Section 5.2 and 5.3.

Examining the results, it was seen that the approach based on the method of least squares did not give any noticeable improvement compared to the work of Fornes and Gabrielsen (Figure 5.2). Thus, the direct approach of calibration based on small strains in the reversed loading, did not manage to recreate the loading history from the experiments (Figure 5.11a and 5.11b). However, the calibration based on the inverse modeling showed a better compliance between the simulations and experiments (Figure 5.11c and 5.11d). It is worth noting the deviation in compression for plastic strain larger than  $\sim 25\%$  (Figure 5.11d). The simulations saturated more than the experiments to achieve better compliance in the reversed loading. This may result in a underestimation of the load level at larger strains than those considered in the inverse modeling (up to 40 %).

Furthermore, the prediction of the reversed yield stress was not recreated as observed in the experiments (Figure 5.11d). This was due to the constitutive relation, assuming a continuous evolution of the isotropic hardening (Equation (5.1)), but not the work-hardening stagnation under reversed deformation. Due to the stagnation for plastic strain larger than  $\sim 25\%$  in compression, the reversed yielding in the simulations occurred at smaller stresses than observed in the experiments (Figure 5.11d). To recreate the work-hardening stagnation a modification of the constitutive relation is needed. The literature shows that this has been performed for the combined relation used in these simulations (Section 2.1.1). However, this thesis was limited by referring to this possible expansion. The deformations of interest were large strains in compression and tension. Thus, the results in Figure 5.11c and 5.11d were considered sufficient.

It is also worth noting that the constitutive relation from the inverse modeling resulted in a better compliance in terms of predicting fracture.

## 5. MATERIAL MODEL

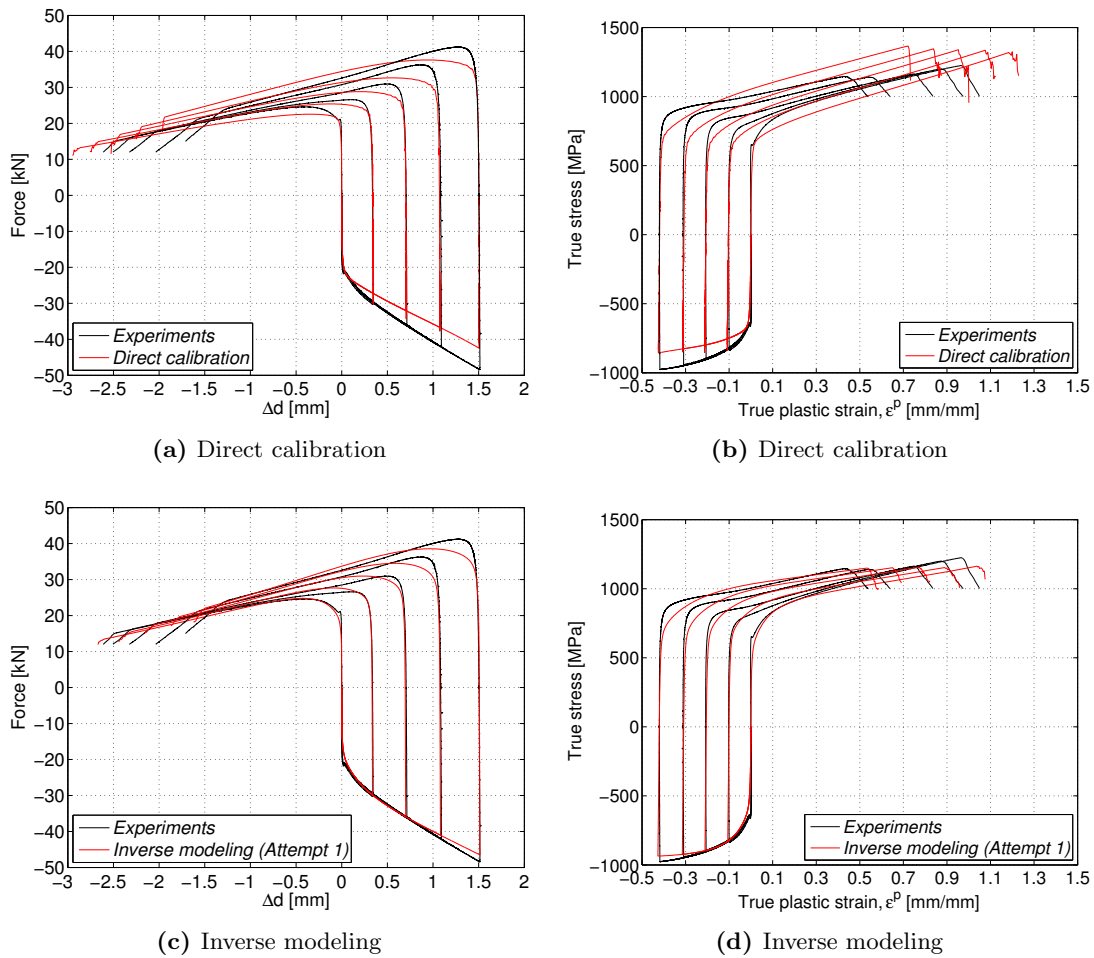


**Figure 5.11:** Numerical simulations with new material models.

## 5.5 Fracture criterion

As mentioned earlier, it was considered appropriate to use the fracture criterion suggested by Slåttedalen and Ørmen (Table 5.6). This was based on the observations from the experiments in Section 4.3.2, which indicated that the fracture criterion should be based on work (Figure 4.12a) and not fracture strain (Figure 4.12b). This criterion was also available in ABAQUS/Explicit, and beneficial when comparing the constitutive relation suggested in this thesis with previous theses.

**Table 5.6:** Fracture criterion suggested by Slåttedalen and Ørmen [3].

Isotropic hardening					
$A$	$B$	$n$	$C$	$\dot{\varepsilon}_0$	
[MPa]					
465.5	410.83	0.4793	0.0104	0.000806	
Cockcroft-Latham based Johnson-Cook fracture criterion					
$D_1$	$D_2$	$D_3$	$D_4$	$D_5^*$	$\dot{\varepsilon}^{p*}$
0.7	1.79	1.21	-0.00239	0	0.000806

\*The temperature effect was excluded in Equation (2.63).

However, to verify the tension tests, a Bridgman correction was performed on the notched tension test (CT0-1) and compared with the smooth tension test conducted by Slåttedalen and Ørmen (Figure 5.12). The Bridgman correction of the notched specimen was performed assuming a constant ratio between  $a$  and  $R$  (Figure 2.24).

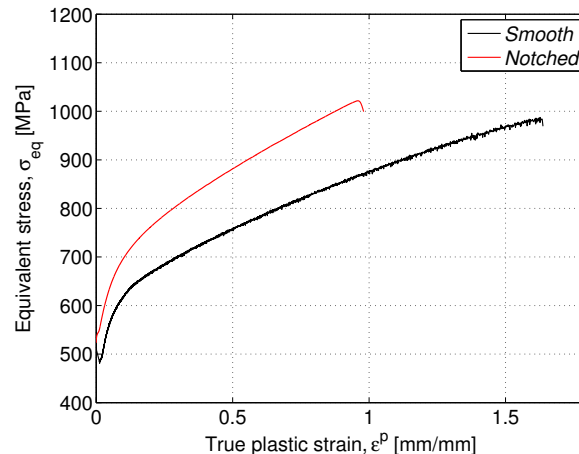


**Figure 5.12:** Comparison of quasi-static tension tests (Bridgman corrected).

## 5. MATERIAL MODEL

---

The comparison of the tension tests in Figure 5.12 revealed interesting results, and could explain the deviations between the numerical simulations and experiments in Figure 5.2 and 5.11. These simulations were run with the constitutive relations calibrated based on the experiments from previous theses (Section 5.2). Thus, it may seem that the material properties of the X65 steel used in the present thesis deviates from previous theses. Therefore, the steel in this thesis might stem from a different batch than the previous steels. Hence, it was of interest to investigate how this influenced the fracture criterion. However, to calibrate a new fracture criterion it was necessary to use the Cockcroft-Latham parameter  $W_c$  for a smooth uniaxial tension test (Section 2.7). Such tests were performed towards the end of this thesis. Therefore the present thesis was limited to only discussing the results in Chapter 8. A fracture criterion based on these tests is suggested as further work.

It is worth noting that the material constant  $W_c$  was determined by calculating the plastic work of the true stress-strain curve. In this calculation the average true stress over the cross-section was used. With reference to Figure 2.23, this calculation then becomes an approximation since  $\sigma_1$  varies over the cross-section after necking.

## 5.6 Evaluation of material model

To evaluate the material model, it was preferred to use experimental results which were not used in the identification of the constitutive relation or the fracture criterion. Therefore, the tension tests conducted by Slåttedalen and Ørmen and the notched tension test in the first parallel (CT0-1 Table 4.1) were used for this purpose. However, it should be noted that the fracture criterion was calibrated based on the uniaxial tension test conducted by Slåttedalen and Ørmen (Section 5.5).

ABAQUS/Explicit was used in the simulations. Both smooth and pre-notched axisymmetric models with mesh geometry as shown in Figure 5.13 were analyzed. The notched specimens have initial notch root radius  $R$  equal to the experimental values, i.e. 0.8, 2.0 and 3.6 mm, while the initial minimum radius  $a$  was 1.5 mm for the three first specimens and 3.6 mm for the last specimen in Figure 5.13. The initial stress triaxiality ratio in the center of the notch was calculated based on the work of Bridgman (Equation (2.61)), and equals  $1/3$  (smooth), 0.652 ( $R = 2.0$  mm), 0.995 ( $R = 0.8$  mm) and 0.703 ( $R = 3.6$  mm).

The specimens were modeled using four-node axisymmetric elements (CAX4R) with reduced integration and hourglass control. As a result of the mesh sensitivity study performed by Slåttedalen and Ørmen, 20 elements were used across the radius, giving an element size in the critical gauge region of approximately  $0.13 \times 0.075$  mm<sup>2</sup>. It is worth noting that 40 elements were used across the radius of the specimen in Figure 5.13d, to achieve approximately the same element size for all specimens in the critical gauge region. This element size resulted in 1600, 2414, 2104 and 5440 elements for the specimens in Figure 5.13, respectively. All degrees of freedom were fixed at the left end, while the right end were given a constant velocity. Since only tension was considered, the models consisted of one loading step. The loading was applied by a smooth loading curve to avoid numerical instabilities in the incipient loading. To retain the quasi-static nature of the experiments, the numerical simulations were performed with the same velocity and time period as in the experiments, and mass scaling was used to speed up the simulations. The numerical simulations were compared to the corresponding experimental data from the respective tests.

## 5. MATERIAL MODEL

---

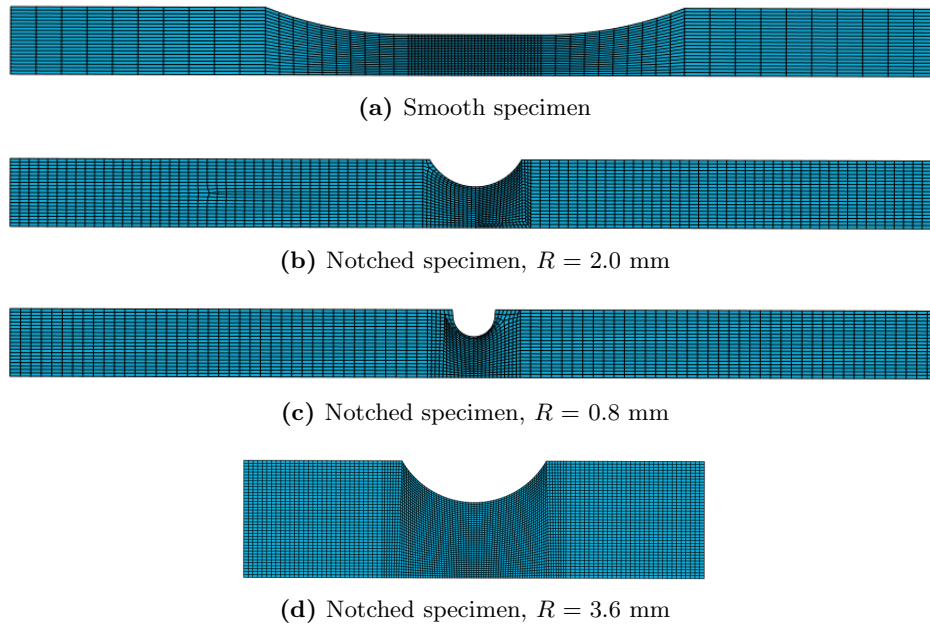


**Figure 5.13:** The mesh used in the evaluation of the constitutive relation. 20 four-node axisymmetric elements were used across the radius (40 in Figure 5.13d).

The explanation of larger deviations in experiments conducted by Slåttedalen and Ørmen (Figure 5.14a) may stem from the observation in Figure 5.12. Thus, the material properties for the present and previous tests seems to be different. Figure 5.12 shows higher strength for the X65 steel used in this thesis. Therefore, to compare experimental data and numerical simulations based on equal terms, the evaluation of the material model was based on the experimental data from the notched tension test (Section 4.3).

It is worth noting, that this difference in material properties may be the explanation of the deviations in compression between numerical simulations and experimental data in Figure 5.2a-5.2b and 5.11a-5.11b. The direct calibrations were based on the experimental data from the previous theses, which seem to have slightly softer material properties compared to the X65 steel in this thesis. However, the final constitutive relation based on inverse modeling of the *CT40-1* test was calibrated with the experimental data from the present thesis. Hence, the evaluation of the material model in terms of Figure 5.14b was highly relevant and assumed as the best comparison.

Overall it is seen from Figure 5.14b that the response of the notched specimen is reasonably well captured by the numerical simulations. Furthermore, a minor overestimation in the simulation for  $\Delta d \leq 0.75$  mm, and a underestimation of the load for  $\Delta d \geq 0.75$  mm was observed. This was a similar observation as in Figure 5.11c-5.11d. The constitutive relation

## 5.6 Evaluation of material model

was calibrated for strains up to 40 %, and therefore underestimates the load at higher strains (Section 5.4). The inverse modeling resulted in a stagnation in compression to give a better fit for the work-hardening stagnation after reversed yielding (Figure 5.11c - 5.11d).

The Cockcroft-Latham based Johnson-Cook fracture criterion calibrated by Slåttedalen and Ørmen (Table 5.6), seem to be representative. The fracture was well captured at approximately the same deformations as in the experiments (Figure 5.14b). This was confirmed by the observations regarding fracture in Figure 5.11c-5.11d.

It was observed oscillations at the end of the force-displacement curves from the numerical simulations. This may stem from the damage evolution and element erosion at incipient fracture, i.e. all the elements were not eroded at the same time. It should also be noted, as pointed out by Slåttedalen and Ørmen, that the fracture is highly mesh sensitive.

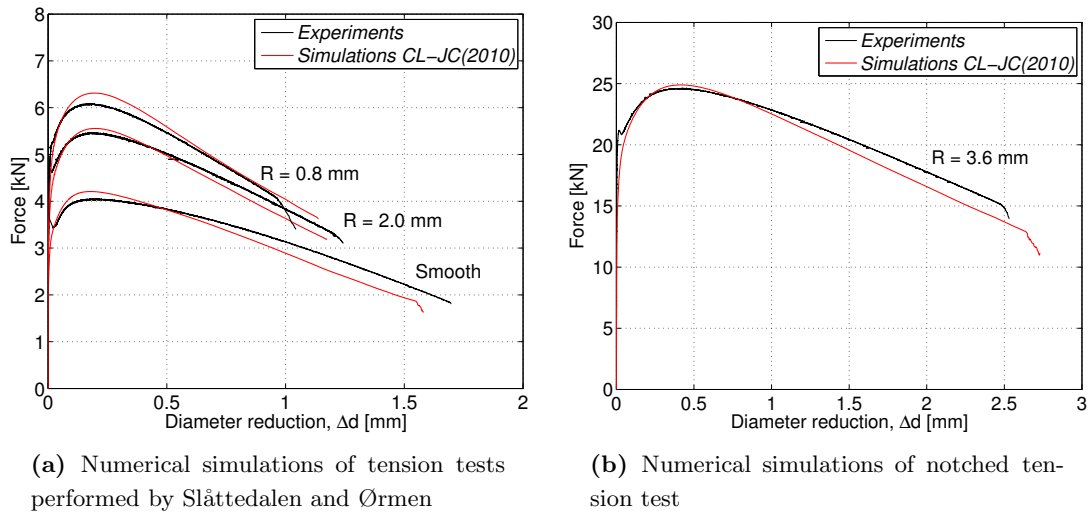


**Figure 5.14:** Evaluation of the material model.

## 5. MATERIAL MODEL

---

## 6 Component tests

Impact against offshore pipelines is a complex problem, therefore it was necessary to conduct relevant tests to investigate the problem. The following study was a continuation of the work carried out in the previous theses [3, 4]. Statoil supplied the pipes for testing, and each pipe was labeled with a letter ( $A-L$ ). Slåttedalen and Ørmen carried out two tests on four pipes (pipe  $A-D$ ), consisting of an impact followed by stretching. They studied the effect of the indenter velocity in the impact against the force in the stretching upon fracture. Fornes and Gabrielsen carried out tests on two parallel pipes ( $G-J$ ). They investigated the effect of pipes filled with water for both open and closed pipes during impact. In this thesis, impact tests were conducted at different velocities on two pipes ( $K$  and  $L$ ). The objective was to examine the microstructure of the deformed pipes, to better understand and investigate incipient fracture.

### 6.1 Impact and stretching of empty pipes

Slåttedalen and Ørmen carried out two different tests on four pipes. The first test was an impact in "the kicking machine", while the subsequent test was stretching the pipes until fracture in a 1200 kN Instron testing machine. The velocity of the indenter during impact varied ( $A = 3.24$  m/s,  $B = 5.13$  m/s,  $C = 3.06$  m/s and  $D = 2.72$  m/s), and the pipes were then stretched. The output from these tests were force and displacement. After impact the pipes were visually inspected, but no fracture could be detected. The tests revealed that the magnitude of deformation during impact, strongly influenced the fracture load in stretching.

For comparison with the two tests conducted in the present thesis, only pipe  $A$  ( $v = 3.24$  m/s) and  $B$  ( $v = 5.13$  m/s) are highlighted. Figure 6.1 shows the force-displacement curve for impact against pipe  $A$  and  $B$ . Table 6.1 lists the after impact deformation measurements.

## 6. COMPONENT TESTS

For a more detailed description of the experimental set-up and additional results it is referred to Slåttedalen and Ørmen [3].

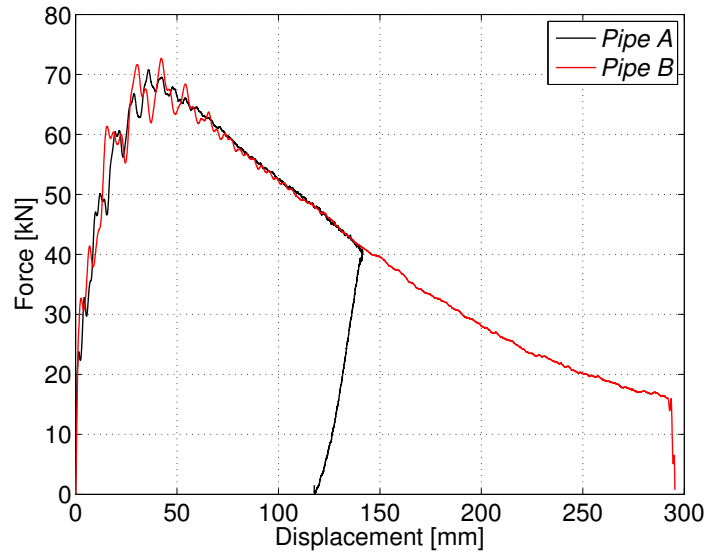


**Figure 6.1:** Force vs displacement for impact against pipe A and B [3].

**Table 6.1:** Measured deformations of pipe A and B after impact [3].

Pipe	A (3.24 m/s)		B (5.13 m/s)	
Inner deformation [mm]	170		333	
Angle at the supports [-]	12		30	
Distance north-north [mm]	1250		1104	
Diameter at measuring points* [mm]	N-S	E-W	N-S	E-W
1 (at support)	131	131	130	130
2	130	131	129.5	131
3	128.8	133	127.3	134
4	125	137	122	140
5	114	146	100	154
6 (at midpoint)	60	180	22.5	199

\*The measuring points are shown in Figure 6.4.

## 6.2 Impact against filled pipes

Fornes and Gabrielsen studied the effect of pipes filled with water subjected to impact [4]. Two parallel tests with different velocity ( $v = 3.2$  m/s and  $v = 5.1$  m/s) were conducted. Pipe *G* and *H* were open filled pipes, while *I* and *J* were closed filled pipes. The effect of the water was investigated by comparing against tests for empty pipes with the same velocities carried out by Slåttedalen and Ørmen. The tests revealed that the open filled pipes had a slightly higher force level (Figure 6.2). However, it is uncertain if this was caused by the resistance from the water or the higher average thickness in the pipe wall (Table 6.2). Closed filled pipes showed a different behavior compared to both empty and open filled pipes, as the decrease in force after reaching its peak was significantly smaller (Figure 6.2). Only results from pipes impacted at  $v \approx 3.2$  m/s are shown in the figure and table below. It is referred to Fornes and Gabrielsen for additional results [4].

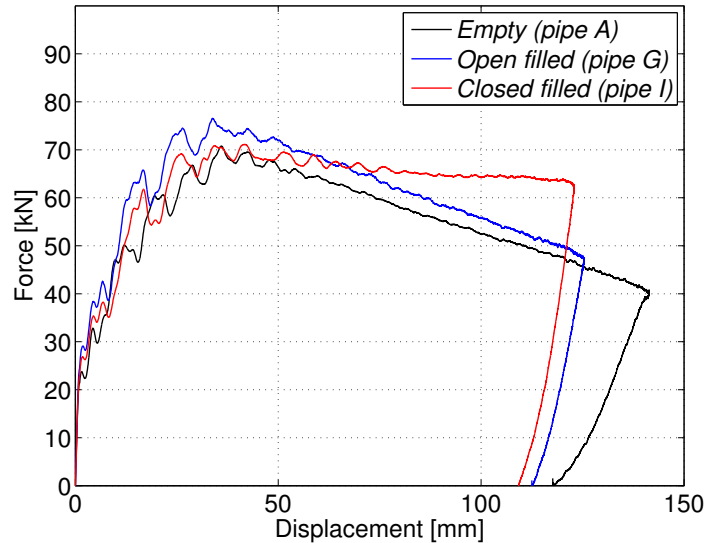


**Figure 6.2:** Force vs displacement for impacted pipes at  $v \approx 3.2$  m/s [4].

**Table 6.2:** Measurements of pipes impacted at  $v \approx 3.2$  m/s prior to testing [3, 4].

Pipe	A(empty)	G(open)	I(closed)*			
	Thickness			Diameter		
$t_{avg}$ [mm]	3.89	4.08	4.02	$D_{avg}$ [mm]	122.56	122.69
$Var(t)$ [mm <sup>2</sup> ]	0.1220	0.0449	0.0513	$Var(D)$ [mm <sup>2</sup> ]	0.0320	0.0318
$Std(t)$ [mm]	0.3593	0.2118	0.2265	$Std(D)$ [mm]	0.1788	0.1785

\*Diameter not measured (closed pipe).

## 6. COMPONENT TESTS

---

### 6.3 Impact against empty pipes

Impact against empty pipes was conducted with the objective of examining the microstructural behavior of pipes exposed to a complex stress state, and investigate incipient fracture. Two pipes ( $K$  and  $L$ ) were impacted at different velocities,  $v = 5.18$  m/s and  $v = 3.26$  m/s, respectively. To make the comparison easier, the test set-up was identical to previous theses. Some of the results from the preceding tests will be reported here for comparison.

#### 6.3.1 Measurement of the pipes

Prior to testing, the thickness and inner diameter of the pipes were measured according to Figure 6.4. They are given together with the variance and standard deviation in Table 6.3. The thickness was measured by ultrasonic measurements, where the accuracy was affected by several different factors [50]. To measure the diameter, tape measuring was used. Therefore, inaccuracies in both the thickness and diameter measurements were introduced, but to what extent was difficult to estimate. For more detailed tables regarding the measurements, it is referred to Appendix B.1.

**Table 6.3:** Pipe measurements prior to testing.

Pipe	K ( $v = 5.18$ m/s)	L ( $v = 3.26$ m/s)
<b>Thickness</b>		
$t_{avg}[mm]$	4.12	4.17
$Var(t)[mm^2]$	0.0674	0.1242
$Stdev(t)[mm]$	0.2596	0.3524
<b>Diameter</b>		
$D_{avg}[mm]$	122.46	122.47
$Var(D)[mm^2]$	0.0686	0.0459
$Stdev(D)[mm]$	0.2619	0.2143

### 6.3.2 Set-up

As mentioned earlier, the test set-up used in this thesis was identical to the impact test set-up in previous theses. However, to refresh the memory of the reader, a short review of the set-up is given. The impact was conducted in the pendulum accelerator, often called the kicking machine, at the Department of Structural Engineering, NTNU. The machine accelerates a trolley on rails towards the pipe, which is fixed to a reaction wall (Figure 6.3). The velocity  $v$  of the trolley was the only variable, thus the mass  $M$  (1472 kg) and the indenter diameter  $d$  (20 mm) were kept constant. The kinetic energy of the trolley was calculated based on Equation (2.10). For further information about the kicking machine it is referred to Hanssen et al. [51].

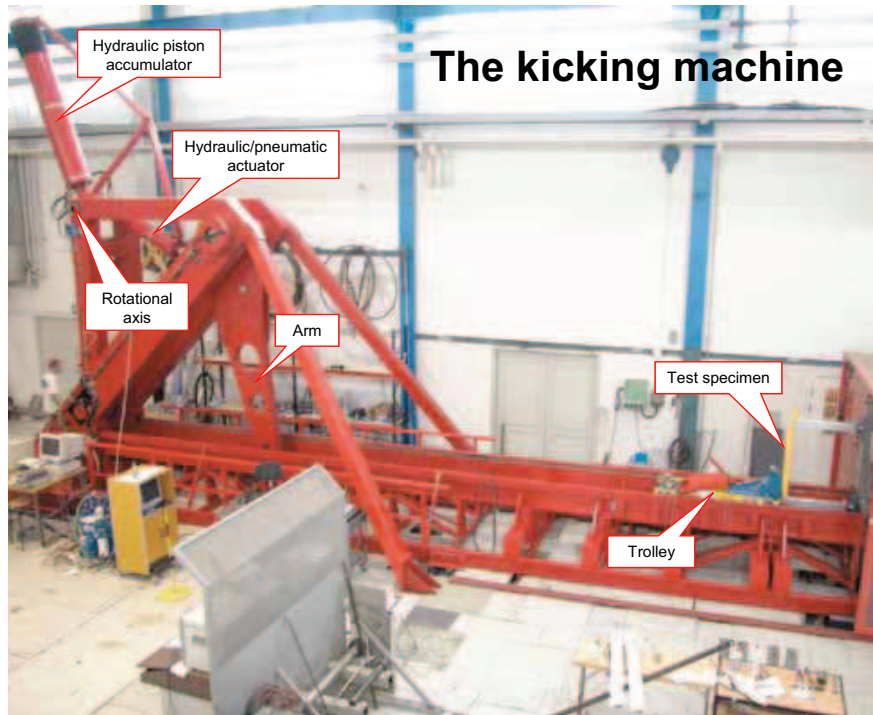


**Figure 6.3:** Pendulum accelerator [52].

Contact force between the indenter and the pipe was sampled against time during the impact. Acceleration, displacement, velocity and mean force were automatically calculated. The test matrix is given in Table 6.4. After impact, deformations were measured according to Figure 6.4. The pipes were then cut and sent for metallurgical investigation.

## 6. COMPONENT TESTS

**Table 6.4:** Impact test matrix.

Pipe	K	L	A	B
Mass of trolley [kg]	1472	1472	1472	1472
Initial velocity [ $m/s$ ]	5.18	3.26	3.24	5.13
Kinetic energy [kJ]	19.75	7.82	7.71	19.36

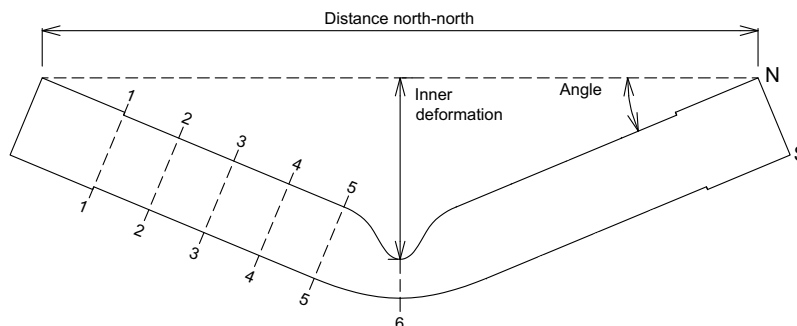


**Figure 6.4:** Measure points along the pipe [4].

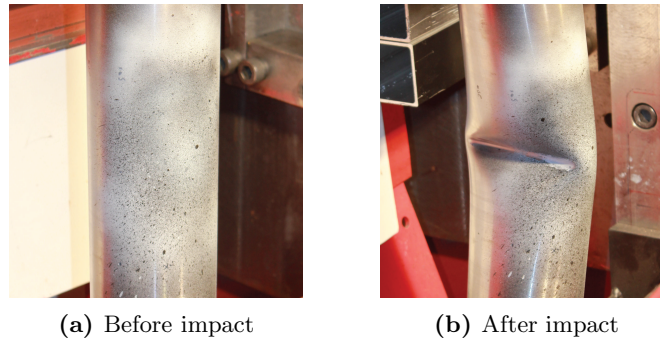
### 6.3.3 Results

Figure 6.5a shows a photo of a pipe before impact, while Figure 6.5b illustrates the typical deformed configuration. Force and displacement values were sampled on the load cell during the impact. In addition, the displacement was measured by a laser for better accuracy. Unfortunately no data was recorded for the impact against pipe  $L$  due to a technical glitch. Therefore, only pipe  $B$  ( $v = 5.13$  m/s) and  $K$  ( $v = 5.18$  m/s) are compared (Figure 6.6). Although there is a significant difference in the force-displacement curve, the difference in the kinetic energy between the two tests was small ( $\sim 2$  %). It is seen from Figure 6.6 that pipe  $K$  has a higher stiffness than pipe  $B$ . The main reason for this difference in the force-displacement, is most likely the difference in average thickness (Table 6.5). This was also supported by Slåttedalen and Ørmen, which stated that the stiffness of the pipes was strongly dependent on the thickness. Another observed phenomenon of the force-displacement curves are the distinct three phases, i.e. crumpling, crumpling and bending and structural collapse (Section 2.3).

Slåttedalen and Ørmen discovered that pipe  $B$  was nearly flattened at the midspan after impact, and the pipe was not able to absorb all the kinetic energy before the trolley hit the aluminum buffers. Impact against pipe  $K$  revealed the same (Figure 6.8a). To illustrate how the impact evolves, a picture series is presented in Figure 6.7. Visual inspection after impact revealed a crack on the surface of the pipe (Figure 6.8b). This was of great interest

### 6.3 Impact against empty pipes

and examined carefully during the metallurgical investigation (Section 6.3.5). Post-crash measurements of pipe *K* and *L* are given in Table 6.6. The measurements show that the deformed configuration was highly influenced by the impact velocity. Comparing Table 6.6 and 6.1 displays approximately the same results. Thus, it is the force-displacement curve which shows significant difference, and not the measurements of the deformed configuration. Appendix B.2 summarizes the entire test program for empty pipes impacted at different velocities.



**Figure 6.5:** Pre- and post crash photo of impacted pipe.

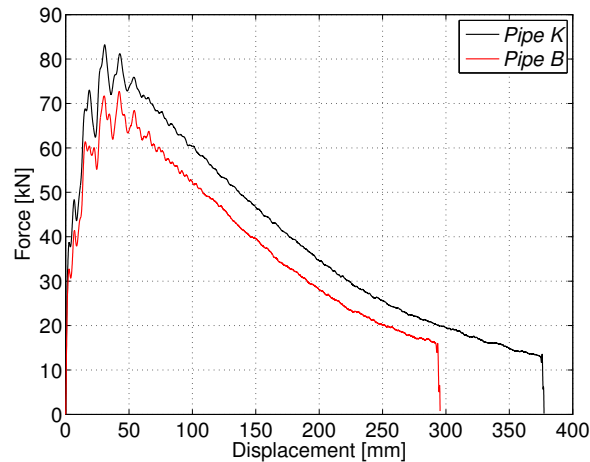


**Figure 6.6:** Force vs displacement for impact tests on pipe *B* and *K*.

**Table 6.5:** Thickness measurements of pipe *B* and *K* prior to testing.

Pipe	B	K
$t_{avg}[mm]$	3.86	4.12
$Var(t)[mm^2]$	0.1180	0.0674
$Stdev(t)[mm]$	0.3434	0.2596

## 6. COMPONENT TESTS

---

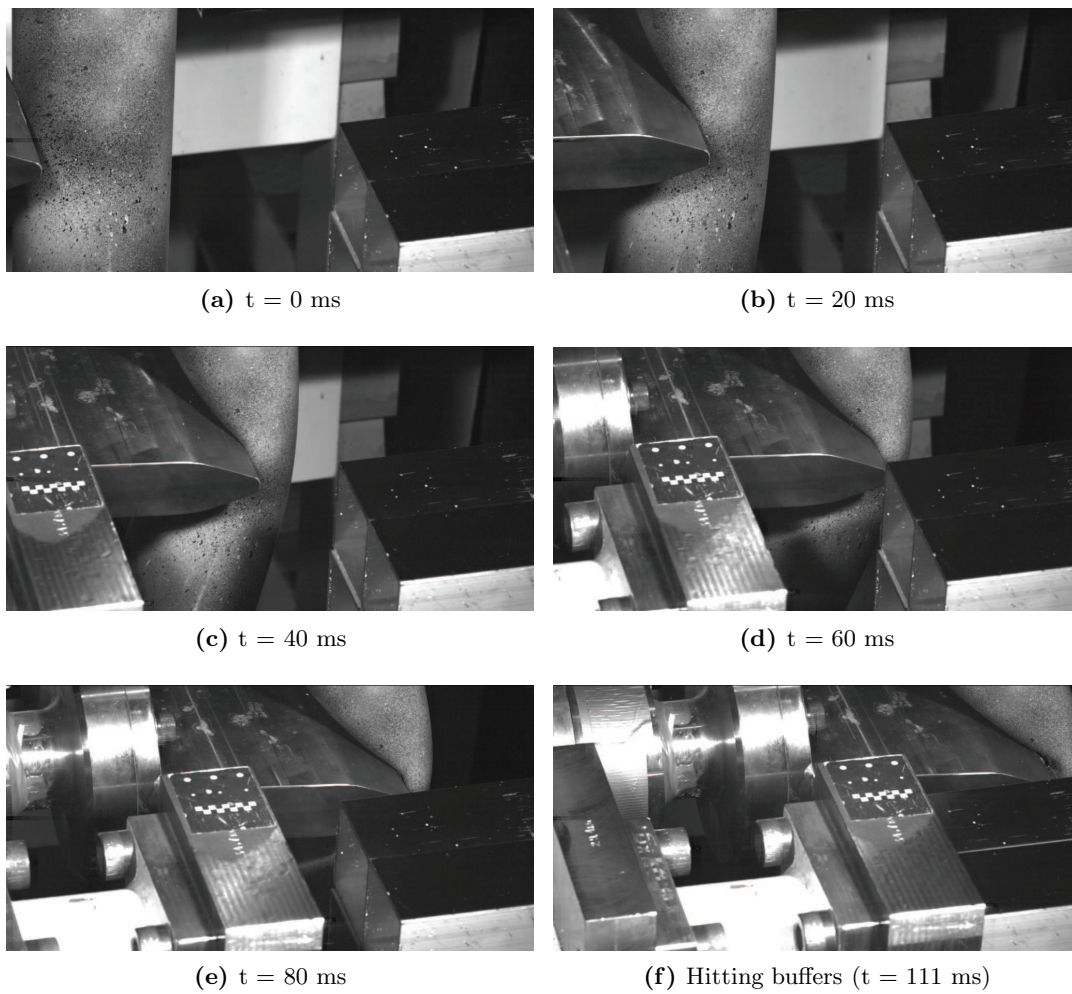


**Figure 6.7:** Photo series from video capturing the impact of pipe  $K$  ( $v = 5.18$  m/s).

**Table 6.6:** Measurements of the impacted pipes.

<b>Pipe</b>	<b>K</b> ( $v = 5.18$ m/s)		<b>L</b> ( $v = 3.26$ m/s)	
Inner deformation [mm]	403		133	
Angle at the supports [-]	33		8.5	
Distance north-north [mm]	1006		1263	
<b>Diameter at measuring points [mm]</b>	<b>N-S</b>	<b>E-W</b>	<b>N-S</b>	<b>E-W</b>
1 (at support)	131.35	131.09	131.30	131.16
2	130.60	131.91	130.99	131.43
3	128.33	134.58	129.32	132.97
4	120.69	140.70	125.63	136.70
5	100.90	154.44	113.50	146.28
6 (at midpoint)	27.02*	201.87	73.40	170.60

\**Inaccurate measurement.*



(a) Pipe *K* flattened after impact

(b) Surface fracture discovered on pipe *K* after impact

**Figure 6.8:** Post-crash deformation and discovery of surface fracture on pipe *K*.

## 6. COMPONENT TESTS

---

### 6.3.4 Correction of the displacement

The load cell in the impact tests can be inaccurate, and not yield the exact result. As mentioned earlier, lasers were installed to improve the accuracy of the result. The load cells register the contact force during impact. From this the acceleration  $a$ , velocity  $v$  and displacement  $d$  are derived, respectively, as

$$a(t) = \frac{F(t)}{1472kg} \quad v(t) = \int_0^t a(t)dt \quad d(t) = \int_0^t v(t)dt \quad (6.1)$$

The calculated displacement from the load cell was adjusted to fit the displacement curve from the lasers. To adjust the values from the load cell, the load cell force  $F_{lc}$  was multiplied with a load factor  $l_f$ .

$$F_{corr} = l_f \cdot F_{lc} \quad (6.2)$$

where  $F_{corr}$  is the corrected force. The load factor  $l_f$  can be calculated as

$$l_f = \frac{d_{lc}}{d_{laser}} \quad (6.3)$$

where  $d_{lc}$  is the load cell deformation and  $d_{laser}$  is the laser deformation. Two approaches were used to calculate the load factor  $l_f$ :

- (1) The ratio between maximum load cell and laser displacement before the trolley hit the buffers.
- (2) Method of least squares, minimizing the difference between the load cell and laser deformation during the entire time span.

**Table 6.7:** Correction of force-displacement curves.

	(1) load cell	(2) least squares
$l_f$	0.984	0.988

Table 6.7 shows the results from the two different approaches. Figure 6.9a depicts the force-time fit. It is seen that both correction approaches give nearly the same result, and are very close to the laser measurements. In Figure 6.9b, the force-displacement for the corrected values and uncorrected value is given.

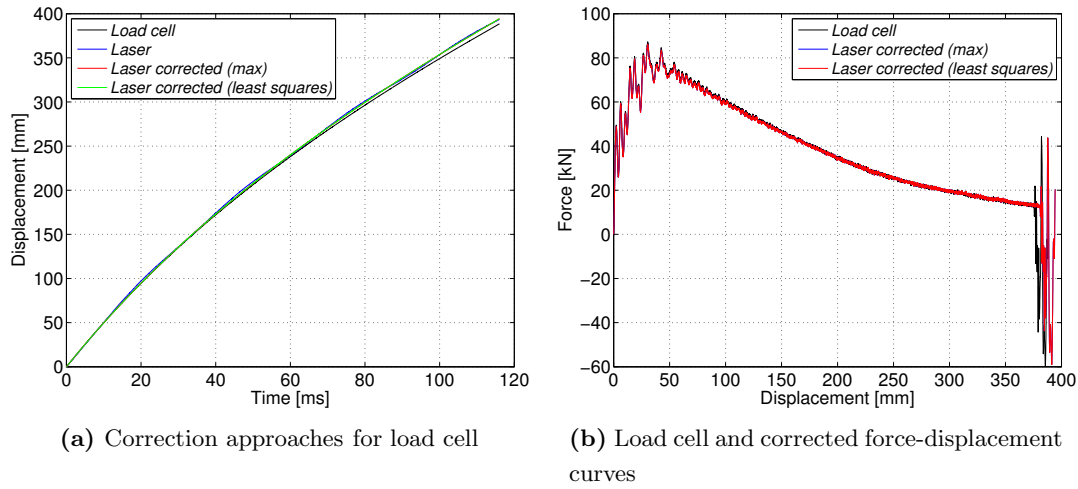


**Figure 6.9:** Correction approaches and force vs displacement for load cell and corrected values.

### 6.3.5 Metallurgical investigation

In the following section a metallurgical investigation has been carried out for pipes subjected to impact only, and pipes subjected to impact followed by stretching. It was of great interest to investigate what initiates the fracture. The pipes subjected to both impact and stretching were obtained from tests conducted by Slåttdalen and Ørmen. This work has been carried out in collaboration with research scientist Dr. Ida Westermann at SINTEF.

Fracture was observed for all the pipes subjected to both impact and stretching. Figure 6.10 shows the typical fracture surfaces for the pipes. It is expected that the fracture starts at the crack-tip (2 in Figure 6.10), making this the most interesting region. Dimples with spherical particles (size varied from a few to approximately  $25 \mu\text{m}$ ) were observed at the crack-tip (Figure 6.11a). Cracked particles were also discovered (Figure 6.11b). This observation was of great interest since it could lower the fracture strength.

The fracture surface in the compression zone (3 in Figure 6.10) was characterized by distinct cleavage (Figure 6.12). The fracture was brittle, and showed no sign of ductility. The multifaceted surface with "river patterns" seen in the figure is typical of cleavage. Comparing Figure 6.12 with Figure 2.30a shows a remarkable similarity. It should be noted that there was observed no visible particles in the compression zone (Figure 6.12).

Furthermore, the fracture surface in the shear zone (1 in Figure 6.10) was ductile with a mix of large and small dimples (Figure 6.13a). The dimples seen in the figure stem from

## 6. COMPONENT TESTS

---

microvoids growing together, leading to a macroscopic flaw. Spherical particles of varying size (2-20  $\mu\text{m}$ ) bounded to the dimples were also discovered (Figure 6.13b).

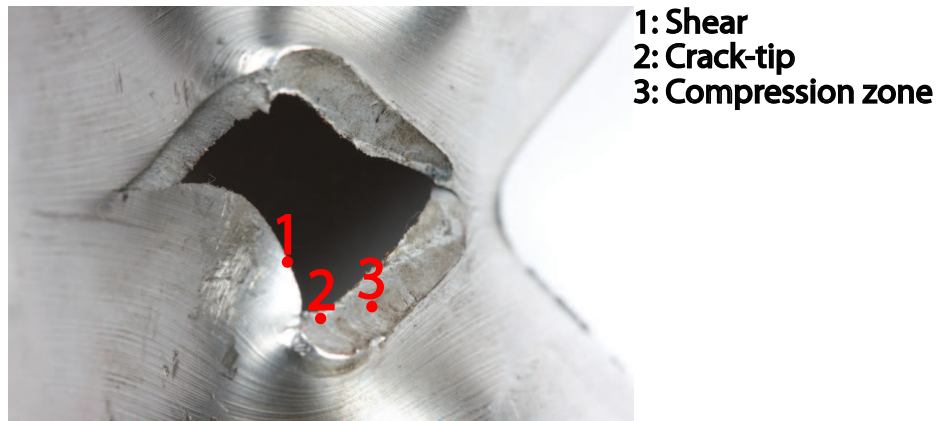


**Figure 6.10:** Fracture surfaces for pipes exposed to impact and stretching.

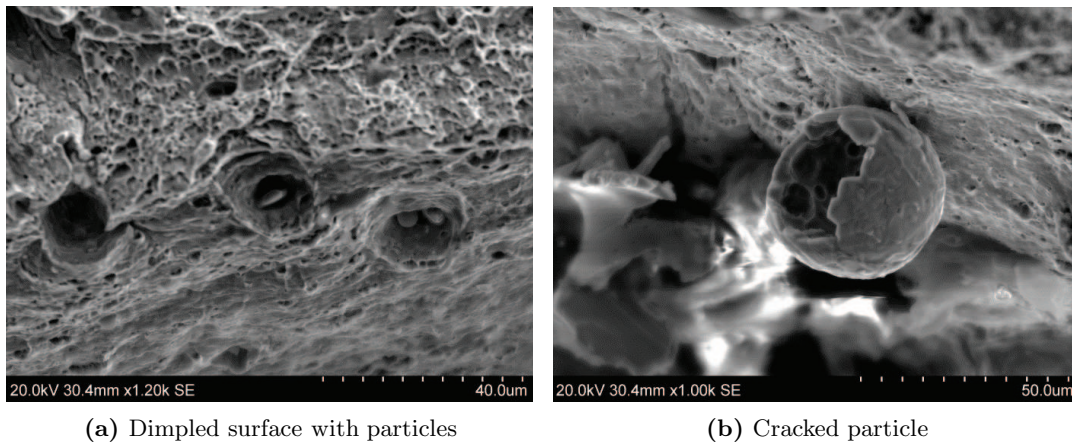


**Figure 6.11:** Dimpled surface with particle and cracked particle at the crack-tip.

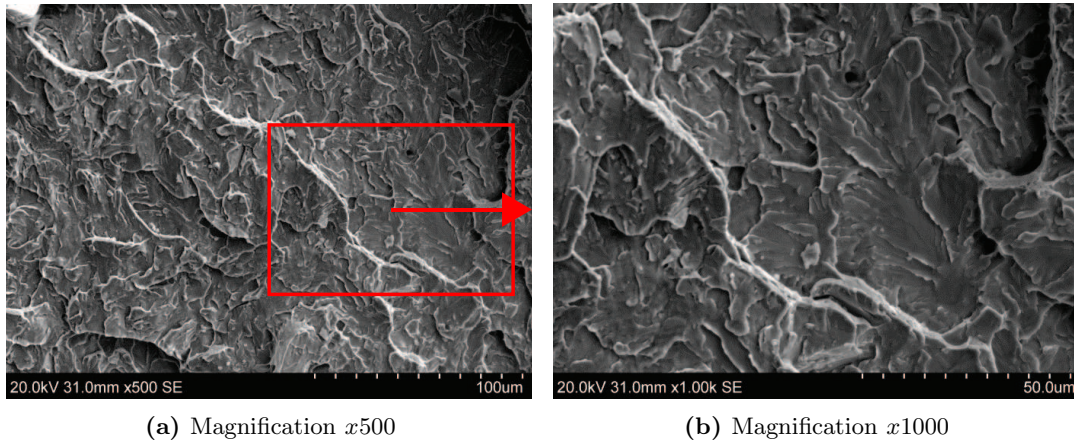


**Figure 6.12:** Cleavage fracture surface at different magnification in the compression zone.

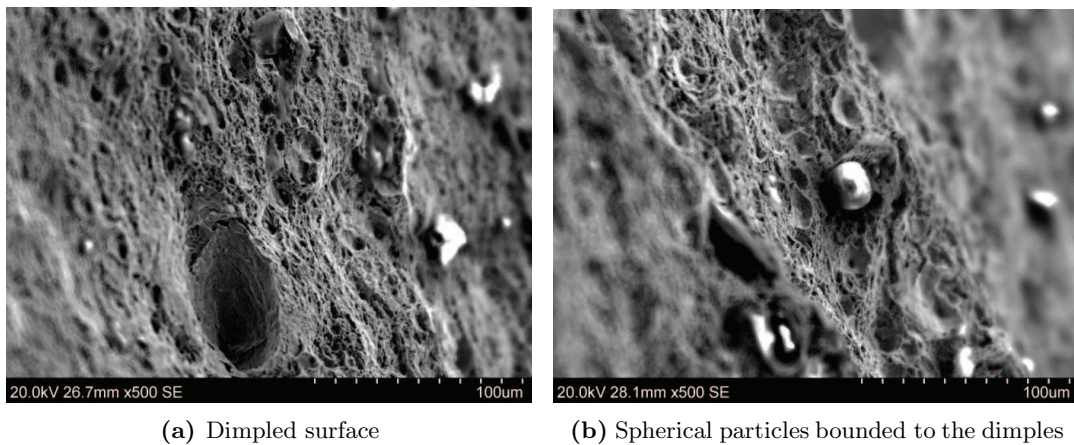


**Figure 6.13:** Dimpled fracture surface and spherical particles bounded to the dimples in the shear zone.

Above, metallurgical investigation of pipes subjected to both impact and stretching were carried out. However, to reveal any incipient fracture already after impact, a metallurgical investigation was carried out on pipes subjected to impact only. Two areas of interest were found, i.e. the surface and V-zone crack (Figure 6.14b).

Macroscopic inspection of pipe *K* ( $v = 5.18$  m/s) revealed a visible crack, both on the surface and in the V-zone (Figure 6.14b and 6.14c). This was clearly of great interest, since a crack will weaken the strength of the pipe. Cross-sectional cuts were taken to further investigate the observed cracks (Figure 6.15).

The microstructural investigation of the cross-sectional cuts for the surface crack (Figure 6.14b) revealed interesting results. A crack through 75 % of the thickness was discovered

## 6. COMPONENT TESTS

---

(Figure 6.16a). It is clear that this crack will weaken both the tensile and fatigue strength of the pipe. The fracture surface of the crack was typical intercrystalline with oblong grains (Figure 6.16d). It was also observed that the deformation of the microstructure decreased near the crack-tip (Figure 6.16c).

As mentioned above, internal damage at the V-zone was also observed. Similar to the surface crack, it was found that the thickness was reduced by 75 %. However, in contrast to the surface crack, this internal crack showed no connection with any visible cracks on the surface at the V-zone (Figure 6.17a). The fracture surface of the crack was characterized as intercrystalline with secondary cracks. No major deformation of the microstructure was observed.

To get an indication of the damage evolution in the pipes, metallurgical investigation of pipe *L* ( $v = 3.26$  m/s) was performed. Similar to that of pipe *K*, cross-sectional cuts of the impacted regions in pipe *L* were investigated (Figure 6.18). Region 1 (Figure 6.19a) showed no sign of fracture at low magnification. However, at higher magnification fracture was discovered in the middle of the pipe wall. The fracture occurred typically along the grain boundaries. Figure 6.19b shows region 2 at high magnification. Investigation of this region revealed similar results to that of region 1, as might be expected since they were taken from similar regions (Figure 6.18). No sign of fracture at low magnification could be seen, however, when increasing the magnification cracks of approximately  $20\ \mu\text{m}$  along the grain boundaries were observed. Region 4 (Figure 6.19d) revealed visible cracks of order  $50\ \mu\text{m}$  on the surface at the impacted region. The cracks appeared to be initiated close to regions with higher toughness, i.e. at the grain boundaries between two planes. No fracture was observed in region 3 (Figure 6.19c), even at high magnification. However, cracks could be present in this region even though they were not detected during the investigation.

The results for pipes subjected to impact depict that fracture and internal damage becomes more evident at increasing velocity of the indenter. However, they are also apparent, at least at high magnification, for lower velocity. No conclusion regarding damage evolution can be drawn from only two tests. To get a clearer picture, more tests and investigation similar that described above must be carried out.

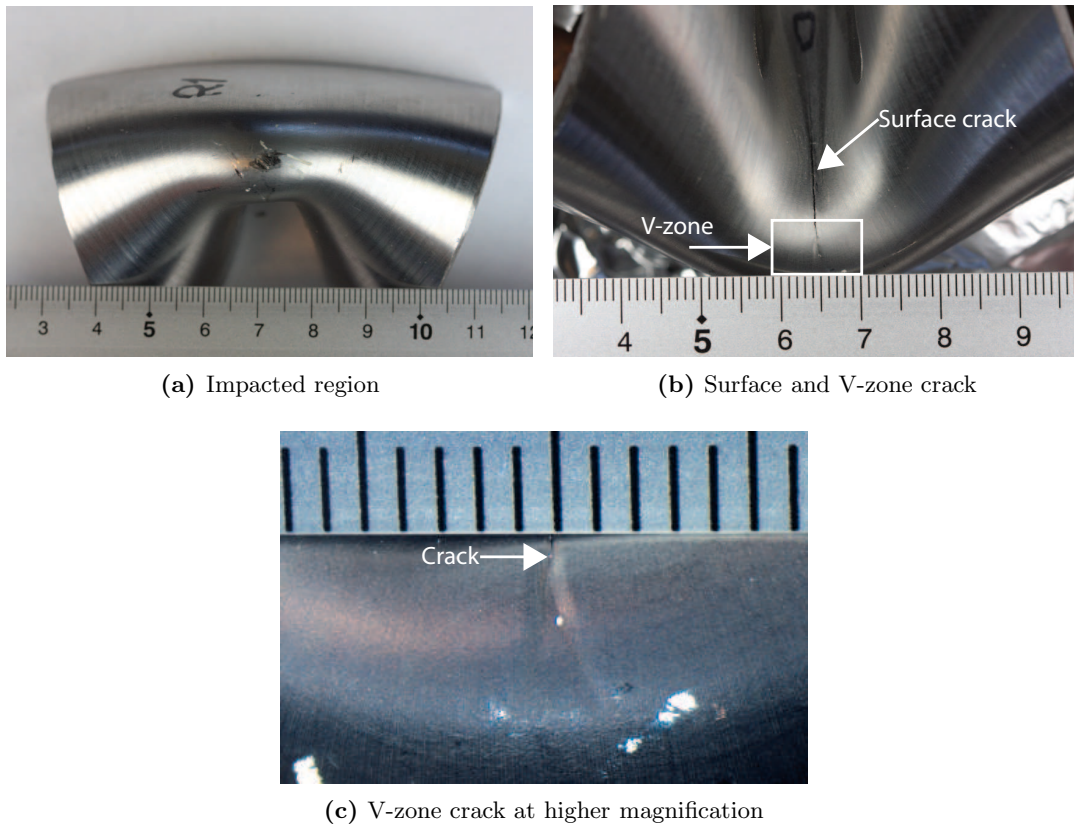


**Figure 6.14:** Macroscopic inspection of impact region from pipe  $K$  ( $v = 5.18$  m/s).

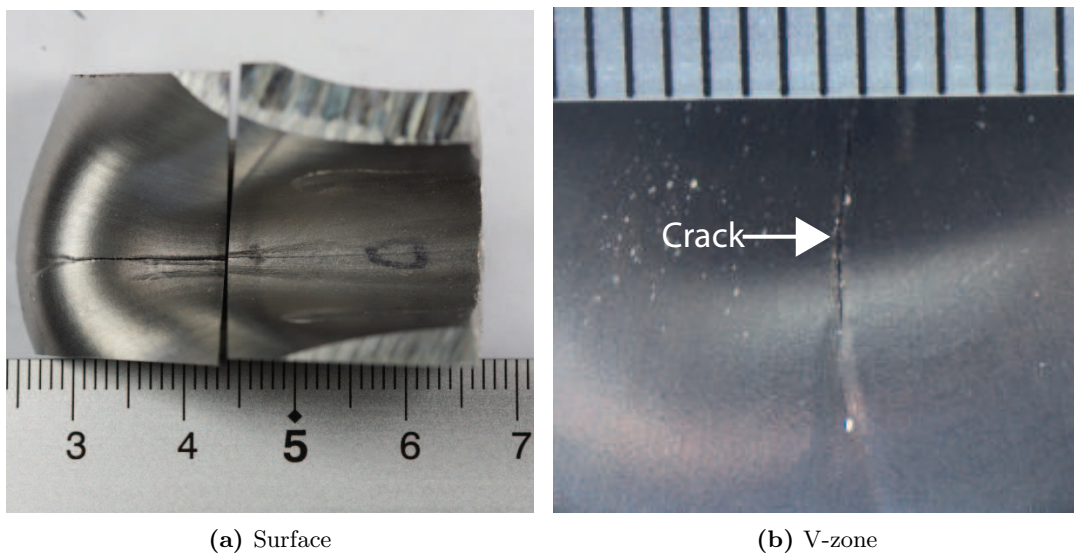


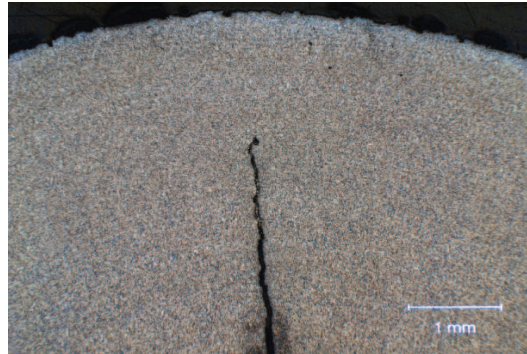
**Figure 6.15:** Cross-sectional cut of surface and V-zone crack for impacted region of pipe  $K$ .

## 6. COMPONENT TESTS

---



(a) Visible crack through 75 % of the thickness



(b) Previous figure from another view

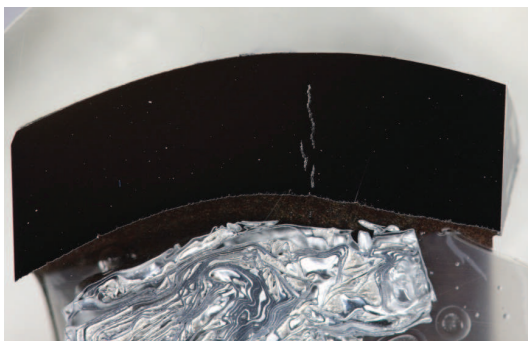


(c) Deformation near crack tip



(d) Intercrystalline fracture

**Figure 6.16:** Internal crack depth at the surface crack region of pipe *K*.



(a) Internal crack



(b) Fracture

**Figure 6.17:** Internal crack in the V-zone region of pipe *K*.

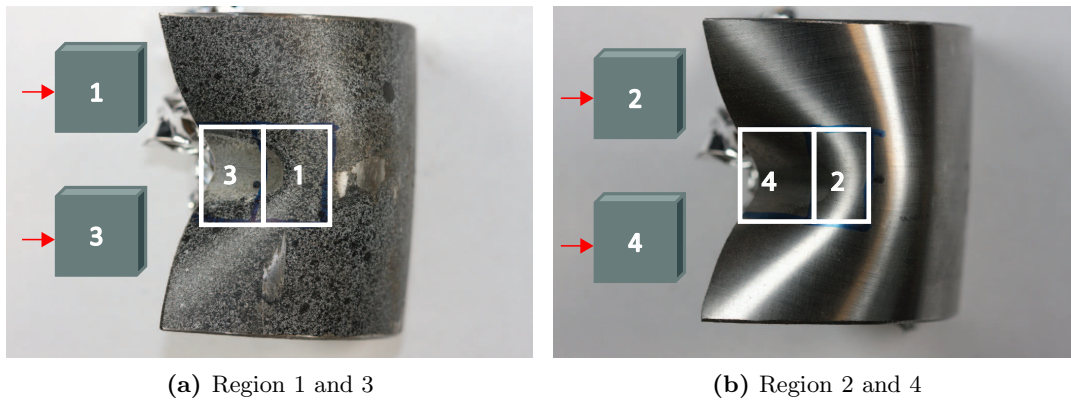


**Figure 6.18:** Illustrating cross-sectional cuts for regions of pipe  $L$  ( $v = 3.26$  m/s). The red arrows indicate the investigated surfaces.

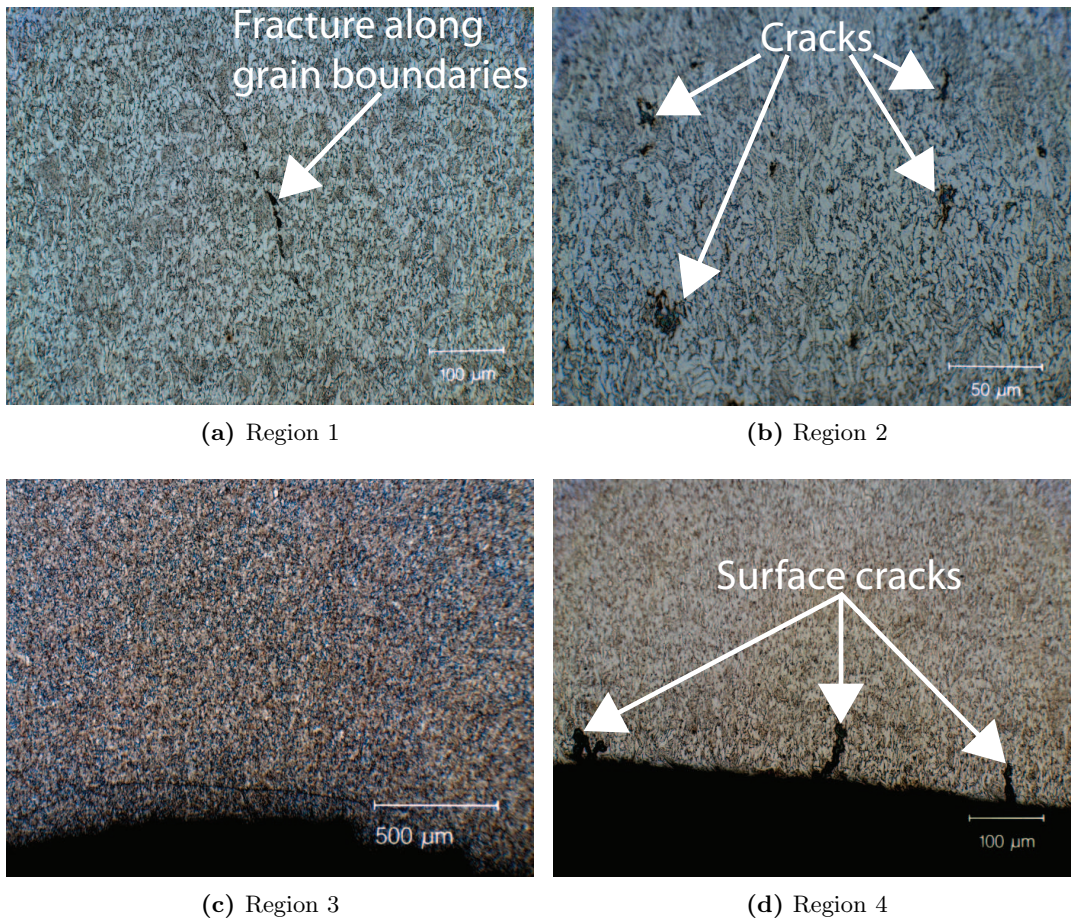


**Figure 6.19:** Investigated regions pipe  $L$ .

## 6. COMPONENT TESTS

---

## 7 Finite Element Analyses (FEA)

This chapter gives a brief presentation of the Finite Element Method (FEM) Theory for dynamic problems and numerical simulations of the component tests. The numerical simulations were performed in ABAQUS/Explicit and LS-DYNA. A shell model in ABAQUS/Explicit was used to investigate the influence of the material model on the global response. In addition, the material model calibrated by inverse modeling was compared with previous theses in terms of the global response, during both impact and stretching. Based on the observations in Section 6.3.5, it was of great interest to model the springback after impact. To investigate the complex stress state, a volume model was established in LS-DYNA. This was the preferred FEM software due to its built-in springback application.

### 7.1 FEM theory

ABAQUS/Explicit 6.11, ABAQUS CAE and LS-DYNA v971 have been used as the FEM software. These softwares are developed by SIMULIA and Livermore Software Technology Corporation (LSTC), respectively. ABAQUS consists of three parts. ABAQUS CAE is a GUI (Graphical User Interface) and is used for pre-processing and post-processing. ABAQUS Standard is the implicit solver and ABAQUS/Explicit is the explicit solver [35]. The latter was used in the present thesis.

LS-DYNA is mainly designed to solve nonlinear transient dynamic FE analyses using explicit time integration. However, it also contains an implicit solver which could be used for static, quasi-static and dynamic problems with a low frequency content [53]. The explicit and implicit solver were used in describing the impact and springback, respectively.

## 7. FINITE ELEMENT ANALYSES (FEA)

---

### 7.1.1 Dynamic equilibrium

The general equation of motion for a multi-degree-of-freedom system may be expressed as

$$\{\mathbf{R}^{ine}(t)\} + \{\mathbf{R}^{dmp}(t)\} + \{\mathbf{R}^{int}(t)\} = \{\mathbf{R}^{ext}(t)\} \quad (7.1)$$

where  $\{\mathbf{R}^{ext}(t)\}$  is the external force vector.

By expressing the inertia force vector, damping force vector and internal force vector, respectively, as

$$\{\mathbf{R}^{ine}(t)\} = [\mathbf{M}]\{\ddot{\mathbf{D}}(t)\} \quad (7.2)$$

$$\{\mathbf{R}^{dmp}(t)\} = [\mathbf{C}]\{\dot{\mathbf{D}}(t)\} \quad (7.3)$$

$$\{\mathbf{R}^{int}(t)\} = [\mathbf{K}]\{\mathbf{D}(t)\} \quad (7.4)$$

the equation of motion can be written in terms of

$$[\mathbf{M}]\{\ddot{\mathbf{D}}(t)\} + [\mathbf{C}]\{\dot{\mathbf{D}}(t)\} + [\mathbf{K}]\{\mathbf{D}(t)\} = \{\mathbf{R}^{ext}(t)\} \quad (7.5)$$

where  $[\mathbf{M}]$ ,  $[\mathbf{C}]$  and  $[\mathbf{K}]$  are the mass, damping and stiffness matrices, respectively. The acceleration  $\{\ddot{\mathbf{D}}\}$ , velocity  $\{\dot{\mathbf{D}}\}$  and displacement  $\{\mathbf{D}\}$  vectors can then be solved by either implicit or explicit solution methods.

### 7.1.2 Explicit integration

The explicit solution method was mainly used in this thesis. The reason was that the method is particularly suitable for problems involving high-speed dynamic simulations, such as the impact problem investigated. In the explicit method, the displacement  $\{\mathbf{D}_{n+1}\}$  at time  $t_{n+1}$  is obtained directly from the equilibrium conditions at one or more preceding time steps  $t \leq t_n$ , without solving an equation system. Hence, the unknown values are obtained from information already known. The method operates with a critical time step  $\Delta t_{cr}$ , that must not be exceeded to avoid an unstable solution. Therefore, the method is only conditionally

stable. Many time steps are often required to find the solution of the problem, however, with small computational cost per increment [26].

The equation of motion for the multi-degree-of-freedom system (Equation (7.5)) can be solved incrementally using the classical central difference method. Using Taylor series expansion of the displacements  $\{\mathbf{D}_{n+1}\}$  and  $\{\mathbf{D}_{n-1}\}$  about time  $t_n$ , and neglecting higher order terms, the velocity and acceleration can be approximated, respectively, as

$$\{\dot{\mathbf{D}}\}_n = \frac{\{\mathbf{D}\}_{n+1} - \{\mathbf{D}\}_{n-1}}{2\Delta t} \quad (7.6)$$

$$\{\ddot{\mathbf{D}}\}_n = \frac{\{\mathbf{D}\}_{n+1} - 2\{\mathbf{D}\}_n + \{\mathbf{D}\}_{n-1}}{\Delta t^2} \quad (7.7)$$

Inserting the velocity and acceleration into the equation of motion, and solving the equation for  $\{\mathbf{D}_{n+1}\}$  gives the incremental solution of the problem

$$\{\mathbf{D}\}_{n+1} = [\mathbf{K}^{eff}]^{-1} \{\mathbf{R}^{eff}\}_n \quad (7.8)$$

where

$$[\mathbf{K}^{eff}] = \frac{1}{\Delta t^2} [\mathbf{M}] + \frac{1}{2\Delta t} [\mathbf{C}] \quad (7.9)$$

and

$$\{\mathbf{R}^{eff}\}_n = \{\mathbf{R}^{ext}\}_n - \left( \frac{1}{\Delta t^2} [\mathbf{M}] - \frac{1}{2\Delta t} [\mathbf{C}] \right) \{\mathbf{D}\}_{n-1} - \left( [\mathbf{K}] - \frac{2}{\Delta t^2} [\mathbf{M}] \right) \{\mathbf{D}\}_n \quad (7.10)$$

As mentioned above, terms containing  $\Delta t$  to power higher than second order are neglected in the Taylor series expansion. Hence, the primary error term is proportional to  $\Delta t^2$ , and the displacement  $\{\mathbf{D}\}$  has second order accuracy. Thus, by reducing the time step by a factor 2 the error in displacement is reduced by a factor 4.

In general dynamic response analysis, it is often desirable to include stiffness-proportional damping  $[\mathbf{C}] = \beta[\mathbf{K}]$  to damp high-frequency numerical noise. Thus, it is required to solve an equation system because the effective stiffness matrix  $[\mathbf{K}^{eff}]$  becomes non-diagonal. Hence, the computational cost per time step greatly increases. However, by establishing the equation

## 7. FINITE ELEMENT ANALYSES (FEA)

---

of motion with the velocity lagging by half a time step, the problem may be overcome [26]. Therefore, the half-step central differences for the velocity are established as

$$\{\dot{\mathbf{D}}\}_{n-1/2} = \frac{1}{\Delta t} (\{\mathbf{D}\}_n - \{\mathbf{D}\}_{n-1}) \quad (7.11)$$

$$\{\dot{\mathbf{D}}\}_{n+1/2} = \frac{1}{\Delta t} (\{\mathbf{D}\}_{n+1} - \{\mathbf{D}\}_n) \quad (7.12)$$

and the acceleration is approximated as

$$\{\ddot{\mathbf{D}}\}_n = \frac{1}{\Delta t} (\{\dot{\mathbf{D}}\}_{n+1/2} - \{\dot{\mathbf{D}}\}_{n-1/2}) = \frac{1}{\Delta t^2} (\{\mathbf{D}\}_{n+1} - 2\{\mathbf{D}\}_n + \{\mathbf{D}\}_{n-1}) \quad (7.13)$$

where the velocity and displacement may be approximated, respectively, as

$$\{\dot{\mathbf{D}}\}_{n+1/2} = \{\dot{\mathbf{D}}\}_{n-1/2} + \Delta t \{\ddot{\mathbf{D}}\}_n \quad (7.14)$$

$$\{\mathbf{D}\}_{n+1} = \{\mathbf{D}\}_n + \Delta t \{\dot{\mathbf{D}}\}_{n+1/2} = \{\mathbf{D}\}_n + \Delta t \{\dot{\mathbf{D}}\}_{n-1/2} + \Delta t^2 \{\ddot{\mathbf{D}}\}_n \quad (7.15)$$

By substituting the half-step central difference approximations into the equation of motion, the following is obtained

$$\frac{[M]}{\Delta t^2} \{\mathbf{D}\}_{n+1} = \{\mathbf{R}^{ext}\}_n - [K] \{\mathbf{D}\}_n + \frac{[M]}{\Delta t^2} (\{\mathbf{D}\}_n + \Delta t \{\dot{\mathbf{D}}\}_{n-1/2}) - [C] \{\dot{\mathbf{D}}\}_{n-1/2} \quad (7.16)$$

The half-step central difference method requires that initial conditions must be introduced to determine  $\{\dot{\mathbf{D}}\}_{-1/2}$ . Using a backward difference approximation, the initial velocity is given as [26]

$$\{\dot{\mathbf{D}}\}_{-1/2} = \{\dot{\mathbf{D}}\}_0 - \frac{\Delta t}{2} \{\ddot{\mathbf{D}}\}_0 \quad (7.17)$$

where the initial acceleration  $\{\ddot{\mathbf{D}}\}_0$  may be obtained by solving the equation of motion at time  $t_0$  as

$$\{\ddot{\mathbf{D}}\}_0 = [M]^{-1} (\{\mathbf{R}^{ext}\}_0 - [C] \{\dot{\mathbf{D}}\}_0 - [K] \{\mathbf{D}\}_0) \quad (7.18)$$

The two central difference methods proposed above can only guarantee first order accuracy. To avoid having to solve an equation system, the mass matrix needs to be diagonal, i.e. lumped masses must be used. Using lumped mass will also correct for the period elongation due to the fact that natural frequencies are underestimated in an explicit analysis [26].

As mentioned earlier, the explicit method is conditionally stable. Hence, the solution is bounded only when the time increment  $\Delta t$  is less than the stable time increment  $\Delta t_{cr}$ . If  $\Delta t > \Delta t_{cr}$  the solution will become unstable and oscillations will occur in the response history. For practical problems, the critical time step is determined as

$$\Delta t_{cr} \leq \frac{2}{\omega_{max}} \left( \sqrt{1 - \xi^2} - \xi \right) \quad (7.19)$$

where  $\omega_{max}$  is the highest natural frequency and  $\xi$  is the corresponding damping ratio. For an undamped material, the critical time step is given as

$$\Delta t_{cr} \leq \frac{2}{\omega_{max}} = \frac{L^e}{c_d} \quad (7.20)$$

where  $L^e$  is the characteristic length of the smallest element, and  $c_d$  is the dilatation wave speed, given as

$$c_d = \sqrt{\frac{E}{\rho}} \quad (7.21)$$

where  $E$  is the modulus of elasticity and  $\rho$  is the mass density. Hence, the critical time step is determined by the smallest, stiffest or least dense element in the FE-model. It is important that the mesh does not contain any elements significantly smaller than other elements, since this may seriously reduce  $\Delta t_{cr}$  for the entire simulation. The physical interpretation of  $\Delta t_{cr}$  is that  $\Delta t$  must be small enough so that information does not propagate more than the distance between the adjacent nodes during a single time step. In addition, higher-order elements should be avoided when using explicit time integration [26].

## 7. FINITE ELEMENT ANALYSES (FEA)

---

### 7.1.3 Implicit integration

Although the explicit solution method has mainly been used in this thesis, the simulation of springback was performed using an implicit analysis. Therefore, a brief comparison between the explicit and implicit method, to clarify the advantages and disadvantages, are given in the present section. Table 7.1 summarizes the two methods.

**Table 7.1:** Explicit vs implicit solution method [26].

---

<b>Explicit method</b>
+ Equation solving not necessary. Hence, each time increment is computationally inexpensive.
+ Equilibrium iterations not necessary. Thus, the convergence is not a issue.
+ Ideal for high-speed dynamic simulations, where very small time increments are required.
+ Usually reliable for problems involving discontinuous nonlinearities. It is the preferable choice when solving contact problems, buckling and material failure problems.
– The method is conditionally stable. Hence, it requires very small time steps.

---

<b>Implicit method</b>
+ The method is unconditionally stable. Hence, the time increment size is not limited and fewer increments are required to complete a simulation.
+ Ideal for problems where either the response period of interest is long or nonlinearities are smooth (e.g. plasticity problems). It requires few iterations to complete the simulation.
– Nonlinear algebraic equations must be solved at each time step. Thus, each time increment is computationally expensive.
– Equilibrium iterations are necessary. Hence, convergence must be obtained for each element.

---

### 7.1.4 Contact

The kinematic constraint method and penalty method are two frequently used contact algorithms in FEM software, e.g. ABAQUS/Explicit and LS-DYNA [35, 53]. As an explicit solution method was used in this thesis, the penalty method was the preferred choice. Applying the penalty method for an explicit analysis leaves the number of unknowns constant, and there is no need to solve an equation system. Another important advantage of the penalty method is that it allows for contact between discrete rigid surfaces, which was an important feature regarding the numerical modeling in this thesis.

The penalty method imposes the contact condition by augmenting the potential energy of the system  $\Pi_p$  by a penalty term [26]

$$\Pi_p^* = \Pi_p + \frac{1}{2}\alpha[C(u)]^2 = \frac{1}{2}ku^2 - mgu + \frac{1}{2}\alpha(u - h)^2 \quad (7.22)$$

where the penalty parameter  $\alpha$  can be seen as a spring stiffness in the contact interface. This is illustrated for a one-degree-of-freedom system in Figure 7.1. This can be seen from Equation (7.22) where the potential energy of the penalty term has the same structure as the potential energy of a simple spring.

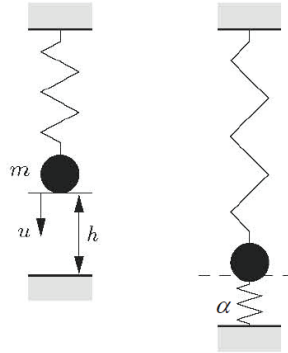


**Figure 7.1:** Penalty method [26].

To satisfy equilibrium, Equation (7.22) needs to be made stationary by

$$\left\{ \frac{\partial \Pi_p^*}{\partial u} \right\} = 0 \quad (7.23)$$

Inserting Equation (7.22) in (7.23) results in the following expression

$$(k + \alpha)u = mg + \alpha h \quad (7.24)$$

## 7. FINITE ELEMENT ANALYSES (FEA)

---

The latter equation could then be solved with respect to the displacement  $u$

$$u = \frac{mg + \alpha h}{(k + \alpha)} \quad (7.25)$$

and the contact condition and contact force then becomes, respectively

$$C(u) = u - h = \frac{mg - kh}{(k + \alpha)} \quad (7.26)$$

$$\lambda = \alpha C(u) = \frac{\alpha}{(k + \alpha)}(mg - kh) \quad (7.27)$$

As can be seen from Equation (7.22), the main advantage of using the penalty method is that the total number of unknowns remains constant and does not destroy the positive definiteness of the equation system. However, Equation (7.25) shows that the solution is dependent on the chosen penalty parameter which requires some engineering judgement about the problem at hand. If the penalty parameter  $\alpha$  is set to a very large number, the spring stiffness becomes very large, and the penetration into the rigid surface will be small. A large penalty parameter could also lead to a ill-conditioned stiffness matrix. In contrast, a small value of this parameter will not satisfy the contact condition in Equation (7.26) sufficiently.

## 7.2 Numerical simulations in ABAQUS/Explicit

The shell model suggested by Slåttedalen and Ørmen was used in the numerical simulations in ABAQUS/Explicit. Pipe *A* was the pipe examined most thoroughly in the previous theses. Therefore, this pipe was used in the numerical simulations for comparison with previous results. Since the numerical model was based on the work by Slåttedalen and Ørmen, this thesis was limited to a brief recapitulation of the model. It is referred to Slåttedalen and Ørmen for further information regarding the numerical model [3].

As in the experiments the numerical simulations were divided into two steps. The velocity, geometry and mass from the experiments were used as input parameters. Impact tests have a short time duration, hence, there was no need to scale the impact step. However, the stretch step needed to be scaled since it was considered quasi-static. The stretch step was scaled by decreasing the total time from 52.8 s to 0.12 s, and increasing the cross-head speed to 880 mm/s.

To save computational time, the symmetry of the pipe was utilized. By using symmetric boundary conditions at the symmetry edges, only one quarter of the pipe needed to be modeled. The mass of the trolley hitting the pipe was divided by four to get the correct kinetic energy in the symmetric model. Measurements of the pipes before the experiments indicated that the inner diameter and thickness of the region with original thickness were relatively constant for all the pipes. Hence, the average measurements were used. The measurements in the area with reduced thickness revealed a large degree of variance. The average thickness of pipe *A* was found to be 3.89 mm with a standard deviation of 0.3593 mm. Slåttedalen and Ørmen performed a sensitivity study on the thickness of the pipe, and found the optimized value as 3.85 mm. Therefore, the numerical model was modeled with a uniform thickness of 3.85 mm. Additional input parameters for the geometry are given in Table 7.2.

**Table 7.2:** Geometry input parameters [3].

Geometry parameter	Input
Inner diameter (mm)	126.6
Thickness (original area)	9.9
Thickness (reduced area)	3.85
Bolt diameter (mm)	40
Length between supports (mm)	1000

## 7. FINITE ELEMENT ANALYSES (FEA)

---

The assembly of the parts in the two steps is illustrated in Figure 7.2. The part with original thickness was modeled as discrete rigid, and tied to the deformable area using a constraint. The mesh consisted of S4R elements with an approximate size of 2 mm in the deformable area. The simulations were run with reduced integration and hourglass control, and the Simpson integration rule with five integration points over the thickness was used. It should be noted that the size of a shell element should not be small compared to the thickness. However, Slåttedalen and Ørmen found this element size acceptable [3].

Since the isotropic component in the combined work-hardening can not be implemented directly into ABAQUS if  $N > 1$ , the data were applied in tabular form. Strain rate dependency was implemented in the keyword editor, as suggested by Fornes and Gabrielsen through the following expression [4]

$$\sigma_{IH}(p, R) = K\sigma_{IH}(p, 0) + (K - 1)\sigma_{KH}(\varepsilon^p) \quad (7.28)$$

where

$$K = \left(1 + C \ln \frac{R}{\varepsilon_0}\right) \quad (7.29)$$

and  $R$  is a given strain rate,  $p$  is the equivalent plastic strain and  $\varepsilon^p$  is the plastic strain. The isotropic work-hardening is denoted  $\sigma_{IH}$  and  $\sigma_{KH}$  is the kinematic work-hardening. The material constant  $C$  and reference strain rate  $\varepsilon_0$  were found by Slåttedalen and Ørmen as 0.0104 and  $0.000806 \text{ s}^{-1}$ , respectively.

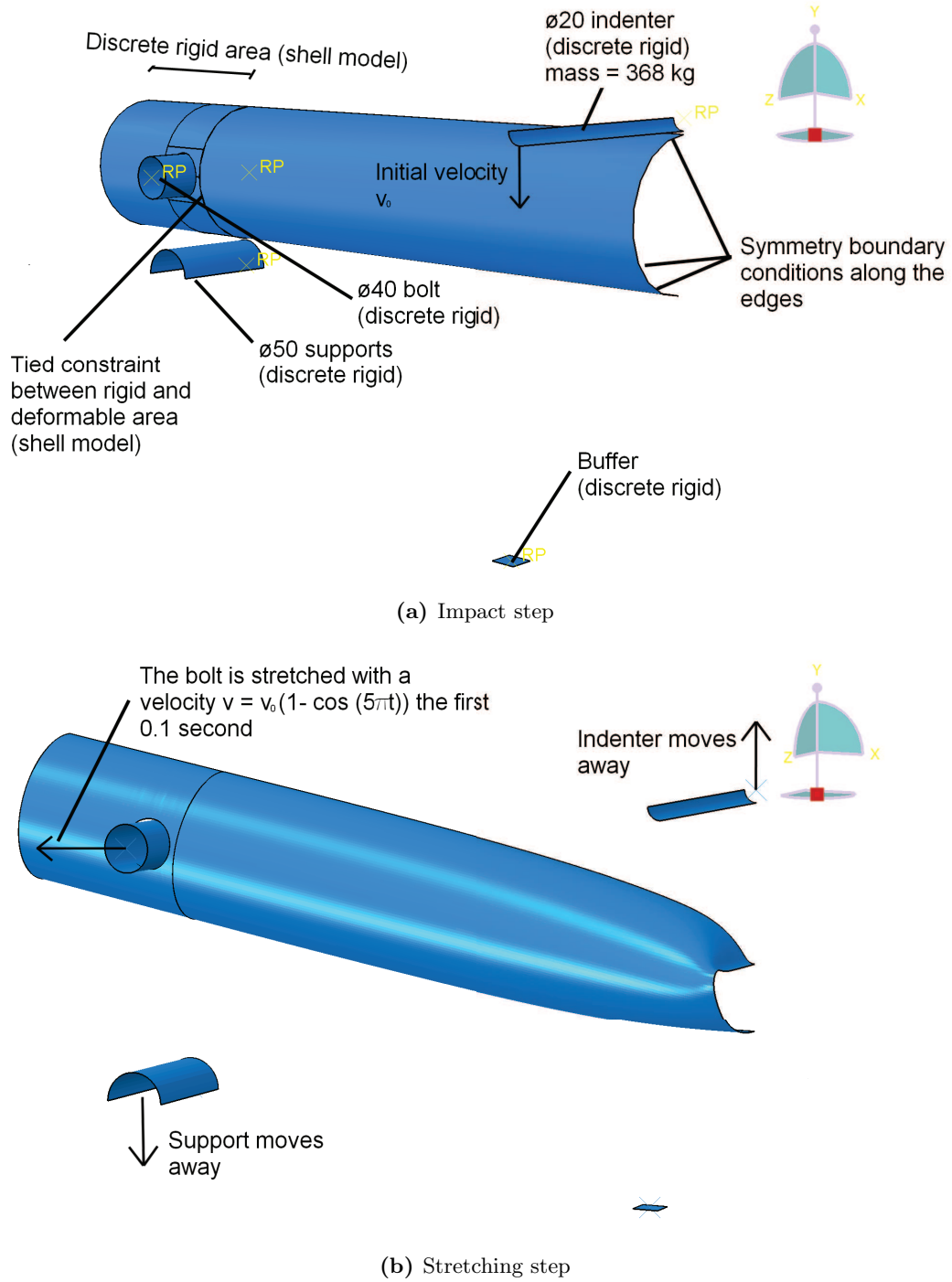


Figure 7.2: Numerical shell model in ABAQUS/Explicit [3].

## 7. FINITE ELEMENT ANALYSES (FEA)

### 7.2.1 Comparing material models

As mentioned earlier, the previous theses found good compliance between experiments and simulations during impact. However, the stretching simulations overestimated the experiments. Therefore, it was of interest to investigate the global response with the material model found by inverse modeling (Section 5.3), and compare this to the response found in previous theses. In addition, a simulation with the material model found by the method of least squares (Section 5.2) was included. The results from the numerical simulations with the shell model are shown in Figure 7.3. It should be noted that the results are somewhat smoothed to better illustrate the trends in the global response. The material models evaluated are summarized in Table 7.3.

**Table 7.3:** Material models evaluated in ABAQUS/Explicit.

Material model	Isotropic hardening								
	$A$ [MPa]	$B$	$n$	$C$		$\dot{\epsilon}_0$ [s <sup>-1</sup> ]			
Slåttedalen & Ørmen	465.5	410.83	0.4793	0.0104		0.000806			
	Combined hardening								
	Isotropic hardening component					Kinematic hardening			
	$\sigma_0$ [MPa]	$Q_1$ [MPa]	$b_1$	$Q_2$ [MPa]	$b_2$	$C_1$ [MPa]	$\gamma_1$	$C_2$ [MPa]	$\gamma_2$
Fornes & Gabrielsen	330.3	703.6	0.47	50.5	34.7	115640.0	916.0	2225.0	22.0
Direct calibration	310.3	35.3	223.2	846.8	0.42	67440.3	425.1	716.3	9.3
Inverse modeling*	299.0	160.0	25.0	400.0	0.25	50401.0	390.7	1279.0	12.8
Fracture criterion	Cockcroft-Latham based Johnson-Cook								
	$D_1$	$D_2$	$D_3$	$D_4$	$D_5$		$\dot{\epsilon}_0$		
	0.7	1.79	1.21	-0.00239	0		0.000806		
Elastic properties & density	$E$ [MPa]			$\nu$			$\rho$ [tonnes/mm <sup>3</sup> ]		
	208000			0.3			7.85 · 10 <sup>-9</sup>		

\*The material parameters from attempt 1 in Table 5.5 are transformed with Equation (5.10).

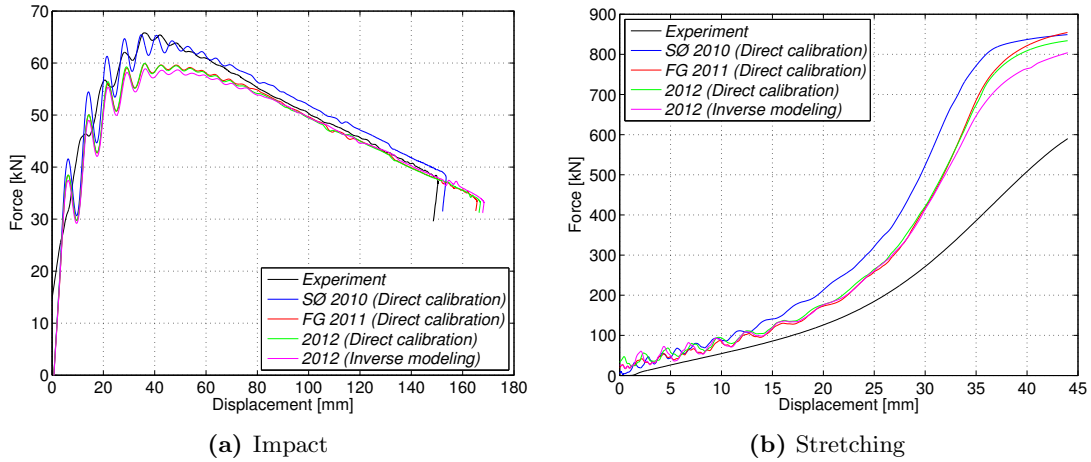


**Figure 7.3:** Comparison material models in ABAQUS/Explicit for pipe A ( $v = 3.24$  m/s). Slåttedalen and Ørmen and Fornes and Gabrielsen are denoted SØ and FG, respectively.

Except for some deviation in the peak load and the final displacement, the force-displacement curves from the impact analyses correspond well with the experiment. For the stretch analyses the curves still deviates significantly from the experimental data. This result indicates that the overly stiff behavior in the stretch step is not only due to the material model. Thus, the material model calibrated by inverse modeling at large strains has a minor effect on the global response.

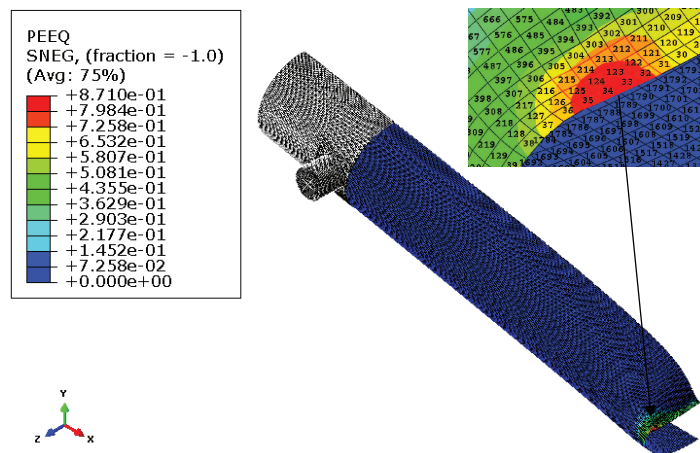
As indicated in Section 2.3 and by Slåttedalen and Ørmen, the global response is highly dependent of the thickness in the pipe. The observations in Section 6.3.5, regarding the reduced thickness in the pipe after impact (Figure 6.16) are therefore of great interest. It should also be noted that the stiffness of the machine used during stretching, is assumed somewhat softer than the rigid connections in the numerical simulations. In addition to the reduced thickness, this may explain the overly stiff behavior in the stretching simulations.

Considering the good compliance between the experiments and simulations in Section 5.4, this observation indicates that the single-parameter assumption regarding the fracture criterion ceases to be valid for the component test. The fracture toughness of the component and notched specimens seem to be different, and it is possible that the two cases fail by different mechanisms. The results in Section 4.3.3 show that the notched specimen fails due to ductile fracture in tension. However, Section 6.3.5 indicates that the pipe may fail due to both ductile shear and cleavage during the impact tests.

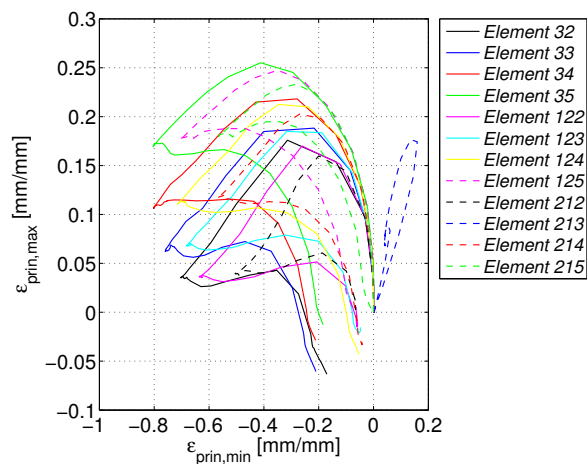
## 7. FINITE ELEMENT ANALYSES (FEA)

### 7.2.2 Critical element in ABAQUS/Explicit

As pointed out by Slåttedalen and Ørmen, a moving plastic hinge during the impact and stretching of the pipe was observed. Therefore, a selection of elements in the critical area was compared in terms of in-plane principal strain. Furthermore, element 35 was determined as the critical element (Figure 7.4b). The results are based on the numerical simulation with the material model found by inverse modeling in Section 5.3.



(a) Selection of elements



(b) In-plane principal strains in integration point

5

**Figure 7.4:** Selection of critical elements at the end of the impact in ABAQUS/Explicit.

It is worth noting that there was excellent compliance between the most exposed area in the experiments and simulations (Figure 6.8b and 7.4a). However, the fracture observed in the experiment was not recreated in the numerical simulations.

The principal stresses and Lode angle parameter are presented in Figure 7.5. The Lode angle parameter in Figure 7.5c was that suggested by Wierzbicki and Xue [24] (Section 2.1.2).

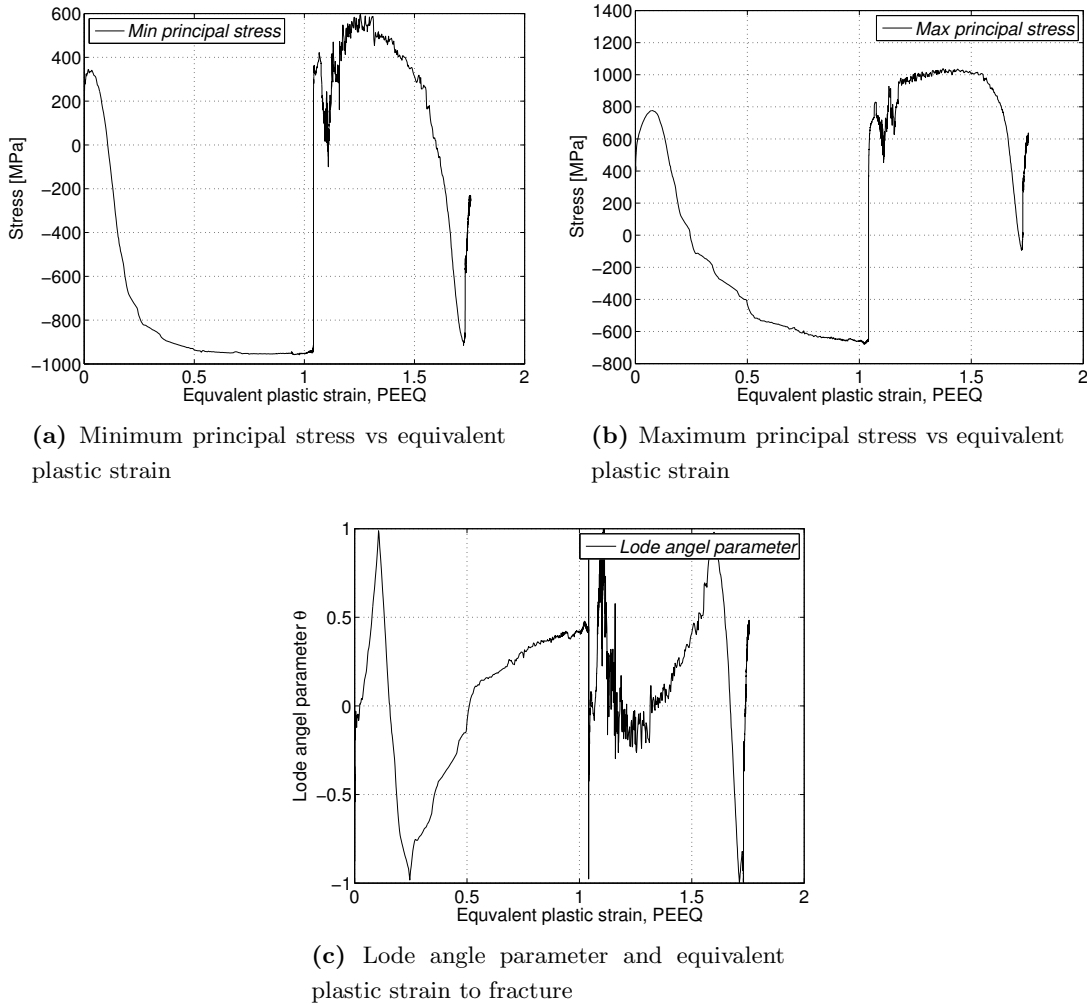


**Figure 7.5:** Results for the critical element in ABAQUS/Explicit (element 35).

It is seen from Figure 7.5 that the critical element was exposed, as expected, to a complex stress history. Therefore, it is not straight forward to determine a single fracture mechanism. This was confirmed by the metallurgical investigation of the pipes in the same area (Section 6.3.5). At the end of the impact it was observed an equivalent plastic strain (*PEEQ* in ABAQUS) of approximately 0.8. The maximum and minimum principal stresses are both positive and negative during the impact. Thus, the critical element experienced both tension and compression during the impact.

## 7. FINITE ELEMENT ANALYSES (FEA)

### 7.3 Numerical simulation in LS-DYNA

A volume element model of pipe *A* was established in LS-DYNA to better describe the triaxial stress state, principal stresses and equivalent plastic strain during the impact and springback. The metallurgical investigation in Section 6.3.5, revealed that incipient fracture occurred before the stretching stage. Therefore, the modeling of this phenomenon was of special interest, and only the impact and springback were modeled. LS-DYNA was the preferred modeling tool due to its springback application [53].

As for the shell model in ABAQUS/Explicit, the analysis was divided into two steps. However, the stretching step was replaced by a springback analysis. The simulation of the impact was solved with a standard explicit dynamic method, and the velocity, geometry and the mass from the experiment were used. The geometry is summarized in Figure 7.6. As in Section 7.2, only one quarter of the pipe was modeled with symmetric boundary conditions at the symmetry edges (Figure 7.7a). The indenter, support and bolt were modeled as discrete rigid. The bolt was included just in case a stretching step would be of interest in later analyses. However, in this thesis the bolt has no function. The indenter was modeled with the same velocity as in the experiments, and the mass was implemented through its material properties and volume, i.e.  $M = 2\pi rL\rho$ . In the latter expression  $r$  and  $L$  are the radius and length of the indenter, i.e. 10 mm and 250 mm, respectively. Thus, the density of the indenter was determined by its scaled mass  $M$  (368 kg) and volume  $V$  (15708 mm<sup>3</sup>). As for the shell model in Section 7.2 the mass of the trolley hitting the pipe was divided by four to adjust the kinetic energy to the symmetric model. Furthermore, the total time period of the impact was modeled similar to the shell model in ABAQUS/Explicit, i.e. 0.18 s.

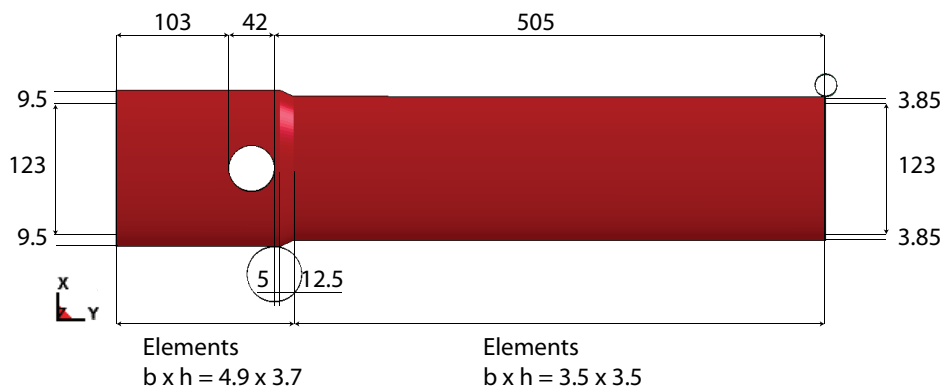


**Figure 7.6:** Dimensions and element size for the volume model in LS-DYNA (mm).

### 7.3 Numerical simulation in LS-DYNA

As shown in Figure 7.6, the thickness of the pipe was based on the optimized model suggested by Slåttedalen and Ørmen, i.e. 3.85 mm. Based on the sensitivity study by Slåttedalen and Ørmen, three elements over the thickness and an element size as shown in Figure 7.6 was considered sufficient. This resulted in a total number of 31440 elements for the pipe. It was used fully integrated eight-node hexahedron solid elements, and the volume integration was performed with the Gaussian quadrature rule. The material was implemented as the combined work-hardening found by inverse modeling and the Cockcroft-Latham fracture criterion. The Cockcroft-Latham parameter from the tension test performed by Slåttedalen and Ørmen was used, i.e.  $W_c = 1595 \text{ Nmm/mm}^3$ . Strain rate dependency was implemented with the material constant  $C$  and reference strain rate  $\dot{\epsilon}_0$  as 0.0104 and  $0.000806 \text{ s}^{-1}$ , respectively. Additional detailed information regarding the material card is found in Appendix C.2.

The contact algorithm in this simulation was the penalty method, and the contact force from the experiment was compared with the contact force between the pipe and the support (Figure 7.7a). As the penalty method was used, it was not that important to distinguish between master and slave nodes. However, the traditional approach that slave nodes can not penetrate the master nodes was used. Therefore, the support was modeled as the master surface and the pipe as the slave surface. The resultant contact force was written as output, and the displacement from the experiment was compared to the nodal displacement of the node below the indenter (Figure 7.7b).

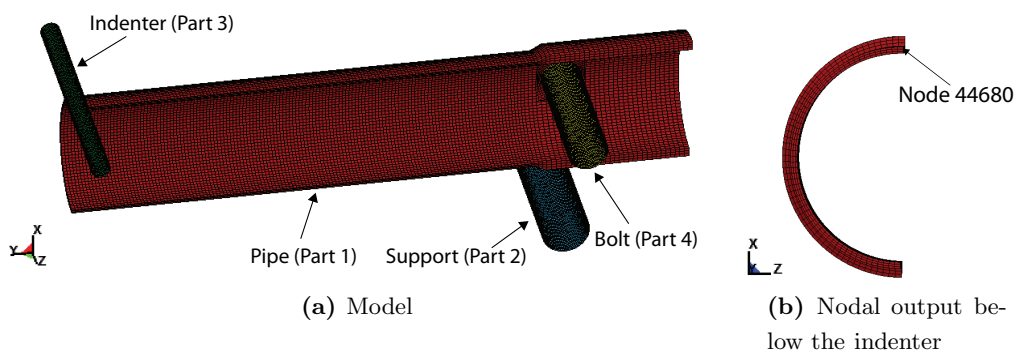


**Figure 7.7:** Numerical model in LS-DYNA.

The result from the explicit impact simulation provided the starting point for the springback simulation. This implies that the accuracy in the impact simulation determines the accuracy of the springback. Springback simulations can be performed by several methods in LS-DYNA. A standard explicit dynamic method may not be used since the objective is to obtain a static springback solution free from dynamic oscillations. If an explicit method should be used a

## 7. FINITE ELEMENT ANALYSES (FEA)

---

possible approach would be the explicit dynamic relaxation method. However, the preferred approach to the modeling of springback was the static implicit method. As shown in Table 7.1, an advantage of the implicit solver compared to explicit integration, is that the number of load or time steps are typically 100 to 10000 times fewer. The main disadvantage is that the cost per step is unknown, since the speed depends mostly on the convergence behavior of the equilibrium iterations which can vary widely from problem to problem. An inaccurate solution will often not converge. The implicit method is stable for nonlinear problems that involve finite strain and arbitrarily large rotations [53].

The solution method for the implicit analysis was set as default, i.e. the equilibrium search was performed using a modified Newton-method. Thus, the stiffness matrix was updated after every 11 iterations. During each time step, the nonlinear solver searched iteratively to find static equilibrium. The static equilibrium was reached when the tolerances had decreased below their respective values *dctol* and *ectol*, where *dctol* is the displacement tolerance and *ectol* is the energy tolerance. The default values of these tolerances were used in the springback simulation, i.e 0.001 and 0.01, respectively. The analysis was performed using 10 implicit steps.

In LS-DYNA, the two most common implicit approaches are the seamless and dynain methods, where the latter was used in this thesis. When using the dynain method, LS-DYNA generates a keyword file named *dynain* at the end of the impact simulation. This file was generated using the keyword *\*INTERFACE\_SPRINGBACK\_LSDYNA*, and contained the deformed mesh, stress and strain state of the pipe. In addition, an optional list of extra nodal constraints was included. These constraints were applied as the dynain file was written. An implicit simulation, computing the springback deformation, was then performed using the dynain file. The dynain file was requested using the keyword *\*INTERFACE\_SPRINGBACK\_DYNA3D* [36].

Extra nodal constraints were included to eliminate rigid body motion in the springback calculation. All static simulations, including implicit springback analyses, require that the rigid body motions are eliminated by defining constraints. These constraints are required since dynamic inertia effects are not included in a static analysis. Without constraints, a tiny applied load would cause the entire pipe to move rigidly an infinite distance without creating any stresses. Mathematically, this means that without any constraints the global stiffness matrix for the pipe is singular. In practice, numerical truncation errors are introduced when rotational degrees of freedom are used to eliminate rigid body motion. The recommended method is therefore to constrain selected translational degrees of freedom at three nodes [53]. However, due to the symmetry in the model, only node 2045 needed to be constrained against

transverse displacement, i.e. the x-direction in Figure 7.8. This constraint eliminated rigid body motion, and the pipe deformed freely without developing any reaction forces at the constrained point.

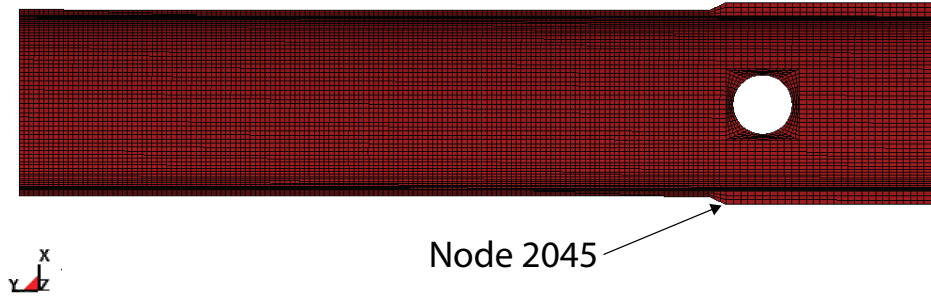


**Figure 7.8:** Springback simulation constrained against rigid body motion at node 2045.

The applied load in the springback simulation resulted from the initial stress in the pipe, which was no longer in equilibrium once the indenter had been removed. Therefore, this load had to be applied slowly over several steps to divide the nonlinear springback response into manageable pieces. Artificial stabilization is the method used in LS-DYNA to distribute springback response over several steps [53]. In this method, springs are artificially introduced to the model which restrict the motion of the pipe. As the solution proceeds the spring stiffnesses are reduced, allowing more springback. When the termination time is reached the springs are completely removed, allowing completely unrestrained springback. It is important to reach the termination time completely, otherwise some artificial stabilization will remain in the model and the results will not be accurate.

To use multiple steps in the springback analysis, the termination time was extended. The termination time in the springback analysis was set to 0.10 s. Based on experience the analysis was performed in four steps [54]. Hence, the initial time step size  $dt_0$  for the implicit analysis was set to 0.025 s.

The initial stiffness of these springs can be scaled using the input parameter *scale*. This parameter must be chosen using some engineering judgement about the flexibility of the object being studied. The parameter was set to a small value 0.0101. This was due to the fact that a small value results in softer springs, allowing more springback in the first few steps of the simulation.

## 7. FINITE ELEMENT ANALYSES (FEA)

### 7.3.1 Global response during impact

To validate the numerical model in LS-DYNA, it was performed a comparison between the simulation and experiment with respect to the global response and deformed configuration. Although the comparison was for the impact, the results from the impact simulation provided the starting point for the springback simulation. Therefore, the accuracy in the impact simulation determines the accuracy in the springback simulation.

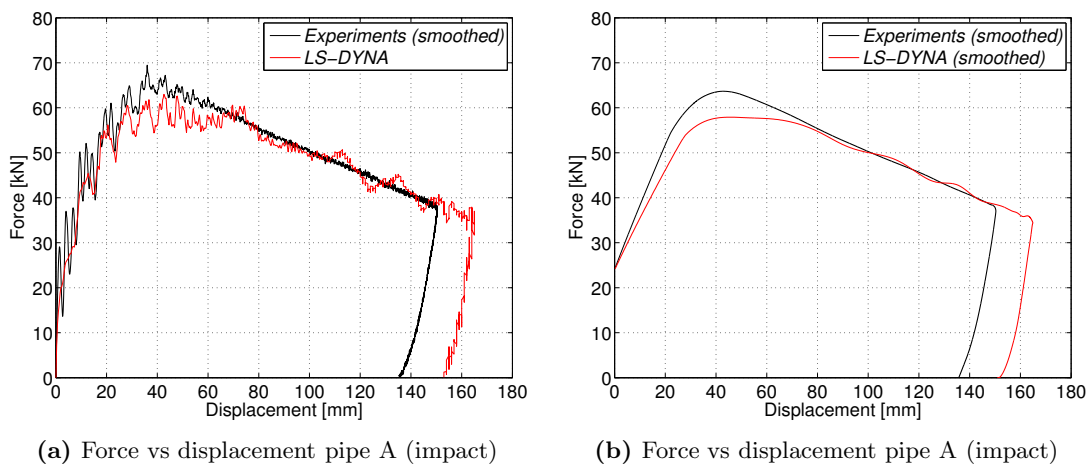


**Figure 7.9:** Validation of the numerical model in LS-DYNA.

Figure 7.9 shows the same trends as in Section 7.2.1, i.e. the material model suggested in this thesis does not recreate the peak load perfectly due to the emphasis on reversed loading (Figure 5.11c). Therefore, the global response during the impact experiment was not perfectly recreated in the simulation, and this will somewhat influence the springback simulation. However, an almost perfect recreation of the impact has been shown by Slåttedalen and Ørmen. Since this thesis focuses on incipient fracture it was of interest to investigate the stress and strain during impact and springback, rather than optimizing the model in LS-DYNA to get a better compliance between simulation and experiment. The impact analysis was therefore considered sufficient to describe the trends in stress and strain.

It is also worth noting how the response is related to the absorption of kinetic energy during the impact (Section 2.2). The overestimation in the final displacement was probably due to the mismatch in terms of the peak load. This is illustrated in Figure 7.9b by large smoothing of the response curves. Figure 7.9b indicates that the energy lost due to the reduction in peak load, is roughly the same as the energy "won" due to the increased final displacement. Hence, the same amount of kinetic energy was absorbed in the experiments and simulation.

### 7.3 Numerical simulation in LS-DYNA

---

The comparison in terms of the deformed configuration is shown in Figure 7.10. This shows very good compliance between the experiment and simulation regarding the deformed shape of the pipe. Hence, the numerical model in LS-DYNA was considered as a good basis for the evaluation of stresses and strains in the fractured area of the pipe.

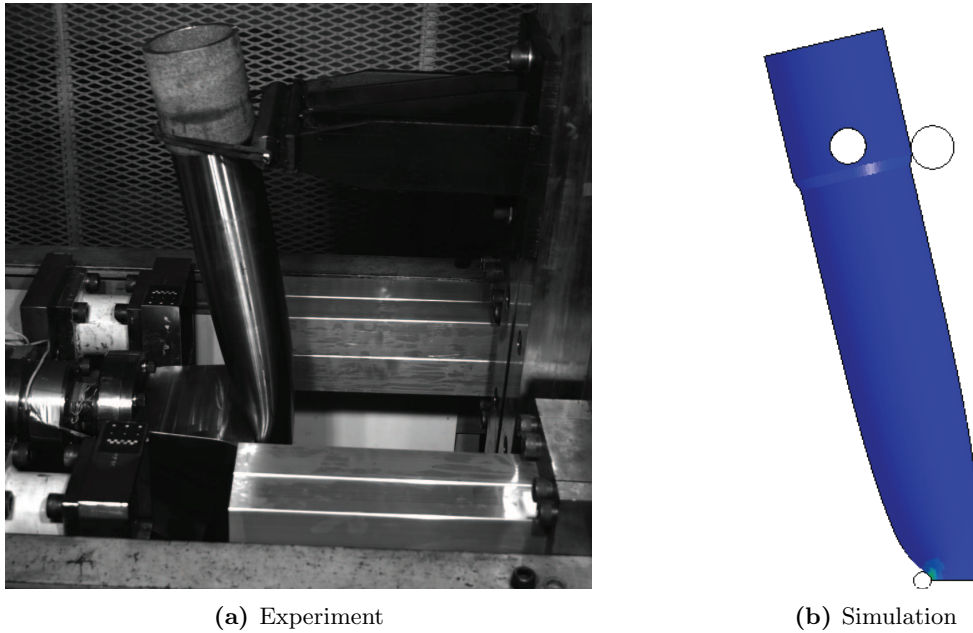


**Figure 7.10:** Comparison between the simulation and the experiment in terms of the deformed configuration for pipe A (impact).

## 7. FINITE ELEMENT ANALYSES (FEA)

### 7.3.2 Critical element in LS-DYNA

As in Section 7.2.2, the region of incipient fracture in the experiments (Figure 6.8b) was of special interest in the numerical simulation. The results with respect to equivalent plastic strain, revealed that the critical element was element 20799 in Figure 7.11.

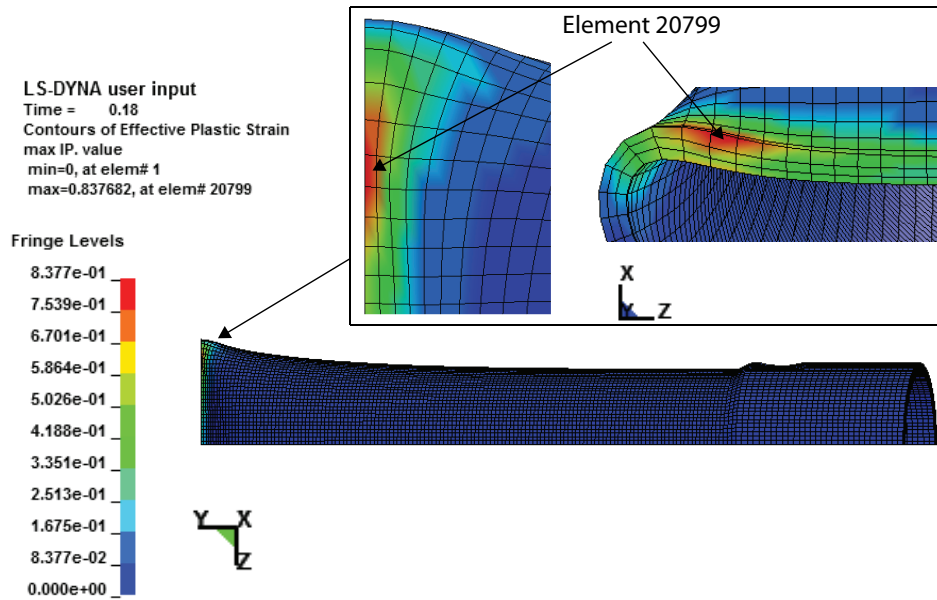


**Figure 7.11:** Critical element with respect to equivalent plastic strain in LS-DYNA ( $t = 0.18$  s).

When investigating the stress state in the critical element, it was convenient to define three subsequent phases in the numerical simulation, i.e. impact, rebound and springback. The impact phase was defined as the time interval involving contact between the indenter and pipe. This phase was followed by the rebound phase, i.e. the phase driven by the built up internal axial stresses. Thus, the rebound could be characterized as the initial redistribution of stresses to obtain equilibrium after maximum deflection. Finally, the springback was defined as the static phase free from oscillations. The respective time intervals in the simulation for these phases are summarized in Table 7.4.

**Table 7.4:** Phases during the numerical simulation in LS-DYNA.

Impact		Rebound		Springback	
Start [s]	End [s]	Start [s]	End [s]	Start [s]	End [s]
0	~0.11	~0.11	0.18	0.18	0.28

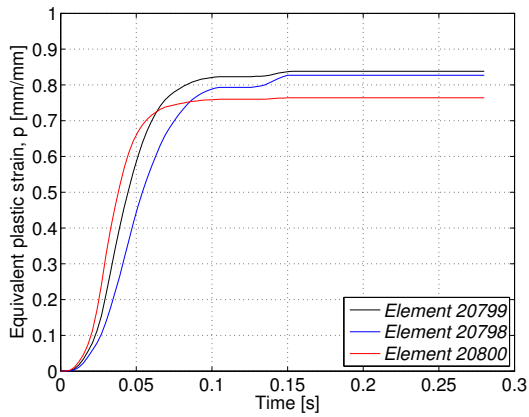
Figure 7.11 illustrates that the element undergoing the most severe strain history was located in the area where fracture occurred in the experiments (Figure 6.8b). It was also interesting to note the similarity between the contour plot in Figure 7.11 and the crack observed in Figure 6.16. Both observations indicate that the crack initiates at the surface and propagates through the thickness of the pipe.

To examine the stress situation in the critical element during the respective phases in Table 7.4, the principal stresses and triaxiality ratio from the numerical simulation were plotted in Figure 7.12. In addition, the Lode parameter and equivalent plastic strain in the neighboring elements were included. To relate these values to the phases in Table 7.4, all the values were plotted against time. This made it easier to examine where the incipient fracture may occur.

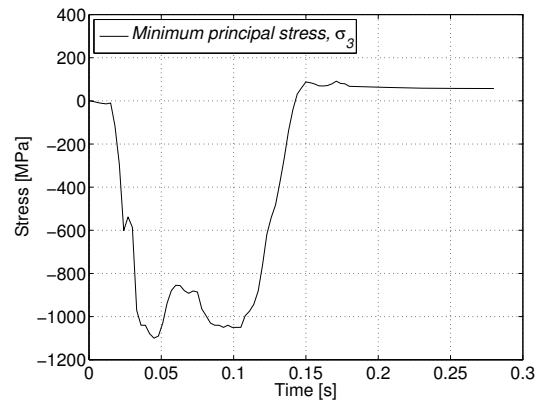
As expected, Figure 7.12 revealed that the critical element was exposed to a complex stress state. The discovered triaxiality during the rebound phase was of special interest (Figure 7.12e). This indicated that hydrostatic tension occurred during the rebound, and that incipient fracture could occur during this phase. It is also worth noting the static nature of the springback, and that the redistribution of stresses was mainly present during the rebound phase (Figure 7.12b-7.12d). Hence, the springback simulation could be neglected in further studies.

To highlight the complex stress state, the Lode parameter  $\mu_\sigma$  was plotted against stress triaxiality. The Lode parameter may be used to indicate which stress states the critical element undergoes. With reference to Section 2.1.2, Figure 7.12f indicates that the critical elements undergo various subsequent stress states during the impact simulation.

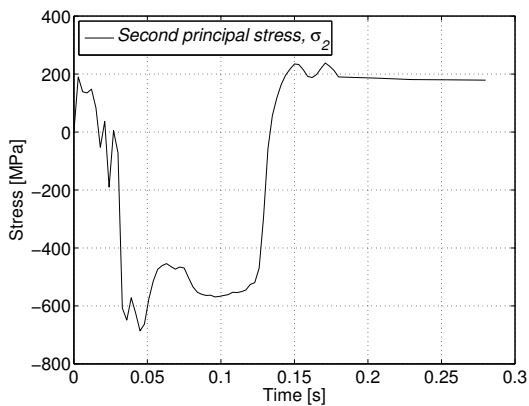
## 7. FINITE ELEMENT ANALYSES (FEA)



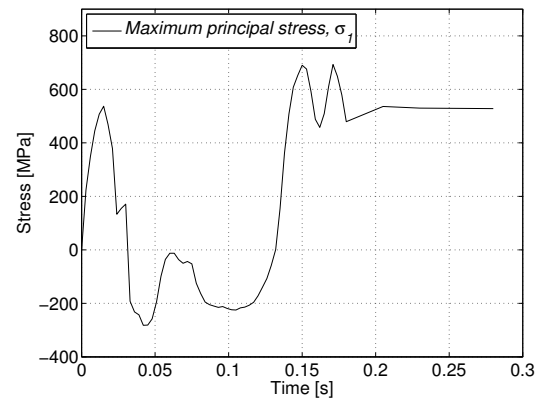
(a) Equivalent plastic strain  $p$  vs time  $t$



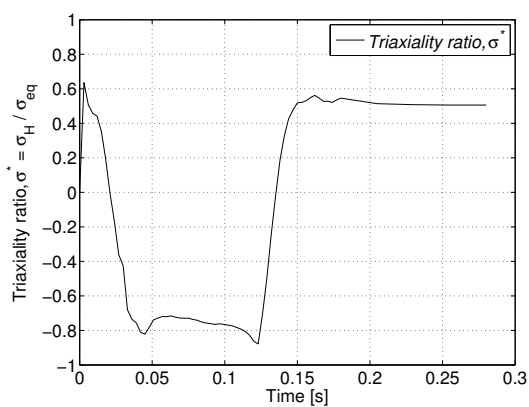
(b) Minimum principal stress  $\sigma_3$  vs time  $t$



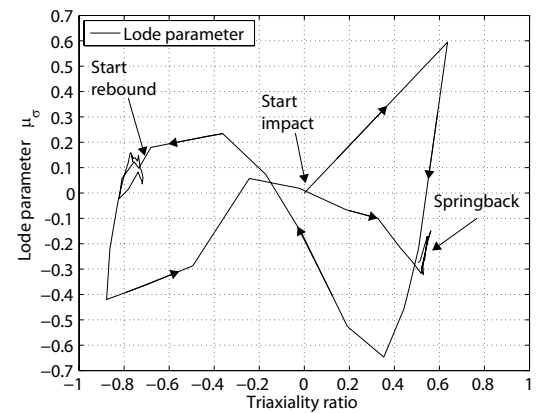
(c) Second principal stress  $\sigma_2$  vs time  $t$



(d) Maximum principal stress  $\sigma_1$  vs time  $t$



(e) Triaxiality ratio  $\sigma^*$  vs time  $t$



(f) Lode parameter  $\mu_\sigma$  vs triaxiality ratio  $\sigma^*$

**Figure 7.12:** Results from critical element in LS-DYNA (Element 20799).

## 8 Discussion

Figure 8.1 shows the comparison for pipe *A* in terms of global response for the experiment and numerical simulations. As seen in Figure 8.1a, the experiment and numerical simulations comply well for the impact. However, Figure 8.1b indicates that the work-hardening models considered results in a overly stiff behavior during stretching. Hence, the work-hardening model presented in the present thesis has a minor influence on the global response similar to that of previous theses. This result indicated that the overly stiff behavior in the stretch step was not only due to the work-hardening in the material.

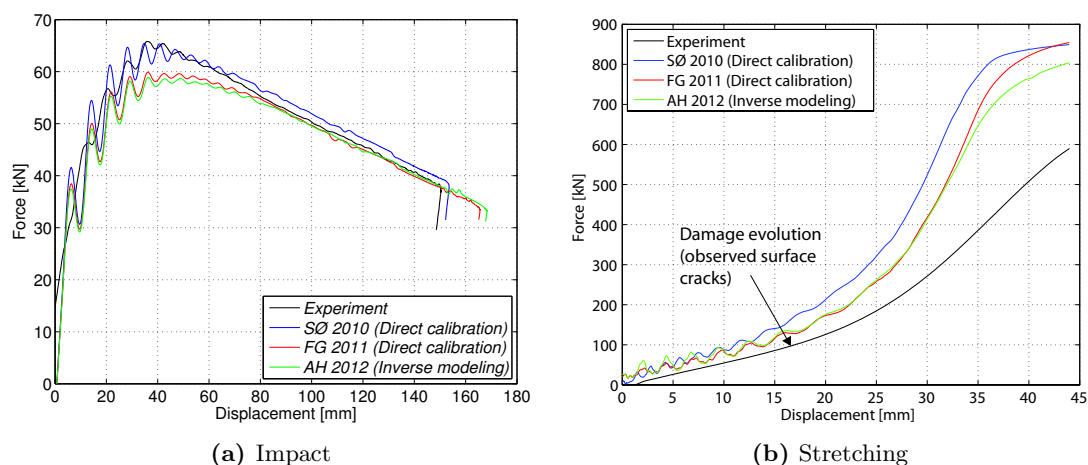


**Figure 8.1:** Global response with various material models. Numerical simulations in ABAQUS/Explicit of pipe A ( $v = 3.24$  m/s).

The metallurgical investigation in Section 6.3.5 revealed incipient fracture and internal damage already after the impact tests. In the most extreme case, the crack went 75 % through the thickness of the impacted region. The fracture criteria considered were not able to account for such incident. Therefore, the simulations failed to predict the fracture accurately. It should also be noted that the stiffness of the machine used during stretching, is assumed somewhat softer than the rigid connections in the numerical simulations. In addition to the

## 8. DISCUSSION

---

reduced thickness, this may explain the overestimated load level in the simulations (Figure 8.1b).

Based on the good compliance between the material tests and simulations in Section 5.4, this indicates that the single-parameter assumption regarding the fracture criterion used in this thesis ceases to be valid for the component test. The fracture toughness of the component and notched specimens seem to be different, and the two cases fail by different mechanisms. The results in Section 4.3.3 show that the notched specimen fails due to ductile fracture in tension. Furthermore, Section 6.3.5 indicates that the pipes exposed to both impact and stretching may fail due to both ductile shear and cleavage.

The ductile shear fracture is assumed to evolve after damage initiation, i.e. during stretching. Observations at the crack-tip in Figure 6.11 indicates that the fracture may be initiated due to cleavage. Cracked particles were discovered which was of great interest with reference to Section 2.6.2. A Cracked particle is assumed to act as a microcrack. Hence, if the stress concentration between the matrix and the particle is sufficient, the microcrack propagates into the matrix causing failure by cleavage.

The metallurgical investigation of the compressed material tests in Section 4.3.3 showed no signs of oval voids around particles (Figure 4.20), i.e. possible stress or strain concentrations. However, these tests were unable to highlight the particle behavior satisfyingly. Hence, such oval voids could exist even if they were not discovered. Therefore, the stress concentration was illustrated with ABAQUS/Explicit as a plane strain shell model with symmetric boundary conditions. The surrounding matrix consisted of the material model calibrated by inverse modeling (Section 5.3), and the particle was assumed to have significantly higher fracture toughness than the surrounding matrix. Therefore, the particle was modeled with elastic material and five times the stiffness of the surrounding matrix. The boundary between the particle and matrix was modelled with the penalty method and a friction coefficient of 0.2. The results in compression and incipient tension are shown in Figure 8.2.

As can be seen from Figure 8.2, large deformations in compression could cause an oval void and a localized stress concentration at the boundary between the matrix and particle. The particle is assumed to crack during compression or load reversal. The latter could occur due to stress concentration and plastic strain in the surrounding matrix accumulated during loading in compression (Figure 8.2b). This acts like a residual stress when the loading is reversed (Figure 8.2d), and could lead to a cracked particle. In addition, the adhesive strength in the interfacial bonds between the particle and matrix may contribute to the initiation of damage in the particle at load reversal.

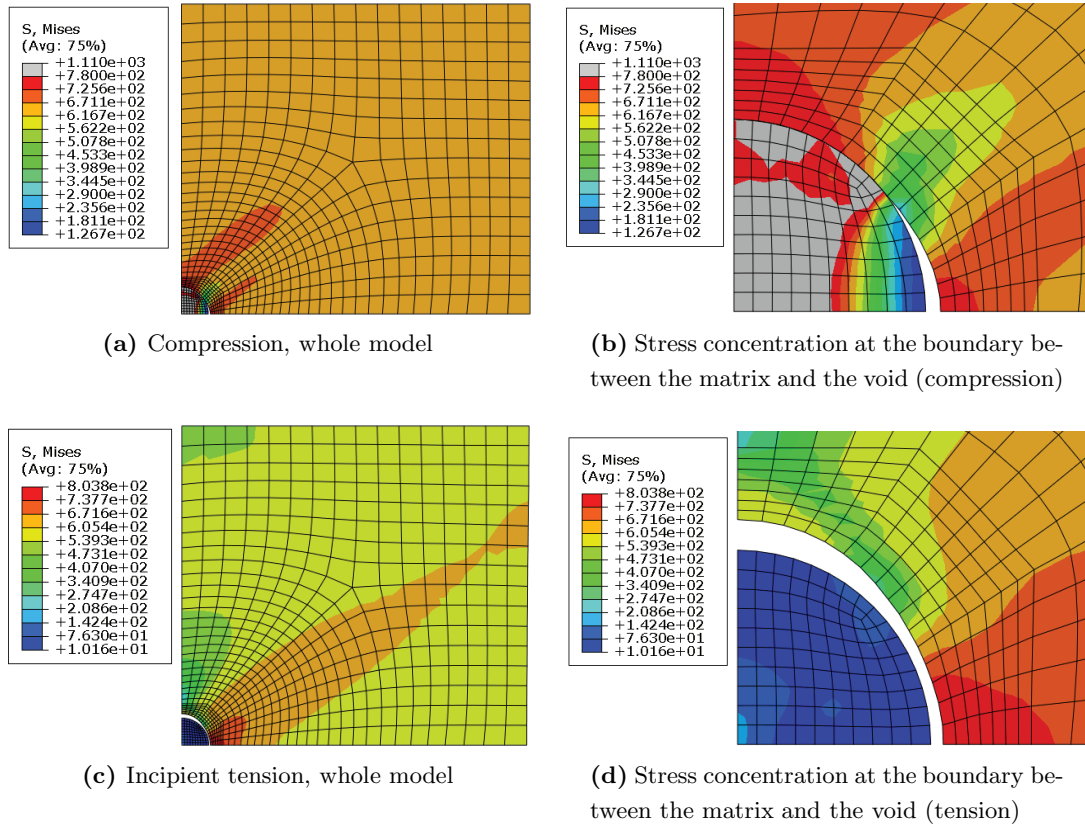


**Figure 8.2:** Microstructural analysis in ABAQUS/Explicit.

As pointed out by Anderson [41], the larger particles are most exposed since they are more likely to contain small defects. Such cracked particles were observed both at the crack-tip for the stretched pipes (Figure 6.11b) and in the pre-compressed tension tests (Figure 4.19).

It should also be emphasized that large nonmetallic inclusions, such as oxides and sulfides found in the X65 steel (Section 4.1), may be damaged during fabrication [41]. Thus, some of these particles could be cracked or debanded prior to plastic deformation.

As pointed out in Section 2.6, the initiation of fracture is driven by hydrostatic stress in tension which is related to the triaxial stress state through Equation (2.60). The observation regarding the triaxiality ratio in the numerical simulation in LS-DYNA (Figure 7.12e) is therefore interesting. The areas of interest are highlighted in Figure 8.3.

As seen in Figure 8.3, the fracture could be initiated both during the impact, rebound and springback phase. However, due to the sufficient compliance between simulation and experiment during the impact step (Figure 7.9), incipient fracture is assumed to initiate at the second appearance of hydrostatic tension (2 in Figure 8.3), i.e. during the rebound or spring-

## 8. DISCUSSION

---

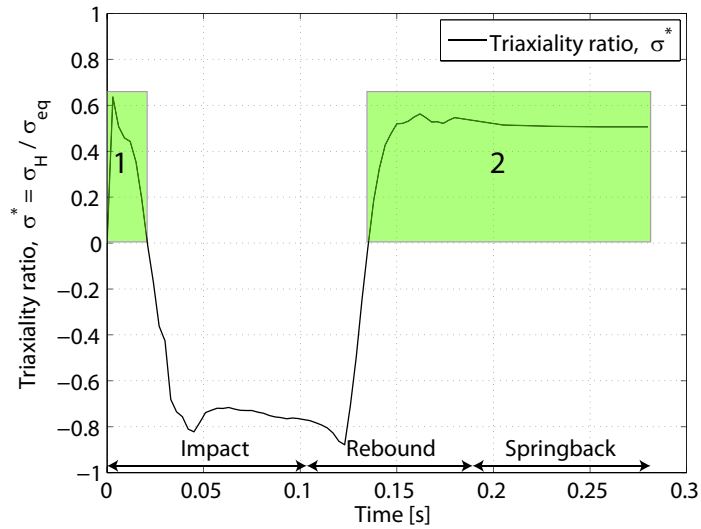
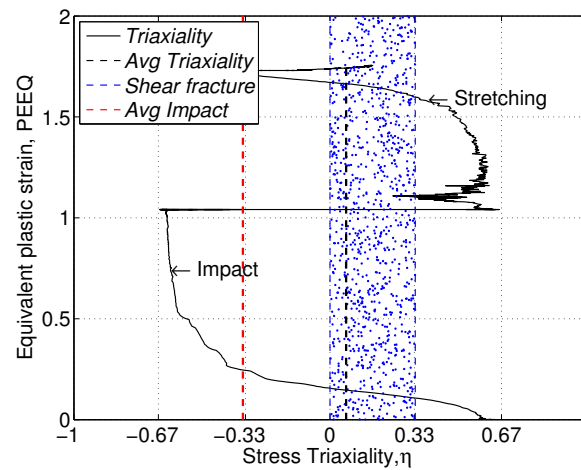


**Figure 8.3:** Areas of interest in terms of triaxiality ratio.

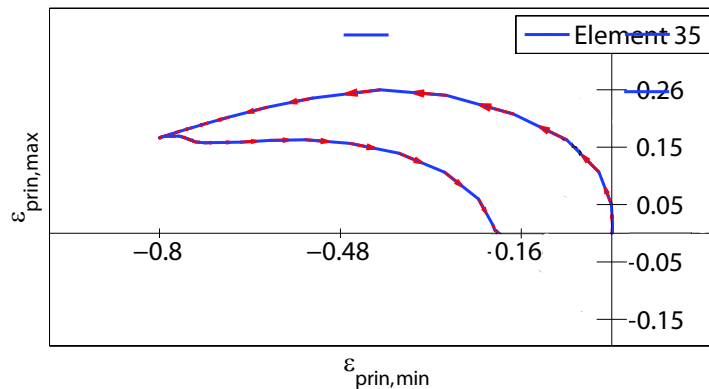
back phase. This was supported by observations in Figure 7.9, which showed no significant drop in the force-displacement curve, neither in experiment nor simulation. Furthermore, Figure 8.3 shows that the main redistribution of stresses occur during the rebound. Hence, incipient fracture may be assumed initiated during this phase.

In the present thesis two uncoupled fracture criteria were used (Section 2.7). Hence, the damage is defined by an external variable which is uncoupled from plasticity internal variables. The Cockcroft-Latham based Johnson-Cook criterion showed good compliance between the material tests and simulations. However, no fracture occurred in the numerical simulations of the pipe with neither of these criteria. To numerically describe the phenomenon in Figure 8.2, a fracture criterion considering the evolution of voids and internal damage evolution may be considered. The observations in Section 6.3.5 should be emphasized to model the stiffness degradation due to the observed crack (Figure 6.16b). Although cleavage is often characterized as a brittle fracture, it can be preceded by large-scale plasticity and ductile crack growth. Therefore, a coupling of the damage variable and plastic internal variables, by describing the void growth and their interactions in a phenomenological way (e.g. Xue [55]), may be a better approach for the modeling of fracture. The advantage of the coupled approach is that the softening effect of damage is accounted for in the formulation. Damage softening may be important to capture strain localization prior to fracture. Therefore, the coupled approach is assumed to be more accurate than the uncoupled one. However, the identification of parameters for coupled damage models are more complex.

Although the incipient fracture is assumed due to cleavage, it is worth noting the observation regarding the critical element in ABAQUS/Explicit (Figure 8.4). The principal strains indicates that shear fracture may be of interest. To simulate shear fracture the Modified Mohr-Coulomb (MMC) fracture criterion suggested by Li et al. [25], assuming plane stress, may be used (Section 2.1.2). Therefore, to highlight the relevance of this criterion, the stress triaxiality and in-plane principal strains for the shell model based on inverse modeling are shown in Figure 8.4.



(a) Triaxiality ratio and equivalent plastic strain to fracture



(b) In-plane principal strains

**Figure 8.4:** Critical element in ABAQUS/Explicit (element 35 in the shell model).

## 8. DISCUSSION

---

The shaded area in Figure 8.4a represents the range where shear fracture could occur. The black and red dotted lines are the average triaxiality ratio for both impact and stretching and impact only, respectively. This implies that there is a possibility for shear fracture during the impact step.

The unexpected behavior during compression in the numerical simulations based on the combined work-hardening (Section 5.1 and 5.4), found by the method of least squares, motivated new uniaxial tension tests. The same geometry and experimental set-up as suggested by Slåttdalen and Ørmen were used [3]. Specimens were taken at four different locations in the cross-section (Figure 8.5a). The objective of the experiments was to compare the material properties for the X65 steel with that of previous theses. The results are presented in Figure 8.5b.

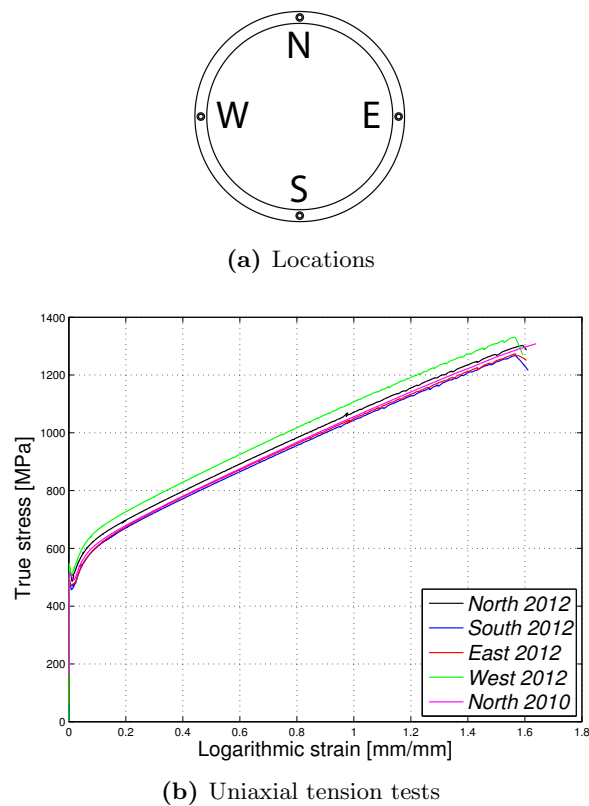


**Figure 8.5:** New smooth uniaxial tension tests.

The minor scatter observed in Figure 8.5b, indicates that the material used in this thesis has the same properties as the previous theses. Hence, the Cockcroft-Latham parameter based on the uniaxial tension test by Slåttdalen and Ørmen (North 2010 in Figure 8.5b) is assumed representative. Thus, the observed deviations in Figure 5.2 and 5.11 can not be explained

---

based on these results. This observation was not given any further interest due to the good results from the inverse modeling. The results from the direct calibration was only used for comparison, and not in the investigation of the critical element.

Previous theses have highlighted the need for a method to calculate the residual strength in pipelines exposed to accidental loads. The observations in Section 6.3.5 may contribute to the understanding of the damage evolution. The incipient fracture in the pipes can be investigated experimentally by conducting additional impact tests at different velocities. The deformed pipes could be investigated metallurgically to describe the crack growth. This could be used in a procedure to determine the residual strength in the pipelines.

It should be noted that the damage does not necessarily accumulate linearly with equivalent plastic strain. In fact from a micromechanical point of view the void formation and evolution are followed by a gradually void coalescence, which could be described as nonlinear damage accumulation. Previous research has showed experimentally that damage accumulates in a nonlinear way [19].

## 8. DISCUSSION

---

## 9 Conclusion

This thesis suggests that incipient fracture occurs during rebound due to cracked particles. This will reduce the residual strength of the pipe, and cracks will propagate through the thickness earlier than expected during stretching. The fracture is assumed initiated by cleavage and to evolve as ductile shear during stretching.

Pre-compressed tension tests at large compressive plastic strains (up to 40%) were conducted. The tests revealed a distinct Bauschinger effect, transient and permanent softening, as well as work-hardening stagnation during reversed loading. Based on these tests, a material model with combined work-hardening were calibrated by inverse modeling using the optimization tool LS-OPT. The material model gave good compliance between the numerical simulations and the pre-compressed tension tests. However, numerical simulations of the pipe in ABAQUS/Explicit, consisting of impact and stretching, yield little improvement compared to previous theses.

Impact tests were conducted to carry out metallurgical investigation of the impacted regions in the pipes. Fracture and internal damage were observed already after impact. In the most extreme case, a crack through 75 % of the thickness was discovered. It is clear that this decreases the strength of the pipes.

To investigate the stress-strain state during the impact test, a volume element model of the impact and springback was established in LS-DYNA. The numerical simulation recreated the component test sufficiently. Therefore, the model was used to examine the stress-strain state in the critical element. Investigations revealed a complex stress history, which was also supported by observations of the internal damage during the metallurgical investigation of the pipes. The numerical simulation gave excellent compliance with the experiments regarding the location of the most exposed region. Incipient fracture is assumed to appear due to hydrostatic tension during the rebound phase of the impact. Together with the assumed soft behavior in the testing machine compared to the FE model, this may explain the overestimated load level during stretching in ABAQUS/Explicit.

## 9. CONCLUSION

---

The fracture criteria based on the uniaxial tension test are not able to describe incipient fracture in the pipe. This indicates that the single-parameter assumption regarding the fracture criterion used in this thesis ceases to be valid for the component test. To recreate the fracture in the impacted pipes an additional formulation must be included.

The uniaxial tension tests conducted at the end of this thesis showed no significant difference in the material properties compared to previous theses.

## 10 Further work

Although this thesis has shown that the combined work-hardening has little influence on the global response, it still remains to calibrate a material model based on the strain range of application, i.e. approximately 80 %. Therefore, more pre-compressed tension tests at the strain range experienced during the impact should be conducted. These tests should also be used to investigate the evolution of ductility to verify the observed trends in this thesis. To avoid localization of necking in the threaded area of the specimen, a machining of the specimens before stretching is necessary. Alternatively the pre-compression could be conducted in successively compression stages with corresponding machining to avoid geometrical instabilities.

Inverse modeling in terms of multiple cases may be used as an alternative approach for the calibration of strains up to 80 %. Such a calibration can be performed with LS-OPT based on the uniaxial tension tests and pre-compressed tension tests performed in this thesis.

Based on the experience from test series 2, it should be performed new experiments in compression. However, to get a better understanding of the damage evolution at compressive strains, the loading should be reversed and the specimen somewhat stretched. This could ease the study of the microstructure and give better insight in the material behavior at large strains.

Since incipient fracture is assumed during the rebound, the elastic nature of the rebound and the transient Bauschinger effect should be given further interest. Thus, the observations regarding the decrease in Young's modulus and work-hardening stagnation should be included in the constitutive relation. To recreate the observed fracture in the impacted pipes an additional formulation must be included.

The overestimation of load level in the numerical simulations, motivates the need to measure the machine stiffness used in the stretching of the pipes. This stiffness should be included in the FE model.

## 10. FURTHER WORK

---

Finally, a method to calculate the residual strength in pipelines exposed to accidental loads should be suggested. This could be done by further investigation of the relation between the velocity of the indenter, dent size and crack growth.

## References

- [1] Petroleumstilsynet. Presentasjon sikkerhetsforum 29.11.2007 alvorlige hendelser. [http://www.ptil.no/getfile.php/Tilsyn%20p%25C3%25A5%20nettet/vrige/5\\_07\\_siforum\\_alvorlige\\_hendelser.pdf](http://www.ptil.no/getfile.php/Tilsyn%20p%25C3%25A5%20nettet/vrige/5_07_siforum_alvorlige_hendelser.pdf), Cited date:[13 May 2012].
- [2] Statoil. Annual Report 2008. [http://www.statoil.com/AnnualReport2008/no/CountrySpotlight/Norway/Pages/3-1-7-1\\_OperationsNorthSea.aspx](http://www.statoil.com/AnnualReport2008/no/CountrySpotlight/Norway/Pages/3-1-7-1_OperationsNorthSea.aspx), Cited Date:[13 May 2012].
- [3] K. Slåttedalen and A. Ørmen. Impact Against Offshore Pipelines. *MSc Thesis, Structural Impact Laboratory, Departement of Structural Engineering, Norwegian University of Science and Technology*, 2010.
- [4] J. Fornes and S. Gabrielsen. Impact Against Offshore Pipelines. *MSc Thesis, Structural Impact Laboratory, Departement of Structural Engineering, Norwegian University of Science and Technology*, 2011.
- [5] P. W. Bridgman. Effects of High Hydrostatic Pressure on the Plastic Properties of Metals. *Reviews of Modern Physics*, 17(1):3–14, 1945.
- [6] P. O. Bouchard, L. Bourgeon, H. Lachapèle, E. Maire, C. Verdu, R. Forestier, and R. E. Logé. On the influence of particle distribution and reverse loading on damage mechanisms of ductile steels. *Materials Science and Engineering: A*, 496(1-2):223–233, November 2008.
- [7] B. Peeters, M. Seefeldt, C. Teodosiu, and S. R. Kalidindi. Work-Hardening/Softening Behaviour of B.C.C. Polycrystals During Changing Strain Paths : Part I. *Acta Materialia*, 49:1607–1619, 2001.
- [8] F. Yoshida, T. Uemori, and K. Fujiwara. Elastic-plastic behavior of steel sheets under in-plane cyclic tension-compression at large strain. *International Journal of Plasticity*, 18:633–659, 2002.

## REFERENCES

---

- [9] T. Uemori, T. Okada, and F. Yoshida. Simulation of Springback in V-bending Process by Elastoplastic Finite Element Method with Consideration of Bauschinger Effect. *Metals and Materials*, 4(3):311–314, 1998.
- [10] T. Uemori, T. Okada, and F. Yoshida. FE Analysis of Springback in Hat-bending with Consideration of Initial Anisotropy and the Bauschinger Effect. *Key Engineering Materials*, 177-180:497–502, 2000.
- [11] J. L. Chaboche and G. Rousselier. On the Plastic and Viscoplastic Constitutive Equations, part I and II. *ASME Journal of Pressure Vessel Technology*, 105:153–164, 1983.
- [12] K. Yamaguchi, H. Adachi, and N. Takakura. Effects of Plastic Strain and Strain Path on Young’s Modulus of Sheet Metals. 4(3):420–425, 1998.
- [13] F. Yoshida and T. Uemori. A model of Large-strain Cyclic Plasticity Describing the Bauschinger Effect and Work-hardening Stagnation. *International Journal of Plasticity*, 18:661–686, 2002.
- [14] N. Christodoulou, T. Woo, and S. R. Macewen. Effect of Stress Reversals on the Work Hardening Behaviour of Polycrystalline Copper. *Acta Metall.*, 34(8):1553–1562, 1986.
- [15] J.L. Chaboche, K. Dang Van, and G. Cordier. Modelization of the Strain Memory Effect on the Cyclic Hardening of 316 Stainless Steel. *Transaction of the 5th International Conference on Structural Mechanics in Reactor Technology*, Volume L(L11/3), 1979.
- [16] J. Lubliner. *Plasticity Theory. Dover Books on Engineering*, 2008.
- [17] Y. Bai and T. Wierzbicki. A New Model of Metal Plasticity and Fracture with Pressure and Lode Dependence. *International Journal of Plasticity*, 24(6):1071–1096, June 2008.
- [18] K. S. Zhang, J. B. Bai, and D. Francois. Numerical Analysis of the Influence of the Lode Parameter on Void Growth. *International Journal of Solids and Structures*, 38:5847–5856, 2001.
- [19] M. Basaran, S. D. Wölkerling, M. Feucht, and D. Weichert. An Extension of the GISSMO Damage Model Based on Lode Angle Dependence. *LS-DYNA Anwenderforum, Bamberg*, 2010.
- [20] J. W. Hancock and A. C. Mackenzie. On the Mechanics of Ductile Failure in High-Strength Steels Subjected to Multi-axial Stress-states. *Journal of the Mechanics and Physics of Solids*, 24, 1976.

## REFERENCES

---

- [21] G. R. Johnson and W. H. Cook. Fracture Characteristics of Three Metals Subjected to Various Strains, Strain Rates, Temperatures and Pressures. *Engineering Fracture Mechanics*, 21(I):31–48, 1985.
- [22] W. Lode. Versuche über den Einfluss der mittleren Hauptspannung auf das Fließen der Metalle Eisen Kupfer und Nickel. *Zeitung Phys*, 36:913–939, 1926.
- [23] O. S. Hopperstad. Some Basic Relations in Plasticity Theory & Representation of Stress in Haigh-Westergaard Space. *Work in progress, Structural Impact Laboratory, Department of Structural Engineering, Norwegian University of Science and Technology*, 2012.
- [24] T. Wierzbicki and L. Xue. On the Effect of the Third Invariant of the Stress Deviator on Ductile Fracture. *Technical report, Impact and Crashworthiness Laboratory, Massachusetts Institute of Technology, Cambridge, MA*, 2005.
- [25] Y. Li, M. Luo, J. Gerlach, and T. Wierzbicki. Prediction of Shear-Induced Fracture in Sheet Metal Forming. *Journal of Materials Processing Technology*, 210(14):1858–1869, November 2010.
- [26] K. M. Mathisen. Lecture Notes TKT4197 Nonlinear Finite Element Analysis. *Department of Structural Engineering, Norwegian University of Science and Technology*, 2011.
- [27] M. Langseth and A. G. Hanssen. Lecture Notes on Crashworthiness of Aluminium Structures. *Department of Structural Engineering, Norwegian University of Science and Technology*, 2002.
- [28] S. G. Thomas, S. R. Reid, and W. Johnson. Large Deformations of Thin-Walled Circular Tubes Under Transverse Loading - I. *International Journal of Mechanical Science*, 18:325–333, 1976.
- [29] A. R. Watson, S. R. Reid, W. Johnson, and S. G. Thomas. Large Deformations of Thin-Walled Circular Tubes Under Transverse Loading - II. *International Journal of Mechanical Science*, 18:501–509, 1976.
- [30] S. R. Reid, W. Johnson, and A. R. Watson. Large Deformations of Thin-Walled Circular Tubes Under Transverse Loading - III. *International Journal of Mechanical Science*, 18:387–397, 1976.
- [31] T. H. Søreide. Ultimate Load Analysis of Marine Structures. *Tapir Akademisk Forlag*, 1981.

## REFERENCES

---

- [32] F. Xuan, P. Li, and S. Tu. Plastic Limit Load of Welded Piping Branch Junctions Under Internal Pressure. *Nuclear Engineering and Design*, 224(1):1–9, 2003.
- [33] O. S. Hopperstad and T. Børvik. Lecture notes TKT4135 Mechanics of Materials. *Department of Structural Engineering, Norwegian University of Science and Technology*, 2012.
- [34] T. Børvik. Lecture note TKT4135: The Tension Test. *Department of Structural Engineering, Norwegian University of Science and Technology*, 2012.
- [35] SIMULIA. Abaqus Analysis User’s Manual. 6.10 and 6.11 edition, 2010/2011.
- [36] Dr. B. Gladman. LS-DYNA Keyword User’s Manual. *Livermore Software Technology Corporation (LSTC)*, Version 971, 2007.
- [37] J. L. Chaboche and J. Lemaitre. Mechanics of Solid Materials. *Cambridge University Press*, pages 161–252, 1990.
- [38] S. Dey. High - Strength Steel Plates Subjected to Projectile Impact. *PhD Thesis, Structural Impact Laboratory, Department of Structural Engineering, Norwegian University of Science and Technology*, 2004.
- [39] G. E. Dieter. Bend, and Shear Testing Mechanical Behavior Under Tensile and Compressive Loads. *ASM Handbook: Mechanical Testing and Evaluation*, 8:99–108, 2000.
- [40] G. E. Dieter. Mechanical Metallurgy. *McGraw-Hill Book Company*, 1988.
- [41] T. L. Anderson. Fracture Mechanics - Fundamentals and Applications. *Taylor and Francis Group, third edition*, 2005.
- [42] M. G. Cockcroft and D. J. Latham. Ductility and the Workability of Metals. *Journal of the institute of metals*, 96, 1968.
- [43] G. R. Johnson and W. H. Cook. A Constitutive Model and Data for Metals Subjected to Large Strains, High Strain Rates and High Temperatures. *Proceedings of the 7th International Symposium on Ballistics, Hague*, pages 541–547, 1983.
- [44] A. Sabih and J. A. Nemes. Internal Ductile Failure Mechanisms in Steel Cold Heading Process. *Journal of Materials Processing Technology*, 209(9):4292–4311, May 2009.
- [45] N. Stander, W. Roux, T. Goel, T. Eggelston, and K. Craig. LS-OPT User’s Manual: A Design Optimization and Probabilistic Analysis Tool. *Livermore Software Technology Corporation (LSTC)*, 2011.

## REFERENCES

---

- [46] J. Croxon. The Properties of Steel Grade X65. [http://www.ehow.com/list\\_7492075\\_properties-steel-grade-x65.html%20](http://www.ehow.com/list_7492075_properties-steel-grade-x65.html%20), Cited date:[21 March 2012].
- [47] A. Manes. The Behaviour of an Offshore Steel Pipeline Subjected to Bending and Stretching. *Structural Impact Laboratory, Departement of Structural Engineering, Norwegian University of Science and Technology, Politecnico di Milano, Department of Mechanical Engineering*, 2009.
- [48] B. Opheim. Bending of Thin-Walled Aluminum Extrusions. *PhD Thesis, Departement of Structural Engineering, Norwegian University of Science and Technology*, 1996.
- [49] SIMLab. Theory Manual SIMLab Metal Model: Models for Metals and Alloys. *Structural Impact Laboratory, Departement of Structural Engineering, Norwegian University of Science and Technology*, 2012.
- [50] T. Nelligan. Ultrasonic Thickness Gaging. <http://www.olympus-ims.com/en/applications-and-solutions/introductory-ultrasonics/introduction-thickness-gaging/>, Cited date:[20 May 2012].
- [51] A. G. Hanssen, T. Auestad, T. Tryland, and M. Langseth. The Kicking Machine: A Device for Impact Testing of Structural Components. *International Journal of Crashworthiness*, 8(4):385–392, 2003.
- [52] SIMLab. Annual Report 2009. *Structural Impact Laboratory, Departement of Structural Engineering, Norwegian University of Science and Technology*, 2009.
- [53] J. O. Hallquist. LS-DYNA Theory Manual. *Livermore Software Technology Corporation (LSTC)*, 2006.
- [54] B. N. Maker and X. Zhu. Input Parameters for Springback Simulation using LS-DYNA. *Livermore Software Technology Corporation (LSTC)*, pages 1–11, 2001.
- [55] L. Xue. Stress Based Fracture Envelope for Damage Plastic Solids. *Engineering Fracture Mechanics*, 76(3):419–438, 2009.

## REFERENCES

---

# Appendices



# Appendix A

The relevant page of the material certificate regarding the composition of the X65 steel is included in Appendix A.1.



# Appendix B

The following appendix contains the measurements of pipe  $K$  and  $L$  (Appendix B.1) and a summary of impact against empty pipes (Appendix B.2).

## B.

---

### B.1 Measurement pipes

The measurements were conducted in the same manner as suggested by Slåttdalen and Ørmen (Figure B.1).

The measurement accuracy of the thickness and diameter was controlled by performing 30 measurements at the same point. The results are given in Table B.1.

The two pipes were measured at 32 points in the thickness direction with a PosiTector UTG (Ultrasonic Thickness Gage). The inner diameter of the pipe was measured at the two ends in four directions.

In the circular direction the pipes were divided into north  $N$ , south  $S$ , east  $E$  and west  $W$  direction. The longitudinal direction was divided into five zones (Figure B.1). The results in terms of the thickness are given in Table B.2 and B.3. In addition the average thickness, variance and standard deviation are included in the respective tables.

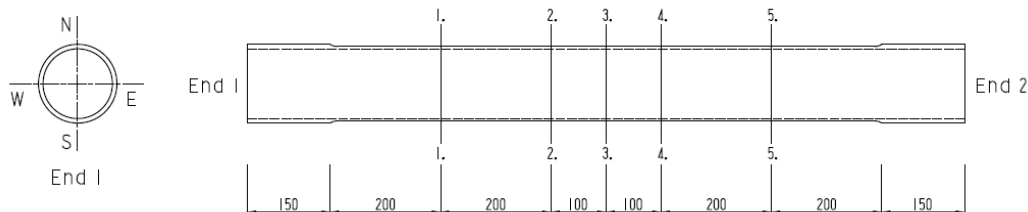


**Figure B.1:** Measuring points along the pipe [3].

The inner diameter of the pipes was measured at four different directions at both sides. Measured diameters for the two pipes are given in Table B.4 and B.5. In addition the average diameter, variance and standard deviation are included in the respective tables.

Table B.1: Thickness and diameter measurement accuracy.

Test number	Thickness (mm)	Test number	Diameter (mm)
1	4.20	1	122.65
2	4.20	2	122.41
3	4.15	3	122.58
4	4.18	4	122.33
5	4.19	5	122.47
6	4.18	6	121.83
7	4.14	7	121.97
8	4.23	8	122.66
9	4.18	9	122.64
10	4.24	10	122.64
11	4.15	11	122.52
12	4.13	12	122.40
13	4.15	13	122.39
14	4.16	14	121.93
15	4.19	15	122.61
16	4.18	16	122.16
17	4.14	17	122.10
18	4.13	18	122.72
19	4.20	19	122.38
20	4.16	20	122.63
21	4.13	21	122.50
22	4.20	22	122.47
23	4.13	23	122.12
24	4.10	24	121.92
25	4.12	25	122.08
26	4.11	26	122.23
27	4.15	27	122.23
28	4.15	28	122.18
29	4.11	29	122.18
30	4.14	30	122.00
$t_{\text{avg}}[mm]$	4.16	$D_{\text{avg}}[mm]$	122.33
$\text{Var}(\mathbf{t})[mm^2]$	0.00122	$\text{Var}(\mathbf{D})[mm^2]$	0.06594
$\text{Stdev}(\mathbf{t})[mm]$	0.03492	$\text{Stdev}(\mathbf{D})[mm]$	0.25678

**B.**

---

**Table B.2:** Thickness measurements on pipe K (mm).

<b>Direction</b>	1	2	3	4	5
<b>N</b>	4.10	4.07	3.96	3.90	3.50
<b>NW</b>		4.01	3.95	4.06	
<b>W</b>	3.96	4.03	4.06	4.15	4.02
<b>SW</b>		4.64	4.69	4.60	
<b>S</b>	4.26	4.27	4.19	4.20	4.39
<b>SE</b>		4.47	4.42	4.31	
<b>E</b>	4.03	4.01	3.85	3.71	3.78
<b>NE</b>		4.20	4.08	3.99	
<b>Summary</b>					
$t_{\text{avg}}[mm]$			4.12		
$\text{Var}(\mathbf{t})[mm^2]$			0.0674		
$\text{Stdev}(\mathbf{t})[mm]$			0.2596		

**Table B.3:** Thickness measurements on pipe L (mm).

<b>Direction</b>	1	2	3	4	5
<b>N</b>	4.20	3.98	3.71	3.70	3.78
<b>NW</b>		4.00	3.82	3.62	
<b>W</b>	3.93	3.97	3.85	3.71	3.53
<b>SW</b>		4.31	4.48	4.40	
<b>S</b>	4.22	4.30	4.43	4.46	4.36
<b>SE</b>		4.48	4.79	4.90	
<b>E</b>	4.60	4.29	4.33	4.52	4.67
<b>NE</b>		4.07	3.93	4.02	
<b>Summary</b>					
$t_{\text{avg}}[mm]$			4.17		
$\text{Var}(\mathbf{t})[mm^2]$			0.1242		
$\text{Stdev}(\mathbf{t})[mm]$			0.3524		

**Table B.4:** Diameter measurements on pipe  $K$  (mm).

Direction/pipe side	1	2
N-S	122.50	122.32
E-W	122.96	122.75
NW-SE	122.17	122.50
NE-SW	122.26	122.20
Summary		
$D_{\text{avg}}[mm]$	122.46	
$\text{Var}(\mathbf{D})[mm^2]$	0.0686	
$\text{Stdev}(\mathbf{D})[mm]$	0.2619	

**Table B.5:** Diameter measurements on pipe  $L$  (mm).

Direction/pipe side	1	2
N-S	122.49	122.38
E-W	122.80	122.74
NW-SE	122.50	122.07
NE-SW	122.37	122.39
Summary		
$D_{\text{avg}}[mm]$	122.47	
$\text{Var}(\mathbf{D})[mm^2]$	0.0459	
$\text{Stdev}(\mathbf{D})[mm]$	0.2143	

## B.

### B.2 Summary impact against empty pipes

In the following the test matrix (Table B.6) and impact against empty pipes are summarized (Figure B.2).

**Table B.6:** Test matrix empty pipes.

Name	Date	Velocity (m/s)	Average Thickness (mm)	Comment
Pipe-A	16.03.2010	3.24	3.89	-
Pipe-B	16.03.2010	5.13	3.86	-
Pipe-C	04.05.2010	3.06	4.04	No movie
Pipe-D	04.05.2010	2.72	4.26	-
Pipe-E	21.10.2010	4.14	4.19	-
Pipe-F	21.10.2010	2.69	4.09	-
Pipe-K	15.02.2012	5.24	4.12	-
Pipe-L	15.02.2012	3.26	3.86	No data

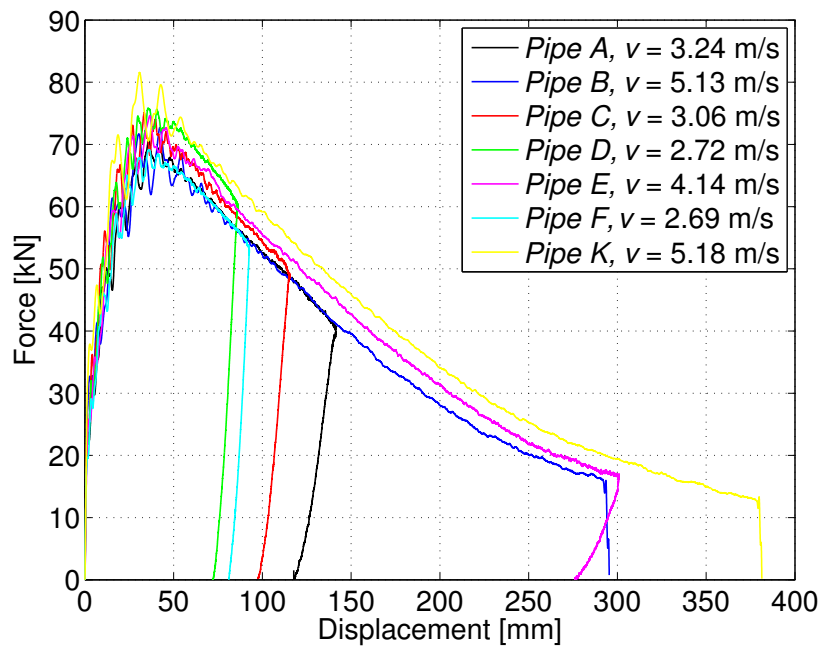


**Figure B.2:** Summary of impact tests on scaled pipes.

# Appendix C

The following appendix contains the input files for the numerical models in ABAQUS/Explicit (Appendix C.1) and LS-DYNA (Appendix C.2). Due to the size of the input files only the most important keywords and corresponding values are included. It is referred to the attached CD for the complete input files.

---

## C.1 Input file ABAQUS/Explicit

To make comparison of the material models easier, the numerical model was based on the work by Slåttedalen and Ørmen [3]. Therefore, the only new input was the material models described in Table 7.3.

```
*Heading
  Logaritmisk strainrate from 0.1 to 100
  %ADDITIONAL INFO IS FOUND IN THE CD ATTACHED TO THIS THESIS%
** PARTS
*Part, name=BOLT
*Node
%INPUT IS FOUND IN THE CD ATTACHED TO THIS THESIS%
*End Part
*Part, name=INDENTER_10MM
*Node
%INPUT IS FOUND IN THE CD ATTACHED TO THIS THESIS%
*End Part
*Part, name=RIGIDPIPE
%INPUT IS FOUND IN THE CD ATTACHED TO THIS THESIS%
*End Part
*Part, name=SHELLPIPE
%INPUT IS FOUND IN THE CD ATTACHED TO THIS THESIS%
*End Part
** ASSEMBLY
%INPUT IS FOUND IN THE CD ATTACHED TO THIS THESIS%
** Constraint: CONSTRAINT-1-1
% TIES THE DEFORMABLE AND RIGID PART OF THE PIPE%
*Tie, name=CONSTRAINT-1-1, adjust=yes, no rotation
%INPUT IS FOUND IN THE CD ATTACHED TO THIS THESIS%
** ELEMENT CONTROLS
*Section Controls, name=EC-1, ELEMENT DELETION=YES,
hourglass=RELAX STIFFNESS,
second order accuracy=YES
1., 1., 1.
*Amplitude, name=COS_MAX0_1 %AMPLITUDE STRETCHING STEP%
%INPUT IS FOUND IN THE CD ATTACHED TO THIS THESIS%
** MATERIALS
*Material, name=OPT
```

## C.1 Input file ABAQUS/Explicit

---

```
%MATERIAL MODEL FOUND BY INVERSE MODELING (AUNE & HOVDELIEN 2012)%
*Damage Initiation, criterion=JOHNSON COOK
  0.7,    1.79,    1.21, -0.00239,    0.,    1800.,    300., 0.000806
*Damage Evolution, type=DISPLACEMENT
  0.001,
*Density
  7.85e-09,
*Elastic
208000., 0.3
*Plastic, hardening=COMBINED, datatype=PARAMETERS, number backstresses=2
  299.00, 50401, 390.70, 1279,    12.80
*Cyclic Hardening, Rate=0.0
%INPUT ISOTROPIC HARDENING IS FOUND IN THE CD ATTACHED TO THIS THESIS%
*Cyclic Hardening, Rate=0.1
%INPUT ISOTROPIC HARDENING IS FOUND IN THE CD ATTACHED TO THIS THESIS%
*Cyclic Hardening, Rate=1.0
%INPUT ISOTROPIC HARDENING IS FOUND IN THE CD ATTACHED TO THIS THESIS%
*Cyclic Hardening, Rate=10
%INPUT ISOTROPIC HARDENING IS FOUND IN THE CD ATTACHED TO THIS THESIS%
*Cyclic Hardening, Rate=100
%INPUT ISOTROPIC HARDENING IS FOUND IN THE CD ATTACHED TO THIS THESIS%
*Material, name=DC
%MATERIAL MODEL FOUND BY DIRECT CALIBRATION (AUNE & HOVDELIEN 2012)%
*Damage Initiation, criterion=JOHNSON COOK
  0.7,    1.79,    1.21, -0.00239,    0.,    1800.,    300., 0.000806
*Damage Evolution, type=DISPLACEMENT
  0.001,
*Density
  7.85e-09,
*Elastic
208000., 0.3
*Plastic, hardening=COMBINED, datatype=PARAMETERS, number backstresses=2
  310.3, 67440.3, 425.1, 716.3,    9.3
*Cyclic Hardening, Rate=0.0
%INPUT ISOTROPIC HARDENING IS FOUND IN THE CD ATTACHED TO THIS THESIS%
*Cyclic Hardening, Rate=0.1
%INPUT ISOTROPIC HARDENING IS FOUND IN THE CD ATTACHED TO THIS THESIS%
*Cyclic Hardening, Rate=1.0
%INPUT ISOTROPIC HARDENING IS FOUND IN THE CD ATTACHED TO THIS THESIS%
```

## C.

---

```
*Cyclic Hardening, Rate=10
%INPUT ISOTROPIC HARDENING IS FOUND IN THE CD ATTACHED TO THIS THESIS%
*Cyclic Hardening, Rate=100
%INPUT ISOTROPIC HARDENING IS FOUND IN THE CD ATTACHED TO THIS THESIS%
*Material, name=FG4
%MATERIAL MODEL FOUND BY DIRECT CALIBRATION (FORNES & GABRIELSEN 2011)%
*Damage Initiation, criterion=JOHNSON COOK
  0.7,    1.49,    1.21, -0.00239,    0.,    1800.,    300., 0.000806
*Damage Evolution, type=DISPLACEMENT
0.,
*Density
  7.8e-09,
*Elastic
208000., 0.3
*Plastic, hardening=COMBINED, datatype=PARAMETERS, number backstresses=2
  330.3,115640.,  916.,  2225.,  22.
*Cyclic Hardening, Rate=0.0
%INPUT ISOTROPIC HARDENING IS FOUND IN THE CD ATTACHED TO THIS THESIS%
*Cyclic Hardening, Rate=0.1
%INPUT ISOTROPIC HARDENING IS FOUND IN THE CD ATTACHED TO THIS THESIS%
*Cyclic Hardening, Rate=1.0
%INPUT ISOTROPIC HARDENING IS FOUND IN THE CD ATTACHED TO THIS THESIS%
*Cyclic Hardening, Rate=10
%INPUT ISOTROPIC HARDENING IS FOUND IN THE CD ATTACHED TO THIS THESIS%
*Cyclic Hardening, Rate=100
%INPUT ISOTROPIC HARDENING IS FOUND IN THE CD ATTACHED TO THIS THESIS%
*Material, name=X65
%MATERIAL MODEL FOUND BY DIRECT CALIBRATION (SLÅTTEDALEN & ØRMEN 2010)%
*Damage Initiation, criterion=JOHNSON COOK
  0.7,    1.49,    1.21, -0.00239,    0.,    1800.,    300., 0.000806
*Damage Evolution, type=DISPLACEMENT
0.,
*Density
  7.8e-09,
*Elastic
208000., 0.3
*Plastic, hardening=JOHNSON COOK
  465.5, 410.83, 0.4793,    1.,  1800.,  300.
*Rate Dependent, type=JOHNSON COOK
```

```

0.0104, 0.000806
** INTERACTION PROPERTIES
*Surface Interaction, name=NOFRIC
*Friction
0.,
*Surface Behavior, pressure-overclosure=HARD
** BOUNDARY CONDITIONS
%SYMMETRIC BOUNDARY CONDITIONS ALONG THE EDGES OF THE PIPE (REF FIGURE 7.2)%
%INPUT IS FOUND IN THE CD ATTACHED TO THIS THESIS%
** PREDEFINED FIELDS
%INPUT IS FOUND IN THE CD ATTACHED TO THIS THESIS%
** STEP: Impact
*Step, name=Impact
Pipe A - Shell elements - 3,24m/s - t=3,85
, 0.18 %DURATION OF IMPACT IN SECONDS%
*Bulk Viscosity
0.06, 1.2
** INTERACTIONS
%INPUT IS FOUND IN THE CD ATTACHED TO THIS THESIS%
** OUTPUT REQUESTS
%INPUT IS FOUND IN THE CD ATTACHED TO THIS THESIS%
*End Step
** -----
** STEP: Stretching
*Step, name=Stretching
Pipe A - Shell Elements - 3,24m/s - t = 3,85
*Dynamic, Explicit
, 0.12 %DURATION STRETCHING STEP IN SECONDS%
*Bulk Viscosity
0.06, 1.2
** BOUNDARY CONDITIONS
%BOUNDARY CONDITIONS ARE FOUND IN THE CD ATTACHED TO THIS THESIS%
** OUTPUT REQUESTS
%INPUT IS FOUND IN THE CD ATTACHED TO THIS THESIS%
*End Step

```

## C.2 Input files LS-DYNA

In the following, the material card found by inverse modeling is included. It should be noted that this card only works in the SIMLab Metal Model. In addition, the input files for the impact and springback are included. These numerical models were originally made by Dr. Torodd Berstad. The only changes made in this thesis were additional output and implementation of the material card found by inverse modeling.

### C.2.1 Material card

```
*PARAMETER %MATERIAL PARAMETERS FOUND BY INVERSE MODELING%
R sigma0  299.00000
R thetar1 4000.0000
R qr1     160.00000
R thetar2 100.00000
R qr2     400.00000
R thetaX1 50401.000
R qX1     129.00000
R thetaX2 1279.0000
R qX2     100.00000
*MAT_USER_DEFINED_MATERIAL_MODELS %MATERIAL MODEL FOUND BY INVERSE MODELING%
1, 7.8500E-9, 41, 40, 35, 1, 39, 40
1, 1, 0, 0, 0, 0, 40
2, 1, 0, 0, 0, 0, 1, 0
0, 0, 0, 1, 0, 0, 0
$      E, nu, IFLAG1, IFLAG2, IFLAG3, WC, phi, gamma
2.0800E+5, 0.3,      1,      1,      1, 1595, 1,      1
$      S0, thetar1, qr1, thetar2, qr2, thetar3, qr3, m
&sigma0,  &thetar1, &qr1, &thetar2, &qr2,      0, 0, 0
$
0, 0, 0, 0, 0, 0, 0, 0
$
0, 0, 0, 0, 0, 0, 0, 0
$ yield, yield, thetaX1, qX1, thetaX2, qX2,      BULK,      SHEAR
0,      0,      &thetaX1, &qX1,&thetaX2,&qX2, 1.7333e+05, 0.8000e+05
$ cs, ps, ms, cq, pq, mq, alpha, me
0.0104, 0.000806, 0, 0, 0, 0,      0, 0
$ T, TO, TM, TC, RHO, CT, BETATQ
```

```

293, 293, 1993, 0, 7.8500E-9, 490,      0
$ s0, qsa, asa, bsa, csa, dotpsa, beta, dcr
  0,  0,  0,  0,  0,      0,  0,  0
$ mw1, wc0, v01, wmin, wmax, mw2, sc0, v02
  0,  0,  0,  0,  0,  0,  0,  0
$ scmin, scmax, dtsc, soft
  0,  0,  0,  0
$ updtflag, epsps, T, epspsdot, R1, R2, R3, X11
$      0,  0, 0,      0, 0, 0, 0,  0
$ X12, X13, X14, X15, X16, X21, X22, X23
$      0,  0, 0,      0, 0, 0, 0,  0
$ X24, X25, X26
$      0,  0, 0

```

### C.2.2 Impact analysis

```

*KEYWORD 200M %MEMORY NEEDED TO BE EXTENDED%
*PARAMETER %MATERIAL PARAMETERS FOUND BY INVERSE MODELING%
R sigma0  299.00000
R thetar1 4000.0000
R qr1     160.00000
R thetar2 100.00000
R qr2     400.00000
R thetaX1 50401.000
R qX1     129.00000
R thetaX2 1279.0000
R qX2     100.00000
*CONTROL_CONTACT
%INPUT IS FOUND IN THE CD ATTACHED TO THIS THESIS%
*CONTROL_CPU
%INPUT IS FOUND IN THE CD ATTACHED TO THIS THESIS%
*CONTROL_DAMPING
%INPUT IS FOUND IN THE CD ATTACHED TO THIS THESIS%
*CONTROL_ENERGY
%INPUT IS FOUND IN THE CD ATTACHED TO THIS THESIS%
*CONTROL_OUTPUT
%INPUT IS FOUND IN THE CD ATTACHED TO THIS THESIS%
*CONTROL_SHELL
%INPUT IS FOUND IN THE CD ATTACHED TO THIS THESIS%

```

C.

---

```
*CONTROL_TERMINATION %DURATION IMPACT IN SECONDS%
$#  endtim    endcyc    dtmin    endeng    endmas
    0.180000      0    0.000    0.000    0.000
*CONTROL_TIMESTEP
%INPUT IS FOUND IN THE CD ATTACHED TO THIS THESIS%
*DATABASE_BNDOUT
%INPUT IS FOUND IN THE CD ATTACHED TO THIS THESIS%
*DATABASE_RCFORC
%INPUT IS FOUND IN THE CD ATTACHED TO THIS THESIS%
*DATABASE_GLSTAT
%INPUT IS FOUND IN THE CD ATTACHED TO THIS THESIS%
*DATABASE_MATSUM
%INPUT IS FOUND IN THE CD ATTACHED TO THIS THESIS%
*DATABASE_NODOUT
%INPUT IS FOUND IN THE CD ATTACHED TO THIS THESIS%
*DATABASE_BINARY_D3PLOT
%INPUT IS FOUND IN THE CD ATTACHED TO THIS THESIS%
*DATABASE_EXTENT_BINARY
%INPUT IS FOUND IN THE CD ATTACHED TO THIS THESIS%
*DATABASE_HISTORY_NODE %NODAL OUTPUT%
$#    id1    id2    id3    id4    id5    id6    id7    id8
    44680    51448     0     0     0     0     0     0
*CONTACT_SURFACE_TO_SURFACE
$#    cid                                title
$#    ssid    msid    sstyp    mstyp    sboxid    mboxid    spr    mpr
     1     2     3     3         0         0     0     0
%INPUT IS FOUND IN THE CD ATTACHED TO THIS THESIS%
*CONTACT_SURFACE_TO_SURFACE
$#    cid                                title
$#    ssid    msid    sstyp    mstyp    sboxid    mboxid    spr    mpr
     1         3     3     3         0         0     0     0
%INPUT IS FOUND IN THE CD ATTACHED TO THIS THESIS%
*CONTACT_SURFACE_TO_SURFACE
$#    cid                                title
$#    ssid    msid    sstyp    mstyp    sboxid    mboxid    spr    mpr
     1     4     3     3         0         0     0     0
%INPUT IS FOUND IN THE CD ATTACHED TO THIS THESIS%
*PART
$# title
```

## C.2 Input files LS-DYNA

```

$#      pid  secid   mid  eosid  hgid  grav  adpopt  tmid
          1    1     1     0     0     0     0     0
*SECTION_SOLID
$#  secid  elform    aet
          1     2     0
*MAT_USER_DEFINED_MATERIAL_MODELS %MATERIAL FOUND BY INVERSE MODELING%
1, 7.8500E-9, 41, 40, 35, 1, 39, 40
1, 1, 0, 0, 0, 40
2, 1, 0, 0, 0, 0, 1, 0
0, 0, 0, 1, 0, 0, 0
$      E, nu, IFLAG1, IFLAG2, IFLAG3, WC, phi, gamma
2.0800E+5, 0.3,      1,      1,      1, 1595, 1, 1
$  S0, thetar1, qr1, thetar2, qr2, thetar3, qr3, m
&sigma0,  &thetar1, &qr1, &thetar2, &qr2,      0, 0, 0
$
0, 0, 0, 0, 0, 0, 0, 0
$
0, 0, 0, 0, 0, 0, 0, 0
$ yield, yield, thetaX1, qX1, thetaX2, qX2, BULK, SHEAR
      0,      0,&thetar1, &qX1, &thetar2, &qX2, 1.7333e+05, 0.8000e+05
$ cs, ps, ms, cq, pq, mq, alpha, me
      0.0104, 0.000806, 0, 0, 0, 0, 0, 0
$ T, T0, TM, TC, RHO, CT, BETATQ
293, 293, 1993, 0, 7.8500E-9, 490, 0
$ s0, qsa, asa, bsa, csa, dotpsa, beta, dcr
      0, 0, 0, 0, 0, 0, 0, 0
$ mw1, wc0, v01, wcmin, wcmax, mw2, sc0, v02
      0, 0, 0, 0, 0, 0, 0, 0
$ scmin, scmax, dtsc, soft
      0, 0, 0, 0
$ updtflag, epsps, T, epspsdot, R1, R2, R3, X11
$      0, 0, 0, 0, 0, 0, 0, 0
$ X12, X13, X14, X15, X16, X21, X22, X23
$      0, 0, 0, 0, 0, 0, 0, 0
$ X24, X25, X26
$      0, 0, 0
*PART
$# title
$#      pid  secid   mid  eosid  hgid  grav  adpopt  tmid

```

C.

---

```

      2      2      2      0      0      0      0      0
*SECTION_SHELL
$#  secid  elform  shrf   nip  propt  qr/irid  icomp  setyp
      2      2  0.000   0     1     0     0     1
*MAT_RIGID
$#   mid    ro      e      pr      n    couple  m    alias
      2  7.8500E-6  2.1000E+5  0.300000  0.000  0.000  0.000
%ADDITIONAL INPUT IS FOUND IN THE CD ATTACHED TO THIS THESIS%
*PART
$# title
$#   pid  secid   mid  eosid  hgid  grav  adpopt  tmid
      3    3     3     0     0     0     0     0
*SECTION_SHELL
$#  secid  elform  shrf   nip  propt  qr/irid  icomp  setyp
      3      2  0.000   0     1     0     0     1
%ADDITIONAL INPUT IS FOUND IN THE CD ATTACHED TO THIS THESIS%
*MAT_RIGID %RO CALCULATED AS DESCRIBED IN SECTION 7.3%
$#   mid    ro      e      pr      n    couple  m    alias
      3  2.3451E-5  2.1000E+5  0.300000  0.000  0.000  0.000
%ADDITIONAL INPUT IS FOUND IN THE CD ATTACHED TO THIS THESIS%
*PART
$# title
$#   pid  secid   mid  eosid  hgid  grav  adpopt  tmid
      4    4     4     0     0     0     0     0
*SECTION_SHELL
$#  secid  elform  shrf   nip  propt  qr/irid  icomp  setyp
      4      2  0.000   0     1     0     0     1
%ADDITIONAL INPUT IS FOUND IN THE CD ATTACHED TO THIS THESIS%
*MAT_RIGID
$#   mid    ro      e      pr      n    couple  m    alias
      4  7.8500E-6  2.1000E+5  0.300000  0.000  0.000  0.000
%ADDITIONAL INPUT IS FOUND IN THE CD ATTACHED TO THIS THESIS%
*INITIAL_VELOCITY_RIGID_BODY %VELOCITY INDENTER FIGURE 7.7%
$#   pid  vx      vy      vz  vxr   vyr   vzr  icid
      3 -3240.0000  0.000  0.000  0.000  0.000  0.000  0
*SET_PART_LIST
%INPUT IS FOUND IN THE CD ATTACHED TO THIS THESIS%
*INTERFACE_SPRINGBACK_LSDYNA %GENERATES THE DYNAIN FILE (SECTION 7.3)%
$#   psid      nshv      ftype
```

```
      1      20      0
$#   nid      tc      rc
      2045      1      0

*ELEMENT_SOLID
%INPUT IS FOUND IN THE CD ATTACHED TO THIS THESIS%
*ELEMENT_SHELL_THICKNESS_BETA
%INPUT IS FOUND IN THE CD ATTACHED TO THIS THESIS%
*NODE
%INPUT IS FOUND IN THE CD ATTACHED TO THIS THESIS%
*END
```

---

### C.2.3 Springback analysis

```
*KEYWORD 200M %MEMORY NEEDED TO BE EXTENDED%
*PARAMETER %MATERIAL PARAMETERS FOUND BY INVERSE MODELING%
R sigma0    299.00000
R thetar1   4000.0000
R qr1       160.00000
R thetar2   100.00000
R qr2       400.00000
R thetaX1   50401.000
R qX1       129.00000
R thetaX2   1279.0000
R qX2       100.00000
*CONTROL_TERMINATION %DURATION SPRINGBACK IN SECONDS%
  0.1000000  0  0.0000000  0  0.0000000
*CONTROL_SHELL
%INPUT IS FOUND IN THE CD ATTACHED TO THIS THESIS%
*CONTROL_OUTPUT
%INPUT IS FOUND IN THE CD ATTACHED TO THIS THESIS%
*DATABASE_BINARY_D3PLOT
%INPUT IS FOUND IN THE CD ATTACHED TO THIS THESIS%
*DATABASE_BINARY_D3THDT
%INPUT IS FOUND IN THE CD ATTACHED TO THIS THESIS%
*DATABASE_EXTENT_BINARY
%INPUT IS FOUND IN THE CD ATTACHED TO THIS THESIS%
*DATABASE_SECFORC
%INPUT IS FOUND IN THE CD ATTACHED TO THIS THESIS%
*DATABASE_BINARY_INTFOR
%INPUT IS FOUND IN THE CD ATTACHED TO THIS THESIS%
*CONTROL_CPU
%INPUT IS FOUND IN THE CD ATTACHED TO THIS THESIS%
$*INTERFACE_SPRINGBACK_DYNA3D %REQUESTS THE DYNAIN FILE%
$ 1
$ 1  2
*$SET_PART_LIST
$ 1
$ 1  2
$
$*****
```

```

*CONTROL_IMPLICIT_GENERAL
%TIME STEPS AND INCREMENT IMPLICIT ANALYSIS (SECTION 7.3)%
$  imflag  dt0    imform  nstepsb  igs  CNSTN  FORM
    1      0.025  1       10      0   0      6
*CONTROL_IMPLICIT_SOLUTION
%TOLERANCES EQUILIBRIUM ITERATIONS (SECTION 7.3)%
$  nlsolvr  ilimit  maxref  dctol    ectol  rctol  lstol
    2       1     200    0.001    0.01  0     999.
%INPUT IS FOUND IN THE CD ATTACHED TO THIS THESIS%
*CONTROL_IMPLICIT_SOLVER
%INPUT IS FOUND IN THE CD ATTACHED TO THIS THESIS%
*CONTROL_IMPLICIT_STABILIZATION
%ARTIFICIAL STABILIZATION AND SCALED SPRING STIFFNESS (SECTION 7.3)%
$  ias  scale  tstart  tend
    0   .0101  0       0
$*****
$
*MAT_USER_DEFINED_MATERIAL_MODELS %MATERIAL MODEL FOUND BY INVERSE MODELING%
1, 7.8500E-9, 41, 40, 35, 1, 39, 40
1, 1, 0, 0, 0, 40
2, 1, 0, 0, 0, 0, 1, 0
0, 0, 0, 1, 0, 0, 0
$      E, nu, IFLAG1, IFLAG2, IFLAG3, WC, phi, gamma
2.0800E+5, 0.3,      1,      1,      1, 1595, 1,      1
$  S0, thetar1, qr1, thetar2, qr2, thetar3, qr3, m
&sigma0,  &thetar1, &qr1, &thetar2, &qr2,      0,  0, 0
$
0, 0, 0, 0, 0, 0, 0, 0, 0
$
0, 0, 0, 0, 0, 0, 0, 0
$ yield, yield, thetaX1, qX1, thetaX2, qX2, BULK,      SHEAR
  0,      0,      &thetaX1, &qX1, &thetaX2, &qX2, 1.7333e+05, 0.8000e+05
$ cs, ps, ms, cq, pq, mq, alpha, me
  0.0104, 0.000806, 0, 0, 0, 0, 0, 0
$ T, T0, TM, TC, RHO, CT, BETATQ
293, 293, 1993, 0, 7.8500E-9, 490,      0
$ s0, qsa, asa, bsa, csa, dotpsa, beta, dcr
  0,  0,  0,  0,  0,      0,  0,  0
$ mw1, wc0, v01, wmin, wmax, mw2, sc0, v02

```

C.

---

```
0, 0, 0, 0, 0, 0, 0, 0
$ scmin, scmax, dtsc, soft
0, 0, 0, 0
$ updtflag, epsps, T, epspsdot, R1, R2, R3, X11
$ 0, 0, 0, 0, 0, 0, 0, 0
$ X12, X13, X14, X15, X16, X21, X22, X23
$ 0, 0, 0, 0, 0, 0, 0, 0
$ X24, X25, X26
$ 0, 0, 0
*SECTION_SOLID
$# secid elform aet
1 2 0
*PART
1 1 1 0 0 0 0 0
*INCLUDE
dynain
%CONTAINS THE DEFORMED MESH, STRESS AND STRAIN STATE FROM IMPACT ANALYSIS%
*END
```

# Appendix D

Finally, the machine drawings of the notched test specimens are included.

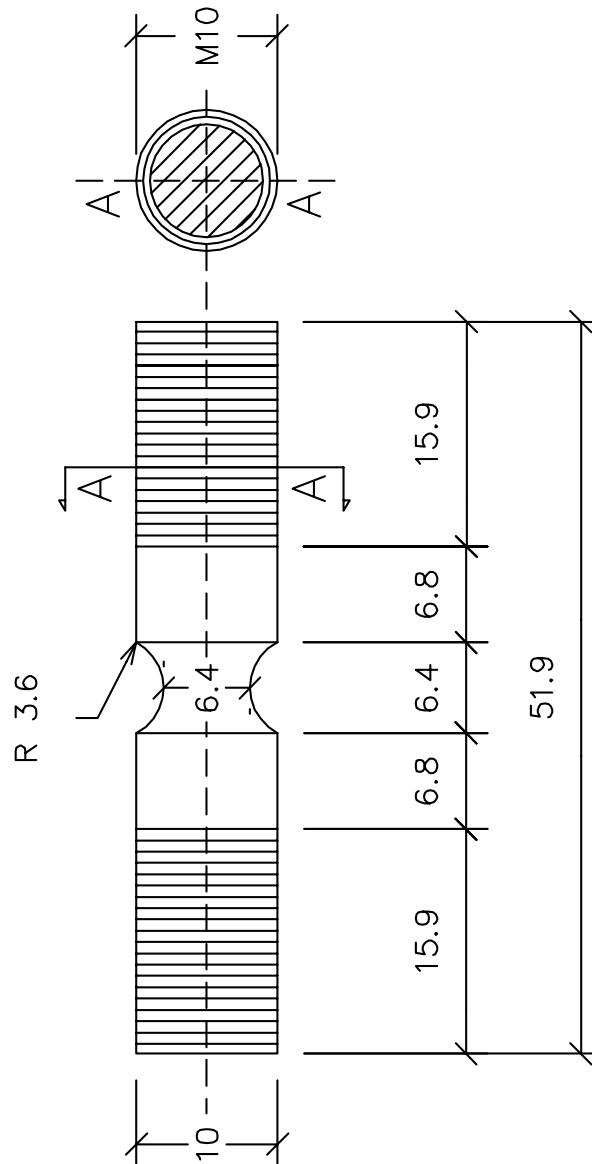
D.

---

## D.1 Machine drawings

### D.1.1 Material testing series 1

#### Machine Drawing Notched Specimen Test Series 1 (All measures in mm)



D.1.2 Material testing series 2

**Machine Drawing**  
Notched Specimen Test Series 2  
(All measures in mm)

